Ville Saarnio

Fluorescent Probes, Noble Metal Nanoparticles and their Nanocomposites

Detection of Nucleic Acids and Other Biological Targets

UNIVERSITY OF JYVÄSKYLÄ

FACULTY OF MATHEMATICS
AND SCIENCE

Ville Saarnio

Fluorescent Probes, Noble Metal Nanoparticles and their Nanocomposites

Detection of Nucleic Acids and Other Biological Targets

Esitetään Jyväskylän yliopiston matemaattis-luonnontieteellisen tiedekunnan suostumuksella julkisesti tarkastettavaksi maaliskuun 12. päivänä 2021 kello 12.

Academic dissertation to be publicly discussed, by permission of the Faculty of Mathematics and Science of the University of Jyväskylä, on March 12, 2021 at 12 o'clock.

JYVÄSKYLÄN YLIOPISTO
UNIVERSITY OF JYVÄSKYLÄ

JYVÄSKYLÄ 2021

ABSTRACT

This thesis covers the usage of fluorescent probes, noble metal nanoparticles, and their nanocomposites for applications in biological research. The use of cyanine dyes for nucleic acid detection was focused on with presentation of synthesis, characterization of the new compounds, as well as their interactions with nucleic acids, and their applications. New cyanine dyes were synthesized to produce covalently linkable derivatives based on the chemical structure of SYBR Green II. One of the new compounds showed sensitivity to RNA above its commercial predecessor. These molecules were used to detect the viral genome of echovirus 1 using *in vitro* assays. Furthermore, the possibility of improving the photophysical properties of the dyes was explored by synthesizing another set of molecules. With simple changes on the dye chromophore, significant improvement in the brightness, nucleic acid binding, and photostability were achieved. Based on this series, some conclusions on the structure – activity relationship were made for these dyes.

In the second part of the thesis, gold nanoclusters were studied as a potential solid support for conjugation of fluorescent probes. A synthesis for a new size of monolayer *para*-mercaptobenzoic acid -protected gold nanocluster was developed and characterized with PAGE and NMR spectroscopy. These clusters were then used to conjugate an azatriangelium dye to the cluster surface. The developed nanocomposite showed pH sensitivity with a fluorescence turn-on happening at a low pH. This was found to be due to the electrostatic binding and release of the dye from the quenching nanocluster proximity, due to the protonation of the ligand layer of the cluster. The literature review covers some of the advances in application of such nanocomposites employing larger, plasmonic noble metal nanoparticles. While the presented experimental work does not contain their use, they represent the logical next step for this research, due to their potential for further enhancing fluorescence detection.

Keywords: cyanine dye, fluorescence, nanochemistry, nucleic acid, supramolecular chemistry, gold nanocluster, noble metal nanoparticle

ABSTRAKTI

Väitöskirja käsittelee fluoresoivia koettimia, jalometallinanopartikkeleita, näiden nanokomposiitteja, sekä edellä mainittujen tuotteiden käyttöä biologisessa tutkimuksessa. Erityisesti teoksessa keskityttiin syaniiniväriaineiden käyttöön nukleiinihappojen havainnoinnissa, sisältäen näiden aineiden synteesiin, karakterisointiin, nukleiinihappovuorovaikutuksiin ja sovelluksiin liittyvää tutkimusta. Työssä tuotettiin uusia, kovalenttisesti kiinnitettäviä syaniiniväriaineita, jotka pohjautuivat aiemmin tuntemattoman SYBR Green II molekyylin rakenteeseen. Yksi uusista molekyyleistä osoitti suurempaa herkkyyttä RNA:ta kohtaan ylitse kaupallisten tuotteiden. Valmistettuja tuotteita käytettiin havaitsemaan echovirus 1 -viruksen RNA genomia koeputkiolosuhteissa. Lisäksi väriaineiden fotofysikaalisia ominaisuuksia parantamista tutkittiin syntetisoimalla toinen sarja syaniinivärejä. Yksinkertaisilla muutoksilla värin kromoforissa saatiin aikaan merkittäviä parannuksia fluoroforien kirkkaudessa, nukleiinihappositoutumisessa ja fotostabiilisuudessa. Tähän synteesisarjaan perustuen voitiin tehdä johtopäätöksiä värien rakenne – toiminta suhteista.

Väitöskirjan toisessa osassa tutkittiin kultananoklustereita potentiaalisina kiinteinä kiinnittymispintoina edellä mainituille fluoroforeille. Työssä kehitettiin synteesimetodi uuden *para*-merkaptobentsoehappo -suojatun kultananoklusterin kehittämiseksi ja tuote karakterisoitiin PAGE ja NMR spektroskopia menetelmien keinoin. Näitä klustereita käytettiin azatriangelium värin kovalenttiseen sitomiseen kultaklusterin pinnalle. Kehitetty nanokomposiitti omasi herkkyyden ympäristön pH:lle, fluoresenssi emission tapahtuessa vain matalassa pH:ssa. Tämän havaittiin johtuvan elektrostaattisesta sitoutumisesta ja vapautumisesta nanoklusterin vaikutusalueelta, riippuen ligandikerroksen protonoitumisasteesta. Kirjallisuuskatsaus kattaa osan mainitun kaltaisten nanokomposiittien kehityksestä isompien, plasmonisten jalometallinanopartikkelien kanssa. Vaikka kokeellinen osa työstä ei sisällä suurempien partikkelien käyttöä, ne esittävät loogisen seuraavan askeleen tälle tutkimukselle, johtuen niiden tarjoamasta suuresta potentiaalista fluoresenssipohjaisen havainnoinnin edistämisessä.

Author's address   Ville Saarnio
                          Department of Chemistry
                          Nanoscience Center
                          University of Jyväskylä
                          P.O. Box 35
                          FI-40014 Jyväskylä
                          ville.k.saarnio@jyu.fi

Supervisors   Docent Tanja Lahtinen
                          Department of Chemistry
                          University of Jyväskylä
                          P.O. Box 35
                          FI-40014 Jyväskylä

                          Professor Varpu Marjomäki
                          Department of Cell and Molecular Biology
                          University of Jyväskylä
                          P.O. Box 35
                          FI-40014 Jyväskylä

Reviewers   Associate Professor Jianping Xie
                          Department of Chemical & Biomolecular Engineering
                          National University of Singapore
                          Singapore

                          Associate Professor Byron Purse
                          Department of Chemistry & Biochemistry
                          San Diego State University
                          USA

Opponents   Associate Professor Nonappa
                          Faculty of Engineering and Natural Sciences
                          Tampere University
                          Finland

PREFACE

The year 2021 marks the ten-year anniversary of the day that I first set foot in the Department of Chemistry and Nanoscience center at University of Jyväskylä. Needless to say, such a timespan has given me the opportunity to meet most of the amazing people working at the department and its students throughout my development in the house. This also means, that I owe a great debt of gratitude to the many people I've had the pleasure to work with, be it from the simple coursework exercises to operating complex devices in my experiments.

One of these people is Adjunct Professor Tanja Lahtinen, who took me in at a very early stage and saw me all the way to the finish line of this PhD work as my supervisor. I am thankful for the received care in making sure things were running accordingly by and around me, and trust in giving me increasingly independence and space in order to learn to stand on my own two feet. My greatest gratitude goes to my second supervisor Professor Varpu Marjomäki, who provided me with a group of colleagues employed with a wholehearted attitude to work with. Your enthusiasm in science has been highly contagious and state of excitation so high, that I believe I have yet to observe you in your ground state. In the Marjomäki group I have had the honor to meet many aspiring scientists with great futures ahead of them. Particularly I would like to thank Visa and Sailee, for sticking their head down the rabbit hole and for their contributions in my research. Mira, Dhanik, Paula, Mari and the rest, thank you for your comradery.

Since starting my PhD work in 2017, I have had many people contribute to my development throughout the years. First, my gratitude is offered to my mentors in spectroscopy, Eero and Satu, who were always ready to help me with any issues in my research. Similarly, it has been nice to enjoy the friendly atmosphere we've had in the synthesis lab and around which I would like to thank Kirsi, Kaisa, Evgeny, Margarita, Mikael, Johanna A., Johanna S., Małgorzata, Nemanja, and others for. It's been also a joy of having a great band of professionals, who not only provided help with any problem one can imagine, were also up for a friendly chat inbetween keeping the circus running. Johanna H., Pia, Elina, Satu, Esa, Heikki and Pasi, your work is appreciated.

I greatly appreciate the support I have received throughout this period in order to be part of presenting these collective works to the world. This includes everyone who I've been given the opportunity to collaborate with, both in practice and writing. Particularly, I would like to thank Professors Mika Pettersson, Hannu Häkkinen and Associate Professor Jussi Toppari for the possibilities they have offered me along the way. I am grateful for the financial support Jane and Aatos Erkko foundation and Vilho, Yrjö and Kalle Väisälä foundation, for making this work possible. One of the most memorable moments of my PhD was meeting Professor Marcus Wilhelmsson in Glasgow and the following collaboration with him and Jesper Nilsson with my first research article. My deepest gratitude goes to these two men for their pivotal contribution to this work and with that to my thesis as a whole. Additionally, I

LIST OF INCLUDED PUBLICATIONS

I   Tanja Lahtinen, Eero Hulkko, Karolina Sokołowska, Tiia-Riikka Tero, Ville Saarnio, Johan Lindgren, Mika Pettersson, Hannu Häkkinen, and Lauri Lehtovaara, Covalently Linked Multimers of Gold Nanoclusters Au_{102}(p-MBA)$_{44}$ and $Au_{\sim250}$(p-MBA)$_n$, *Nanoscale*, **2016**, 8, 18665 – 18674.

II   Karolina Sokołowska, Sami Malola, Manu Lahtinen, Ville Saarnio, Perttu Permi, Katariina Koskinen, Matti Jalasvuori, Hannu Häkkinen, Lauri Lehtovaara, and Tanja Lahtinen, Towards Controlled Synthesis of Water-Soluble Gold Nanoclusters: Synthesis and Analysis, *Journal of Physical Chemistry C*, **2019**, 123, 2602 – 2612.

III   Ville Saarnio, Kirsi Salorinne, Visa Ruokolainen, Jesper Nilsson, Tiia-Riikka Tero, Sami Oikarinen, Marcus Wilhelmsson, Tanja Lahtinen, and Varpu Marjomäki, Development of functionalized SYBR green II related cyanine dyes for viral RNA detection, *Dyes and Pigments*, **2020**, 177, 108282.

IV   Ville Saarnio, Johanna Alaranta, and Tanja Lahtinen, Systematic study of SYBR Green chromophore reveals major improvement with one heteroatom difference, *submitted manuscript*.

V   Eero Hulkko, Tanja Lahtinen, Varpu Marjomäki, Emmi Pohjolainen, Ville Saarnio, Karolina Sokołowska, Ardra Ajitha, Mikael Kuisma, Lauri Lehtovaara, Gerrit Groenhof, Hannu Häkkinen, and Mika Pettersson, Link and release - Coupling of a gold nanocluster with a fluorophore for intracellular pH imaging, *submitted manuscript*.

Author's contribution

The author conducted the synthesis development and synthesis of the $Au_{\sim250}$(p-MBA)$_n$ cluster in article **I** and **II**. He carried out the characterization of gold nanoclusters using NMR and DOSY spectroscopy in article **II** and gel electrophoresis in article **V**. The fluorescence spectroscopy titrations of the unbound dye – gold nanocluster were done by the author in article **V**. The design and conduction of the syntheses, spectroscopic characterization of the products and their photophysical properties, including nucleic acid interactions (LD spectroscopy not included) in papers **III** and **IV** were handled by the author. Additionally, the author contributed to the design and supervision of the biological measurements and applications in paper **III**.

ABBREVIATIONS

AgNP	Silver nanoparticle
AuNC	Gold nanocluster
AuNP	Gold nanoparticle
AuMPC	Monolayer protected gold nanocluster
BSA	Bovine serum albumin
bp	Basepair
DCM	Dichloromethane
DMSO	Dimethylsulfoxide
DNA	Deoxyribonucleic acid
DOX	Doxorubicin
EDTA	Ethylenediaminetetraacetic acid
FL	Fluorecein
FRET	Förster resonance energy transfer
GFP	Green fluorescent protein
HOMO	Highest occupied molecular orbital
HPLC	High-performance liquid chromatography
LOD	Limit of detection
LUMO	Lowest unoccupied molecular orbital
MEF	Metal-enhanced fluorescence
MUDA	11-mercaptoundecanoic acid
NP	Nanoparticle
PAGE	Polyacrylamide gel electrophoresis
PBS	Phosphate buffered saline
PDT	Photodynamic therapy
pMBA	*Para*-mercaptobenzoic acid
PTT	Photothermal therapy
QY	Quantum yield
R6G	Rhodamine 6G
RhB	Rhodamine B
RNA	Ribonucleic acid
ROS	Reactive oxygen species
SEC	Size exclusion chromatography
SERS	Surface-enhanced Raman spectroscopy
SG	Glutathione
SiF	Silver island films
SPR	Surface plasmon resonance
TEA	Triethyl amine
TEM	Transmission electron microscopy
Tris	Tris(hydroxymethyl)aminomethane
TO	Thiazole orange
YO	Oxazole yellow

# CONTENTS

1   INTRODUCTION

Nanochemistry, as the name suggests, combines nanoscience and conventional chemistry to study phenomena in the 1-100 nanometer scale.[1] From the viewpoint of conventional chemistry, which deals mostly with assembly of atoms into molecules of desire, nanochemistry expands its focus into bigger structures and phenomena related to their shape, size and self-assembly. A great example of this is polymer chemistry, where instead of focusing on control over their building blocks, nanochemistry seeks control over their joining into polymers. This in turn leads to introduction of statistics in their manufacture, which conventional chemistry rarely deals with.

From the viewpoint of nanoscience, nanochemistry emphasizes the bottom-up approach in its manufacture.[2] In practice, this means that different nanosystems are built from smaller pieces into bigger ones, sometimes atom by atom. The work in this thesis is based on some of the most exciting topics in homogeneous solution phase nanochemistry, such as noble metal nanoparticles and clusters. A large portion of the thesis is dedicated to fluorescent probes exhibiting highly interesting supramolecular behaviour and their application in cell and molecular biology.

1.1   Fluorescent probes

Every person on Earth has first-hand experience with organic dyes. Everyone is familiar with the beautiful green colours of the flora, the blue colour of a pair of jeans and the red surface of an apple. What is common to all these colour molecules is their structure, which usually consists of large aromatic, often heterocyclic systems. Such structural features impart the molecules with delocalized π electrons, which are able to absorb photons in the electromagnetic spectrum of visible light. Absorption is an event where an incoming photon quantum excites the electrons from their ground energy state (S_0) to a higher excitation state ($S_{\geq 1}$) as shown in the Jablonski diagram below (Figure **1**).[3] The

energy of the photon interacting with the organic dye needs to match the gap between the two energy states in order for absorption to happen. Because of this, each molecule can absorb only certain wavelengths of photons, which gives each dye its specific colour.
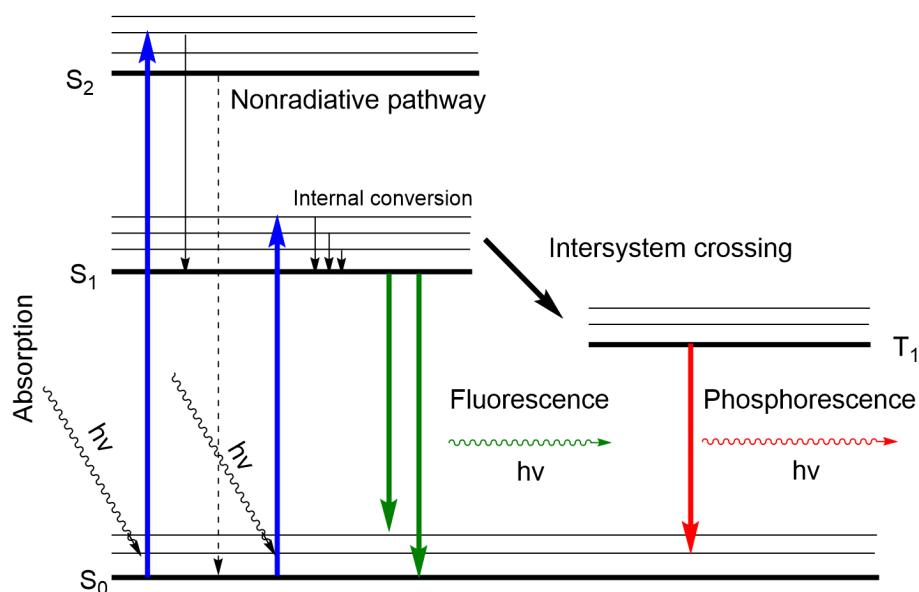
Figure 1. Jablonski diagram for excitation to higher energy states, fluorescence, phosphorescence, and other possible relaxation pathways of a chromophore.[3]

Once in excited state, the molecule can return to its ground state through multiple pathways.[3] This is known as internal conversion. In all cases, at least some amount of energy is lost as heat through motion and vibration of the molecule. In the non-radiative pathway, the whole excitation energy of the chromophore is lost this way. However, some organic dyes can recover their ground state through a quantized pathway, luminescence. In luminescence, the energy of the excited state is converted into a photon, which the molecule emits. The most common pathway for such emission happens through internal conversion from S_1 state to S_0, also known as fluorescence. Another possible way for emitting a photon is for molecule to make an intersystem crossing to a longer lasting triplet state (T_1), from where the emission of photon and return to S_0 is known as phosphorescence.

With fluorescent dyes, the radiative (luminescent) and non-radiative pathways offer two competing ways for the relaxation back to ground state.[3,4] The resulting amount of emission is determined by the rate that each pathway takes place *i.e.* if the non-radiative pathway is faster, then less photons are emitted by the molecule. To compare this efficiency between different dyes, quantum yield (Φ) is used to describe the fraction of absorbed photons that are converted into emission. Naturally, higher values correspond to more fluorescence, with 100 % value meaning that every absorbed photon is converted into fluorescence. Similarly for absorption, molar absorptivity coefficient (ε) is used to describe the efficiency of chromophores to get excited by photons passing through a solution of the chromophore in question. A

common way to compare fluorescent probes between each other is reporting brightness of the molecules, which can be derived by multiplying the molar absorptivity with the quantum yield of the molecule.

While the brightness of a fluorescent probe is a pivotal variable when evaluating the superiority of different dyes, many other factors are important to consider, particularly for biological applications.[4] For example, photostability of the chromophore is an important factor that describes how resistent they are to photobleaching *i.e.* becoming non-fluorescent. In order to be used in biological applications, the dyes should be non-cytotoxic and should possess high solubility in aqueous solutions, which is not trivial as many organic dyes lack hydrophilicity. If the desired application of fluorescent probe involves a turn-on mechanism for the fluorescence, additional factors need to be considered, as described in chapter 1.3. Regardless of the strict requirements for fluorescent probes for application in biological systems, countless different molecules are available for different purposes, covering the whole visible spectrum of light. These dyes include the many derivatives of coumarin-based dyes, as well as the highly employed xanthane dyes based on rhodamine and fluorescein chromophores. Equally important are the widely used cyanine dyes which will be covered in chapter 2.

1.2 Nanoparticles

Nanoparticle is a term covering all small particulate matter in the 1-100 nm scale.[5] They come in all shapes, from the simple spherical shapes to the more complex rods, stars and cubic structures. Nanoparticles can be produced from a plethora of different elements, including many transition metals as well as silicon dioxide, clay, carbon and some other organic materials. Production methods are available for both bottom-up and top-down synthesis. Making matter into miniscule particles like this leads to new material properties, which have already found applications in everyday products such as sunscreens, clothes and even hockey sticks.

With metallic nanoparticles the new properties show high promise for application in the field of medicine. These properties are inherent due to surface plasmon resonance (SPR), which is stimulated by interaction with light.[6] Most common metal particles used in applications taking advantage of the SPR are gold and silver nanoparticles.[7,8] SPR is the movement of electrons similar to the delocalization that is present in bulk metals. However due to the size restriction of the nanoscale, this movement turns into an oscillation of electron density from one end of the particle to the other, creating partial positive and negative charges in the particle (Figure **2**). Subsequently, this resonant oscillation leads to a surface plasmon polariton *i.e.* an electromagnetic surface wave, on the nanoparticle surface. This phenomenon has been employed in enhancing several spectroscopic measurement methods, most notably the Raman scattering.[9]
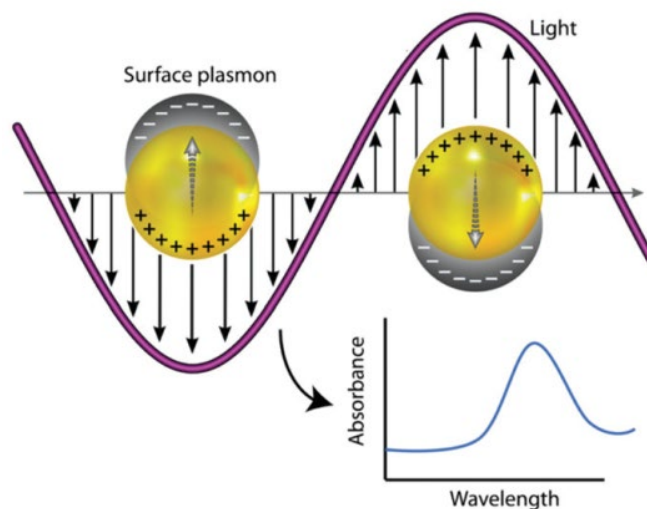
Figure 2. Surface plasmon resonance of a nanoparticle experiencing an electromagnetic wave, showing the oscillation of electron density within the particle. The SPR shows as an absorption at a metal specific wavelength, as shown by the inset spectrum. Reproduced from Ref. 10 with permission from The Royal Society of Chemistry.

The strength of the SPR is dependent on the size of the metal particle, where decreasing the size reduces the strength of the SPR.[11] Similarly, with reduced size, also the metallic character of the particle diminishes. The transition from metallic into semiconducting and then molecular electronic structure happens at size of hundreds of atoms. For example for gold, a particle containing >150 atoms is still metallic, whereas particle with <130 atoms has lost this character.[12] These nanoparticles comprising from small number up to few hundred metal atoms at most are known as nanoclusters.[13] Another major difference is that nanoclusters often have a specific atomic composition, like molecules, whereas the larger nanoparticles are a statistical size distribution of many different sizes. Not only do nanoclusters provide a great subject for understanding the new theoretical topics introduced with nanoparticles, but they also present a completely new species of molecules ready to be applied in novel ways. Chapter 3 focuses on the chemistry of colloidal nanoparticles (NP) and gold nanoclusters, which were employed in this work for new applications.

1.3 Supramolecular Chemistry

Similar to the way conventional chemistry aims to build novel molecules by forming new bonds between existing molecules, supramolecular chemistry aims for the same thing using non-covalent interactions.[14] These interactions include interactions between ions and dipoles as well as even weaker phenomena, such as hydrogen bonds, hydrophobic interactions, π – π stacking and van der Waals forces. Supramolecular chemistry aims to produce

complexes that have novel properties, where multiple weak interactions lead to stable bonding between two molecules, rivaling the covalent bond in strength.[15] These interactions can lead to spontaneous self-assembly and molecular folding between molecules, which are the backbone of this field. This type of behaviour is prominent in biomolecules found in nature. Great examples are the substrate bonding mechanism of enzymes or the hydrogen binding between DNA bases that keep the DNA helix intact. In a sense, supramolecular chemistry can be thought of as an attempt of chemists to mimic nature.

The key concept of this field is the host-guest chemistry, where the design of one or the other aims to be as complementary to its target of binding as possible. This complementarity then induces the spontaneous formation of a supramolecular complex.[16,17] For example the crown ethers are able to bind alkali metal ions into the center of the molecule due to the complementary size to the ionic radius of the guest and the free electron pairs on the oxygen atoms, complementing the positivity of the ions. This approach shows great promise for applications involving delivery of smaller molecules to a target location or removing components from complex mixtures. For fluorescent probes, the combination of supramolecular binders has introduced many possibilities for lighting up probes in the presence of target analytes or some other environmental change.[18]

The basic mechanism is that the formation of the supramolecular complex activates the fluorescent dye. As the formation of the complex depends on non-covalent interactions which can form and break, the complexation becomes an equilibrium reaction.[19] This means that depending on the concentration of guest and host molecules in the environment, the complex disassociates and forms at certain rates and reaching the equilibrium only means that the two events are happening at the same rate. In combination with fluorescent probes, not only can the concentration of a guest/analyte be determined qualitatively but also quantitatively, if the concentration of the host in the system is known. Thus, the combination of supramolecular chemistry with fluorescent probes gives many novel highly potent tools for researchers to analyze *e.g.* environmental samples or biological systems with increased accuracy. The same weak interactions involved in supramolecular chemistry also govern the interactions that different nanoparticles have with different compounds in their surroundings. The combination of fluorophores and nanoparticles in chemical sensing opens up novel applications through different interactions between the two species and different analytes, as will be shown in this work. This combination has also been used in this thesis to improve biological sensing and its applications with fluorescent probes, as will be shown below.

2 CYANINE DYES

The characteristics that define cyanine dyes are two nitrogen atoms sharing a cationic charge across a conjugated aromatic system, connected through a polymethine bridge, as shown in Figure **3**.[20]
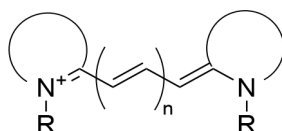
Figure 3. General chemical structure of cyanine dyes.

Depending on the number of connecting vinylene carbons in the polymethine chain, the molecules are further subcategorized. For example dyes bridged through one carbon atom are monomethine cyanine dyes, whereas a bridge containing seven carbon atoms classifies as a heptamethine dye. The two nitrogen atoms can be at a terminal position or part of a heterocyclic ring in the molecule. In streptocyanines both nitrogens are in a terminal location of the molecule, whereas with hemicyanines the other nitrogen is part of a heterocycle. Many kinds of heteroaromatic moieties are commonly observed with these dyes, either at one or both ends. Most often seen groups are for example benzoxazole, indole, quinoline and benzothiazole. If the substituents at different ends of the methine bridge are the same, the dye is considered to be symmetrical and otherwise unsymmetrical. As is evident, cyanine dyes are a diverse group of organic dyes and hence in order to draw conclusions on their characteristics and behavior, the above-described classification plays a crucial role. This chapter is divided to focus on monomethine dyes and dyes that contain longer methine bridges separately. Monomethine probes have been primarily applied for detection of nucleic acids and thus are in the pinpoint of the thesis. First, the synthetic methods for producing cyanine dyes are explored in chapter 2.1., after which their exemplary photophysical properties will be covered in chapter 2.2., leading to the topic of highest interest, their use in nucleic acid detection in chapter 2.3. In this chapter, the properties of these compounds will be covered

with a focus to the phenomena related to their use in life science applications, starting with the preparation of these molecules, as described below.

2.1   Synthesis

The first synthesis of a cyanine dye was reported by Williams in 1856.[21] Since then, countless new derivatives have been made spanning the whole visible light spectrum. Many of these new compounds have found widespread application, not only as simple colouring dyes, but for example as recording agents in CD and DVD technologies.[22] Additionally, many different types of cyanine dyes have become fluorescent probes of choice for life science laboratories worldwide. Perhaps most notable of these products are the Cy-family of dyes, shown in chapter 2.1.2.[23] Developing these dyes has required a significant progress in the synthetic methods in making them and has also led to increasingly exquisite molecules as well as completely novel types such as the hemi-, merocyanines, styryls and squarylium dyes. In this section the synthetic methods for producing different cyanine dyes will be covered. Increased emphasis will be put towards the synthesis of monomethine unsymmetrical cyanine dyes, the focus of the experimental work.

2.1.1   Synthesis of monomethine cyanine dyes

The synthesis of monomethine cyanine dyes has produced countless different dye compounds. The most common approach for their synthesis has been through cyanine condensation reaction of two quaternary ammonium salts (Figure **4**).[24] These salts are often prepared through nucleophilic substitution reactions of tertiary amine and a halogen, which offers possibilities for variation. For the production of monomethine moiety, it is important that one of these salts is methyl substituted and the other reactant contains a good leaving group, which is removed in the process. Commonly used leaving groups in cyanine condensation include chloride, sulfonate and more recently, methyl thiolate groups. While the methyl group can also contain a leaving group, in most cases in order for a sp^2 hybridized carbon to be formed, a proton leaves the molecule. This is often promoted by conducting the reactions in basic conditions with the use of organic bases, such as the triallyl amines. This approach for synthesizing monomethine cyanine dyes has remained the general approach.
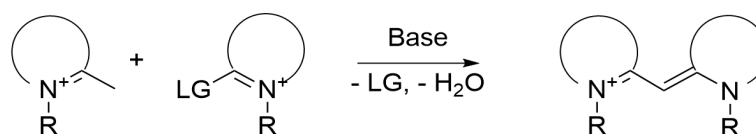
Figure 4. Synthesis of monomethine cyanine dyes through cyanine condensation of two quaternary ammonium salts. LG stands for leaving group.[20]

The most recent developments have focused on solvent-free approaches to further improve it. For example, microwave-assisted synthesis was pioneered by the group of Zhang, resulting in higher yields and shorter reaction times compared to the conventional methods.[25,26] A further advancement was made by the group of Deligeorgiev that achieved similar results using simple melting reactions without the presence of base.[27]

While the reaction mechanism of this classical condensation has not been conclusively established, many educated proposals have been made, for example the one from Fu *et al.*, presented in Figure **5**.[26] In the proposed mechanism the base deprotonates the methyl group, which is stabilized by the resonance structure between the cationic nitrogen. Then the carbanion reacts in a S_N1 type of fashion with the carbon containing a leaving group of the other reactant. The cationic nitrogen first stabilizes the reaction intermediate by accepting an electron pair, after which the leaving group is removed and the deprotonation of the methine bridge finalizes the cyanine dye structure.
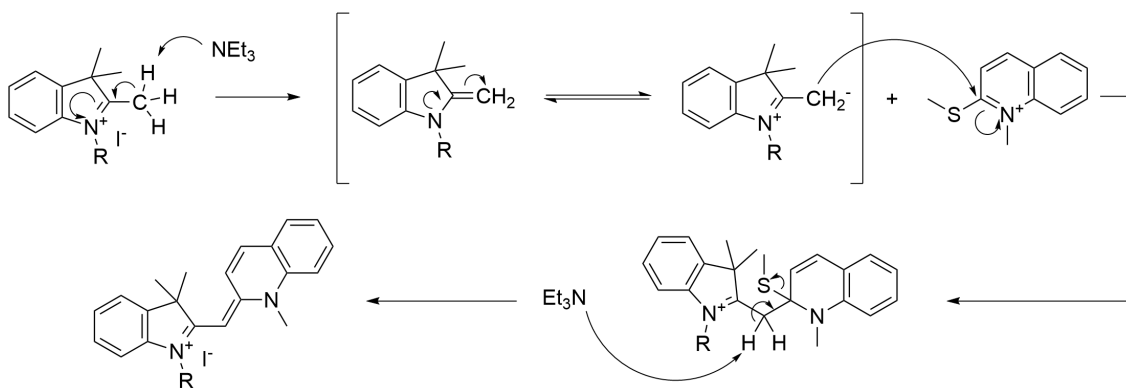
Figure 5. Proposed reaction mechanism for the cyanine condensation reaction employing methylthiolate as the leaving group, as proposed by Fu *et al.* in Ref. 26.

With the unsymmetrical monomethine cyanine dyes the thiazole orange (TO), first synthesized in 1942, has served as an important foundation for developing new dyes. Despite its early inception, the surge in development of new dyes only started after identification of its nucleic acid sensing capabilities in 1986.[28] Not long after this, TO and a close structural comparison, oxazole yellow (YO), together with their homodimers were identified as potent probes for nucleic acid sensing (Figure **6**).[29] These two compounds served as a starting point for countless new compounds in attempts to improve their nucleic acid sensing characteristics. Substitution of the cyanine nitrogen atoms has been a very popular target of improvement attempts. The nitrogen has been substituted with longer, charged substituents to improve water solubility[30,31] or to introduce new functional groups[32,33] for further applications. Introduction of carboxylic acid and pyridine groups has been particularly popular. Also the use of fluoride as a substituent and its effects has been evaluated, showing improvement with both quantum yield and photostability.[34,35] Most importantly, the addition of a phenyl substituent on the quinoline moiety

coupled with a 2-diallylamine substituent led to the conception of commercial dyes, such as the SYBR Green family (Figure **6**), that are among the most used nucleic acid stains in laboratories worldwide.[36]
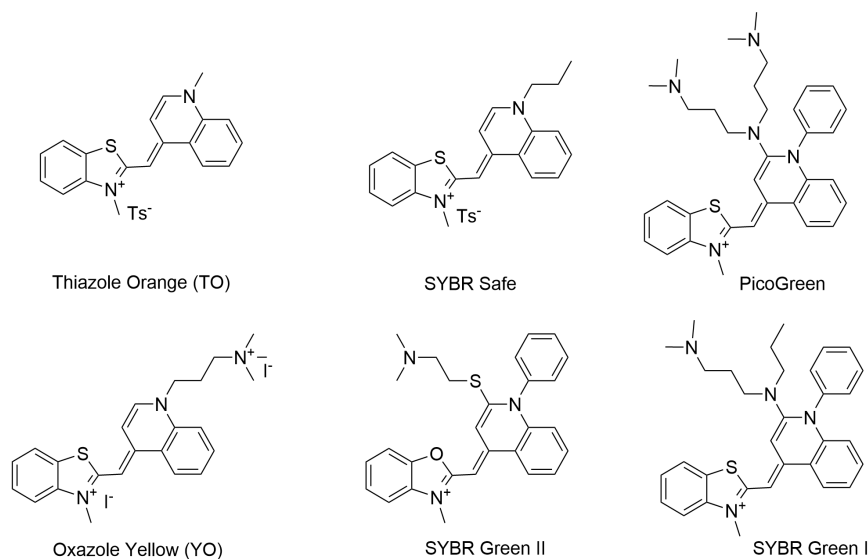
Figure 6. Chemical structures of the well-known Thiazole Orange and Oxazole Yellow together with the known commercial nucleic acid sensors of the SYBR family.[33,37–39]

Similarly, the substitution of the chromophore has been extensively explored. The benzothiazole has been substituted with many different functional groups including methoxy, nitro and different halogens.[40] Furthermore, even additional heterocyclic substituents on the thiazole, such as repeating thiazole/oxazole units, have been explored.[41] Apart from variation of substituents and heteroatoms in the chromophore, the possibilities offered by completely replacing the quinoline with another heteroatomic moiety have been researched.[42,43] Additionally a derivative with an acridine moiety has been studied as a replacement of the quinoline.[44] In summary, a plethora of TO and YO –based organic dye derivatives have been synthesized in attempt to improve their fluorogenic properties through a multitude of ways. The way these changes affect their photophysical properties and potency in nucleic acid sensing will be further evaluated in chapters 2.2 and 2.3.

2.1.2 Synthesis of multimethine cyanine dyes

The principle for obtaining cyanine dyes with longer (di – hepta)methine bridges is largely the same as for making monomethine derivatives; reacting two quaternary ammonium salts together in a cyanine condensation. However, the longer bridging unit both demands and makes possible alternative synthetic approaches. While the above described thioether method of Brooker *et al.* has been used to synthesize also tri- and pentamethine cyanines[45], the commonplace methods make use of aldehydes and dipyridines. The aldehyde method is highly potent for forming particularly trimethine cyanines. A methyl

group on one of the starting reagents can be transformed into a Vilsmeier reagent with phosphorus oxychloride and dimethyl formamide (DMF) in basic conditions.[46] After this, another ammonium salt is able to react with the carbocation of the aldehyde to form the propyl bridge. In the final step of the reaction a water molecule is eliminated from the structure and the trimethine bridge is produced (Figure 7). This cyanine condensation through nucleophilic attack to aldehyde carbon and elimination of water offers another general pathway for production of cyanine dyes. However, production of penta- or heptamethine derivatives often increases the complexity of the process with requirement of more complex reagents[47] or increased reaction steps[48].
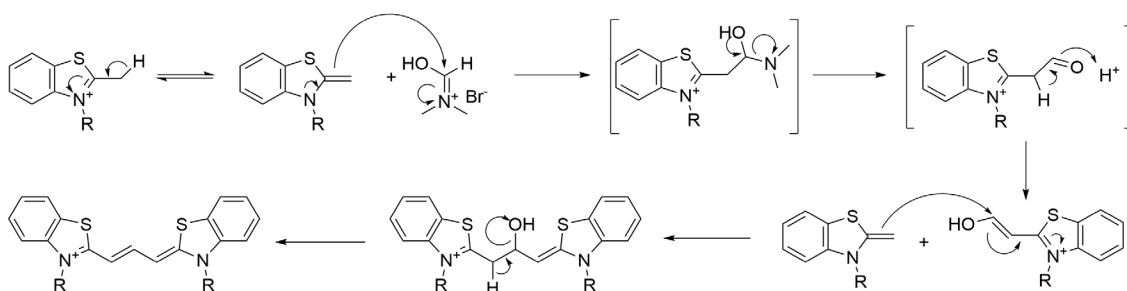
Figure 7. Suggested reaction mechanism of the aldehyde method employing a Vilsmeier-like reagent, as presented by El-Shishtawy *et al.*[46]

Another well-established method for synthesizing the longest methine bridges is known as the hemicyanine method. Using this method, the bridge moiety is introduced in the form of hemicyanine linker that reacts with two methyl substituted ammonium salts. In the reaction, the aniline group acts as a leaving group in the presence of acetate ion (Figure 8). As shown in the figure, the acetate ion binds to the nitrogen atom in the hemicyanine, promoting leaving group behaviour. The versatility of this method is significant, as only simple adjustments are needed to adjust the synthesis for different products; the hemicyanine starting material offers opportunities for simple changes to the methine bridge substitution. In order to produce symmetric cyanines, using a 2:1 ammonium salt to hemicyanine ratio is needed. In contrast, to synthesize unsymmetrical dyes, a 1:1 ratio together with adjustments to reaction time and temperature are made in order to replace a single aniline group on the hemicyanine. Subsequent addition of the second ammonium salt then produces the unsymmetrical cyanine dye.
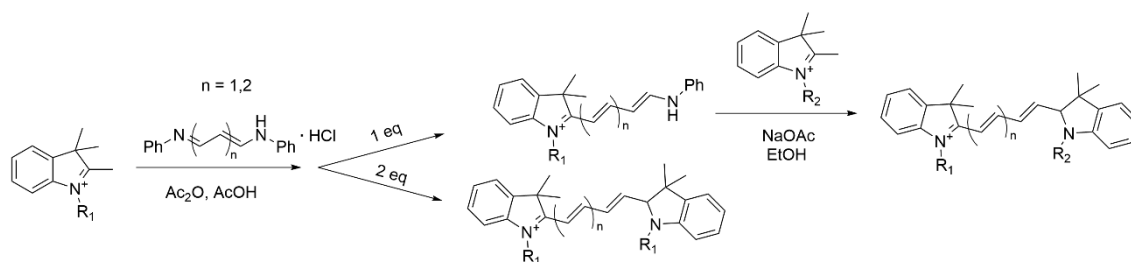
Figure 8. The generalized reaction scheme for the hemicyanine method, applied from Ref 24. Using two equivalents of starting quaternary ammonium salt, a symmetrical cyanine dye can be produced. By using one equivalent, the reaction intermediate can be reacted further with a completely different quaternary salt.

Similar to the importance of TO and YO for the research on monomethine cyanine dyes, the Cy family of cyanine dyes (Figure **9**) has served as foundation for longer derivatives since they were first made. After the Waggoner group synthesized the symmetrical 3-dimethylindole tri-, penta- and heptamethine cyanine dyes (Cy3, Cy5 and Cy7 respectively), they have become some of the world's most used fluorescent markers.[23] Also alike to the TO and YO, the cyanine nitrogens offer easy reaction site for introduction of additional functionality for the dyes.[49,50] Similarly many changes to the indole, from simple substitution of hydrogens to completely replacing the indole with *e.g.* thiazole or oxazole and their different substitution, has been an object of prolific research.[51] In addition, the ease of introducing new substituents to the methine bridging moiety has further increased the possibilities for improving the properties of the longer dyes. These new substituents have included single halogen or methyl groups to the creation of cycloalkane rings in the methine bridge. Even additions of other heterocycles to the methine bridge have been conducted, including another cyanine condensation on the methyl substituted trimethine. Some of the most intriguing transformations were produced by Yagupolskii *et al.* by producing a fluorine-substituted pentamethine bridge through a novel synthetic pathway.[52] Equally intriguing is the first report of a heteroatom, a nitrogen, in the methine bridge by Meguallati *et. al.*[53] Their approach employed first the hemicyanine method to attach the first heterocycle to the methine bridge, after which the second amine group was converted into an aldehyde and reacted with a 2-amine substituted benzoxazole to yield the final product. Evidently, the possibilities for altering the structure of these cyanine dyes are endless. Each of the alterations described here affect the way light interacts with these compounds. The effects these compounds and the structural changes have on these interactions will be covered in the chapter below.
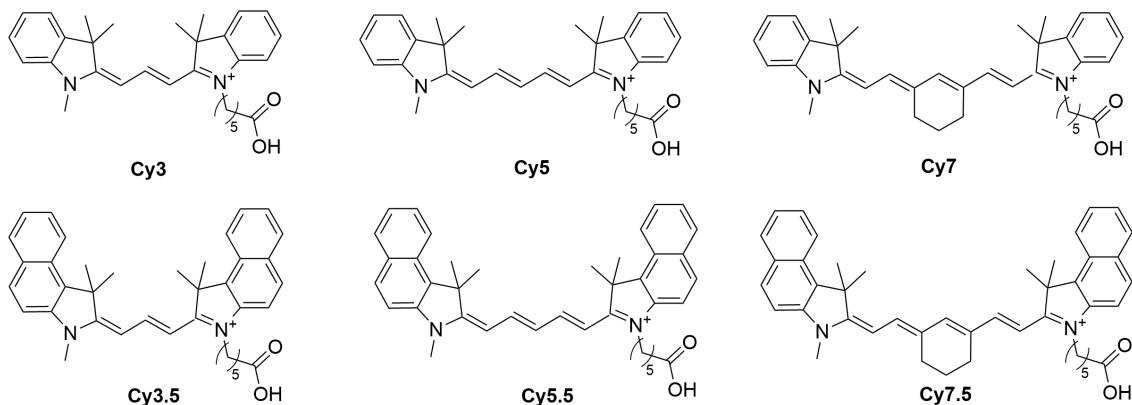
Figure 9. Chemical structure of the best known examples of commercial Cy dyes.[23]

2.2   Photophysical properties

Cyanine compounds are photophysically a versatile group of highly potent organic dyes covering most of the visible light spectrum.[32,54] They exhibit deep colours that are inherent to their high absorption coefficients ranging from 10 000 cm^{-1}M^{-1} up to 250 000 cm^{-1}M^{-1}. Typically, the highest-absorbing compounds are based on longer methine bridging units, whereas the absorptivity of monomethine cyanines remains in the order of 10^4 cm^{-1}M^{-1}. This character is credited to the ease of HOMO to LUMO transition that the similarity of the two states allows.[55] Additionally, what follows from this is that the dyes do not generally exhibit solvatochromic behaviour, *i.e.* their spectral properties do not change based on solvent polarity. However, they do have a tendency for aggregation behaviour. The aggregation can happen by plane-to-plane stacking (H-aggregate) leading to blue-shifted absorption, or by head-to-tail arrangement (J-aggregate) that causes a red shift. While H-aggregates cause excitation peak broadening and lowered emission intensity, J-aggregates have an opposite effect.[56] Aggregated dyes are more prone to undergo photodegradation and hence attempts to reduce this with introduction of steric protection, electrostatic repulsion, as well as stabilizing functional groups[57] have been attempted.

Spectrally, cyanines exhibit narrow excitation bands with a minor shoulder at a higher energy wavelength, rising from the vibrational transitions of the first excited state. The fluorescence spectrum is found to be the mirror image of the excitation spectrum with a relatively small Stokes shift. The position of the excitation and emission peaks is highly dependent on the length of the methine bridge with minor contributions from the constitution of the rest of the chromophore. With monomethine cyanine dyes, the excitation peak is usually found at ~450 – 500 nm and each additional vinyl group (-C=C-) contributes a bathochromic redshift of ~100 nm to it, with trimethine dyes absorbing at 500 – 600 nm.[20] Following this, heptamethine dyes absorb commonly at around 700 – 800 nm region, well in the near infrared (NIR) region.

Free in solution, the cyanine dyes often exhibit low fluorescence intensities. The quantum yields of monomethine compounds tend to be close to zero, whereas with increasing methine bridge length the values increase up to ~30 %, similar to their absorption characteristics.[58] However, as a drawback the photostability of the longer cyanines is reduced, particularly in the presence of singlet oxygen. The methine bridge is also a major contributor to the lower emission quantum yields by providing pathways for nonradiative relaxation. This happens through ultrafast photoisomerization, where the rotation of the methine bond between *cis* and *trans* conformations depletes the excitation.[59,60] This event is highly favoured as it does not have an activation barrier apart from microscopic friction of the rotation.[61] This phenomenon was studied in detail with the monomethine TO by Karunakaran *et al.*, who elaborated the step-by-step mechanism of the torsional motion of benzothiazole and quinoline moieties around the central methine bridge.[62] To circumvent their low quantum yields when free in solution, some cyanine dyes can be rigidified through binding to other molecules through non-covalent interactions.[63] This in turn reduces the excited-state relaxation through non-radiative pathways, which increases the emission intensity of the dyes in question. This behaviour has been particularly advantageous with monomethine cyanine dyes, making their application possible as fluorescent probes for nucleic acid sensing, as the following chapter will show.

2.3   Nucleic acid binding

Albeit cyanine dyes have been succesfully used in probing many different biological targets, their use as fluorescent probes for nucleic acid sensing has been utilized the most. The monomethine cyanine dyes in particular have been employed for this application. This is due to their preference of binding to nucleic acids through intercalation. In intercalation a guest molecule inserts itself between two base pairs of a nucleic acid, driven by non-covalent interactions including electrostatic interactions, different hydrophobic interactions and, most importantly, co-planar π – π stacking (Figure **10**).[64] In response to the guest binding, the DNA double helix has to unwind approximately 3.4 Å to accommodate it. The positive charge is thought to be mandatory in order for intercalation to happen.[65] Binding like this restricts the movement of the molecule dramatically. As discussed in the previous chapter, the major pathway for non-radiative relaxation of the excited states on monomethine cyanine dyes happens through torsion around the methine bridge.[62] Thus, when this movement is restricted, massive increases in the emission intensity of these dyes are often observed. Another option for binding to nucleic acids is minor groove binding, meaning the compound binds lengthwise to the narrower groove of the DNA helix. The preference of minor groove binding over intercalation increases as the compound gets longer, but oftentimes molecules are able to exhibit both types of binding.[41] This clearly

depends on the length of the methine bridge, as shown by Lerman by changing the minor groove binding of pinacyanol into intercalation simply by removing a single vinylene moiety from the bridging unit.[66]
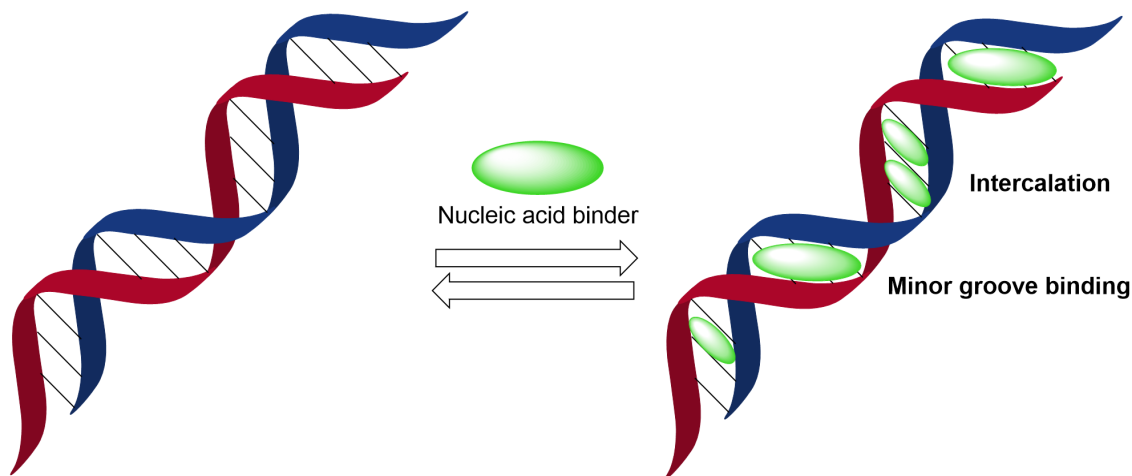
Figure 10. Schematic of nucleic acid binding to double-stranded nucleic acids through intercalation or minor groove binding.[64]

As expected, the TO dye behaves as an intercalator in binding with nucleic acid. However, the well-studied commercial derivatives of TO, Pico Green[67] and SYBR Green I[38,68] show an example of compounds exhibiting both intercalation and minor groove binding simultaneously. Both compounds have the TO-derived chromophore containing the intercalation character, but additional aminoallyl pendant arms contribute a minor groove-binding character to the molecules by binding along the DNA helix. This additional groove binding adds 10-12 kJ/mol to the Gibbs energy of the Pico Green and total binding energies of approximately -46 kJ/mol.[38,67] This corresponds to incredibly high binding constants (in the order of 10^9 M^{-1}) compared to conventional intercalators that often have values ranging between 10^4 and 10^6 M^{-1}.[64] This is logical, as minor groove binders have a tendency for higher binding constants, usually found in the order of 10^5 to 10^9 M^{-1}.[64] This strong binding character has made this family of dyes a highly employed choice for detecting smallest amounts of nucleic acids, both in solution[69,70] and gel electrophoresis[71]. It is even possible to discern between mixtures of single and double-stranded nucleic acids employing these dyes.[72,73] The interactions between intercalators and DNA are highly dynamic, meaning that complexation and dissociation between the two happens rapidly. For example a study on anthraquinone revealed an individual molecule to spend less than 1 ms intercalated to the DNA.[74] As for many applications a higher stability of the complex is desired, scientists developed compounds with two or more intercalating units connected with cationic allyl bridges to achieve higher binding constants. The binding affinity of a dimer should theoretically be squared compared to its monomer.[75] This has also been proven as a valid strategy for the TO and YO fluorescent probes, as the synthesis of dimeric forms of both dyes led to increased

sensitivity and binding with the synthesis of TOTO and YOYO derivatives.[76] In summary, fluorescent cyanine dyes, particularly the unsymmetrical monomethine compounds, offer a non-invasive, highly potent tool for sensing nucleic acids. In their primary binding mode through intercalation they can exhibit fluorescence enhancements of 100 to above 1000 times in intensity compared to the intensity of the free dye in solution. This character has made them a daily compound of choice in laboratories worldwide for this purpose and thus, improvement to their sensitivity and other characteristics has been and will continue to be of high interest.

3   NOBLE METAL NANOPARTICLES

Noble metals can be defined as elements highly resistant to corrosion and oxidation with completely filled d-bands in their electronic structure. In the most classical sense this includes gold, silver, copper and arguably platinum, which are highly inert metals. However, when nanoparticles of these elements are produced, they are found to express high reactivity.[77] These new properties arise from the increased surface-to-volume-ratio of nanoparticles compared to bulk materials. Nanoparticle surfaces show high potential in many novel heterogeneous processes, particularly with catalysis. Combined with the size-related SPR, as well as the unique electronic, optical and thermal properties expressed by these compounds, they show promise in addressing many challenges, such as splitting water.[78]

However, with such high reactivity, their stability becomes a problem in practical use. To counter this problem, the noble metal nanoparticles are often enclosed by a ligand shell, *i.e.* a cover of organic ligands bound to the surface covalently or noncovalently.[79] This ligand shell stabilizes the particles and works as an intermediate between the nanoparticle metal core and its environment. This means that the choice of ligands protecting the nanoparticles needs to be adjusted accordingly to the desired application. The methods for addressing these demands have been developed significantly in recent times.[80] Common for the different ways of producing noble metal nanoparticles through bottom-up approach include a reduction of a precursor metal salt with a reductant of choice in the presence of an organic molecule that creates the ligand shell. The larger colloidal nanoparticles often come with a non-covalently bound ligand layer, requiring further surface functionalization before bioapplications. While the AuMPCs feature defined molecular structure, high stability due to covalently bound ligand layer, the smaller size while advantageous also diminishes the SPR that sometimes plays a role in NP applications. The focus of this chapter is to review and present the common synthetic procedures for production of gold nanoclusters and colloidal nanoparticles. Additionally, the chemistry available for tuning and altering their ligand shell is covered to provide understanding for the possibilities that

these types of molecules offer for application in the field of cell and molecular biology. The exciting photophysical and chemical properties relevant for these applications are shortly discussed in chapter 4 to provide sufficient background for understanding the new possibilities these novel properties allow.

3.1 Gold nanoclusters

Monolayer-protected gold nanoclusters (AuMPCs) are the smallest of (below 5 nm) stable nanoparticles attainable, with the smallest ones starting from as few as 10 gold atoms.[81] Ranging up to few hundreds of atoms compared to general nanoparticles, their most important aspect is their molecule-like defined structure. This means that it is possible to obtain these particles in bulk amounts, where each particle shares the atomic composition with the next one. The general composition of these compounds starts from a gold core formed by together clustered Au(0) atoms. Certain numbers of gold atoms, known as magic numbers N, in this core are preferred according to equation 1

$$N = \frac{(2n + 1)(5n^2+5n+3)}{3} \tag{1}$$

where n is any positive whole number, leading to a filled electronic shell on the core.[82] In order to stabilize the core, it needs to be surrounded by a protecting ligand layer. With gold nanoclusters, this layer consists of Au(I) and organic molecules arranged as staples, covering the surface of the core. Most often the organic molecules used have a thiol functional group due to the high affinity between sulphur and gold, although other examples employing *e.g.* carbenes[83-85] and phosphines[86] exist. Depending on the choice of organic molecule, the clusters can be either water- or organosoluble. The ligands most commonly used for producing lipophilic AuMPCs include phenylethanethiol (PET), alkanethiols and 4-*tert*-butylbenezethiol, whereas hydrophilic clusters are acquired using glutathione, mercaptopropionic acid or *para-* and *meta-*benzoic acid (pMBA and mMBA, respectively) as the stabilizing ligand. Some of the hallmark clusters that have been synthesized and structurally characterized with atomic precision have been the $Au_{25}(SR)_{18}$,[87] $Au_{38}(PhCH_2CH_2S)_{24}$,[88] $Au_{102}(p\text{-MBA})_{44}$[89] and $Au_{146}(p\text{-MBA})_{57}$,[90] (Figure **11**) serving as prototype systems to study their unique physicochemical properties.
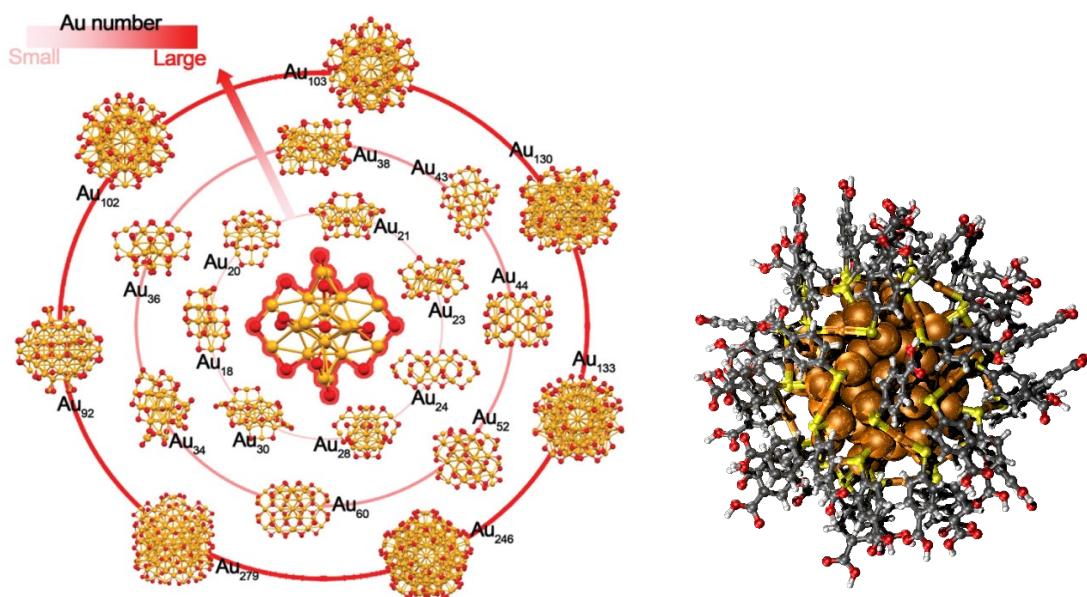
Figure 11. Left: Examples of different thiolate protected gold nanoclusters that have been synthesized. Yellow = gold, red = sulphur. The ligand layer of the clusters is excluded in the figure. Reproduced from Ref. [87] with permission from The Royal Society of Chemistry. Right: Complete structure of $Au_{102}(p\text{-MBA})_{44}$ with the ligand layer included. Orange = gold, yellow = sulphur, black = carbon, red = oxygen, white = hydrogen. Courtesy of Sami Malola.

As is easy to imagine, the task of synthesizing these molecules at an atomic precision is no simple task. While many methods taking advantage of additional energy input[91] or templates included to the system[92], the direct-synthesis Brust-Schiffrin method is the most common way of producing thiolate-protected AuMPCs (Figure **12**).[93] First, the starting material Au(III) forms a complex in the presence of the organic ligand, forming a Au(I)-SR polymeric structure. After this, a strong reductant is introduced to the mixture, most often a strongly reducing NaBH₄, which initiates the nucleation through formation of Au(0) and the subsequent formation of the AuMPC. Due to its simplicity this method is also known as the "one-step synthesis method". The role of the reductant is crucial in determining the composition of the particles formed. Additionally, by variations to the type[94] and concentration of the reactants, as well as the solvent system[95], its pH[96], reaction times[97] and temperature[98], different sizes of clusters can be made.[99,100]
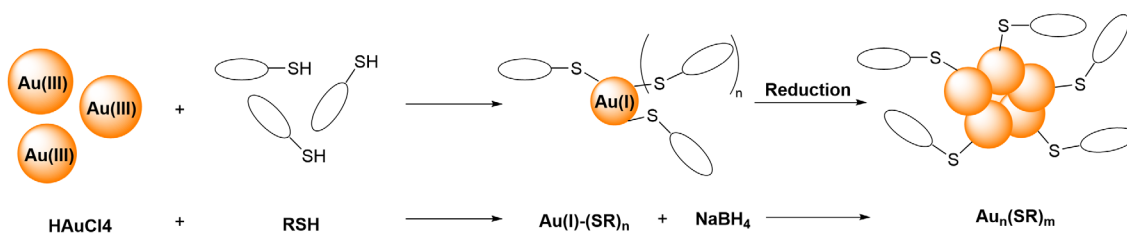
Figure 12. General Brust-Schiffrin method of synthesis of AuMPCs.[93]

While few synthetic methods exist that produce only one specific size of nanocluster, oftentimes at least a few different sizes of clusters are observed and further size control or purification is required. The size focusing methods involve taking a polydisperse nanocluster sample, purified from its starting materials and maturing it further until a single particle size is achieved.[97,98] The maturing can be sometimes induced by simply aging a solution of polydisperse nanoclusters, while at times increasing the temperature promotes the formation of a single size of cluster. Etching is a powerful tool to reduce the size of metastable clusters into most favoured ones by adding large excess of thiol ligands to remove some of the gold atoms. However, as developing size focusing methods is an arduous effort, different separation methods are more commonly used to separate different cluster sizes from each other. Simplest way of doing this is through fractional precipitation, where the solubility of different cluster sizes is used by adjusting solvent system conditions so that that only part of the AuMPCs in a sample precipitate and are collected.[101] For separation of large amounts of clusters, different chromatographic methods such as high-performance liquid chromatography (HPLC, separation based on ligand composition)[102] and size-exclusion chromatography (SEC, separation based on hydrodynamic radius)[103] are used. For smaller amounts, polyacrylamide gel electrophoresis (PAGE) is a widely used method, where clusters are separated based on their charge, size and shape, based on their movement through the gel material under an electric current.[104] The PAGE is also used for characterizing the reaction products, when compared to the running distance of a known sample. Other commonly used methods include transmission electron microscopy (TEM), UV-vis spectroscopy, powder X-ray diffraction, NMR, and thermogravimetric analysis. TEM gives information on the size of the cluster core and, with sufficient resolution, even information on the lattice orientation of the AuMPCs.[105] However, powder X-ray diffraction is more often employed method for gaining lattice information.[89] UV-vis spectroscopy shows the absorption energy characteristics of the nanoclusters, and from it the emergence of the SPR character can be observed. Thermogravimetric analysis gives information on the ratio of organic matter *vs.* metal in the sample, while NMR can be used to gain information on the ligand layer constitution, orientation and the hydrodynamic radius of the clusters. The production of monodisperse AuMPCs is crucial for their implementation, since different nanoclusters might have completely different effects for specific applications. Compared to colloidal nanoparticles, the potential to produce the same exact atomic structure each time is an advantage compared to the statistical size distribution obtained from synthesizing larger NPs. For biological applications they exhibit a wide range of possibilities with smallest molecular clusters exhibiting fluorescence, whereas the larger ones are suitable for application in electron microscopy or plasmonics.

3.2 Colloidal noble metal nanoparticles

Unlike AuMPCs, colloidal nanoparticles don't exhibit a uniform structure and are made oftentimes of gold or silver with sizes spanning from 5 nm to 100 nm and higher. Compared to gold, silver nanoparticles (AgNPs) exhibit significantly stronger SPR characteristic, making them a great choice for plasmonic applications.[106] Unlike chemically inert gold nanoparticles (AuNPs), in biological applications, AgNPs are harmful to living organisms. While this makes their use in non-invasive applications more challenging, it has also found application as antibacterial material.[107] Similar to AuMPCs, the core of these NPs is made of elemental gold/silver covered by positive Au(I)/Ag(I) ions, but the ligand shell covering the particle differs significantly. The metal ions are most commonly stabilized through ion-dipole interactions with molecules such as citrate, lipoic acid[108], polyvinylpyrrolidone[109], cetyl trimethyl ammonium bromide[110,111] or branched polyethyleneimine[112], to name a few examples.[113,114] Au(I) behaves similarly, although its interaction towards amines is weaker, complimented by stronger attraction to sulphur. The weakly bound ligand layer makes the NPs incredibly sensitive to their environment. The native particles form aggregates even at an introduction of *e.g.* small concentrations of salt, due to their negatively charged surface. However, this also makes NPs highly reactive in further reactions and makes their surface functionalization a highly useful tool. Additionally their sensitivity to the environment and easily observable aggregation with a notable colour change has led to multiple applications using them as chemosensors. While the thiol-silver binding energy is significantly lower compared to the one with gold, thiol-covered AgNPs can also be produced.[115]

The synthetic method most commonly used for producing colloidal noble metal nanoparticles was developed by Turkevich *et al.* in 1951.[116] The method makes use of an Au(I)/Ag(I) salt as the metal source, with tetrachloroauric acid and silver nitrate being the most dominant choices, respectively. For silver also acetate, perchlorate and citrate use have been reported.[113] In the presence of the surfactant and a reductant the mixture is boiled, which leads to the formation of corresponding NPs. In order to form larger particles, weaker reductants such as trisodium citrate, ascorbic acid or hydrogen peroxide are used.[80] NaBH$_4$ has been also employed when smaller sizes of nanoparticles are desired.[117] Citrate reductant has been the dominating choice for this role due to its ability to act as a surfactant as a dual purpose reagent. The AgNPs made with the Turkevich method show high polydispersity of the final product which has led to search for additives to reduce this, such as tannic acid.[118] NPs larger than 50 nm are often synthesized by seeding the previously produced NPs with more metal salt in a process known as Ostwald ripening.[119] Biological approaches to synthesize AgNPs have also been gathering large scientific attention as a green method for synthesizing them. Instead of using a chemical reductant, different bacteria, fungi or plant extracts have been employed for the reduction of the

silver salts.[120] While the high reactivity of AgNPs thanks to their weakly stabilized surface makes them unstable and hard to control, their surface serves as a great foundation for further modification in a multitude of ways, as the following chapter will show.

3.3   Surface modification

As previously mentioned, the ligand surface controls the interactions between nanoparticles and their environment. Thus, accurate control over the layer of organic molecules covering nanoparticles is highly desired. There are two approaches to gain this control. The first (and possibly the most employed) approach aims to replace the initial ligand molecules with new ones; this will be covered in the following chapter. The chemical conjugation approach (covered in chapter 3.3.2) on the other hand takes advantage of the molecules covering the nanoparticle, by synthetically further modifying or attaching new substituents on them. Attaining accurate control over this process remains still a grand challenge in the field of nanoparticles. While the high surface-to-volume ratio of nanoparticles makes them ideal foundation for introducing multiple biomolecules in a single system, the combination of weak interactions with covalent binding and different physical interactions is a complicated problem for synthesizing products of choice. However, both approaches have methods for making a high amount of different kinds of ligand coverage, ready for applications in many different fields, as will be shown below.

3.3.1   Ligand exchange

Due to their metastable nature, metal nanoparticles make for a great platform for post-synthetic modification.[121-124] Their dynamic nature affords the exchange of organic molecules off the surface by introducing new molecules in solution happen readily. The difficulty of replacing the molecules on the surface with new ones depends on the binding strength of the intial ligand, as well as the affinity of the new ligand towards the particle and the particle itself. Naturally, non-covalently bound ligands such as the citrate moiety are easily overtaken, whereas thiols form more stable covalent bonds. For example, the thiol-gold bond has a bond strength up to ~47 kcal/mol[125] and is commonly taken advantage of in ligand-exchange reactions. Despite the ease of introducing new molecules on the surface of metal nanoparticles, achieving a complete exchange with the incoming ligand requires a huge excess of the new compound[126] or otherwise destabilizing conditions, such as increased temperature.[127] This is particularly true for the gold nanoclusters, due to the Au-S –staple units having a high, but differing binding strength, leading to preferential ligand exchange of certain thiolate sites.[126] However, even with these compounds a full exchange on the ligand surface is achievable; this has also been used as a size focusing method, to create more stable clusters out of

the metastable ones. Obtaining discreet sizes of AuMPCs is desirable for having the optimal optoelectronic properties or other applications.

In practice ligand exchange is conducted simply by mixing the new ligand in excess with the starting metal nanoparticles. With thiols, an activating compound meant to sever the unreactive dithiol bridges such as BSPP, TCEP or DTT has been used to improve reactivity.[128] The chemisorption of the thiol molecules happens fast in the initial step, but for complete coverage more time is needed as the thiol molecules reorganize to make room for the final amount of ligands, each thiol requiring approximately two gold atoms to bind to the surface.[129] At times the adsorption of the whole molecule to the surface through weak interactions happens instead of the reactive functional group.[115] Especially increased size of the initial ligand shell can hinder the binding through covalent bonding. In addition to organic thiols, dithiocarbamates and thiotic acids have also been employed.[114] The stability of binding can be further enhanced by introducing multiple binding moieties on a single ligand, making the dissociation of the ligand exchange product less favoured.[130]

However, for certain applications products binding with lower affinity are desired, *e.g.* when controlled release of the ligand is wanted. This is at times true also for thiolated nanoparticles in cell contexts, as a high concentration of glutathione present in cells can replace the thiols on the nanoparticle surface.[131] Phosphines are also known to form covalent bonds with gold, albeit weaker compared to ligands containing sulphur.[132] Despite its covalent character, it is easily replaced, making phosphine-functionalized nanoparticles highly reactive. Other ligands employed in non-covalent ligand exchange are amines (6 kcal/mol), nitriles and carboxylic acids, which bind to the surface electrostatically.[124] Nevertheless, thiols remain the priority choice for conducting ligand exchange on all types of particles. The different organosulfur compounds offer a versatile toolbox to introduce otherwise unattainable functional groups or even large biomolecules to the ligand shell that can even be further chemically altered, as will be covered in the next chapter.

3.3.2   Chemical conjugation

As discussed above, the ligand exchange is a potent method for introducing metal nanoparticles with new functional groups ready for further modification.[133] With these precursors, different synthetic methods can be readily employed, provided that the nanoparticles themselves are not decomposed in the process. Commonly introduced functional groups include amines, carboxylic acids, hydroxyl, aldehydes as well as halides.[133,134] The carboxylic acid (and hydroxyl) group facilitates the use of esterification reaction. For example, the Steglich esterification was taken advantage of by Marjomäki *et al.* to conjugate the $Au_{102}(pMBA)_{44}$ with a cysteine-binding maleimide moiety.[135] The carboxylic acid has been used in many cases to form amide bonds through NHS-coupling with primary amines and vice versa.[136] Similar result can be achieved by reacting aldehydes with amines as well. On the other hand, halides are readily transformed into other functional groups in nucleophilic

substitution reactions. The transformation into azides has been of particular interest with the introduction of NaN_3, due to the added potential of the click reactions that azides go through in the presence of alkynes and Cu(II).[137] As is evident, many methods are available for covalent conjugation to introduce new substituents, but additional possibilities are offered by noncovalent bonding.

From the abovementioned functional groups, the amines and carboxylic acids are potent noncovalent binders in their protonated/deprotonated forms. The sulphonate moiety acts in a similar manner. Introducing multiple weakly binding groups has found application in inducing complexation with *e.g.* metal ions such as Hg^{2+}, Cu^+, Ar^{3+} and many more.[138] The possibilities are even further increased when introducing biomolecules by covalently binding them with the aforementioned methods. Thionylated ssDNA offers sequence-specific targeting possibilities as only highly complementary sequences are able to bind together to form fully double-stranded DNA.[139] Similarly, biochemical recognition for nanoparticles can be achieved with the introduction of certain amino acid sequences or even enzymes.[121] The advantage of chemical conjugation is that the structure of the nanoparticle is more likely to be retained. On the other hand, the reactions required to do so are oftentimes more demanding compared to ligand exchange. For example, the simple addition of thiols into gold nanoparticles is enough to induce ligand exchange, whereas the chemical conjugation with azides requires Cu(II) as the catalyst. Naturally, it is also possible to produce nanoparticles with pre-conjugated ligands. However alteration has potential to change the structure of the produced nanoparticle, and with nanoclusters one would be unlikely to obtain the same product with a tried protocol. The diverse chemistry that makes possible endless combinations of two or more molecules on the surface of a single nanoparticle has made them an extremely attractive platform for many different applications. Further interest in their use comes from the increased value that the properties of metal nanoparticles offer in certain applications. The following section focuses on displaying the many possibilities that nanoparticles offer in the field of cell and molecular biology.

4 BIOAPPLICATIONS OF NOBLE METAL NANO-PARTICLES, NANOCLUSTERS, ORGANIC DYES AND THEIR COMPLEXES

The synthetic methods enabling conjugation of virtually any molecule on the surface of nanoparticles has made possible their use in applications in the field of cell and molecular biology. Their use as a platform to make nanodevices able to perform designed tasks at targeted locations in the cells is widely spread. With the correctly chosen surface chemistry, even controlled release at destination can be achieved.[121] For example, combining a mixture of a targeting molecule and a functional molecule on the nanoparticle surface shell is a widely used approach. This chapter presents some of the wide spectrum of applications that have been reported over the years, divided based on the nanoparticle used. Chapter 4.1 covers gold nanoclusters, while chapters 4.2 and 4.3 focus on developments using colloidal gold and silver nanoparticles, respectively. Using nanoparticles in this way as a simple platform for other bioactive molecules is universal regardless of the nanoparticle type, provided that surface functionalization chemistry is available. The use of noble metal nanoparticles provides novel properties to the nanoparticle–dye composites making more exquisite approaches possible.

The emerging new properties in noble-metal nanoparticle – chromophore interactions are inherent to the SPR-induced electromagnetic field around the particles.[140,141] This electromagnetic field focuses exciting light, creating a focal area proportional to the particle radius. This in turn permits energy transfer between the dye molecules in the surface vicinity and the metal particle. The effect of the interaction between the two depends on multiple factors, deciding whether quenching or enhancement of the fluorophore ensues. Naturally, the metal nanoparticle and the dye play a major role. The magnitude of the interaction depends on the strength of the electromagnetic field created by the nanoparticle, as well as its extinction spectrum. The extinction spectrum of nanoparticles constitutes of absorption and scattering elements. It is important to note that smaller nanoparticles (< 20 nm) have minor to negligible scattering

character, as the scattering increases with size (covered later on). The metal enhancement character goes along with the scattering, making larger particles show stronger metal enhancement and smaller ones being stronger quenchers. Together with the excitation/emission spectrum of the dye, the orbital overlap of the two interacting units determines the extent of coupling between the two.[142] The third major variable in the behaviour of these nanocomposites is the distance between the two constituents. These three factors determine whether the nanoparticle acts as a donor or acceptor when the composite is interacting with light.

When a dye molecule gets excited in close proximity to the metal, typically 1 – 10 nm away[143], its excited state is quenched. The metal particle acts as an electron acceptor and the excited state energy gets transferred to the nanoparticle through dipole – dipole coupling. In the case of fluorophores this will lead to complete quenching of the initially fluorescent molecules. While quenching a fluorescent dye might not seem desirable, it has sparked a whole field of biochemical sensors taking advantage of the Förster Resonance Energy Transfer (FRET).[143] With gold nanoparticles this property has been employed to gain turn-on fluorescent compounds with a controlled release/extension of the fluorescent probe from the surface of the nanoparticle, as will be covered in more detail in chapter 4.2.

As the distance between the metal surface and the fluorophore increases, the quenching effect dissipates (with d^{-3} dependence on the distance[144]) and the metal-enhanced fluorescence (MEF) starts to take effect (Figure **13**). MEF can take place through two different pathways. First the localization plasmon-induced localization of the electromagnetic waves (*i.e.* light) leads to an increase in the excitation of the chromophore and thus increase in emission intensity.[141] The prerequisite for this so called "lightening rod effect" is that the dye in the surface vicinity has a significant spectral overlap in its absorption with the SPR band of the metal. In other words, the absorptivity of the molecule is increased. The second pathway for MEF is through another radiative relaxation pathway for the chromophore after its excitation. Sufficient distance and overlap of the metal's SPR peak and emission spectra of the dye make it possible for the excited state to relax through energy transfer to the metal surface that scatters the photon received from the dye molecule. Naturally, the enhancement of fluorescence this way requires a quantum yield smaller than 100 % for the new radiation pathway to produce more photons. In addition to the increased quantum yields, the interactions between NPs and fluorescent dyes also lead to increase in photostability of the probes in response to the decreased excitation lifetimes. However, the distance from metal and number of molecules on the particle surface both need to be carefully balanced for best results, as surface-bound dye molecules can also quench each other.
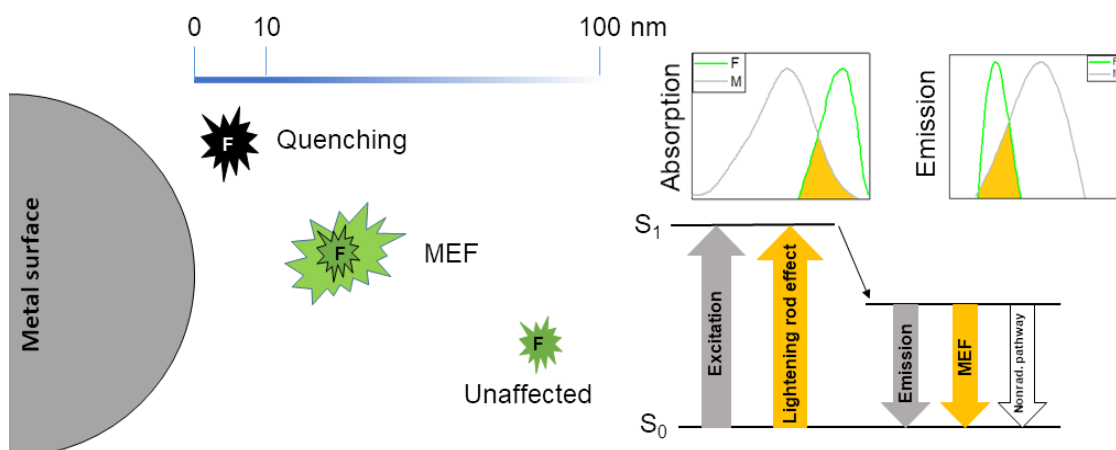
Figure 13. Left: the dependence of the distance from the metal (M) to the effect on the fluorescence of the fluorophore (F). Right: the Jablonski diagram displaying the effects of the metal enhancement on the fluorescence.[141]

In addition to the exciting interplay between noble-metal nanoparticles and fluorescent dyes, the particles themselves exhibit certain properties showing high potential for application in biology. Their tendency to convert absorbed photons into heat or otherwise has high potential in itself. For example the conversion of an excited state into reactive oxygen species (ROS) around its environment has use in photodynamic therapy (PDT) as particles destroying malicious reactive singlet oxygen.[145] Production of heat to do this is known as photothermal therapy (PTT). Equally promising, yet less explored are the possibilities for using noble-metal nanoparticles for photon upconversion.[146] The capability of converting two lower-energy photons into a single high-energy photon could serve as a tool of vital importance to access increasingly deeper layers of tissues with *in vivo* applications. In this final chapter of the literature review, emphasis will be put on bioapplications of noble metal nanoparticles, where the NP itself plays an active role. Particular interest is placed upon applications involving the interactions between fluorescent probes and nanoparticles as described in this chapter.

4.1 Gold nanoclusters

Gold nanoclusters (AuNC) can be readily employed in different biological applications due to their non-cytotoxic and biocompatible character.[96,147] Inherent to their smaller size compared to larger nanoparticles, they are more readily internalized *in vitro* and *in vivo*, as well as are less likely to inhibit the behaviour of their targets if bound to substrates. On the other hand, through surface modification, highly biocompatible clusters can be made, whereas organic dyes often suffer from aggregation, diffusion and other undesired phenomena in bioapplications. The most explored use of gold nanoclusters has

been with the smallest, luminescent particles. Despite being riddled with lower quantum yields compared to conventional dyes, they have been succesfully tested for sensing both heavy metals and different biological analytes.

Fluorescence sensing of desired analytes takes advantage of quenching or enhancement after interaction with the analyte, similar to many organic dyes. The unique detection mechanism with AuNCs is based on the metallophilic d^{10}-d^{10} interaction. This makes possible the detection of metals with full d^{10} electron shell such as Hg^{2+}, Cu^{2+} and Ag^+. The interaction of such metals with a fluorescent AuNC causes quenching and hence detection, as shown by Xie *et al.* using red-emitting Au_{25} as the probe.[148] The group of Chang was able to obtain a limit of detection (LOD) value 5 nM by synthesizing 2 nm AuNCs functionalized with 11-mercaptoundecanoic acid (MUDA).[149] MUDA functionalized particles have also been used to detect As^{3+},[150] and Cr^{3+},[151], with an addition of ethylenediaminetetraacetic acid (EDTA) removing other quenchers in the chromium sensing application. By employing a FRET pair of oligomeric silsesquioxane and an AuNC, the quenching of the AuNC with Hg^{2+} adsorption and subsequent fluorescence recovery of the silsesquioxane moiety was able to push the detection limit as low as 0.1 nM.[152] Similarly, Cu^{2+} has been successfully detected by the group of Pradeep using the same principal, but employing bovine serum albumin (BSA) stabilized Au_{38} cluster for the purpose.[153] Similar cluster was then used by Durgadas and co-workers to determine intracellular Cu^{2+} levels with the LOD of 50 µM.[154] Conversely, the detection Ag^+ was achieved by MEF of silver ion interaction with $Au_{25}(SG)_{18}$[155] and BSA-stabilized Au_{18} clusters[156] with LOD values of ~200 nM observed with the former compound. In detection of anions, AuNCs have been implemented for observation of CN^- (through cyanide etching)[157], S^{2-} (through etching)[158], NO^{2-} (in compilation with NO^{2-} induced Fe^{2+}/Fe^{3+} oxidation reaction and subsequent quenching)[159] and I^- (by using $Au_{25}(SG)_{18}$ as the probe)[160].

Gaining information on different inorganic species in biological contexts is vital for gaining new insights. Even more important is knowledge on the many bioanalytes that play a crucial role in the behaviour of cells.[161] One such compound is glucose that was determined up to LOD of 1 µM accuracy by employing glucose oxidase enzyme to react with the analyte, producing H_2O_2 in the process, which then reduced the fluorescence intensity of the MUDA-functionalized AuNCs in the process.[162] A more refined use of H_2O_2 was achieved by Abarghoei *et al.* using cysteine-capped AuNCs in the detection of citrate.[163] The method was based on the ability of this nanocluster to oxidize a blue dye in the presence of hydrogen peroxide, leading to a colour change in the sample. Citrate prohibits this reaction from happening, making colorimetric analysis of its contents in a sample possible. Some other bioanalytes measured in response to their fluorescence quenching processes implied on the AuNCs include amino acid trypsin[164], methotrexate[165] and dopamine[166], sensed using BSA-stabilized nanoclusters after the host-ligand binding to the guest. The same approach also works on increasingly complex biomolecules. For example, scientists were able to use poly(amidoamine) functionalized AuNCs. After

functionalization with antibody against human immunoglobulin G, the introduction of this protein led to diminished fluorescence.[167] An opposite approach using fluorescence recovery has also been tested. The groups of Chen and Chen have used AuNCs quenched with Fe^{3+} for the detection of phosphate-containing biomolecules. Phosphate-containing compounds are able to chelate the iron ion on the AuNC surface leading to fluorescence recovery which was shown to work with BSA/3-mercapto propionic acid-functionalized gold clusters and alkaline phosphatase[168], as well as glutathione (GS)-covered AuNCs in interaction with adenosine triphosphate[169].

Other useful ways to induce reduction in fluorescence intensity on the nanoclusters is by inducing either etching or aggregation of the particles. Detection of biologically important thiols can be achieved by observing the etching of susceptible AuNCs in their presence, such as Au_8 with GS from a drop of blood[170]. The aggregation behaviour on the other hand was used with mannose AuNCs for detection of protein concanavalin A and the bacteria *E. coli* with completely opposite reactions.[162] With concanavalin A, the fluorescence of the particles was quenched (with impressive LOD of 75 pM achieved), whereas interaction with *E Coli* yielded highly fluorescent accumulation of particles within the bacteria. Controlling the aggregation of particles with finesse has its own applications. The assembly into higher-ordered superstructures can be achieved by controlling the environment of the nanoclusters. There are numerous ways to achieve this. The group of Ikkala has achieved spherical superstructures by using bidentate Sn^{2+} as a connecting ligand between GSH-functionalized AuNCs, increasing the quantum yield of the particles significantly ($\Phi = 3.5 \rightarrow 25$ %) by doing so.[171] Earlier, the same group was able to produce both spherical capsids as well as 2D nanosheets out of the nonfluorescent Au_{102}-pMBA$_{44}$ cluster by slowly increasing methanol content of a water solution through dialysis.[172] Yahia-Ammar *et al.* achieved spherical assembly of Au(GS) particles in the presence of poly(allylamine hydrochloride), achieving similar enhancement of fluorescence as the Ikkala group did.[173] The produced 120 nm superstructures had pH-dependent swelling properties. An interesting approach for such assembly was also explored by Rival *et al.*, where nanodiscs of Au_{25} nanoclusters functionalized with a chiral ligand could be assembled and disassembled using illumination of light at 345 nm and 435 nm, respectively.[174] This was due to the photoisomerization of the ligand surface permitting the self-assembly at higher excitation energy. Kauscher *et al.* took a more biological approach by assembling hydrophobic tetraoctylammoniumbromide AuNCs around extracellular vesicles to achieve spherical superstructures.[175] The scientists were then able to follow the internalization and movement of these particles in cells using electron microscopy. The benefits of such superstructures is their improved ease of observation *in vivo*. However the highest potential in their use lies in controlled release, if control over the assembly/disassembly can be achieved, *e.g.* with light.[174] Such superstructures can serve as drug carriers[176,177] (that are easy to follow) in therapeutic applications in the future.

AuNCs have been used in targeted *in vivo* imaging applications in tandem with the use of different targeting molecules conjugated on their surface, such as peptides, polyethylene glycol, avidin, streptavidin, folic acid and BSA.[178] This not only offers possibilities for tracking cellular targets with confocal microscopy, but also electron microscopy can be employed, provided that the clusters have sufficient electron absorptivity. For example, functionalizing the $Au_{102}pMBA_{44}$ cluster with compounds targeting cysteines[135] or specific binding pocket[179] on the surface of an enterovirus made it possible to clarify structural elements of this 30 nm virus. The targeted imaging of cancer cells and other diseases such as Alzheimer's with the fluorescent AuNCs has been of high interest in their application to fluorescent imaging. This has been achieved in many different ways, even in models of live mice, targeting the overexpressed receptors on cells related to the disease, as reviewed elsewhere.[161,180–182]

However, the greatest strength of using AuNCs in bioapplications is combining their sensing properties with therapeutic modes of action (*i.e.* theranostics), made possible by other properties the clusters express. The gold clusters have a high potential as radiosensitizing compounds, which enhances the effects of radiation. Zhang and co-workers showed this with Au_{25} clusters covered with both GS and BSA, where intake caused by enhanced permeability of cancer cells lead to accumulation of these clusters and subsequent radiotherapy destroyed the cells.[183,184] Increased efficacy in killing malicious cellular organisms can be achieved through photodynamic- and photothermal therapy as well. Zhang *et al.* were able to create a $[Au_{13}(diphenylphosphinoethane)_5Cl_2]Cl_3$ cluster arranged in a propeller-like shape.[185] This compound showed exciting quantum yield of 71 % for production of singlet oxygen radical, exhibiting potential for further use in PDT-related applications. A more sophisticated approach was taken by Jiang *et al.* by conjugating four PDT-active indocyanine dye molecules onto $Au_{25}GS$ surface through an amide bond.[186] By activation of the dye through NIR excitation, tumours on live mice were obliterated at higher efficiency compared to free dye, through combination of PDT and PTT (as observed from increased temperature). Another dual-targeting nanocluster conjugate was prepared by combining a fluorescent AuNC with two cancer cell-targeting moieties and a NIR absorbing dye MPA, or a widely used cancer drug doxorubicin (DOX) on its surface.[187] In this model the fluorerescent MPA-conjugated cluster could be used for tumour imaging and the doxorubicin-conjugated cluster for tumour destruction.

The use of gold nanoclusters in biology has been predominantly governed by the smallest, fluorescent AuNCs, as shown from the numerous examples above. However, the use of bigger sized AuNCs might become more relevant in the near future, as the many plasmon-related applications such as the PTT increases in efficacy as the size of the cluster and subsequently the strength of the plasmon increases. Naturally, the bigger gold nanoparticles (> 5 nm) show this effect the strongest, however due to their poor pharmacological clearance might force researchers to find a compromise inbetween. The combination of

organic dyes with AuNCs has not been very actively studied so far. The reason for this might be in the molecular behaviour of the smallest particles, which mainly permits quenching-related applications. However, as the chemistry of these compounds develops further to include atomically exact products in increasing size, the semi-conducting gold nanoclusters might produce novel composites and thus, new applications in the future.

4.2 Gold nanoparticles

Colloidal gold nanoparticles (AuNP) have highly similar character as the silver nanoparticles, inherent to the SPR character the two metal particles share. However, there are few crucial differences that have made AuNPs the source of more prolific research in biological contexts. First, the biocompatibility compared to silver is significantly better, due to their non-toxic nature.[188] Although the use of AuNPs *in vivo* isn't without problems, as they often accumulate into organs instead of clearing out of the organism, they are not inherently poisonous. Additionally, for different light-activated applications *in vivo*, the wavelength of the AuNP plasmon resonance (λ = ~530 nm) is red-shifted significantly compared to silver nanoparticles, bringing it closer to the NIR window of light that cells are the most permeable to. Albeit with both elements, by controlling the shape of the nanoparticle the SPR peak can be shifted towards more favorable position for this, gold has an advantage to begin with. The main benefit of silver over gold is in the stronger SPR it exhibits, making different plasmon-enhanced phenomena more potent in their presence. However, even in these applications AuNPs serve as a potential candidate, as has been shown in their use for many sensing applications as well.

AuNPs have been used to detect a wide range of different analytes. Similar to silver, AuNPs also experience major colorimetric changes upon aggregation and this has been used as an advantage for many targets of interest. In the case of inorganic analytes, AuNPs have been used in detection of *e.g.* Cr^{6+} (LOD = 2.5 nM), Hg^{2+} (6.0 nM) and Sb^{3+} (1.2 mg/l).[120] In a more broadspectrum approach, Sener *et al.* were able to combine MUDA-capped AuNPs with amino acids, to simultaneously sense Hg^{2+}, Cd^{2+} Fe^{3+}, Pb^{2+}, Al^{3+}, Cu^{2+} and Cr^{3+} from the same sample with LOD as low as 20 µM for each ion.[189] Also organic compounds, such as creatinine (53.4 nM), melamine (0.17 mg/l), tobramycin (23.3 nM), vitamins B1 and B6 (8 ng/ml and 15 ng/ml, respectively), betamethasone (6 ng/ml), cyanide (0.2 pM), spermine (136 pM) and L-cysteine (0.51 nM) have successfully been determined using gold nanoparticles of different functionalities.[120]

Similar sensitivity has also been achieved with many compounds of biological importance. Considerable information on nucleic acids can be achieved using similar methods as with AgNPs. One such method includes DNA-conjugated fluorescent dye, which without the presence of target nucleic acid is quenched by the gold particle, but upon target binding extends fully

exhibiting MEF instead.[190] Degliangeli *et al.* developed a method for detection of micro RNA in amounts as small as 0.2 fmol with such method, but additionally the nucleic acid was cleaved off the AuNP surface after successful binding.[191] Similarly Hu *et al.* were able to detect dissociation of a DNA hairpin from the AuNP surface at 3 nM concentration of the target micro RNA.[192] In another approach, Guo *et al.* mixed two different ssDNA-functionalized AuNPs together that formed a Y-shaped complex with the target DNA upon binding.[193] This approach allowed only the formation of NP dimers, increasing the assay sensitivity and improving the LOD up to 1.0 pM. However, the highest sensitivity was achieved by Shen and coworkers, who employed a signal amplification method that bound AuNP-bound complementary DNA strands to their targets selectively.[194] The amplification in 30 cycles of ligation chain reaction allowed detection of 20 aM concentration of analyte DNA in the sample. Even more impressively, Sanromán-Iglesias *et al.* were able to selectively detect a single mismatch of a nucleic acid in a sequence with LOD down to 10.85 fmol.[195] Other biomolecules of interest include proteins such as lectin (LOD = 4.9 nM)[196], steroid stanozol (2.4 nM)[197], ATP (1.7 nM)[198], Alzheimer's disease markers[199], human breast cancer markers[200] and a plethora of others[201]. Another impressive sensing mixture was shown by Li *et al.* by discriminating between 10 different proteins in a sample at 0.5 μM concentration with a mixture of five different unmodified AuNPs.[202] The same assay was also used to differentiate between six different bacteria in a similar manner. Another approach of AuNP-based sensing is binding fluorescent dyes to their surface in competition assays. The group of Rotello was able to use AuNP-GFP (Green Fluorescent Protein) conjugate in differentiating some proteins present in human serum, namely fibrinogen, human serum albumin, α-antitrypsin, transferrin and immunoglobulin G even in the mammalian cells themselves.[203] The same group used a fluorescent conjugated polymer on a hydrophobic AuNP surface to differentiate between nine different bacteria.[204] Finally, by the addition of cucurbit[7]uril functionalization to the AuNP surface in their GFP-based assay, the group was able to sense cancer cells with 95 % accuracy from only 1000 cells.[205]

In bioimaging applications, AuNPs have found particularly widespread use. Their wide biocompatibility has encouraged their use *in vivo* in bioimaging through most imaginable methods in mouse models. The common techniques include electron absorption as well as fluorescence-based imaging (through conjugation of a dye molecule to AuNP). The AuNPs not only serve as a physical scaffold for the fluorescent probes, but also have potential to serve as a nanoantenna for two-photon upconversion applications.[146] However, also techniques commonly employed in medicine such as magnet resonance imaging (MRI), computed tomography (CT), positron emission tomography (PET) and even ultrasound imaging could be used.[206] These imaging methods will not be covered in detail herein for coherence purposes, for the greatest *in vivo* applications are the use of AuNPs in theranostic purposes.

Use of gold nanoparticles for theranostic (*i.e.* therapy and diagnosis combined) applications has been a target of increased interest in the recent times. The practicality of nanoparticle conjugation has made the attachment of different targeting/imaging/drug mixtures on particle surfaces a common practice.[207] With this, the target-specific molecules carrying one or more therapeutic compounds along to the target, which can be followed with surface-bound imaging agents, have been made possible.[208] The most common target for theranostic applications has been cancer, as it poses the highest threat to human health in the modern times.[209] The common anticancer drugs used in conjugation to AuNPs are DOX, cis-platin, Tamoxifen, Paclitaxel, 6-mercaptopurine, campothecin, Kahalilide F, fluorouracil and irinotecan, whereas targeting can be achieved with binding factors that are increasingly taken in by cancer cells, such as folic acid.[121,210] The release of these drug molecules at target location can be achieved through many ways. For example, Song *et al.* produced DOX-functionalized AuNPs with drug release happening in response to changes in the pH of the environment.[211] For an active release approach, another group showed a photoactivated release of surface-bound DNA hairpin structures, that housed DOX between its basepairs through intercalation.[212] The release of the drug was a consequence of the AuNP heating due to the light-excited SPR. The heating upon excitation gives the gold nanoparticles a way for killing malicious cells in itself through photothermal therapy. The therapeutic use of PTT requires a higher intensity light source, *i.e.* laser light exposure to produce enough heat for cell death, although some initial studies on radioactivated PTT have also been conducted.[213] For example, Park *et al.* were able to follow albumin-encrusted particle aggregates through Cy5.5-functionalized fluorescence and engage in PTT at target location by optimizing the AuNP aggregation within the BSA shell.[214] A multitude of successful PTT tests *in vitro*, *in vivo* and even first clinical trials on humans having been conducted, the AuNP heat therapy itself poses great potential for application in medicine.[215,216] However, the highest potential in treatments is the use of two or more therapeutic options on the same molecule. This was achieved by Gao's group with BSA-coated indocyanine green-labelled ~20 nm AuNPs. The particles showed therapeutic activity against breast cancer through target accumulation with hyaluronic acid and combinatorial cell death inducement with PTT from the AuNP, as well as a contribution from the indocyanine green dye.[217] Similarly, Li *et al.* combined AuNPs, Cathepsin E as a PDT prodrug, U11 peptide for localization and Cy5.5 dye for imaging against ductal adenocarcinoma, all on the same particle.[218] The combination of PTT and the *in vivo*-produced protoporphyrin IX and subsequent ROS production proved to be a highly lethal combination, showing tumour size reduction on live mice. As shown in this chapter, AuNPs have a high potential in many different facets of our daily lives. The many applications and novel ensembles they allow display their versatility and potential as products that will have a high biological impact.

4.3 Silver nanoparticles

Silver nanoparticles have found widespread use in multiple every day applications, such as infood industry, clothing and medical products among others.[219] The impressive properties of these particles enable application *e.g.* in diagnostics, electronics and optics. However, their cytotoxic character and impact on the environment has become an increasing concern as of late.[107,220,221] This has also been turned into an advantage in their widespread use for disinfection purposes in different coatings and otherwise. The cytotoxic effect AgNPs have on cells is caused by particle adhesion on cell surfaces, penetration into the cells, generation of ROS that damage DNA and other cell organelles as well as release of toxic Ag^+ from the high surface area of the particles, all leading to cell death in the end.[221] The destruction of malicious cells (*i.e.* cancer) has been extensively studied. However, for *in vivo* applications the accurate targeting of these cells is of high importance due to their highly cytotoxic character.[221] In a combinatorial treatment, AgNPs were combined with anti-seizure drugs to effectively treat against amoebae in the brain in an infection of central nervous system. The generation of ROS could be enhanced by the strong plasmonic character of the AgNPs, as shown with Rose Bengal photosensitizer-functionalized SiO_2-shelled particles photoinducing the ROS production in target bacteria.[222]

The intense SPR response of AgNPs has been of particular interest for implementation in sensing methods. The employment of metal-enhanced fluorescence has been strongly pioneered by the research groups of Geddes and Lakowicz.[223] The MEF of practically any fluorophore can be achieved, as long as the aforementioned photophysical properties are met. An additional advantage to the method is miniscule sample requirement, with fluorescence of Rhodamine 6G (R6G) and fluorescein (FL) observed from 3 µl of micromolar solutions.[224] The approach of Lakowicz *et al.* was through deposition of silver islands on a glass slide (*i.e.* silver island films (SiFs)) to achieve enhancement, first presented with the sulforhodamine 101 dye.[225] This first approach already promoted a six-fold increase to the fluorescence intensity of the dye. Since then, this method has been used to induce MEF on *e.g.* indocyanine green[226] (20-fold increase), Fluo-3 and 4 (>100-fold increase)[227], and PicoGreen (7-fold increase)[228]. Fluo-3/4 is commonly used in Ca^{2+} sensing whereas, PicoGreen is a highly potent nucleic acid sensor. For glutathione determination, a Cu^{2+}-quenched Alizarin Red S dye was liberated by the presence of glutathione.[229] The restored fluorescence was then enhanced 104-fold by the silver particles present in the system, lowering the LOD down to 250 fM. A more sophisticated approach on nucleic acid detection was taken by sequence-specific binding of a 484-mer RNA strand to the silver surface and 5-Carboxytetramethylrhodamine fluorophore in order to acquire an impressive 5 fmol LOD.[230] With biological samples, fluorescent dye conjugation of enzymes has made possible detection of amounts smaller than 2 ng[231], whereas bioengineering bioluminescent

bacteria *E. coli* made their detection possible.[232] By imposing a SiF-acridan dye surface bound through horseradish peroxidase to microwave irradiation, the dye fluorescence gets even further increased.[233] Using this platform, the Geddes group was able to sense protein concentration in a sample as low as 156 fM based on the changes in dye fluorescence, induced by the competitive binding of the protein analyte against the dye-bound protein. Similar approach was used in a high-throughput 96-well system to measure FL isothiocyanate bound to avidin, which in turn bound to the biotin present on the silver surface.[234] The binding was accelerated by the microwave radiation, making it 90-fold faster and enhancing emission intensity 5-fold. FL isothiocyanate was also used to determine trypsin concentrations in samples where the analyte induced cleavage of the dye-conjugated protein from sample wells, resulting in reduced fluorescence.[231]

The detection of inorganic ions has been achieved in solution phase as well. Prosposito *et al.* synthesized AgNPs with 3-mercaptopropane sulphonate ligand layer to detect Ni^{2+} in solution.[235] The synthesized particles experienced changes in absorption spectrum upon binding to the target ion, making it possible to determine the concentration of the analyte, LOD being 0.3 ppm. With methods taking advantage of quenching of dyes on the particle surface, also the concentration of Hg^{2+}, Cu^{2+}, glutathione as well as 6-thioguanine have been determined. With Hg^{2+}, Sahu *et al.* used a RhB quenched nanocomposite bound to the AgNP-graphene. When the Hg^{2+} got introduced to the system, the RhB dye was liberated and subsequently its fluorescence was restored, allowing detection at 2 nM in optimized conditions.[236] The detection of Cu^{2+} was done with Au_{38}@BSA-based analysis as described in chapter 4.1, but the luminescence intensity of the cluster was significantly improved by the presence of AgNPs.[153] Similarly, the detection of 6-thioguanine was achieved with a LOD of 5.3 nM in a reaction where the analyte replaced the surface-bound acridine orange and the release-inducing change in fluorescence revealed the concentration of analyte in the sample.[237] However, for solution-based sensing of analytes using AgNPs, the silica-shelled particles have been the predominant choice for application.[238] The silica coating provides a physical barrier between the fluorophore and nanoparticle, making it easy to acquire particle-dye nanocomposites with suitable distance for MEF. Aslan *et al.* were able to conjugate Cy3 on the surface through Cy3-conjugated streptavidin binding to a AgNP-surface adsorbed, biotin-functionalized BSA. DNA-sensing has also been achieved with silica coated AgNPs. An elaborate plan to detect oligonucleotides associated with Alzheimer's disease was brought to fruition by Zhou *et al.*.[239] Magnetic nanoparticles and FL-covered AgNPs were prepared with complementary ssDNA strands, causing the target ssDNA to hybridize between the two nanoparticles, creating a sandwich complex. With this method the oligonucleotide concentration could be determined down to 1 pM concentration. With a similar approach, Pang *et al.* determined the concentration of recombinant hemagglutinin protein associated with H5N1 influenza with LOD of 2-3.5 ng/ml concentration.[240] Their approach relied on

formation of a guanine G-quadruplex formation upon binding of the target protein on the AgNP surface, which was successively detected through DNA-binding thiazole orange MEF. However, the highest specificity to discreet DNA sequences was achieved by Kim and co-workers with a detection limit of 100 aM using their AgNP product.[241] The AgNPs were covered with polydiacetylene shells, which were functionalized with DNA sequences complementary to the target DNA. Upon binding of the complementary DNA strand, the fluorescence intensity of the particles increased significantly. Additionally the metal enhancement made it possible to detect the target DNA sequence using Raman scattering, with a 100-fold increase observed in the phenomenon.

In addition to fluorescence, also Raman scattering has the potential to be enhanced by a factor of $10^8 - 10^{12}$ with use of the plasmon resonance of silver nanoparticles.[242] Surface-enhanced Raman scattering (SERS) has been used to a great extent to improve the detection sensitivity of many biological analytes with AgNPs. The general approach for achieving SERS for a compound of interest is the same as for MEF, inducing proximity to the silver surface using any type of binding interaction.[243] The benefit with SERS compared to MEF is that quenching does not play a role, hence the analytes can be even introduced inside the ligand layer of the particles through weak interactions. The SERS is particularly intense in a plasmonic hotspot between two nanoparticles. Even the assignment of bacterial species with SERS has been achieved through antibody conjugation to a silver surface and the subsequent enhancement of Raman signal providing a fingerprint spectrum.[244] SERS also serves as a method to employ Raman scattering in live cell imaging, making possible the imaging of certain fingerprint signals in cells. This was displayed by Ardini *et al.*, who were able to follow the alkyne functional group signal at 2045 cm-1 on the AgNP surface *in vivo*.[245]

Aggregation of the nanoparticles leads to an increase in their plasmonic properties and when done controllably, can be utilized as another detection method for AgNPs. For example, using an absorption/scattering approach, a research group was able to determine Hg^{2+}, CH_3Hg^+ and Pb^{2+} based on the aggregation-induced reduction in scattering and changes in UV-vis spectrum.[246] In a similar colorimetric sensing application, the concentration of Cr^{3+} was determined up to LOD of 1 nM with cysteine-functionalized AgNPs.[247] The detection of DNA using SERS was achieved with sequence specifically so that the target DNA-connected ssDNA-functionalized silver particle and silver surface together creating a Raman hotspot and leading to significant Raman enhancement of the reporter molecule on the silver surface.[248] In another instance, the complementary target ssDNA lead to aggregation of dye-functionalized AgNPs and sequentially the SERS experienced by the AgNP-surface bound dyes increased.[249] A combinatorial method, using Cy3 and IgE-binding aptamer-functionalized AgNPs made possible the detection of said antigen.[250] At the event of IgE binding, a larger aggregate of AgNPs were formed, significantly increasing the MEF experienced by Cy3 and allowing the

detection of the target analyte at almost 200 fM concentration. The enhancement of sensing sensitivity with larger NPs taking advantage of the phenomena covered in this chapter offers exciting possibilities. As the methodologies for their synthesis and use develop, these nanocomposites are bound to provide improvement broadly to the different sensing and theranostic applications in the future.

5   EXPERIMENTAL METHODS

In this chapter, some of the methods related to this thesis will be briefly covered. With cyanine dyes (and other fluorophores), the different fluorescence methods to employ and evaluate their emission characteristics are covered in chapter 5.1. Additionally the theoretical model applicable to nucleic acid binding that further the understanding in these host-guest interactions are explained. In chapter 5.2, the methods related to estimating the true size of nanoparticles and the valuable information attainable from this will be briefly explored. These methods include diffusion-ordered spectroscopy (DOSY), dynamic light scattering spectroscopy (DLS) and polyacrylamide gel electrophoresis (PAGE).

5.1   Fluorescence methods

The basic principle of measuring fluorescence from an emitting sample is similar regardless of the selected instrumentation; exciting light is directed to the sample of interest, after which the photons emitted by the sample are detected by a photodetector. The detected photons are then amplified using a photomultiplier to strengthen the signal observed from the sample. The main differences arise from how the light is manipulated during the measurements. The fluorescence spectrophotometers Varian Cary Eclipse and Horiba Aqualog 800-C, together with fluorimeter Perkin Elmer Victor Multilabel plate reader, were employed in the course of this work. The Eclipse and Aqualog detect light wavelength-specifically in two different ways. The Eclipse uses prisms to scan through the wavelength area of interest, whether excitation or emission, and detects the emission intensity at each increment separately. The Aqualog on the other hand uses gratings to diffract the excitation light and the light emitted from the sample. The light from the sample is then diffracted as a full spectrum to a detector, leading to simultaneous detection of the whole visible light spectrum, contrary to the Eclipse. The amount of light to and from the sample can be controlled using their respective slits with the Eclipse. In addition to the

possibility to control the scanned area, this machine has the benefit of cutting out undesired parts of light from the sample (*i.e.* scattering and secondary photons), whereas with the Aqualog only the incoming light intensity can be affected by determining the amount of time that light is collected. Contrary to the two others, the Victor platereader does not give wavelength-specific results; the device detects total emission from the sample. The light that makes it to the detector is controlled with the use of light cut-off/pass filters that allow only certain wavelength window to pass through. This creates a requirement for complementarity between the fluorophore and filters employed, so that excitation light reaching the sample and the emission from the sample to the detector fit to the fluorophore in question. The benefit of this is that multiple fluorophores in the same sample can be detected quickly by changing the filters used for sensing emission. Comparing Victor to the two other spectrophotometers, measurement of hundreds of samples in low volumes simultaneously is made possible, whereas the Eclipse and Aqualog are limited to a single sample cell at a time. The different instruments available for measuring fluorescence compliment each other and understanding their performance is crucial for choosing the right methods for the work.

5.1.1 Determining nucleic acid binding parameters

To understand the binding of proteins and other ligands to DNA, McGhee and von Hippel approached the phenomenon theoretically, considering DNA as a single continuous lattice.[251] The lattice consists of repeating binding sites, the nucleic acids, each offering a single unit in the lattice for ligand binding. With the introduction of the ligands to such system, the binding of the ligand is expressed as an equilibrium reaction

$$\frac{[Bound\ ligand]}{[Free\ ligand]} = K \times [Free\ ligand\ binding\ sites]\ , \tag{2}$$

where *K* represents the association constant related to the ligand binding. However, the ligand binding to the lattice happens at an arbitrary location and hence the binding of the following ligands to the same lattice depends on the location of the first one. This means that after binding of two (or more) ligands, not only the bound sites, but also free space between the previous two might become unavailable, if insufficient binding area is available. Thus, the authors considered the probability of a suitable gap existing for the next incoming ligand in this situation. Without going into detail of this process, the probabilities for an available and unavailable binding sites for the incoming ligand are

$$P_{free} = \frac{1-nv}{1-(n-1)v} \tag{3a}$$

and

$$P_{bound} = \frac{v}{1-(n-1)v} \qquad (3b)$$

respectively, where v is the binding density of ligands on the lattice and n corresponds to the area in the lattice acquired by a single ligand, in the situation where ligands do not interact with each other. If the ligands either repel or attract each other, this affects the binding site probabilities in their vicinity and needs to be accounted for. However, in the study of nucleic acid binding cyanine dyes, the use of the model for non-interacting ligands is commonly used and thus the case of interacting ligands will not be covered herein. Finally, the equilibrium of ligand binding from equation 2 can be expressed as

$$\frac{v}{L} = K_a \frac{(1-nv)^n}{(1-nv+v)^{n-1}} \qquad (4)$$

where L is the amount of unbound ligands and K_a the association constant of the ligand to DNA binding. In other words, the model describes the ratio of bound and free ligands by the effect of association constant and the size of the binding site of the ligand as a function of the bound dye molecules.

Hence, in order to apply this model to experimental data, one needs to determine the amounts of free and bound ligands in an experiment. In the case of cyanine dyes, the fluorescence of the dyes can be used for this purpose. As the dyes exhibit turn-on fluorescence only upon binding to double-stranded nucleic acids, while otherwise non-emissive, this division can be used to differentiate between bound and unbound states. Using this property, the fraction of dye molecules can be determined as

$$\theta = \frac{F}{F_b}, \qquad (5)$$

where F is the observed fluorescence from a sample and F_b is at the fluorescence of a 100 % bound dye at equal concentration of dye. The F_b can be obtained from extrapolating to a linear fit of fluorescence data, where a high excess of binding sites are available and thus the amount of unbound dye is negligible. From this, both the concentration of the free dye in the sample, as well as the binding density to the DNA can be determined with the following equations:

$$L = (1 - \theta)c \qquad (6)$$

and

$$v = \theta \frac{c}{c_{DNA}}, \qquad (7)$$

where L corresponds to the concentration of unbound dye molecules, c to the total concentration of dye in the sample, and c_{DNA} the concentration of DNA in the solution. By plotting the experimental data as v/L as a function of v, the equation 4 can be utilized to find the experimental parameters related to the

nucleic acid binding. With such dyes as the monomethine cyanine dyes, the understanding of the binding parameters is crucial for their application. Thus, the determination of these binding values is imperative addition to the usual brightness-related values when evaluating the properties of these dyes. This applies also to other such dyes with supramolecular turn-on mechanisms, as long as the suitable theoretical expressions are available.

5.2   Size determination of nanoparticles

In nanoparticle research transmission electron microscopy (TEM) has become an established method for evaluating the quality of synthesis products.[252] However, electrons cannot be used to image the complete size of the nanoparticles, as the organic ligand layer does not provide enough contrast to be seen in the images. Consequentially, making observations on changes in the ligand structure is neither possible. Having realistic estimates on the nanoparticle size is of major importance, particularly for their application *in vivo*. Fortunately, other methods for acquiring this information are available.

These methods rely on determining the movement of the sample of interest in different media. With NMR spectroscopy, diffusion-ordered spectroscopy (DOSY) can be used to address this. In DOSY, a two-pulse program is used to first cause a magnetization of the spins to the x-y plane with a 90° pulse, followed after a waiting period by a 180° pulse that would refocus the spin after which the radio-frequency signal from the sample is recorded. After both pulses, two magnetic gradients of opposite direction to each other are applied. This causes the spins of the nuclei present in the sample to not refocus properly, leading to dampening of the signal. The signal dampening is related to the spatial diffusion (*i.e.* movement) of the nuclei in the solution. In addition, the dampening is also related to the difference of the two gradients applied, which can be used to create a series of signal dampening in the sample intensity, by varying the gradient difference in the measurement. This series serves as the experimental data set for fitting into Stejskal-Tanner formula[253], from which the diffusion coefficient D of the sample can be determined when the other instrument pulse program related variables are known. The diffusion coefficient relates to the hydrodynamic radius through Stokes-Einstein equation[254]

$$D = \frac{k_b T}{6\pi\eta r_h} \tag{8}$$

where k_b, T, η and r_h correspond to Boltzmann constant, temperature, solvent viscosity and hydrodynamic radius, respectively. While DOSY is a great method for characterizing nanoparticles of distinct molecular composition, it does not work well for characterizing polydisperse products, such as the larger nanoparticle products tend to be. Dynamic light scattering (DLS) uses light as a

means to determine the same diffusion coefficient.[255] It is well known, that larger particles (from few nanometers to micrometers) scatter incoming light through Rayleigh scattering. Under constant radiation, the intensity of the scattered light fluctuates, depending on the Brownian motion of the particles over time. By recording the change in light intensity over time in the sample, an autocorrelation function can be constructed and from it the decay rate of the light intensity is determined. As the decay rate is related to the diffusion coefficient of the sample, the hydrodynamic radius of the sample can be determined from this using equation 8 similarly to DOSY experiments. However, DLS works better for larger particle systems, as the proportion of the light scattered from the sample increases with particle size. DLS works better for polydisperse particle samples, whereas DOSY requires samples of molecular nature to give reliable results. Hence DLS is widely used for the characterization of colloidal nanoparticle systems, where the acquired size distribution as a result corresponds better to the reality of these products.

In addition to DOSY and DLS, gel electrophoresis is a simple method for acquiring knowledge on the size of different nanoparticles. In essence, the nanoparticles of interest are set to move through a gel polymer with an electric field used to induce the movement. As such, the larger and bulkier nanoparticles will move slower through the gel, whereas smaller particles pass through itfaster. The choice of gel and its permeability can be adjusted to different samples. In practice, polyacrylamide is often chosen for nanocluster samples, whereas with colloidal nanoparticles, better results are acquired with the use of agarose. Contrary to DOSY and DLS, the traversing velocity is also dependent on the charge of the nanoparticle, as the movement is induced by an electric field. Additionally in gel electrophoresis, no exact values are obtained, but sample run distances can be compared to a known reference sample.

These methods and their combination can be utilized to gain valuable information on the nature of the nanoparticle ligand layer, otherwise unattainable using TEM for example. It is important to note that the shape of these products is always assumed to be spherical and in the case of products shaped otherwise, the results will correspond to the largest facet. When attempting the alteration of the nanoparticle surface, the comparison of the starting material and product can yield valuable information on the success of one's syntheses. For example, the exchange of surface ligands into larger ones compared to initial ligands can be observed with both DLS and DOSY, whereas changes in the ligand charge are best visualized using gel electrophoresis. In the case of gel electrophoresis, the intactness of the metal core can be usually assumed, based on the unchanged product colour. These methods offer additional tools for characterizing different nanoparticle systems and are highly complementary to the traditional characterization methods for addressing the elusive ligand layer of the nanoparticles that quite often presents the area of highest interest in these molecules, as will be shown in the next chapter.

6   RESULTS AND DISCUSSION

The aim of this work was to produce novel fluorescence-based probes for sensing nucleic acids. The need for producing nucleic acid sensors with both increased brightness and better targeting capabilities arose from the desire to track the viral genome of enteroviruses *in vivo*. What makes this a formidable challenge is first the low quantity of single-stranded RNA present in individual virus particles (~7000 bases in a genome). Second, the abundance of cellular DNA and RNA poses a great source of background emission from these fluorescent probes that is difficult to distinguish from the target signal. However, solving this challenge would enable researchers to gain further understanding on the infection mechanisms of viruses, allowing new targets for antiviral treatments to be found. For example the mechanism of enteroviruses' RNA release to the cytoplasm after viral particle entry through endocytosis (*i.e.* inside a lipid particle from the cell surface) is still unknown. Currently no antiviral therapies exist against the whole genus of enteroviruses (responsible for *e.g.* meningitis and polio) despite big efforts, making research for new targets even more valuable. This work aimed to provide suitable tools for addressing this issue.

In this chapter, the main results from papers **I-III** will be covered and coupled with unpublished results on a series of improved cyanine dyes **IV** (chapter 6.1) and a gold nanocluster-fluorescent dye nanohybrid employed as a pH sensor *in vivo* **V** (chapter 6.3). Two approaches were chosen to address the problem described above. The first was to understand and improve the properties of the monomethine cyanine dyes used as fluorescent sensors. This was approached using the widely used SYBR Green dyes as a starting point, adding a covalently binding moiety to the compounds[III] and adjusting the heteroatomic constitution of the chromophore to further improve the brightness of the dyes.[IV] The nucleic acid binding properties of the dyes and application of the covalently linked moiety was studied, as further explored in the following chapter. The second approach involved the use of gold nanoclusters as a solid support for fluorescent dyes in order to achieve better localization. For this, a new size of gold nanocluster was synthesized[I] and comprehensively

characterized[II] as covered in section 6.2. Gold nanoclusters were then employed to produce dye – nanoparticle hybrids with an azatriangelium dye and one of the new SYBR Green derivatives. Quenching of the fluorescence by the gold nanoclusters created a possibility to use the azatriangelium dye for pH sensing, involving a turn-on mechanism (covered in chapter 6.3). With the nucleic acid sensing probe the quenching rendered the nanocomposite useless for nucleic acid sensing and thus will not be covered further in this work.

6.1   Nucleic acid binding cyanine dyes[III, IV]

6.1.1   Synthesis of monomethine cyanine dyes

The precursors for the products in this work were synthesized using previously reported protocols. The oxazolium starting material **4** was synthesized with the N-methylation of benzoxazole with o-methyltosylate.[33] The benzothiazole precursor was synthesized using 2-chloroaniline and potassium ethyl xanthogenate as the starting materials to yield an intermediate thione.[256] Next the sulfur was methylated using methyl iodide following the same N-methylation as before. The methyl phenyl quinolone starting reagent **1** was synthesized using the Ullman condensation to substitute the nitrogen in the hydroxyquinoline starting reagent with a phenyl group.[36] The dyes in this work were synthesized using the classical cyanine condensation, using benzoxazole or benzothiazole and quinoline as starting materials. For this, the synthesis of Karlsson and co-workers was applied, where equimolar amounts of the two quaternary salts were mixed with four equivalents of triethylamine (TEA) overnight in dichloromethane (DCM).[41] However, it was found possible to include two additional reaction steps in a one-pot reaction before the final step (Figure **14**).[III] First the ketone in phenyl quinoline **1** was chlorinated using $POCl_3$ in 1,2-dichloroethane overnight at 70 ˚C into **2**. Next, the chloride was replaced by a thiol in a nucleophilic substitution reaction in dry DCM over a few days for **3**. 11-mercaptoundecanoic acid and 11-mercaptoundecanol were used, providing sufficient spacer for further covalent linking of the final products **7** and **6**, respectively. Additionally the leaving group from the benzoxazole **4** reacted in the final step of the reaction to yield compound **5**. Finally the benzoxazole/benzothiazole was added with TEA and after an overnight stirring the products were separated with 5-20 % methanol – DCM eluent in a silica gel column chromatography. For the whole reaction, product yields between 10 – 30 % were observed. For the covalent conjugation and for improving the water solubility of **7**, the product was conjugated with a succinimide and methyl groups to yield **8** and **9**, respectively. This was achieved by conducting a Steglich esterification with the hydroxysuccinimide and methanol as the second reagents.[257] The yields for these reactions were 15 – 30 %.
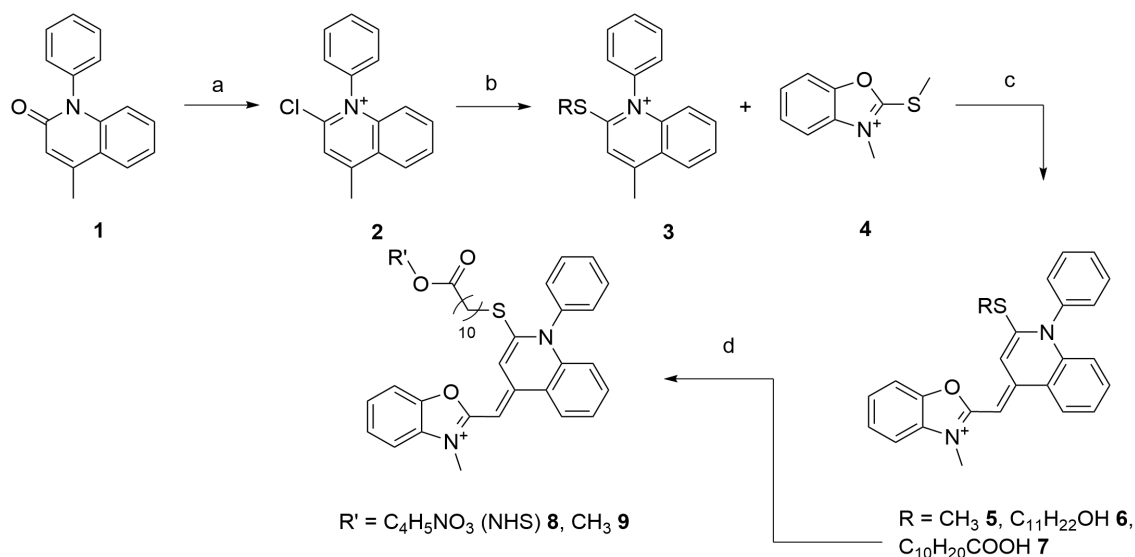
Figure 14. Synthesis scheme for the products studied in article III. a) $POCl_3$, 1,2-dichloroethane, Δ; b) HSR (R = $C_{11}H_{22}OH$ or $C_{10}H_{20}COOH$), Et_3N, DCM; c) Et_3N, DCM; d) N,N'-Dicyclohexylcarbodiimide, 4-dimethylaminopyridine and methanol or N-hydroxysuccinimide.

In the case of the unpublished manuscript, the order of reactions was slightly altered.[IV] It was observed that introducing the amine moiety before cyanine condensation made the final step ineffective. Thus, a 2-chloride substituted dye (Appendix **IV**, Chart 1) was collected first by conducting the cyanine condensation before the nucleophilic substitution step. The chloride was then substituted by dimethylamine in acetonitrile over four hours to yield the final products. However, the observed yields were significantly lower (3 – 10 %), possibly due to the intermediary purification of the chloride product. By varying the chemical structures of the salts involved in the cyanine condensation a variety of fluorescent nucleic acid binding cyanine dyes were made, shown in Appendix **IV**, Chart 1. Following this, the synthesized dyes were spectroscopically evaluated with and without the presence of nucleic acids.

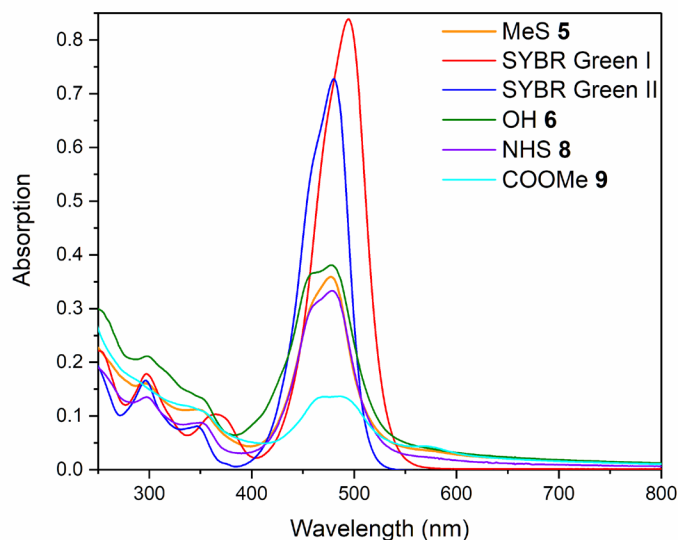### 6.1.2 Photophysical and nucleic acid binding properties

To evaluate the suitability of all the dyes involved in this work, their photophysical properties were evaluated and compared to the reported values for the SYBR Green family dyes, where possible. First, the dye brightness related parameters (molar absorptivity and QY) were determined. The absorptivities of all dyes were determined by measuring their absorption in five different concentrations of the dye. The increase of absorption is linear in relation to the concentration and the slope of this line corresponds to the molar absorptivity coefficient of the dye. The solvents of choice for evaluation were 1x Tris-EDTA (TE) buffer and a less polar solvent to remove the low water solubility of the dyes as a factor. Similarly, the fluorescence quantum yields were determined in accordance to the protocol of Wurth *et al.*[258] using

fluorescein as the standard with 89 % quantum yield value. The QY of the unknown sample is proportional to the standard by the ratio of the slopes of a linear fit made in a fluorescence *vs.* absorption graph, when the same measurement parameters have been employed. The products measured in paper **III** had molar absorption coefficients of ~20,000 $M^{-1}cm^{-1}$ in TE buffer, increasing to ~30,000 $M^{-1}cm^{-1}$ when measured in DCM (Table 1). Particularly the long alkyl linker reduced the water solubility of the corresponding dyes, as observed by the H-type aggregation in TE buffer indicated by the secondary blue-shifted shoulder in absorption spectra, nonexistent in DCM (Figure **15**). Surprisingly, the presence of the functional group at the end of the alkyl linker had a major impact on the brightness of the products. The hydroxyl group-functionalized dye **6** exhibited slightly elevated absorptivity compared to the "unfunctionalized" methyl subsituted dye **5**, while the carboxymethyl substitution diminished the absorption roughly to a third compared to others. However, compared to the reported molar absorptivity coefficient value of 75,000 $M^{-1}cm^{-1}$ for SYBR Green I[68] the observed values were quite low. Similarly, the quantum yields of the synthesized dyes were lower compared to the 80 % of SYBR Green I[259], varying between 47 – 63 %, with the carboxymethyl substituted product **9** giving a too low result for determination (Table 1).[III] Majority of these differences were contributed by the one heteroatom change (thiazole → oxazole) in the chromophore comparing SYBR Green I and SYBR Green II to each other.

Table 1. Brightness related parameters determined in work **III**.

| Dye	$\varepsilon_{\text{TE Buffer}}$ **($M^{-1}cm^{-1}$)**	ε_{DCM} **($M^{-1}cm^{-1}$)**	QY Φ (%)
SYBR Green I	75,000[68]	-	80[259]
SYBR Green II	-	-	36[260]
5	19,200	31,100	60
6	22,000	38,800	47
8	18,500	30,300	63
9	7900	11,600	-

Figure 15. Absorption spectra of the dyes synthesized in article **III** at 19.6 μM concentration in TE Buffer in room temperature.

Evaluation of this hypothesis served as the motivation to conceive the dyes presented in the unpublished manuscript (Appendix IV, Chart 1). The values determined for these dyes gave significant support to the initial assumption as the molar absorption coefficients were observed to double or even triple, when compared to compound **5** from article **III**. The compounds of the unpublished manuscript **IV** will be referred to with **M**-prefix and can be seen in Appendix **IV** Chart 1. Interestingly the highest brightness (47,300 $M^{-1}cm^{-1}$) was observed for compound **M2**, largely ascribed to its 100 % QY (Appendix **IV**, Table 1). The reason for this was postulated to be the molecule consisting of solely second period elements, whereas replacing one of the heteroatoms with a sulphur reduced the QY to 76 % (**M3**) and 68 % (**M4**), and replacing both heteroatoms lowered the quantum yield down to 14 % (**M5**). A chlorine atom present in the chromophore had even more devastating effect, with a single atom causing a decrease of QY down to 18 % (**M1**). Also the spectral characteristics change along with the changes of heteroatoms. The brightest dye **M2** also absorbed highest energy of light at 464 nm, with replacement of a single and two heteroatoms with sulphur leading to decrease in absorption energy to 487 – 491 nm and 514 nm, respectively (Appendix **IV**, Fig. 1a). In addition to this, the photostability of the dyes of this work were evaluated, both in TE buffer, and fully bound to calf thymus (ct) DNA. This was done by exposing 2 ml of equimolar dye solutions to a halogen lamp with 44 mW light power over a 2 cm^2 area. While no trends in the photostability of the dyes related to the chemical structure were noticeable, the differences among dyes were notable. The chlorine-containing dye **M1** had the highest photostability in both solvents, 6.3 h in TE buffer and 35.9 h bound to ctDNA (Appendix **IV**, Table 2). Free in TE buffer, dyes **M2** and **M5** had half-lives of 2.9 h and 2.4 h, respectively, while

the degradation of **M3** and **M4** was faster with a 0.5 h half-life value. All the tested dyes experienced a major increase in photostability when bound to ctDNA. However, the enhancement of this stability was the highest with compounds **M2** and **M3** increasing their stability to similar magnitude with **1**. The enhancements observed for **M4** and **M5** lead to much shorter lifetimes compared to the others, with compound **M4** decaying at a half-life of 1.6 h, even in the presence of ctDNA.

The binding to nucleic acids was evaluated through fluorescence spectroscopy on the dyes of this work in comparison with SYBR Green I and SYBR Green II.[III] The six fluorescent probes were evaluated in the presence of limited amount of five different types of nucleic acid in fluorescence titration experiments (Figure **16a**). With this, the differences the secondary structures of DNA had on the probe binding and fluorescence saturation were evaluated (Figure **16b**). The tested nucleic acids included a 50-base sequence of completely linear (liDNA), another 50-base self-pairing hairpin-forming sequence (hpDNA), ctDNA (few thousand basepairs of dsDNA), bacterial plasmid DNA that is circular double strand (λDNA), and ribosomal RNA extracted from cells (rRNA). Expectedly, the linear DNA without base-pairing gave negligible signal compared to other nucleic acids, whereas the mostly double-stranded hpDNA immediately gave the highest fluorescence values among the tested DNA. However, the differences between the sources of DNA were minor between each other, most likely due to small amounts of single-stranded DNA present in the samples. Also the order of fluorescence intensity among the tested dyes remains the same; SYBR Green I had the strongest emission, followed by methylthiol substituted compound **5** as the second, preceding SYBR Green II by a slight margin, and the long alkyl-substituted dyes **6**, **8**, and **9** giving significantly lower intensity compared to the former products. While with rRNA the long alkyl chain did not improve the emission either, the order of the three best dyes changed. As promised, the SYBR Green II surpasses SYBR Green I in emission intensity when bound to RNA.
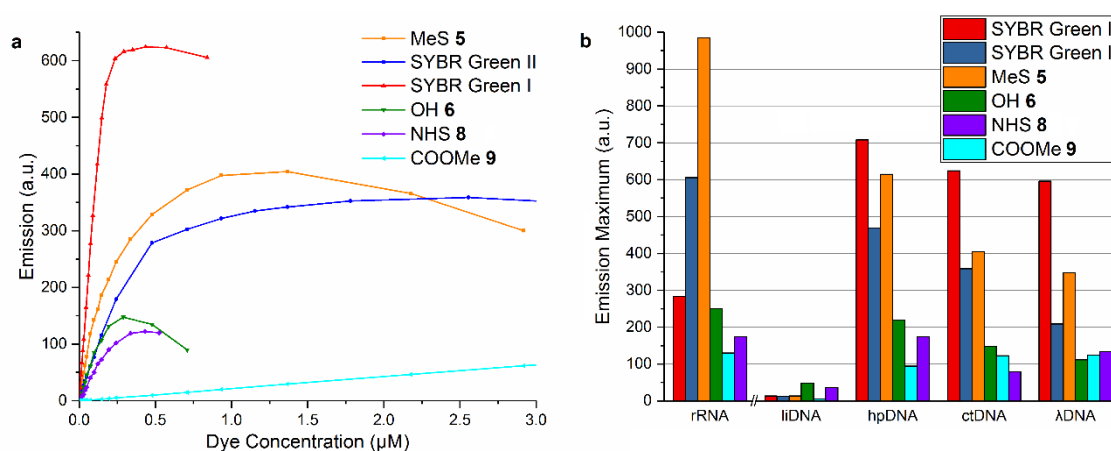
Figure 16. a) Emission peak values of dyes titrated in 0.52 µM ctDNA in TE Buffer in room temperature. **b**) Highest observed emission values throughout titration with different tested nucleic acids.

However, dye **5** was found to produce even higher emission values compared to SYBR Green II. To understand the reasons for these results, the nucleic acid binding parameters of these compounds were determined.

Conducting the necessary fluorescence titrations (Figure **16a**) and processing the data according to the protocol presented in section 5.1.1 yielded the association constants and binding site sizes for the compounds presented in article **III** (Table 2), as well as for the dyes in the unpublished manuscript **IV** (Appendix **IV**, Table 2). As the temperature of the experiment was known, the Gibbs free energy of the ctDNA binding could be determined from the association constant. The determined binding site sizes support the hypothesis presented by Dragan *et al.*, stating that the 2-substituent contributes to the DNA binding by settling into the minor groove of the DNA, increasing the area required by a singular dye molecule.[67,261] As the length of the "arm" moiety on the molecules increased, so did the size of the binding site. This effect was even more notable when the dyes were bound to λDNA, making it possible to draw a reasonably linear dependence between the binding site size and the length of the alkyl substituent (Figure **17**). The values varied between 2.2 basepairs for the shortest molecule **5**, increasing up to 4.7 basepairs reserved by the undecanol-functionalized **6**.[III] The dyes in the unpublished manuscript **IV** were substituted with either a chlorine, methylmercapto or dimethylamine functional groups that required low binding sites in general. The determination of binding site size for these dyes revealed similarly a small increase from the addition of another methyl group to the dye molecule; the binding site size for methylmercapto compounds was ~1.7 basepairs, increasing to 2.1 with the addition of another methyl group in compound **M4**.

The determination of Gibbs free energies for the DNA binding gave information on the effects that the arm moieties have on the binding (Table 2).[III] The presence of the positively charged diallylamine moiety at the end of the 2-substituent improves the binding, as observed by a lower binding energy observed for the commercial dyes SYBR Green I and SYBR Green II, compared to compound **5**.

Table 2. Summary of ctDNA binding parameters achieved from the fits of equation 4 into the Scatchard plots.

| Dye	SYBR Green I	SYBR Green II	5	6	8
Association constant K_a (10^6 M^{-1})	7.6	35	3.9	4.8	5.4
Binding site size n (bp)	3.1	2.6	2.3	4.7	4.1
Gibbs free energy ΔG (kJ/mol)	-38.8	-42.5	-37.1	-37.6	-37.9
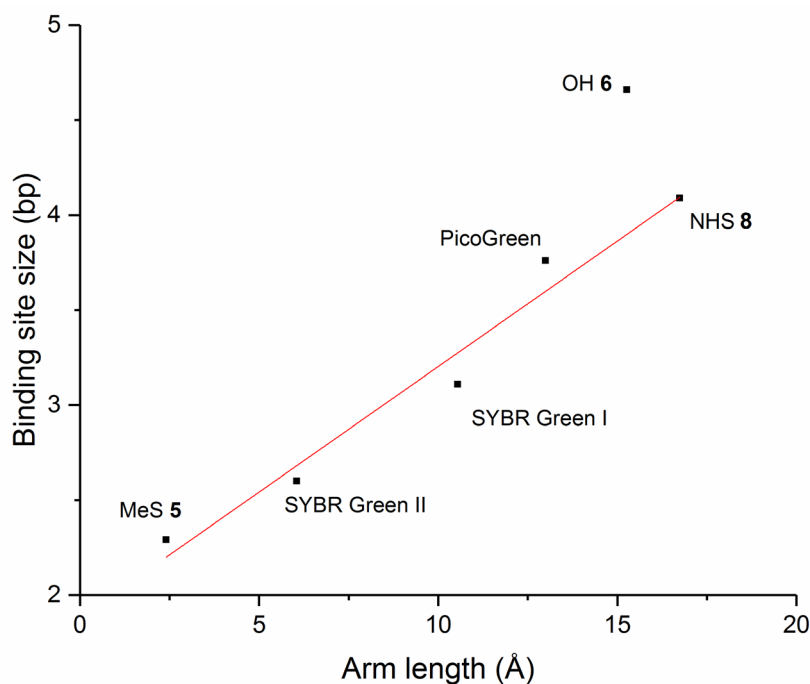
Figure 17. The linear relation between the length of the 2-substituent and the size occupied by a single dye molecule when bound to λDNA.

On the other hand, the long undecyl arm moiety was expected to have a minor positive contribution to the binding energy. In the case of ctDNA this was not the case, but in binding with λDNA a minor <1 kJ/mol decrease in the free energy values were observed for compounds **6** and **8**. The difference between DNAs might be inherent to imperfect insertion of the arm moiety along the helix in the case of ctDNA, due to the weakness of the hydrophobic effect. Some of the positive contribution could also be negated by the electronegative functional groups at the end of the arms. In the unpublished work **IV**, the structural changes between different products were ascribed down to single atoms or functional groups and hence more reliable conclusions for their binding energy differences could be made. The electronegative atom chlorine in compound **M1** has a clear negative contribution to the binding energy, giving the worst binding value in the whole series -34.6 kJ/mol. On the other hand, the positive contribution from oxazole and dimethylamine groups gave the lowest binding energy -39.0 kJ/mol for dye **M2** (Appendix **IV**, Table 2). From this, replacing the heteroatoms in the dye had negative impacts on the binding energy; going from oxazole to thiazole moiety led to 0.9 kJ/mol decrease, whereas replacing the dimethylamine group with the methylthiol lowered the binding energy by 1.5 kJ/mol, while both of these changes led to a 3.2 kJ/mol decrease with molecule **M5**. With the oxazole → thiazole change the contribution to binding energy comes only from the change in heteroatom, whereas changing the arm moiety carries an additional methyl group that contributes to this change. From this, it is possible to estimate the contribution of the methyl group to be around 0.6 kJ/mol, although another series of dyes

should be used to confirm this suggestion. However, the adverse effects of introducing thiols to this species of dyes was quite evident. The reduction in binding energy might be inherent to the electronegativity of the atoms, suggesting that introducing electronegative moieties to the dye chromophores has a positive effect to the binding.

6.1.3 *In vitro* **sensing of viral RNA**

As the RNA-sensing properties of the synthesized dye **5** were determined to be better compared to the RNA-sensing probe SYBR Green II, they were tested for *in vitro* sensing of viral RNA.[III] Additionally, the covalently binding dye **8** was conjugated to the protein capsid of Echovirus 1 and tested along with the two dyes, after removal of the excess unbound dye through dialysis. These three samples were tested in viral capsid opening experiments, where the virus environment was controlled to induce opening of the viral capsid and subsequent release of the viral genome to the solution. This was achieved by increasing temperature in a thermal assay or by controlling the salt concentrations in the solution to induce the opening (Figure **18a** and **18b**, respectively). By following the fluorescence from the samples as a function of temperature or time, the slowly opening virus capsid releases an increasing amount of single-stranded RNA into the solution, increasing the fluorescence from the probe. In both cases the synthesized **5** surpassed SYBR Green II in fluorescence intensity. The virus conjugated **8** gave a significantly lower, yet observable signal, as expected due to the low amount of dye molecules present on the virus surface compared to probes free in solution. Interestingly, the virus conjugated dye signal peaked in the chemical opening of the capsid, indicating possibly the average time of RNA release from within the capsid. With the methylthiol dye **5**, even further information on the secondary structure of the viral RNA genome was obtained. Contrary to SYBR Green I and SYBR Green II, compound **5** was found to have a linear dependence in its fluorescence on the ratio of RNA that was double-stranded (Appendix **III**, Fig. 12). By using a 50mer ssRNA strand as a template and pairing it with 15mer, 30mer and 45mer complimentary ssRNA strands, it was possible to establish a standard curve, to which an unknown sample of equal RNA mass in the same conditions could be compared. By estimating the amount of RNA in a known mass of Echovirus 1, such standard curve was used to establish 51 % as the amount of RNA duplex in the genome (Appendix **III**, Fig. 13). This corresponded well to the estimates presented previously in literature.[262,263] Albeit the covalently virus capsid linked **8** could be used in detecting the viral RNA release from within the capsid, the fluorescence signal from this was deemed too low for microscopic detection *in vivo*. Thus, noble metal nanoparticles were evaluated as a potential physical support for delivering larger amounts of the fluorescent probe to target to enhance the detection, starting with gold nanoclusters.
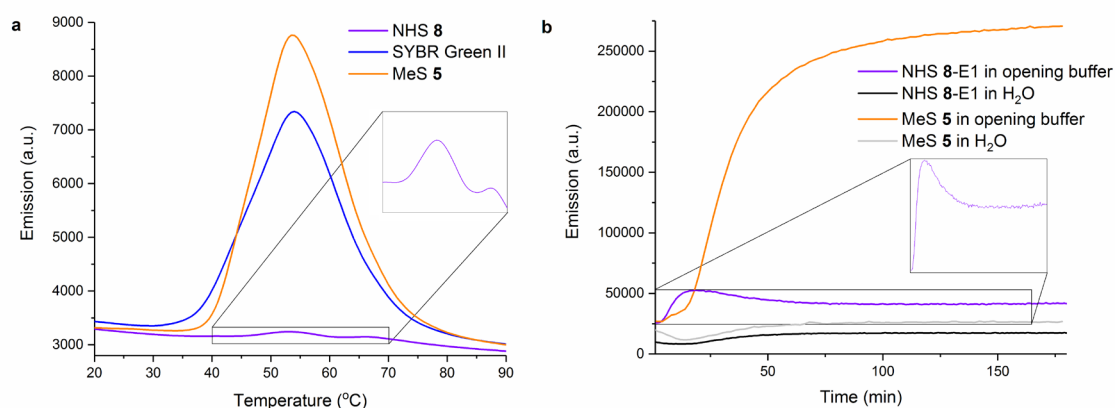
Figure 18. a) Thermal assay melting curve for the tested cyanine dyes in the presence of opening echovirus 1. NHS **8** was conjugated covalently to the surface of the viral particle. The inset shows a magnification for the echovirus 1-**8** conjugate emission. **b**) Emission of compound **5** and echovirus capsid conjugated **8** in virus opening inducing solution (20 mM NaCl, 6 mM KH_2PO_4, 12mM K_2HPO_4, pH 7.2 at 37 °C). Inset shows the observed emission peaking at ~15 minutes.

6.2 pH sensing with gold nanoclusters *in vivo*

6.2.1 Synthesis and characterization of gold nanoclusters[I,II]

In this work, monolayer-protected gold nanoclusters (AuMPCs) of discreet chemical composition were synthesized using *para*-mercaptobenzoic acid (pMBA) as the surface ligand. To achieve such monodispersity, a modified version of the Brust-Schiffrin synthesis was employed.[93] Generally, a mixture of $HAuCl_4 \cdot 3\ H_2O$, serving as the source of gold, was mixed in a mixture of water and methanol together with the surface ligand pMBA. The pH of the solution at this stage is a determining factor for the AuMPC constitution as shown below. NaOH solution was used to adjust it accordingly. The solution was stirred for 20 hours, leading to formation of a gold-thiolate polymer. After this, $NaBH_4$ is added to the solution as a reductant, inducing the formation of the final product after further mixing of ~5 hours. With this procedure, the well known $Au_{102}pMBA_{44}$ (Au102) was synthesized using a previously published procedure[264], together with a novel higher size nanocluster with $Au_{210-230}(pMBA)_{70-80}$ (Au250)[I] structure (Figure **19**). The main differences governing the end product constitution are the pH of the solution, its water-methanol ratio and the amount of reagents used. Between the two synthesized clusters the pH in Au102 synthesis was 13, whereas a reduced basicity of pH 11 gave Au250. Au102 is synthesized using three equivalents of pMBA to gold, while with Au250 this is doubled to six equivalents. Finally the methanol to water ratio is lowered in Au250 synthesis, 28 % of the volume, while Au102 uses 47 %. However, the end results also differ in quality with the two synthesis protocols, as Au250 synthesis produces a single size of AuMPCs straight from

the synthesis, while Au102 crude product has a mixture of sizes that need to be separated.
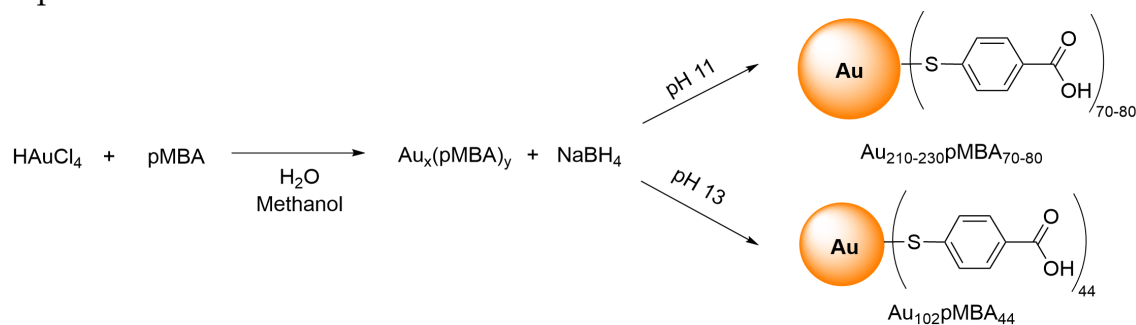

Figure 19. Synthesis scheme for the production of the AuMPCs involved in this work.

The pure Au102 was collected by taking advantage of the solubility of different sizes of AuMPCs through fractional precipitation. First, the crude product (dissolved in water) was adjusted to 6:4 methanol – water ratio *v/v*, causing the nanoclusters larger than Au102 to precipitate. After separating the precipitate by centrifugation at 3500 rpm for 15 minutes, the amount of methanol in the supernatant was increased to 78 % together with an addition of ammonium acetate, leading to Au102 precipitation while the smaller clusters remain in solution. Another centrifugation then yields the pure Au102 as a solid. Similarly, an addition of cations is used to induce precipitation of Au250, where addition of NaCl makes the collection of final product as a solid possible. The purity of the samples was established primarily using the PAGE, comparing a reference sample (another known Au102 sample) running distance to the synthesis products. Larger AuMPCs run slower in the gel compared to smaller ones as can be seen from Figure **20a**, making it easy to differentiate between the two cluster sizes. The narrow band was a clear indication of good product purity, whereas polydisperse products would show a longer band on the gel. Additional information on the clusters was seen from the emergence of the gold SPR peak at 530 nm, which is observed with Au250 and nonexistent with Au102, that is known to be a molecular AuMPC (Figure **20b**). Additional information on the ligand layer of the clusters was collected using ^{1}H and DOSY NMR spectroscopy, together with the previously unknown Au500 (Au$_{426\text{-}442}$pMBA$_{112\text{-}115}$).[II] The ^{1}H NMR spectrum of the AuMPCs is quite similar regardless of the cluster size. The binding to the gold surface leads to both shielding and de-shielding of the protons on the pMBA molecules, as manifested in the widespread peak at the aromatic region between 5.2 – 9.2 ppm (Figure **20c**). Interestingly, the ^{1}H NMR spectrum of Au500 contained multiple distinguishable doublet signals, in addition to the one observed from free pMBA in solution. However, no explanation for this observation was found. From the attempts of DOSY NMR experiments on Au250, no realistic values were obtained. Despite using 1,4-dioxane as an internal standard in the samples, the acquired values were too small to complement the TEM data of the same cluster. The size of the tested Au250 could be already over the limit of the

instrumentation/experimental parameters used and thus, smaller values for diffusion were observed. With this, DLS spectroscopy could be a better suited method for measuring the hydrodynamic radius of AuMPCs of this size range. However, this was not within the scope of this work, and thus was not attempted.
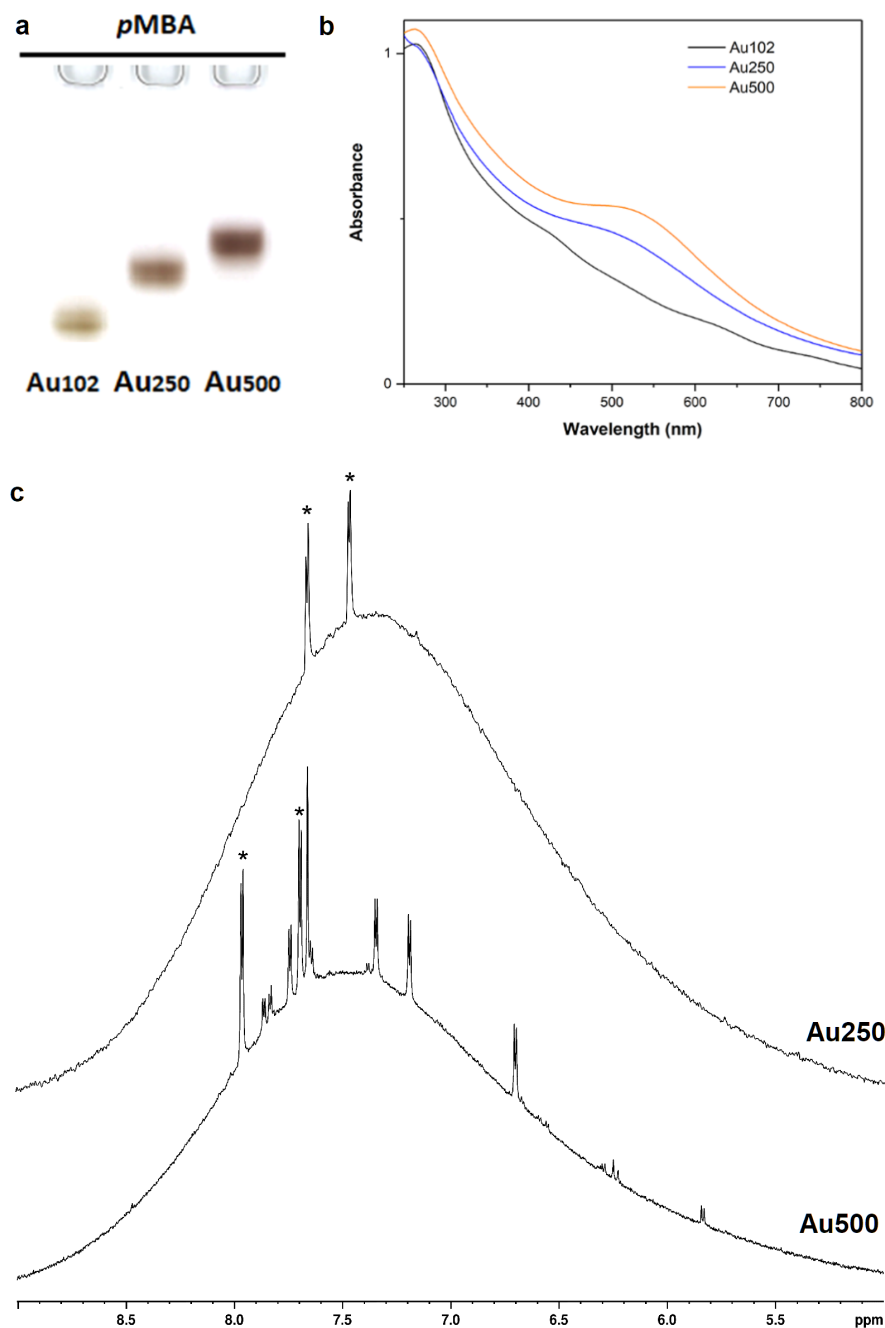
Figure 20. a) PAGE gel run of pure samples of the Au102, Au250 and Au500. **b)** UV-vis spectra of the three clusters, showing the emergence of the SPR at ~530 nm. **c)** Aromatic area of the ^{1}H spectrum for the Au250 and Au500 AuMPC.

6.2.2 Surface functionalization[V]

The pMBA ligand layer on the synthesized Au102 and Au250 was used as a foundation for further surface functionalization. The carboxylic acid functional group in the pMBA molecule can serve as a foundation for many post synthetic reactions. In this work, the previously published protocol employing Steglich esterification was used (Figure **21**).[135] The grand challenge of conducting this moisture-sensitive reaction with a water-soluble AuMPCs is establishing the water-free environment. This was achieved by dissolving the starting gold nanocluster in dry dimethylsulfoxide (DMSO) with the help of sonication. After this, the hydroxyl-functionalized ligand of desire was added followed by reactant N,N´dicyclohexylcarbodiimide addition in an ice bath, both dissolved in dry DCM. The reaction mixture was then allowed to warm up to room temperature and stirred overnight. Possible aggregates were removed from the solution by centrifugation at 3500 rpm for 5 minutes, following the complete precipitation of the suprenatant with an addition of methanol and ammonium acetate with vigorous mixing. The final product was then collected through another 10 min 3500 rpm centrifugation. The synthesis product was evaluated using PAGE, where a succesful synthesis was indicated with an appearance of a tail after the cluster band compared to the starting material AuMPC. In order to conjugate a fluorescent dye to the Au102 surface, a hydroxypropyl-functionalized azatriangelium dye (KU) was used, as shown in Appendix **V**, Figure **1a**. Based on the known absorptivities of dye and Au102, UV-vis (Appendix **V** Figure **2d**) and PAGE (Appendix **V** Figure **2b**) were used to estimate one nanocluster to be conjugated with 1 ± 1 dye molecules.
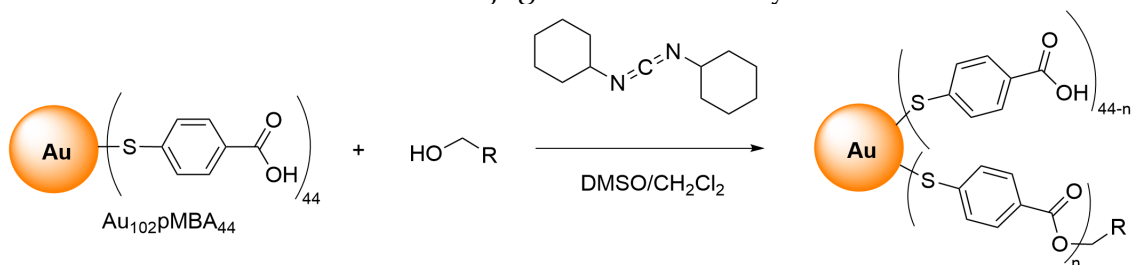
Figure 21. The general synthetic scheme for Steglich esterification of pMBA covered AuMPCs, applied from Ref 135.

6.2.3 Characterization of Au_{102} – KU hybrid fluorescence[V]

The synthesized covalent complex of Au102 and KU dye (from here on called AuKU), was found to have pH-related fluorescence properties. The complex was non-fluorescent in pH above 7, but when the pH of the same sample is adjusted to acidic, the fluorescence quickly increased continuously up to pH 1 (Appendix **V** Figure **2e**). The free KU dye was not observed to share this quality, exhibiting less than 20 % divergence in pH scale 1 to 14 in fluorescence. From the pH titration of the AuKU complex a sigmoidal behaviour of the fluorescence as a function of pH could be fitted, with a pK_a of 2.37 determined

as the acid constant for the fluorescence recovery. Also the pMBA ligands of the Au102 are susceptible to protonation in lower pH. The protonation of the Au102 ligands could cause a transition from a quenching state to a fluorescent state, as the carboxylate anions would stop binding the KU-dye to the cluster surface after protonation. However, the protonation of Au102 has a pK_a = 6.18[265] and thus does not correspond well to the fluorescence recovery in pH lower than 4. In addition, the full protonation of the Au102 pMBAs leads to loss of water-solubility and subsequent precipitation, which makes it hard to explain the behaviour of fluorescence at the lowest pH values. However, at the low pH it is possible for the covalent link, *i.e.* the ester bond, to go through hydrolysis and release the KU dye bound to the cluster surface, leading to fluorescence recovery. After the hydrolysis, the deprotonation of the pMBA ligands could lead to re-complexation at higher pH.

To confirm this theory, the non-covalent interactions of free Au102 and KU dye were evaluated. First, titration of increasing amounts of Au102 into a free solution of KU dye in pH 10 led to continuously decreasing fluorescence intensity, with 1:1 ratio of cluster and dye almost completely quenching emission intensity (Appendix **V** Figure **1d**). However, a recovery of fluorescence could be induced in these experiments by adjusting the acidity of the solution to pH 2. To assess the electrostatic effects in the fluorescence recovery, the possibility to induce the same effect using ions was tested. For this, 1:1 mixtures of Au102 and KU dye at 0.125 µM, 0.25 µM and 0.5 µM concentrations were prepared at pH 9, where the mixture was shown to be non-fluorescent. After this, a titration increasing the ionic strength of the solution with 25x phosphate buffer saline (PBS) or NaCl was conducted. As expected from an electrostatic interaction, the emission intensity increased towards a saturation, as the ionic strength of the solution was elevated using both NaCl and PBS (Appendix **V** Figure **1f**). This result, complemented by other evidence, further supported the mechanism of Au102 quenching the KU dye fluorescence in suitable proximity of the dye to the cluster. At higher pH the carboxylate pMBAs bind the dye to its surface, leading to quenching, while lower pH and/or introduction of ions cause resolution of the dye molecule and fluorescence recovery. With this, the AuKU complex was used to successfully image intracellular pH of live cells (Appendix **V** Figure **4**). The Au102 served as a carrier for the dye, entering the cells only through endocytosis, leading to the localization of the hybrid into endosomes in the cells. The acidification of the local environment then led to the fluorescence recovery in this environment as described above. Thus, the Au102 was employed for selective "cargo" release *in vivo* and as a fluorescence quencher at target location, displaying another example of the possibilities presented from combining nanoparticles and fluorescent probes in a single application.

7   CONCLUSIONS

The aim of this work was to produce novel fluorescence-based probes for sensing of analytes of biological importance. Particularly, this thesis aimed to produce suitable chemical sensors to detect the release of ssRNA genome of enteroviruses during infections of cells. The commercial products currently available for detecting nucleic acids suffer from insufficient localization, as cellular nucleic acids produce overwhelming background emission over the small amount of target RNA in this context. Additionally, the low amount of RNA present in the viral infection requires fluorescent probes with high brightness for visualization *in vivo*.

To achieve better targeting of nucleic acids, cyanine dye **8** with the capability for covalent conjugation was synthesized using the commercially available SYBR Green II as a foundation for their design. Studying the nucleic acid binding of these dyes revealed the effects the substitution of the arm moiety at the 2-position has on the binding of nucleic acids. The long alkyl chains at this position led to observation of lower fluorescence values in binding to nucleic acids due to the higher space requirement in binding with the nucleic acid double-strands, in addition to lower water solubility. Conversely, the methyl-substitution of compound **5** exhibited highest values in rRNA binding, even past the values of the SYBR Green II marketed as a RNA-specific sensor. As the molecule **5** exhibited a highly linear response to the fraction of RNA that was in double-stranded form, an assay to determine this value for unknown samples was developed. This included first forming a calibration curve for the sample conditions, followed by extrapolating the degree of duplex RNA of the sample from the emission value of a RNA mass equal to the mass of RNA used in calibration. Additionally, dye **8** was successfully conjugated to the viral capsid of echovirus 1 and, despite low emission values from the sample, the thermally and chemically induced release of viral RNA genome was observed.

To further increase the brightness of these cyanine dyes, their heteroatom constitution was studied systematically to understand the effects that different substitution has to their photophysical properties. The series of newly

synthesized dyes were varied in their structure by changing between benzoxazole and benzothiazole moieties in the dyes, combined with methylthiol, chlorine or dimethylamine substitution at the 2-position. This series of compounds revealed the oxazole – dimethylamine substituted dye **M2** to exhibit superior brightness and nucleic acid binding characteristics with 28 nm Stoke's shift, 100 % QY, 47,300 $M^{-1}cm^{-1}$ brightness, -39 kJ/mol binding energy, and over 32 h photobleaching half-life in a complex with ctDNA. In general, introduction of the thiazole moiety and/or methylthiol/chlorine as replacement to these substituents showed a decrease in these properties over the other synthesized derivatives.

In another approach to achieve better localization of the fluorescent probes, monolayer-protected gold nanoclusters were synthesized to serve as a scaffold for dye conjugation. The synthesized AuMPCs included the *para*-mercaptobenzoic acid-substituted, watersoluble and well known $Au_{102}pMBA_{44}$ together with a larger $Au_{210-230}(pMBA)_{70-80}$ cluster. The synthesized products were characterized with PAGE together with ^1H NMR and DOSY spectroscopy in an attempt to gain structural information on the newly synthesized Au250. The two synthesized AuMPCs served as precursors for the conjugation of dye molecules onto the surface, using a previously developed synthetic procedure taking advantage of the Steglich esterification. The linking of the azatriangelium dye KU to the surface of Au102 produced a fluorescent turn-on probe that employed the sensing of cellular pH *in vivo*. The fluorescence turn-on was shown to be inherent to the electrostatic interactions between the cationic dye molecule and the pH-dependent protonation state of the pMBA molecules on the nanocluster surface. While the covalently bound dye remains quenched due to the proximity to the nanocluster surface, subjecting the conjugate to low pH hydrolyzed the linking ester bond, leading to regaining of the emission from the fluorescent dye. This example displayed the possibilities included in using nanoparticles as carriers of other molecules to target locations *in vivo* with a possibility of controlled release of these compounds at target location. This kind of nanocomposite offers an interesting carrier for fluorescent molecules, with possibility for energy transfer, as shown with the numerous examples discussed in this work. However, the novel interactions between plasmonic nanoparticles and fluorophores have high potential to improve fluorescent probes further. Particularly creating such products with silver nanoparticles would be of high interest due to their strong plasmon character, as reviewed herein. As such, a great deal of possibilities exists in this direction to provide new materials combining fluorescent probes, nanoparticles and their supramolecular chemistry in novel ways for new applications.

REFERENCES

1. G. B. Sergeev, *Nanochemistry*, 2nd. ed., Elsevier Science, **2006**.
2. V. Balzani, A. Credi, and M. Venturi, *Chem. - A Eur. J.*, **2002**, *8*, 5524–5532.
3. M. J. Hollas, *Modern Spectroscopy*, 4th ed., John Wiley & Sons Ltd, **2004**.
4. R. M. Christie, *Woodhead Publishing Series in Textiles*, vol. 1, Woodhead Publishing, **2011**.
5. I. Khan, K. Saeed, and I. Khan, *Arab. J. Chem.*, **2019**, *12*, 908–931.
6. J. Homola, S. S. Yee, and G. Gauglitz, *Sensors Actuators B Chem.*, **1999**, *54*, 3–15.
7. K. L. Kelly, E. Coronado, L. L. Zhao, and G. C. Schatz, *J. Phys. Chem. B*, **2003**, *107*, 668–677.
8. J. N. Anker, W. P. Hall, O. Lyandres, N. C. Shah, J. Zhao, and R. P. Van Duyne, *Nat. Mater.*, **2008**, *7*, 442–453.
9. A. Campion, and P. Kambhampati, *Chem. Soc. Rev.*, **1998**, *27*, 241–250.
10. J. F. Masson, *Analyst*, **2020**, *145*, 3776–3800.
11. K.-S. Lee, and M. A. El-Sayed, *J. Phys. Chem. B*, **2006**, *110*, 19220–19225.
12. S. Mustalahti, *University of Jyväskylä Research Report Series*, No. 188, University of Jyväskylä, **2015**.
13. T. Tsukuda, and H. Häkkinen, *Frontiers of Nanoscience*, vol. 9, Elsevier, **2015**.
14. J.-M. Lehn, *Angew. Chemie Int. Ed. English*, **1988**, *27*, 89–112.
15. F. Biedermann, and H.-J. Schneider, *Chem. Rev.*, **2016**, *116*, 5216–5300.
16. K. Faulhaber, A. Granzhan, H. Ihmels, and G. Viola, *Pure Appl. Chem.*, **2006**, *78*, 2325–2331.
17. K. Rurack, *Spectrochim. Acta Part A Mol. Biomol. Spectrosc.*, **2001**, *57*, 2161–2195.
18. T. Ueno, and T. Nagano, *Nat. Methods*, **2011**, *8*, 642–645.
19. E. Mattia, and S. Otto, *Nat. Nanotechnol.*, **2015**, *10*, 111–119.
20. M. Mojzych, and H. Maged, *Topics in Heterocyclic Chemistry*, vol. 14, Springer, **2008**.
21. C. H. G. Williams, *Trans. R. Soc. Edinburgh*, **1856**, *21*, 377.
22. M. Fanshun, S. Jianhua, and Y. Songjie, CN1148368C, **2001**.
23. L. A. Ernst, R. K. Gupta, R. B. Mujumdar, and A. S. Waggoner, *Cytometry*, **1989**, *10*, 3–10.
24. M. Henary, and A. Levitz, *Dye. Pigment.*, **2013**, *99*, 1107–1116.
25. X. H. Zhang, L. Y. Wang, Z. X. Nan, S. H. Tan, and Z. X. Zhang, *Dye. Pigment.*, **2008**, *79*, 205–209.
26. Y. Le Fu, W. Huang, C. L. Li, L. Y. Wang, Y. S. Wei, Y. Huang, X. H. Zhang, Z. Y. Wen, and Z. X. Zhang, *Dye. Pigment.*, **2009**, *82*, 409–415.
27. T. Deligeorgiev, S. Kaloyanova, and A. Vasilev, *Dye. Pigment.*, **2011**, *90*, 170–176.
28. L. G. Lee, C. Chen, and L. A. Chiu, *Cytometry*, **1986**, *7*, 508–517.
29. H. S. Rye, S. Yue, D. E. Wemmer, M. A. Quesada, R. P. Haugland, R. A. Mathies, and A. N. Glazer, *Nucleic Acids Res.*, **1992**, *20*, 2803–2812.

30. N. I. Gadjev, T. G. Deligeorgiev, and S. Hong, *Dye. Pigment.*, **1999**, *40*, 7–12.
31. A. Kurutos, I. Balabanov, F. S. Kamounah, K. Nikolova-Ganeva, D. Borisova, N. Gadjev, T. Deligeorgiev, and A. Tchorbanov, *Dye. Pigment.*, **2018**, *157*, 267–277.
32. K. J. Zanotti, G. L. Silva, Y. Creeger, K. L. Robertson, A. S. Waggoner, P. B. Berget, and B. A. Armitage, *Org. Biomol. Chem.*, **2011**, *9*, 1012–1020.
33. M. Thompson, *Bioconjug. Chem.*, **2006**, *17*, 507–513.
34. G. L. Silva, V. Ediz, D. Yaron, and B. A. Armitage, *J. Am. Chem. Soc.*, **2007**, *129*, 5710–5718.
35. K. Funabiki, Y. Saito, T. Kikuchi, K. Yagi, Y. Kubota, T. Inuzuka, Y. Miwa, M. Yoshida, O. Sakurada, and S. Kutsumizu, *J. Org. Chem.*, **2019**, *84*, 4372–4380.
36. L. Ying, US2013/0137875A1, **2013**.
37. W. E. Evenson, L. M. Boden, K. A. Muzikar, and D. J. Oleary, *J. Org. Chem.*, **2012**, *77*, 10967–10971.
38. A. I. Dragan, R. Pavlovic, J. B. McGivney, J. R. Casas-Finet, E. S. Bishop, R. J. Strouse, M. A. Schenerman, and C. D. Geddes, *J. Fluoresc.*, **2012**, *22*, 1189–1199.
39. V. K. Saarnio, K. Salorinne, V. P. Ruokolainen, J. R. Nilsson, T.-R. Tero, S. Oikarinen, L. M. Wilhelmsson, T. M. Lahtinen, and V. S. Marjomäki, *Dye. Pigment.*, **2020**, *177*, 108282.
40. A. Rožman, I. Crnolatac, T. Deligeorgiev, and I. Piantanida, *J. Lumin.*, **2019**, *205*, 87–96.
41. H. J. Karlsson, M. H. Bergqvist, P. Lincoln, and G. Westman, *Bioorganic Med. Chem.*, **2004**, *12*, 2369–2384.
42. T. G. Deligeorgiev, N. I. Gadjev, A. A. Vasilev, V. A. Maximova, I. I. Timcheva, H. E. Katerinopoulos, and G. K. Tsikalas, *Dye. Pigment.*, **2007**, *75*, 466–473.
43. E. Soriano, C. Holder, A. Levitz, and M. Henary, *Molecules*, **2016**, *21*, 23.
44. T. Mahmood, A. Paul, and S. Ladame, *J. Org. Chem.*, **2010**, *75*, 204–207.
45. L. G. S. Brooker, G. H. Keyes, and W. W. Williams, *J. Am. Chem. Soc.*, **1942**, *64*, 199–210.
46. R. M. El-Shishtawy, and P. Almeida, *Tetrahedron*, **2006**, *62*, 7793–7798.
47. X. Peng, Z. Yang, J. Wang, J. Fan, Y. He, F. Song, B. Wang, S. Sun, J. Qu, J. Qi, and M. Yan, *J. Am. Chem. Soc.*, **2011**, *113*, 6626–6635.
48. Y. L. Briks, E. K. Mikitenko, and N. N. Romanov, *Zhurnal Org. Khimii*, **1994**, *30*, 106–114.
49. L. Wang, J. Fan, X. Qiao, X. Peng, B. Dai, B. Wang, S. Sun, L. Zhang, and Y. Zhang, *J. Photochem. Photobiol. A Chem.*, **2010**, *210*, 168–172.
50. Y. Ye, S. Bloch, J. Kao, and S. Achilefu, *Bioconjug. Chem.*, **2005**, *16*, 51–61.
51. M. Henary, S. Paranjpe, and E. A. Owens, *Heterocycl. Commun.*, **2013**, *19*, 1–11.
52. L. M. Yagupolskii, O. I. Chernega, N. V. Kondratenko, A. N. Chernega, Y. G. Vlasenko, R. V. Nedelkov, and Y. L. Yagupolskii, *J. Fluor. Chem.*, **2010**, *131*, 165–171.

53. K. Meguellati, M. Spichty, and S. Ladame, *Org. Lett.*, **2009**, *11*, 1123–1126.
54. B. Strehmel, C. Schmitz, C. Kütahya, Y. Pang, A. Drewitz, and H. Mustroph, *Beilstein J. Org. Chem.*, **2020**, *16*, 415–444.
55. J. Pączkowski, J. Kabatc, and B. Jędrzejewska, *Heterocyclic Polymethine Dyes,* Springer Berlin Heidelberg, **2008**.
56. V. Z. Shirinian, and A. A. Shimkin, *Heterocyclic Polymethine Dyes*, Springer Berlin Heidelberg, **2008**.
57. N. I. Shank, H. H. Pham, A. S. Waggoner, and B. A. Armitage, *J. Am. Chem. Soc.*, **2013**, *135*, 242–251.
58. K. Rurack, and M. Spieles, *Anal. Chem.*, **2011**, *83*, 1232–1242.
59. A. Fürstenberg, M. D. Julliard, T. G. Deligeorgiev, N. I. Gadjev, A. A. Vasilev, and E. Vauthey, *J. Am. Chem. Soc.*, **2006**, *128*, 7661–7669.
60. P. A. Hunt, and M. A. Robb, *J. Am. Chem. Soc.*, **2005**, *127*, 5720–5726.
61. J. E. I. Korppi-Tommola, A. Hakkarainen, T. Hukka, and J. Subbi, *J. Phy*, **1991**, *95*, 8482–8491.
62. V. Karunakaran, J. L. Pérez Lustres, L. Zhao, N. P. Ernsting, and O. Seitz, *J. Am. Chem. Soc.*, **2006**, *128*, 2954–2962.
63. M. Cooper, A. Ebner, M. Briggs, M. Burrows, N. Gardner, R. Richardson, and R. West, *J. Fluoresc.*, **2004**, *14*, 145–150.
64. H. Ihmels, and D. Otto, *Top. Curr. Chem.*, **2005**, *258*, 161–204.
65. J. Sartorius, and H.-J. Schneider, *J. Chem. Soc., Perkin Trans. 2*, **1997**, 2319–2327.
66. L. S. Lerman, *J. Mol. Biol.*, **1961**, *3*, 18–30.
67. A. I. Dragan, J. R. Casas-Finet, E. S. Bishop, R. J. Strouse, M. A. Schenerman, and C. D. Geddes, *Biophys. J.*, **2010**, *99*, 3010–3019.
68. H. Zipper, H. Brunner, J. Bernhagen, and F. Vitzthum, *Nucleic Acids Res.*, **2004**, *32*, e103.
69. B. B. Bruijns, R. M. Tiggelaar, and J. G. E. Gardeniers, *Anal. Biochem.*, **2016**, *511*, 74–79.
70. L. J. Jones, S. T. Yue, C. Y. Cheung, and V. L. Singer, *Anal. Biochem.*, **1998**, *265*, 368–374.
71. X. Jin, S. Yue, V. L. Singer, L. J. Jones, M. P. Beaudet, C.-Y. Cheung, and R. S. Tuma, *Anal. Biochem.*, **2003**, *288*, 278–288.
72. G. Cosa, K. S. Focsaneanu, J. R. N. McLean, and J. C. Scaiano, *Chem. Commun.*, **2000**, *8*, 689–690.
73. L. Beach, C. Schweitzer, and J. C. Scaiano, *Org. Biomol. Chem.*, **2003**, *1*, 450–451.
74. B. Armitage, C. Yu, C. Devadoss, and G. B. Schuster, *J. Am. Chem. Soc.*, **1994**, *116*, 9847–9859.
75. P. H. von Hippel, and J. D. McGhee, *Annu. Rev. Biochem.*, **1972**, *41*, 231–700.
76. T. L. Netzel, K. Nafisi, M. Zhao, J. R. Lenhard, and I. Johnson, *J. Phys. Chem.*, **2005**, *99*, 17936–17947.
77. K. Philippot, and B. Chaudret, *Comptes Rendus Chim.*, **2003**, *6*, 1019–1034.

78. S. Zhao, R. Jin, H. Abroshan, C. Zeng, H. Zhang, S. D. House, E. Gottlieb, H. J. Kim, J. C. Yang, and R. Jin, *J. Am. Chem. Soc.*, **2017**, *139*, 1077–1080.

79. L. M. Rossi, J. L. Fiorio, M. A. S. Garcia, and C. P. Ferraz, *Dalt. Trans.*, **2018**, *47*, 5889–5915.

80. P. Slepička, N. S. Kasálková, J. Siegel, Z. Kolská, and V. Švorčík, *Materials*, **2020**, *13*, 1.

81. Y. Negishi, K. Nobusada, and T. Tsukuda, *J. Am. Chem. Soc.*, **2005**, *127*, 5261–5270.

82. T. P. Martin, T. Bergmann, H. Göhlich, and T. Lange, *J. Phys. Chem.*, **1991**, 6421–6429.

83. K. Salorinne, R. W. Y. Man, C.-H. Li, M. Taki, M. Nambo, and C. M. Crudden, *Angew. Chemie Int. Ed.*, **2017**, *56*, 6198–6202.

84. K. Salorinne, R. W. Y. Man, P. A. Lummis, M. S. A. Hazer, S. Malola, J. C.-H. Yim, A. J. Veinot, W. Zhou, H. Häkkinen, M. Nambo, and C. M. Crudden, *Chem. Commun.*, **2020**, *56*, 6102–6105.

85. H. Shen, G. Deng, S. Kaappa, T. Tan, Y. Han, S. Malola, S. Lin, B. K. Teo, H. Häkkinen, and N. Zheng, *Angew. Chemie*, **2019**, *131*, 17895–17899.

86. J. Yan, B. K. Teo, and N. Zheng, *Acc. Chem. Res.*, **2018**, *51*, 3084–3093.

87. X. Kang, H. Chong, and M. Zhu, *Nanoscale*, **2018**, *10*, 10758–10834.

88. R. L. Donkers, D. Lee, and R. W. Murray, *Langmuir*, **2004**, *20*, 1945–1952.

89. P. D. Jadzinsky, G. Calero, C. J. Ackerson, D. A. Bushnell, and R. D. Kornberg, *Science*, **2007**, *318*, 430–433.

90. S. Vergara, D. A. Lukes, M. W. Martynowycz, U. Santiago, G. Plascencia-Villa, S. C. Weiss, M. J. De La Cruz, D. M. Black, M. M. Alvarez, X. López-Lozano, C. O. Barnes, G. Lin, H. C. Weissker, R. L. Whetten, T. Gonen, M. J. Yacaman, and G. Calero, *J. Phys. Chem. Lett.*, **2017**, *8*, 5523–5530.

91. G. Li, and R. Jin, *Acc. Chem. Res.*, **2013**, *46*, 1749–1758.

92. K. Chaudhari, P. L. Xavier, and T. Pradeep, *ACS Nano*, **2011**, *5*, 8816–8827.

93. M. Brust, M. Walker, D. Bethell, D. J. Schiffrin, and R. Whyman, *J. Chem. Soc. Chem. Commun.*, **1994**, 2473–2670.

94. Y. Chen, C. Zeng, D. R. Kauffman, and R. Jin, *Nano Lett.*, **2015**, *15*, 3603–3609.

95. O. A. Wong, W. S. Compel, and C. J. Ackerson, *ACS Comb. Sci.*, **2015**, 11–18.

96. K. Sokołowska, S. Malola, M. Lahtinen, V. Saarnio, P. Permi, K. Koskinen, M. Jalasvuori, H. Häkkinen, L. Lehtovaara, and T. Lahtinen, *J. Phys. Chem. C*, **2019**, *123*, 2602-2612.

97. M. Azubel, and R. D. Kornberg, *Nano Lett.*, **2016**, *16*, 3348–3351.

98. R. Jin, H. Qian, Z. Wu, Y. Zhu, M. Zhu, A. Mohanty, and N. Garg, *J. Phys. Chem. Lett.*, **2010**, *1*, 2903–2910.

99. I. Chakraborty, and T. Pradeep, *Chem. Rev.*, **2017**, *117*, 8208–8271.

100. Q. Yao, T. Chen, X. Yuan, and J. Xie, *Acc. Chem. Res.*, **2018**, *51*, 1338–1348.

101. Y. Levi-kalisman, P. D. Jadzinsky, N. Kalisman, H. Tsunoyama, T. Tsukuda, D. A. Bushnell, and R. D. Kornberg, *J. Am. Chem. Soc.*, **2011**, *102*, 2976–2982.

102. Y. Negishi, S. Hashimoto, A. Ebina, K. Hamada, K. Wakamatsu, and Y. Niihori, *Bunseki Kagaku*, **2019**, *68*, 825–838.

103. L. Pitkänen, and A. M. Striegel, *Trends Anal. Chem.*, **2016**, *80*, 311–320.

104. K. Sokolowska, E. Hulkko, L. Lehtovaara, and T. Lahtinen, *J. Phys. Chem. C*, **2018**, *122*, 12524–12533.

105. J. D. Aiken, and R. G. Finke, *J. Mol. Catal. A Chem.*, **1999**, *145*, 1–44.

106. E. Petryayeva, and U. J. Krull, *Anal. Chim. Acta*, **2011**, *706*, 8–24.

107. C. Marambio-Jones, and E. M. V. Hoek, *J. Nanoparticle Res.*, **2010**, *12*, 1531–1551.

108. A. Sasidharan, J. E. Riviere, and N. A. Monteiro-Riviere, *J. Mater. Chem. B*, **2015**, *3*, 2075–2082.

109. K. M. Koczkur, S. Mourdikoudis, L. Polavarapu, and S. E. Skrabalak, *Dalt. Trans.*, **2015**, *44*, 17883–17905.

110. R. Fenger, E. Fertitta, H. Kirmse, A. F. Thünemann, and K. Rademann, *Phys. Chem. Chem. Phys.*, **2012**, *14*, 9343–9349.

111. X.-H. Liu, X.-H. Luo, S.-X. Lu, J.-C. Zhang, and W.-L. Cao, *J. Colloid Interface Sci.*, **2007**, *307*, 94–100.

112. A. M. Signori, K. De O. Santos, R. Eising, B. L. Albuquerque, F. C. Giacomelli, and J. B. Domingos, *Langmuir*, **2010**, *26*, 17772–17779.

113. Z. Zhang, and P. C. Lin, *Emerging Applications of Nanoparticles and Architectural Nanostructures: Current Prospects and Future Trends*, Elsevier, **2018**.

114. P. Zhao, N. Li, and D. Astruc, *Coord. Chem. Rev.*, **2013**, *257*, 638–665.

115. W. C. Chang, J. T. Tai, H. F. Wang, R. M. Ho, T. C. Hsiao, and D. H. Tsai, *Langmuir*, **2016**, *32*, 9807–9815.

116. J. Turkevich, P. C. Stevenson, and J. Hillier, *Discuss. Faraday Soc.*, **1951**, *11*, 55–75.

117. N. E. Larm, J. A. Thon, Y. Vazmitsel, J. L. Atwood, and G. A. Baker, *Nanoscale Adv.*, **2019**, *1*, 4665–4668.

118. N. G. Bastús, F. Merkoçi, J. Piella, and V. Puntes, *Chem. Mater.*, **2014**, *26*, 2836–2846.

119. N. G. Bastús, J. Comenge, and V. Puntes, *Langmuir*, **2011**, *27*, 11098–11105.

120. X. Zhao, H. Zhao, L. Yan, N. Li, J. Shi, and C. Jiang, *Crit. Rev. Anal. Chem.*, **2020**, *50*, 97–110.

121. L. Vigderman, and E. R. Zubarev, *Adv. Drug Deliv. Rev.*, **2013**, *65*, 663–676.

122. X. Kang, and M. Zhu, *Chem. Mater.*, **2019**, *31*, 9939–9969.

123. Y. Chen, Y. Xianyu, and X. Jiang, *Acc. Chem. Res.*, **2017**, *50*, 310–319.

124. M.-A. Neouze, and U. Schubert, *Chem. Mon.*, **2008**, *139*, 183–195.

125. H. Sellers, A. Ulman, Y. Shnidman, and J. E. Eilers, *J. Am. Chem. Soc.*, **1993**, *115*, 9389–9401.

126. G. Salassa, A. Sels, F. Mancin, and T. Bürgi, *ACS Nano*, **2017**, *11*, 12609–12614.

127. A. Caragheorgheopol, and V. Chechik, *Phys. Chem. Chem. Phys.*, **2008**, *10*, 5029–5041.

128. R. Wu, L. Jiang, J. Zhu, and J. Liu, *Langmuir*, **2019**, 13461–13468.

129. R. Dinkel, B. Braunschweig, and W. Peukert, *J. Phys. Chem. C*, **2016**, *120*, 1673–1682.

130. K. Wojczykowski, D. Meißner, P. Jutzi, I. Ennen, A. Hu, and D. Volkmer, *Chem. Commun.*, **2006**, 3693–3695.

131. R. Hong, G. Han, J. M. Ferna, B. Kim, N. S. Forbes, and V. M. Rotello, *J. Am. Chem. Soc.*, **2006**, 1078–1079.

132. G. E. Johnson, T. Priest, and J. Laskin, *Chem. Sci.*, **2014**, *5*, 3275–3286.

133. Y. S. Shon, and H. Choo, *Comptes Rendus Chim.*, **2003**, *6*, 1009–1018.

134. S. C. Abeyweera, K. D. Rasamani, and Y. Sun, *Acc. Chem. Res.*, **2017**, *50*, 1754–1761.

135. V. Marjomäki, T. Lahtinen, M. Martikainen, J. Koivisto, S. Malola, K. Salorinne, M. Pettersson, and H. Häkkinen, *Proc. Natl. Acad. Sci. U. S. A.*, **2014**, *111*, 1277–1281.

136. M. Yüce, and H. Kurt, *RSC Adv.*, **2017**, *7*, 49386–49403.

137. Y. Zhou, S. Wang, K. Zhang, and X. Jiang, *Angew. Chemie*, **2008**, *120*, 7564–7566.

138. J. Zhang, X. Sun, and J. Wu, *Appl. Sci.*, **2019**, *48*, 489–507.

139. D. K. Yi, S. Kaushal, S. S. Nanda, S. Samal, and D. K. Yi, *ChemBioChem*, **2019**, *20*, 1–26.

140. R. A. Murray, A. Escobar, N. G. Bastús, P. Andreozzi, V. Puntes, and S. E. Moya, *NanoImpact*, **2018**, *9*, 102–113.

141. C. D. Geddes, and J. R. Lakowicz, *J. Fluoresc.*, **2002**, *12*, 121–129.

142. Y. Chen, K. Munechika, and D. S. Ginger, *Nano Lett.*, **2007**, *7*, 690–696.

143. G. Chen, F. Song, X. Xiong, and X. Peng, *Ind. Eng. Chem. Res.*, **2013**, *52*, 11228–11245.

144. A. Campion, A. R. Gallo, C. B. Harris, H. J. Robota, and P. M. Whitmore, *Chem. Phys. Lett.*, **1980**, *73*, 447–450.

145. L. Minai, D. Yeheskely-Hayon, and D. Yelin, *Sci. Rep.*, **2013**, *3*, 1–7.

146. J. Olesiak-Banska, M. Waszkielewicz, P. Obstarczyk, and M. Samoc, *Chem. Soc. Rev.*, **2019**, *48*, 4087–4117.

147. C. Peng, M. Yu, and J. Zheng, *Nano Let*, **2020**, *20*, 1378–1382.

148. J. Xie, Y. Zheng, and J. Y. Ying, *Chem. Commun.*, **2010**, *46*, 961–963.

149. C.-C. Huang, Z. Yang, K.-H. Lee, and H.-T. Chang, *Angew. Chemie - Int. Ed.*, **2007**, *46*, 6824–6828.

150. S. Roy, G. Palui, and A. Banerjee, *Nanoscale*, **2012**, *4*, 2734–2740.

151. J. Sun, J. Zhang, and Y. Jin, *J. Mater. Chem. C*, **2013**, *1*, 138–143.

152. C. W. Chen, C. H. Wang, C. M. Wei, C. Y. Hsieh, Y. T. Chen, Y. F. Chen, C. W. Lai, C. L. Liu, C. C. Hsieh, and P. T. Chou, *J. Phys. Chem. C*, **2010**, *114*, 799–802.

153. M. A. H. Muhammed, P. K. Verma, S. K. Pal, A. Retnakumari, M. Koyakutty, S. Nair, and T. Pradeep, *Chem. Eur. J.*, **2010**, *16*, 10103–10112.

154. C. V. Durgadas, C. P. Sharma, and K. Sreenivasan, *Analyst*, **2011**, *136*, 933–940.

155. Z. Wu, M. Wang, J. Yang, X. Zheng, W. Cai, G. Meng, H. Qian, H. Wang, and R. Jin, *Small*, **2012**, *8*, 2028–2035.

156. Y. Yue, T. Y. Liu, H. W. Li, Z. Liu, and Y. Wu, *Nanoscale*, **2012**, *4*, 2251–2254.

157. Y. Liu, K. Ai, X. Cheng, L. Huo, and L. Lu, *Adv. Funct. Mater.*, **2010**, *20*, 951–956.

158. W. Y. Chen, G. Y. Lan, and H. T. Chang, *Anal. Chem.*, **2011**, *83*, 9450–9455.

159. H. H. Deng, K. Y. Huang, M. J. Zhang, Z. Y. Zou, Y. Y. Xu, H. P. Peng, W. Chen, and G. L. Hong, *Food Chem.*, **2020**, *317*, 126456.

160. M. Wang, Z. Wu, J. Yang, G. Wang, H. Wang, and W. Cai, *Nanoscale*, **2012**, *4*, 4087–4090.

161. Y. Tao, M. Li, J. Ren, and X. Qu, *Chem. Soc. Rev.*, **2015**, *44*, 8636–8663.

162. Y. Shiang, C. Huang, and H. Chang, *Chem. Commun.*, **2009**, 3437–3439.

163. S. Abarghoei, N. Fakhri, Y. S. Borghei, M. Hosseini, and M. R. Ganjali, *Spectrochim. Acta - Part A Mol. Biomol. Spectrosc.*, **2019**, *210*, 251–259.

164. L. Hu, S. Han, S. Parveen, Y. Yuan, L. Zhang, and G. Xu, *Biosens. Bioelectron.*, **2012**, *32*, 297–299.

165. M. Liu, F. Tang, Z. Yang, J. Xu, and X. Yang, *J. Anal. Methods Chem.*, **2019**, *2019*, 1–10.

166. Y. Tao, Y. Lin, J. Ren, and X. Qu, *Biosens. Bioelectron.*, **2013**, *42*, 41–46.

167. R. C. Triulzi, M. Micic, S. Giordani, M. Serry, W. A. Chiou, and R. M. Leblanc, *Chem. Commun.*, **2006**, 5068–5070.

168. H. Deng, Q. Deng, K. Li, Q. Zhuang, Y. Zhuang, and H. Peng, *Spectrochim. Acta Part A Mol. Biomol. Spectrosc.*, **2020**, *229*, 117875.

169. P. H. Li, J. Y. Lin, C. T. Chen, W. R. Ciou, P. H. Chan, L. Luo, H. Y. Hsu, E. W. G. Diau, and Y. C. Chen, *Anal. Chem.*, **2012**, *84*, 5484–5488.

170. T. Chen, and W. Tseng, *Small*, **2012**, *8*, 1912–1919.

171. S. Chandra, Nonappa, G. Beaune, A. Som, S. Zhou, J. Lahtinen, H. Jiang, J. V. I. Timonen, O. Ikkala, and R. H. A. Ras, *Adv. Opt. Mater.*, **2019**, *7*, 1900620.

172. Nonappa, T. Lahtinen, J. S. Haataja, T.-R. Tero, H. Häkkinen, and O. Ikkala, *Angew. Chemie - Int. Ed.*, **2016**, *55*, 16035–16038.

173. A. Yahia-ammar, D. Sierra, and F. Me, *ACS Nano*, **2016**, *10*, 2591–2599.

174. J. V Rival, Nonappa, and E. S. Shibu, *Appl. Mater. Interfaces*, **2020**, *12*, 14569–14577.

175. U. Kauscher, J. Penders, A. Nagelkerke, M. N. Holme, V. Nele, L. Massi, S. Gopal, T. E. Whittaker, and M. M. Stevens, *Langmuir*, **2020**, *36*, 3912–3923.

176. R. Gui, A. Wan, X. Liu, and H. Jin, *Chem. Commun.*, **2014**, *50*, 1546–1548.

177. T. Chen, S. Xu, T. Zhao, L. Zhu, D. Wei, Y. Li, H. Zhang, and C. Zhao, *Appl. Mater. Interfaces*, **2012**, *4*, 5766–5774.

178. N. Goswami, J. Li, and J. Xie, *Protected Metal Clusters: From Fundamentals to Applications*, vol. 9, Elsevier, **2013**.

179. M. Martikainen, K. Salorinne, T. Lahtinen, S. Malola, P. Permi, H. Häkkinen, and V. Marjomäki, *Nanoscale*, **2015**, 17457–17467.

180. Nonappa, *Beilstein J. Nanotechnol.*, **2020**, *11*, 533–546.

181. X. Qu, Y. Li, L. Li, Y. Wang, J. Liang, and J. Liang, *J. Nanomater.*, **2015**, *2015*, 1–23.

182. C. J. Lin, J. K. Li, C. Lee, J. Hsieh, H. Wang, W. H. Chang, J. Shen, W. Chan, and H. Yeh, *J. Med. Biol. Eng.*, **2009**, *29*, 276–283.

183. X. D. Zhang, D. Wu, X. Shen, P. X. Liu, F. Y. Fan, and S. J. Fan, *Biomaterials*, **2012**, *33*, 4628–4638.

184. X. D. Zhang, J. Chen, Z. Luo, D. Wu, X. Shen, S. S. Song, Y. M. Sun, P. X. Liu, J. Zhao, S. Huo, S. Fan, F. Fan, X. J. Liang, and J. Xie, *Adv. Healthc. Mater.*, **2014**, *3*, 133–141.

185. J. Zhang, Y. Zhou, K. Zheng, H. Abroshan, D. R. Kauffman, and J. Sun, *Nano Res.*, **2018**, *11*, 5787–5798.

186. X. Jiang, B. Du, Y. Huang, M. Yu, and J. Zheng, *Bioconjug. Chem.*, **2020**, *31*, 1522–1528.

187. D. Chen, B. Li, S. Cai, P. Wang, S. Peng, Y. Sheng, Y. He, Y. Gu, and H. Chen, *Biomaterials*, **2016**, *100*, 1–16.

188. N. Lewinski, V. Colvin, and R. Drezek, *Small*, **2008**, *4*, 26–49.

189. G. Sener, L. Uzun, and A. Denizli, *ACS Appl. Mater. Interfaces*, **2014**, *6*, 18395–18400.

190. S. Zhu, T. Fischer, W. Wei, A. Descalzo, and K. Rurack, *Top. Curr. Chem.*, **2011**, *300*, 51–91.

191. F. Degliangeli, P. Kshirsagar, V. Brunetti, P. P. Pompa, and R. Fiammengo, *J. Am. Chem. Soc.*, **2014**, *136*, 2264–2267.

192. Y. Hu, L. Zhang, Y. Zhang, B. Wang, Y. Wang, Q. Fan, W. Huang, and L. Wang, *ACS Appl. Mater. Interfaces*, **2015**, *7*, 2459–2466.

193. L. Guo, Y. Xu, A. R. Ferhan, G. Chen, and D.-H. Kim, *J. Am. Chem. Soc.*, **2013**, *135*, 12338–12345.

194. W. Shen, H. Deng, A. K. L. Teo, and Z. Gao, *Chem. Commun.*, **2012**, *48*, 10225–10227.

195. M. Sanromán-Iglesias, C. H. Lawrie, T. Schäfer, M. Grzelczak, and L. M. Liz-Marzán, *ACS Sens.*, **2016**, *1*, 1110–1116.

196. B. K. Gorityala, Z. Lu, M. L. Leow, J. Ma, and X.-W. Liu, *J. Am. Chem. Soc.*, **2012**, *134*, 15229–15232.

197. M. P. Kreuzer, R. Quidant, J.-P. Salvador, M.-P. Marco, and G. Badenes, **2008**, *391*, 1813–1820.

198. F. Sang, X. Zhang, J. Liu, S. Yin, and Z. Zhang, *Spectrochim. Acta Part A Mol. Biomol. Spectrosc.*, **2019**, *217*, 122–127.

199. D. Liu, W. Chen, Y. Tian, S. He, W. Zheng, J. Sun, Z. Wang, and X. Jiang, *Adv. Healthc. Mater.*, **2012**, *1*, 90–95.

200. O. Yavas, S. S. Aćimović, J. Garcia-Guirado, J. Berthelot, P. Dobosz, V. Sanz, and R. Quidant, *ACS Sens.*, **2018**, *3*, 1376–1384.

201. H. Aldewachi, T. Chalati, M. N. Woodroofe, N. Bricklebank, B. Sharrack, and P. Gardiner, *Nanoscale*, **2018**, *10*, 18–33.

202. D. Li, Y. Dong, B. Li, Y. Wu, K. Wang, and S. Zhang, *Analyst*, **2015**, *140*, 7672–7677.

203. S. Rana, A. K. Singla, A. Bajaj, S. G. Elci, O. R. Miranda, R. Mout, B. Yan, F. R. Jirik, and V. M. Rotello, *ACS Nano*, **2012**, *6*, 8233–8240.

204. R. L. Phillips, O. R. Miranda, C.-C. You, V. M. Rotello, and U. H. F. Bunz, *Angew. Chemie Int. Ed.*, **2008**, *47*, 2590–2594.
205. N. D. B. Le, G. Y. Tonga, R. Mout, S.-T. Kim, M. E. Wille, S. Rana, K. A. Dunphy, D. J. Jerry, M. Yazdani, R. Ramanathan, C. M. Rotello, and V. M. Rotello, *J. Am. Chem. Soc.*, **2017**, *139*, 8008–8012.
206. X. Han, K. Xu, O. Taratula, and K. Farsad, *Nanoscale*, **2019**, *11*, 799–819.
207. W. Wang, J. Wang, and Y. Ding, *J. Mater. Chem. B*, **2020**, *8*, 4813–4830.
208. T. A. Tabish, P. Dey, S. Mosca, M. Salimi, F. Palombo, P. Matousek, and N. Stone, *Adv. Sci.*, **2020**, *15*, 1903441.
209. P. Malik, and T. K. Mukherjee, *Int. J. Pharm.*, **2018**, *553*, 483–509.
210. P. Pedrosa, R. Vinhas, A. Fernandes, and P. Baptista, *Nanomaterials*, **2015**, *5*, 1853–1879.
211. J. Song, J. Zhou, and H. Duan, *J. Am. Chem. Soc.*, **2012**, *134*, 13458–13469.
212. Y.-L. Luo, Y.-S. Shiao, and Y.-F. Huang, *ACS Nano*, **2011**, *5*, 7796–7804.
213. S. Her, D. A. Jaffray, and C. Allen, *Adv. Drug Deliv. Rev.*, **2017**, *109*, 84–101.
214. S. Park, H. Kim, S. C. Lim, K. Lim, E. S. Lee, K. T. Oh, H. G. Choi, and Y. S. Youn, *J. Control. Release*, **2019**, *304*, 7–18.
215. N. S. Abadeer, and C. J. Murphy, *J. Phys. Chem. C*, **2016**, *120*, 4691–4716.
216. J. B. Vines, J.-H. Yoon, N.-E. Ryu, D.-J. Lim, and H. Park, *Front. Chem.*, **2019**, *7*, 1–16.
217. R. Liu, C. Hu, Y. Yang, J. Zhang, and H. Gao, *Acta Pharm. Sin. B*, **2019**, *9*, 410–420.
218. H. Li, P. Wang, Y. Deng, M. Zeng, Y. Tang, W. H. Zhu, and Y. Cheng, *Biomaterials*, **2017**, *139*, 30–38.
219. M. Ahamed, M. S. Alsalhi, and M. K. J. Siddiqui, *Clin. Chim. Acta*, **2010**, *411*, 1841–1848.
220. O. Bar-Ilan, R. M. Albrecht, V. E. Fako, and D. Y. Furgeson, *Small*, **2009**, *5*, 1897–1910.
221. S. H. Lee, and B. H. Jun, *Int. J. Mol. Sci.*, **2019**, *20*, 865.
222. O. Planas, N. Macia, M. Agut, S. Nonell, and B. Heyne, *J. Am. Chem. Soc.*, **2016**, *138*, 2762–2768.
223. K. Aslan, I. Gryczynski, J. Malicka, E. Matveeva, J. R. Lakowicz, and C. D. Geddes, *Curr. Opin. Biotechnol.*, **2005**, *16*, 55–62.
224. R. Knoblauch, and C. D. Geddes, *Nanoscale*, **2019**, *11*, 4337–4344.
225. M. H. Chowdhury, K. Ray, C. D. Geddes, and J. R. Lakowicz, *Chem. Phys. Lett.*, **2008**, *452*, 162–167.
226. J. Malicka, I. Gryczynski, C. D. Geddes, and J. R. Lakowicz, *J. Biomed. Opt.*, **2003**, *8*, 472–478.
227. N. Bondre, Y. Zhang, and C. D. Geddes, *Sensors Actuators, B Chem.*, **2011**, *152*, 82–87.
228. A. I. Dragan, E. S. Bishop, J. R. Casas-Finet, R. J. Strouse, M. A. Schenerman, and C. D. Geddes, *Anal. Biochem.*, **2010**, *396*, 8–12.
229. S. Bhaskar, M. Moronshing, V. Srinivasan, P. K. Badiya, C. Subramaniam, and S. S. Ramamurthy, *ACS Appl. Nano Mater.*, **2020**, *3*, 4329–4341.

230. K. Aslan, J. Huang, G. M. Wilson, and C. D. Geddes, *J. Am. Chem. Soc.*, **2006**, *128*, 4206–4207.

231. E. Lucas, R. Knoblauch, M. Combs-Bosse, S. E. Broedel, and C. D. Geddes, *Spectrochim. Acta - Part A Mol. Biomol. Spectrosc.*, **2020**, *228*, 117739.

232. K. Golberg, A. Elbaz, R. McNeil, A. Kushmaro, C. D. Geddes, and R. S. Marks, *J. Nanoparticle Res.*, **2014**, *16*, 2770.

233. M. J. R. Previte, K. Aslan, S. N. Malyn, and C. D. Geddes, *Anal. Chem.*, **2006**, *78*, 8020–8027.

234. K. Aslan, P. Holley, and C. D. Geddes, *J. Immunol. Methods*, **2006**, *312*, 137–147.

235. P. Prosposito, F. Mochi, E. Ciotta, M. Casalboni, F. De Matteis, I. Venditti, L. Fontana, G. Testa, and I. Fratoddi, *Beilstein J. Nanotechnol.*, **2016**, *7*, 1654–1661.

236. D. Sahu, N. Sarkar, P. Mohapatra, and S. K. Swain, *Microchem. J.*, **2020**, *154*, 104577.

237. V. K. Verma, K. Tapadia, T. Maharana, and A. Sharma, *J. Appl. Spectrosc.*, **2020**, *87*, 357–363.

238. K. Aslan, J. R. Lakowicz, H. Szmacinski, and C. D. Geddes, *J. Fluoresc.*, **2004**, *14*, 677–679.

239. Z. Zhou, T. Li, H. Huang, Y. Chen, F. Liu, C. Huang, and N. Li, *Chem. Commun.*, **2014**, *50*, 13373–13376.

240. Y. Pang, Z. Rong, J. Wang, R. Xiao, and S. Wang, *Biosens. Bioelectron.*, **2015**, *66*, 527–532.

241. S. Kim, B. H. Kim, Y. K. Hong, C. Cui, J. Choi, D. H. Park, and S. H. Song, *Polymers*, **2020**, *12*, 631.

242. S. L. Kleinman, R. R. Frontiera, A. I. Henry, J. A. Dieringer, and R. P. Van Duyne, *Phys. Chem. Chem. Phys.*, **2013**, *15*, 21–36.

243. G. B. Braun, S. J. Lee, T. Laurence, N. Fera, L. Fabris, G. C. Bazan, M. Moskovits, and N. O. Reich, *J. Phys. Chem. C*, **2009**, *113*, 13622–13629.

244. G. Naja, P. Bouvrette, S. Hrapovic, and J. H. T. Luong, *Analyst*, **2007**, *132*, 679–686.

245. M. Ardini, J. A. Huang, C. S. Sánchez, M. Z. Mousavi, V. Caprettini, N. Maccaferri, G. Melle, G. Bruno, L. Pasquale, D. Garoli, and F. De Angelis, *Sci. Rep.*, **2018**, *8*, 1–12.

246. S. Singh, A. Halder, O. Sinha, P. K. Sarkar, P. Singh, A. Banerjee, S. A. Ahmed, A. Alharbi, R. J. Obaid, S. K. Ghosh, A. Mitra, and S. K. Pal, *PLoS One*, **2020**, *15*, e0227584.

247. A. Ravindran, V. Mani, N. Chandrasekaran, and A. Mukherjee, *Talanta*, **2011**, *85*, 533–540.

248. G. Braun, J. L. Seung, M. Dante, T. Q. Nguyen, M. Moskovits, and N. Reich, *J. Am. Chem. Soc.*, **2007**, *129*, 6378–6379.

249. D. Graham, D. G. Thompson, W. E. Smith, and K. Faulds, *Nat. Nanotechnol.*, **2008**, *3*, 548–551.

250. H. Li, W. Qiang, M. Vuki, D. Xu, and H. Y. Chen, *Anal. Chem.*, **2011**, *83*, 8945–8952.

251. J. D. McGhee, and P. H. von Hippel, *J. Mol. Biol.*, **1974**, *86*, 469–489.

252. D. J. Smith, *Nanocharacterisation*, The Royal Society of Chemistry, **2015**.

253. E. O. Stejskal, and J. E. Tanner, *J. Chem. Phys.*, **1965**, *42*, 288–292.

254. A. Einstein, *Ann. Phys.*, **1905**, *17*, 549–560.

255. J. Stetefeld, S. A. McKenna, and T. R. Patel, *Biophys. Rev.*, **2016**, *8*, 409–427.

256. X. Li, S. R. Srinivasan, J. Connarn, A. Ahmad, Z. T. Young, A. M. Kabza, E. R. P. Zuiderweg, D. Sun, and J. E. Gestwicki, *ACS Med. Chem. Lett.*, **2013**, *4*, 1042–1047.

257. B. Neises, and W. Steglich, *Angew. Chemie - Int. Ed.*, **1978**, *17*, 522–524.

258. C. Würth, M. Grabolle, J. Pauli, M. Spieles, and U. Resch-Genger, *Nat. Protoc.*, **2013**, *8*, 1535–1550.

259. Invitrogen, *SYBR® green I nucleic acid gel stain product information sheet*, **2006**, 1–5.

260. Molecular Probes, *SYBR® green II RNA gel stain product information sheet*, **2001**, 1–3.

261. C. D. Geddes, A. I. Dragan, J. R. Casas-Finet, M. A. Schenerman, J. B. McGivney, R. J. Strouse, R. Pavlovic, and E. S. Bishop, *J. Fluoresc.*, **2012**, *22*, 1189–1199.

262. M. Davis, S. M. Sagan, J. P. Pezacki, D. J. Evans, and P. Simmonds, *J. Virol.*, **2008**, *82*, 11824–11836.

263. P. Simmonds, A. Tuplin, and D. J. Evans, *Bioinformatics*, **2004**, *10*, 1337–1351.

264. K. Salorinne, T. Lahtinen, S. Malola, J. Koivisto, and H. Häkkinen, *Nanoscale*, **2014**, *6*, 7823–7826.

265. J. Koivisto, X. Chen, S. Donnini, T. Lahtinen, H. Häkkinen, G. Groenhof, and M. Pettersson, *J. Phys. Chem. C*, **2016**, *120*, 10041–10050.

ORIGINAL PAPERS

I

COVALENTLY LINKED MULTIMERS OF GOLD NANOCLUSTERS AU$_{102}$(P-MBA)$_{44}$ AND AU$_{\sim 250}$(P-MBA)$_N$

by

Tanja Lahtinen, Eero Hulkko, Karolina Sokołowska, Tiia-Riikka Tero, Ville Saarnio, Johan Lindgren, Mika Pettersson, Hannu Häkkinen, and Lauri Lehtovaara 2016.
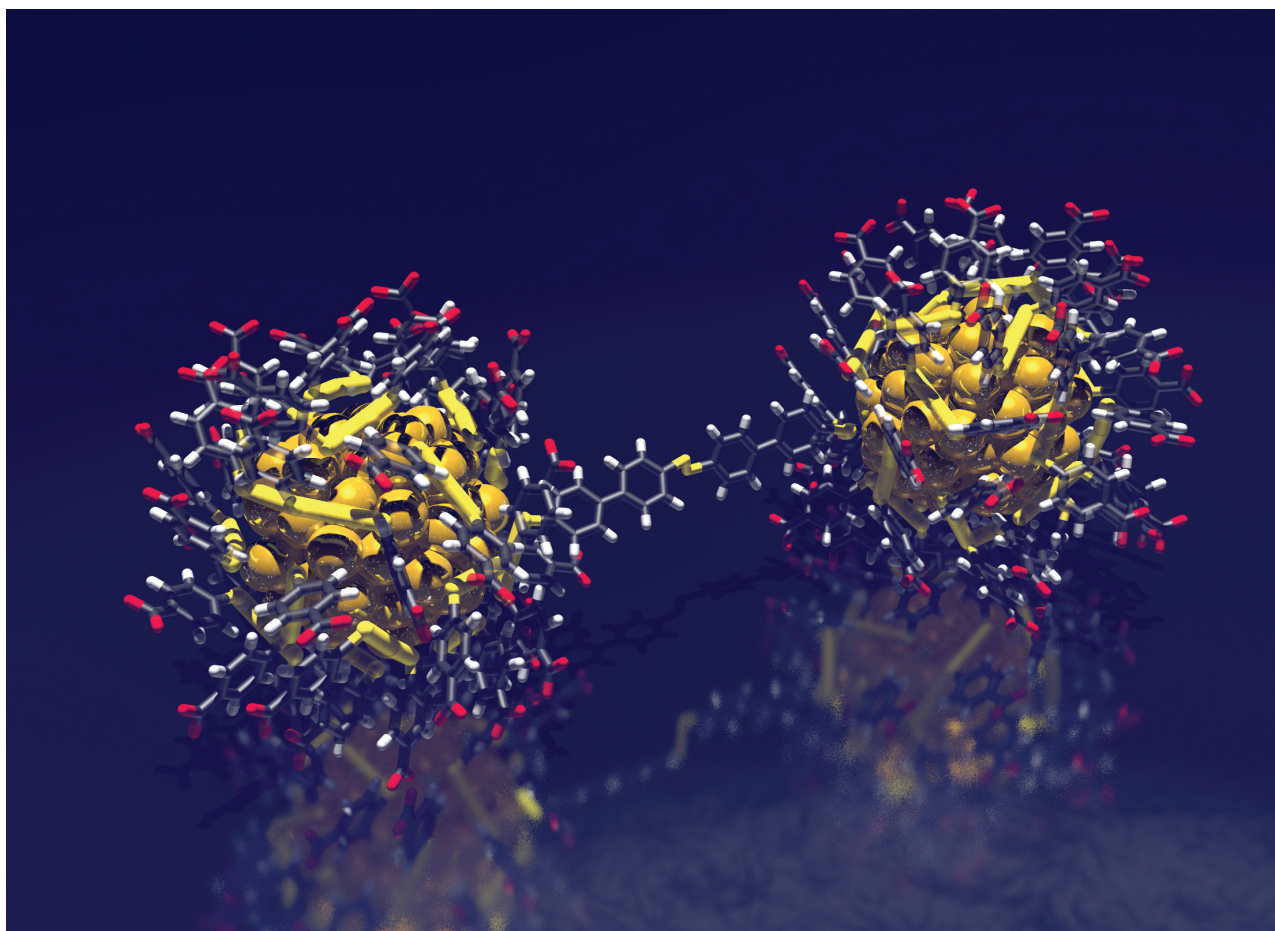
Showcasing work from the Nanoscience Center, Departments of Chemistry and Physics, University of Jyväskylä, Jyväskylä, Finland.

Covalently linked multimers of gold nanoclusters $Au_{102}(p\text{-MBA})_{44}$ and $Au_{\sim250}(p\text{-MBA})_n$

Monolayer protected gold nanoclusters are a special kind of nanoparticles with well-defined molecular structures. Linking them together with covalent molecular bridges enables studies of light-metal interaction in nanoscale with unprecedented precision. While synthesized dimers of $Au_{102}(p\text{-MBA})_{44}$ showed no optical coupling in the visible region, multimers of plasmonic $Au_{\sim250}(p\text{-MBA})_n$ exhibited hybridized plasmon modes with unexpectedly large red-shifts.
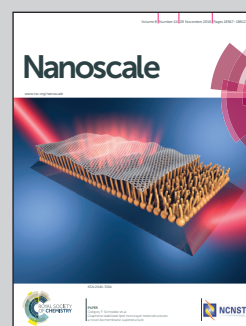
ROYAL SOCIETY OF CHEMISTRY

www.rsc.org/nanoscale

PAPER

Covalently linked multimers of gold nanoclusters Au$_{102}$(*p*-MBA)$_{44}$ and Au$_{\sim250}$(*p*-MBA)$_n$†

Tanja Lahtinen,‡[a] Eero Hulkko,‡[a] Karolina Sokołowska,[a] Tiia-Riikka Tero,[a] Ville Saarnio,[a] Johan Lindgren,[a] Mika Pettersson,*[a] Hannu Häkkinen*[a,b] and Lauri Lehtovaara*[a]

We present the synthesis, separation, and characterization of covalently-bound multimers of *para*-mercaptobenzoic acid (*p*-MBA) protected gold nanoclusters. The multimers were synthesized by performing a ligand-exchange reaction of a pre-characterized Au$_{102}$(*p*-MBA)$_{44}$ nanocluster with biphenyl-4,4′-dithiol (BPDT). The reaction products were separated using gel electrophoresis yielding several distinct bands. The bands were analyzed by transmission electron microscopy (TEM) revealing monomer, dimer, and trimer fractions of the nanocluster. TEM analysis of dimers in combination with molecular dynamics simulations suggest that the nanoclusters are covalently bound *via* a disulfide bridge between BPDT molecules. The linking chemistry is not specific to Au$_{102}$(*p*-MBA)$_{44}$. The same approach yields multimers also for a larger monodisperse *p*-MBA-protected cluster of approximately 250 gold atoms, Au$_{\sim250}$(*p*-MBA)$_n$. While the Au$_{102}$(*p*-MBA)$_{44}$ is not plasmonic, the Au$_{\sim250}$(*p*-MBA)$_n$ nanocluster supports localized surface plasmon resonance (LSPR) at 530 nm. Multimers of the Au$_{\sim250}$(*p*-MBA)$_n$ exhibit additional transitions in their UV-vis spectrum at 630 nm and 810 nm, indicating the presence of hybridized LSPR modes. Well-defined structures and relatively small sizes make these systems excellent candidates for connecting *ab initio* theoretical studies and experimental quantum plasmonics. Moreover, our work opens new possibilities in the controlled synthesis of advanced monodisperse nanocluster superstructures.

Introduction

Nanoparticles (NPs) and their superstructures have attracted a lot of interest in fundamental research as well as in nanotechnological applications. The main reason is that the physicochemical properties of nanoparticles are often strikingly different from their bulk counterparts and depend on the composition, size, shape, and internal structure of the nanoparticles.[1,2] The properties of superstructures are influenced by their immediate surroundings including other nanoparticles. For example, the optical spectrum of metal nanoparticles is dominated by localized surface plasmon

resonance (LSPR) that hybridizes with LSPRs of other nearby NPs.[3] The hybridization leads to the formation of "hotspots" in between the NPs, where the electromagnetic field intensity increases orders of magnitudes. This had led to many applications. For example, nanoparticle dimers can act as nanoscale distance probes because of their sensitivity to interparticle spacing.[4,5] The field enhancement has been employed, for example, in surface enhanced Raman spectroscopy,[6] where sensitivity has reached the single molecule level.[7]

There exist several different approaches to fabricate NP assemblies and superstructures. The most straightforward is to simply aggregate NPs.[8] More stable structures can be achieved with polymer or silica encasing[9,10] or templating polymer layers.[11] Lithography has been extensively used to fabricate plasmonic nanoparticle assemblies in a controlled manner.[12] However, for several applications, it would be desirable to have a controlled, wet-chemistry synthesis of superstructures. Successful wet-chemistry approaches based on self-assembly has been demonstrated, for example, with DNA-templating[13] and with several different molecular linkers.[14–18]

Colloidal nanoparticles, in general, have a serious drawback from the chemical point-of-view. Their structure is not well-defined at the atomic level, and typical nanoparticle synthesis produces a polydisperse sample of different sizes, shapes, and

[a]*Department of Chemistry, Nanoscience Center, University of Jyväskylä, P.O. Box 35, 40014 Jyväskylä, Finland. E-mail: lauri.lehtovaara@jyu.fi, hannu.j.hakkinen@jyu.fi, mika.j.pettersson@jyu.fi*
[b]*Department of Physics, Nanoscience Center, University of Jyväskylä, P.O. Box 35, 40014 Jyväskylä, Finland*

surface structures.[5] This seriously hinders the synthesis of homogeneous NP superstructures, and experiments that require atomic-level control, for example, LSPR hybridization through molecular states, are extremely difficult to carry out reproducibly.

Monolayer protected clusters (MPCs) are a special kind of NP which have a well-defined atomic structure that can be accurately determined by mass spectrometry and by single-crystal X-ray diffraction similar to small molecules.[19] For example, the crystal structure of a *para*-mercaptobenzoic acid (*p*-MBA) protected $Au_{102}(p\text{-MBA})_{44}$ cluster used in this work shows a core of 79 gold atoms protected by 19 RS–Au–SR and two $Au_2(SR)_3$ units in a well-defined motif.[20,21]

The atomically precise structures of MPCs have enabled accurate studies of their chemistry. $Au_{102}(p\text{-MBA})_{44}$ and other MPCs are known to have preferred sites for ligand exchange reactions, *i.e.*, specific ligands are exchanged with higher probability than others.[22,23] A well-defined structure with unequal ligand-exchange activities provides a basis for controlled synthesis of homogeneous NP superstructures.

An additional benefit of using MPCs to study the fundamental aspects of NP superstructures is that depending on the size and shape of the metallic core, the electronic structure of MPC can change from discrete molecular-like energy levels,[19] to a semiconducting,[24,25] and finally to a metallic continuum.[26,27] The changes in the electronic structure are reflected in their physicochemical properties, for example, the UV-vis spectrum changes from discrete peaks[19] to a continuum,[25] and finally to a spectrum with clear LSPR.[26,27]

The well-defined atomic structure, preferred sites for ligand exchange, and the possibility to approach the nanoparticle limit from below in a controlled manner make MPCs excellent candidates for accurate studies of emergent properties in NP superstructures. Moreover, MPC superstructures and their possible MPC specific properties are inherently interesting themselves having potential applications in chemical sensing and biomedical imaging.[28] In this paper, we demonstrate the synthesis of small covalently linked MPC superstructures *via* a ligand-exchange reaction, where a biphenyl-4-4′-dithiol (BPDT) replaces a *p*-MBA ligand and creates a covalent disulfide bridge with another BPDT forming a MPC multimer. Furthermore, we show that the emergence of plasmonic coupling can be studied using these MPC multimers. Previously, MPC dimers have been demonstrated using dynamic diglyme bonding,[29] however, in our approach, dithiol-bridged MPCs form a covalently bound system.

The rest of the paper is structured as follows. We begin by describing the synthesis and purification of $Au_{102}(p\text{-MBA})_{44}$ and $Au_{\sim250}(p\text{-MBA})_n$ clusters and their BPDT linked multimers (see Fig. 1). Experimental analysis methods are described next, followed by computational methods. Results and discussion begin with characterization of $Au_{102}(p\text{-MBA})_{44}$ and analysis of $Au_{\sim250}(p\text{-MBA})_n$ followed by analysis of their multimers. TEM analyses and molecular dynamics (MD) simulations are combined to explain the nature of the linking. In the last part of the paper, we focus on the UV-vis spectroscopy of
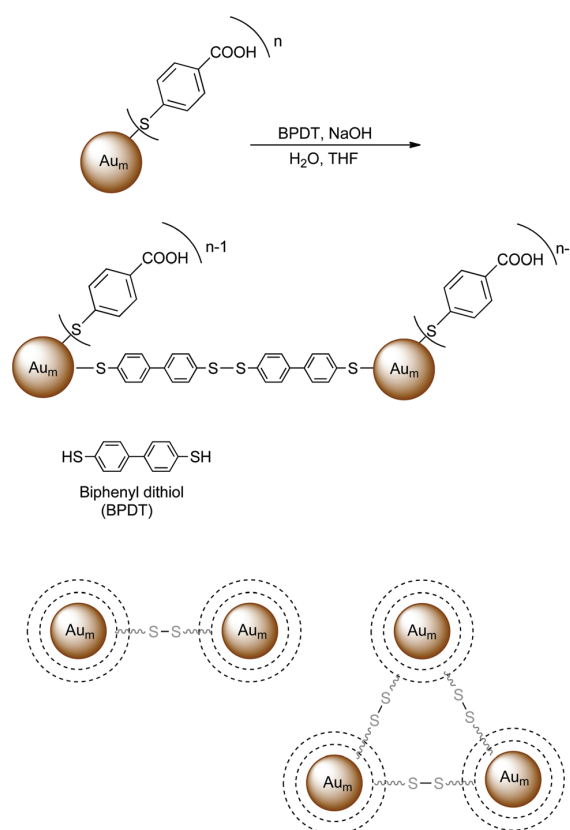
Fig. 1 Schematic representation of the ligand exchange and linking reaction. The scheme shows the molecular structure of biphenyl-4,4′-dithiol (BPDT), the covalent linking *via* two BPDTs as an example, and examples of dimeric and trimeric reaction products.

$Au_{\sim250}(p\text{-MBA})_n$ multimers and the interpretation of observed plasmonic features supported by density functional theory simulations.

Materials and methods

Materials

All reagents were commercially available and used as received unless otherwise mentioned.

Synthesis of nanoclusters. Two different MPCs were synthesized to be used as starting materials for the multimer synthesis. The smaller nanocluster, $Au_{102}(p\text{-MBA})_{44}$, has been extensively studied before.[20–22,24,25,30–32] We followed its previously reported synthesis given in ref. 30. The larger nanocluster of approximately 250 gold atoms and an unknown number of *p*-MBAs (labelled as $Au_{\sim250}(p\text{-MBA})_n$) required treatment of the initial $Au_x(p\text{-MBA})_y$, the polymerization step at a pH of ~11 before the reduction that nucleates the growth of the metal core.[33] The syntheses of both sizes produced milligram

quantities of material. A detailed description of the syntheses and purification is given in the ESI.†

Synthesis of nanocluster multimers. The ligand exchange reaction leading to multimers of $Au_{102}(p\text{-MBA})_{44}$ was carried out as follows. A stock solution of BPDT in THF was added to a water solution of $Au_{102}(p\text{-MBA})_{44}$ (2 : 1 ratio of thiol groups *vs.* gold clusters) together with a few drops of NaOH. The reaction was quenched after 3.5 hours with isopropanol and 5 M NH_4OAc, and the resulting black precipitate was centrifuged. The supernatant was removed and the pellet was washed to remove any remaining free thiol residue. The ligand-exchange reaction of $Au_{\sim250}(p\text{-MBA})_n$ was carried out in the same way.

Separation of nanocluster multimers. Polyacrylamide gel electrophoresis (PAGE) was used to separate reaction products of $Au_{102}(p\text{-MBA})_{44}$ and $Au_{\sim250}(p\text{-MBA})_n$ multimer syntheses. Preparative PAGE was performed with a 2 mm thick gel. Different PAGE bands were mechanically cut from the acrylamide gel and dissolved separately in a small amount of water. Clusters were allowed to dissolve from the gel until significant coloration of the solution was observed (typically overnight). The solution was filtered through a centrifugal filter tube with a pore size of 0.22 μm (time: 60 s, speed: rcf = 1.0) to remove excess gel residues. The separation procedure was repeated for the separated bands to obtain higher purity for TEM imaging and optical absorption spectroscopy.

Experimental techniques

Polyacrylamide gel electrophoresis (PAGE). PAGE was run on a 15 or 20% polyacrylamide gel (29 : 1 acrylamide : bisacrylamide) using a 2X TBE run buffer in Bio-Rad Mini-Protean Tetra System gel electrophoresis apparatus at 130 V.

Mass spectrometry (MS). An electrospray ionization mass spectrum of the $Au_{102}(p\text{-MBA})_{44}$ sample was measured at the University of Tokyo using a homemade TOF mass spectrometer with a similar procedure and parameters as previously reported in ref. 31. The sample was dissolved in 50% (v/v) methanol/water containing 0.07% triethylamine.

Nuclear magnetic resonance (NMR) spectroscopy. ^1H NMR spectra were recorded on Bruker Avance DRX 300 MHz (for $Au_{102}(p\text{-MBA})_{44}$) and 400 MHz (for $Au_{\sim250}(p\text{-MBA})_n$) spectrometers.

UV-vis spectroscopy. Optical absorption measurements were done with a Perkin Elmer Lambda 850 UV/Vis-spectrometer with 2 nm resolution.

Transmission electron microscopy (TEM) and image analysis. TEM samples were prepared by drop-casting 40 mL of dilute deionized water solution of linked nanoclusters on a glow discharged 400 mesh holey carbon copper grid (Ted-Pella ultrathin c). The solution was allowed to deposit for 15 min, after which excess sample was removed and the grid was allowed to dry under vacuum overnight. Samples were imaged with a 0.26 nm point resolution using a JEOL JEM-1400HC TEM operated at 80 kV or 120 kV, equipped with a bottom mounted 11 Megapixel CCD camera (Olympus SIS Quemesa).

TEM images were analyzed by a semi-automatic procedure using an in-house developed code. First, a blob detector filter was applied to TEM images, where the filter is the difference of two Gaussians of widths σ and 2σ, and the value of σ depends on TEM magnification. After the automatic blob detection, the found particles were verified manually, and any false positives were removed from further analysis. A 2D Gaussian function was fitted to a slightly smoothed TEM intensity around each detected and verified particle. Parameters of the fitted 2D Gaussians were stored for further analysis.

Exposure time for determining particle size was chosen not to saturate TEM images at the centers of particles. Size of the particle is reported as the average of the long and short axis full width at half maximum (FWHM). For example, the crystal structure of $Au_{102}(p\text{-MBA})_{44}$ yields a FWHM of 1.1 nm when each atom in the crystal structure is represented as a Gaussian charge distribution with intensity proportional to the atomic number and width equal to 0.2 nm.

Computational methods

Molecular dynamics. The molecular dynamics (MD) simulations were performed with Gromacs 4.6.7 [34] using periodic boundary conditions; a leap-frog integrator with a 2 fs time step; PME electrostatics with 1.0 nm cut-off and 0.12 nm grid spacing; and Lennard–Jones interaction with 1.0 nm cut-off and dispersion correction for energy and pressure. Simulated structures were placed in the center of a cubic box and then solvated using a TIP3P water model. Counterions (Na^+) were added, when needed, to neutralize the system. All simulations model the NPT ensemble using a velocity-rescale thermostat (reference temperature 298.15 K) and a Berendsen barostat (reference pressure 1 bar). Total simulation time was 100 ns and sampling was started after 50 ns.

The force field parameters and charges for the gold–sulphur units and deprotonated and protonated p-MBA ligands were obtained from ref. 35. Existing force field parameters in AMBER12 [36] were used for the BPDT molecule. The partial charges for BPDT were calculated using structures consisting of one, two, or three BPDT(s) capped by gold atoms at the ends. The ground state geometries of the structures were obtained using Gaussian09 software, [37] B3LYP functional, def2-TZVP basis set, and W06 density fitting. The MD partial charges were calculated using Ambertools12 [36] and the RESP charge fitting procedure [38] in two stages with the charge of gold atoms set to zero. The radius of gold atoms was set to 0.17 nm. The partial charges can be found in ESI Table S1.† The force field parameters for BPDT linker molecules and for the atom types are listed in ESI Table S2.†

Dimeric $Au_{102}(p\text{-MBA})_{43}$–$(BPDT)_n$–$Au_{102}(p\text{-MBA})_{43}$ systems for molecular dynamics were constructed by replacing the p-MBA ligand labeled as "pMBA2" in ref. 22 by a BPDT molecule. If the structure contained more than one BPDT molecule, a disulfide bridge (RS–SR) was formed between BPDT molecules.

Paper

Density functional theory. The density functional theory (DFT) calculations were performed using GPAW 0.10.0,[39] GPAW setup 0.9.11271 and the PBE exchange–correlation functional. The initial structure for DFT simulations was taken from a MD simulation of deprotonated $Au_{102}(p\text{-MBA})_{43}$–$(BPDT)_n$–$Au_{102}(p\text{-MBA})_{43}$ where the core-to-core distance was 3.4 nm. Both $Au_{102}(p\text{-MBA})_{43}BPDT$ fragments were replaced by $Au_{314}(SH)_{96}$ from Malola et al.[40] in such a manner that gold atoms in the Au–SH–Au–SH–Au units of $Au_{314}(SH)_{96}$ were aligned with the respective gold atoms of Au–BPDT–Au–p-MBA–Au units of $Au_{102}(p\text{-MBA})_{43}BPDT$. The geometry of the BPDT–BPDT linker was relaxed in a system where only Au–BPDT–Au–SH–Au units were included in the DFT calculation and all gold atoms were fixed.

Results and discussion

Characterization of $Au_{102}(p\text{-MBA})_{44}$

The purified product of $Au_{102}(p\text{-MBA})_{44}$ synthesis was analyzed using PAGE, NMR, MS, TEM, and UV-vis. The synthesis product showed up as a single distinct band in PAGE (see Fig. 2 and ESI Fig. S1†) indicating a monodisperse MPC. MPC was identified as $Au_{102}(p\text{-MBA})_{44}$ based on its NMR and mass spectra. The electrospray ionization mass spectrum (see ESI Fig. S2†) shows peaks that correspond to different mass to charge ratios of partially deprotonated $Au_{102}(p\text{-MBA})_{44}$, and the NMR spectrum (see ESI Fig. S3†) reproduces the characteristic NMR fingerprint of $Au_{102}(p\text{-MBA})_{44}$.[32] The UV-vis spectrum (see Fig. 3) and TEM diameter of 1.2 ± 0.3 nm (see ESI Fig. S4†) are also in agreement with previous studies.[20,25,31]

Analysis of $Au_{\sim250}(p\text{-MBA})_n$

Previous studies have shown that MPCs in this size range have preferred sizes,[26,27,41] and the sizes appear as individual bands in PAGE.[41,42] The product of $Au_{\sim250}(p\text{-MBA})_n$ synthesis forms a single distinct band in PAGE (see Fig. 2) indicating a monodisperse MPC. The band had a lower mobility than
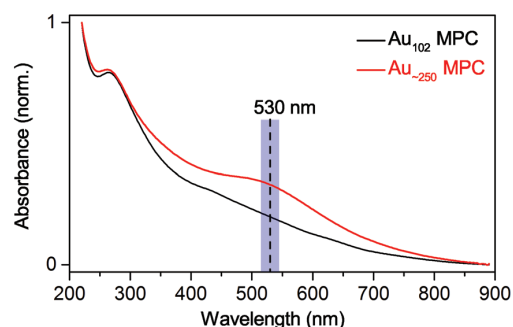

Fig. 3 Normalized UV-vis spectra of $Au_{102}(p\text{-MBA})_{44}$ (black) and $Au_{\sim250}(p\text{-MBA})_n$ (red) clusters in H_2O. LSPR absorption maximum of $Au_{\sim250}(p\text{-MBA})_n$ at 530 ± 15 nm is indicated with a dashed line.

$Au_{102}(p\text{-MBA})_{44}$ in the PAGE run indicating a larger size (see ESI Fig. S1A†). This is consistent with the TEM analysis that yields a 1.6 ± 0.3 nm core diameter (see ESI Fig. S4†). A rough estimate for the number of gold atoms can be obtained by assuming a relatively similar shape and density for the two MPCs ($N_{102}/V_{102} = N_x/V_x$), and then scaling the number of gold atoms in $Au_{102}(p\text{-MBA})_{44}$ by their relative volume calculated from the estimated core diameters: $N_x = 102 \times (1.6 \text{ nm}/1.2 \text{ nm})^3 \approx 240$.

The UV-vis spectrum (see Fig. 3) shows a weak LSPR band at 530 ± 15 nm. Recent studies have shown that LSPR begins to appear when MPCs have approximately 200 gold atoms and becomes stronger as the cluster size increases. Our spectrum is comparable to the reported spectra of 51 kDa,[26] 45 kDa and 53 kDa clusters,[27] with the estimated number of gold atoms at 250, 226, and 253, respectively. We label our larger MPC as $Au_{\sim250}(p\text{-MBA})_n$ based on these TEM and UV-vis estimates.

Analysis of $Au_{102}(p\text{-MBA})_{44}$ multimers

A crude product from the $Au_{102}(p\text{-MBA})_{44}$ ligand-exchange synthesis was analyzed by UV-vis spectroscopy after purification
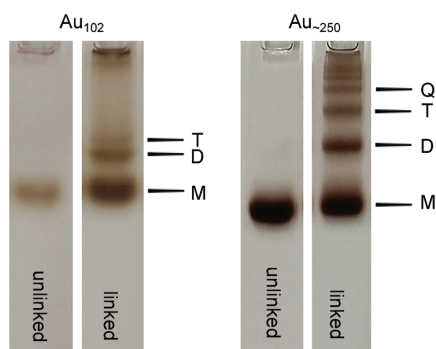

Fig. 2 PAGE bands of the $Au_{102}(p\text{-MBA})_{44}$ and $Au_{\sim250}(p\text{-MBA})_n$ clusters and their linked multimers. $Au_{102}(p\text{-MBA})_{44}$ gels are from a different run than $Au_{\sim250}(p\text{-MBA})_n$ gels, thus the run distances are not comparable. See ESI Fig. S1A† for samples in the same PAGE run.
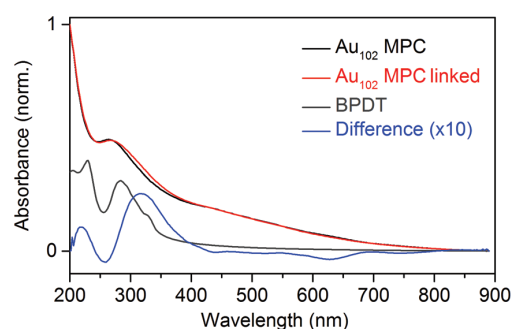

Fig. 4 Normalized UV-vis spectra of $Au_{102}(p\text{-MBA})_{44}$ before (black) and after (red) linking with BPDT in H_2O, the arbitrarily scaled spectrum of molecular BPDT in H_2O (grey), and the difference spectrum of spectra before and after linking (linked Au_{102} MPC − unlinked Au_{102} MPC, blue, scaled by factor 10).

(see Fig. 4). The spectrum essentially reproduces the spectrum of $Au_{102}(p\text{-MBA})_{44}$ in the visible region,[25] indicating that the cluster core remains intact in the reaction. New electronic transitions appear in the UV-region seen as spectral broadening of the ligand transitions, and the difference spectrum (see Fig. 4) reveals a new maximum in the linked clusters at 308 nm. The features closely resemble transitions of molecular BPDT measured in H_2O, but they are red-shifted. Although, optical coupling between the cores of $Au_{102}(p\text{-MBA})_{44}$ cannot be ruled out based on these observations, it is more likely that the observed feature originates from BPDT molecules bound to gold. Similar changes in the UV-vis spectrum have been reported before for diacetylene linked 1.1 nm AuNPs.[17]

The crude synthesis product was further analyzed by PAGE, where the sample separated into several distinct bands (see Fig. 1 and ESI Fig. S1A†). We label the three lowest bands as M, D, and T bands. The most intense and most mobile M band was aligned with the $Au_{102}(p\text{-MBA})_{44}$ reference band indicating that the M band is unreacted $Au_{102}(p\text{-MBA})_{44}$ or monomeric $Au_{102}(p\text{-MBA})_{44-n}(BPDT)_n$. This was confirmed by TEM showing dominantly monomeric MPCs for the M band (see Fig. 5a and ESI Fig. S5†). The D and T bands are clearly less mobile than the M band having a shorter running distance than the $Au_{102}(p\text{-MBA})_{44}$ reference. TEM imaging of these bands shows predominantly dimers for the D band and a large fraction of trimers in the T band (see Fig. 5b, c and ESI Fig. S5B, C†).

TEM analysis of center-to-center distances in the D band yielded a distribution spanning from 1.8 nm up to 3.4 nm (see Fig. 5d). To gain insight into the nature of the bonding between multimers, we performed MD simulations of Au_{102}MPCs linked with one or more BPDT molecules. Atomistic models were constructed based on the known $Au_{102}(p\text{-MBA})_{44}$ X-ray structure[20] as described in Materials and methods. The simulations were performed in water both for the fully protonated and deprotonated forms of the p-MBA ligand surface.

Simulations of the $Au_{102}(p\text{-MBA})_{43}$–BPDT-$Au_{102}(p\text{-MBA})_{43}$ dimer indicated that the linkage by a single BPDT is rather rigid and both sterically and electrostatically demanding. The deprotonated system was not stable unless electrostatic repulsion was screened by adding a significant amount of salt. The simulation in saline solution produced a very narrow center-to-center distance distribution between 2.5–2.7 nm (see Fig. S6A†) that is unable to reproduce the full range of experimentally observed distances.

Simulations of the $Au_{102}(p\text{-MBA})_{43}$–$(BPDT)_2$–$Au_{102}(p\text{-MBA})_{43}$ dimer with a disulfide bridge between the BPDT molecules

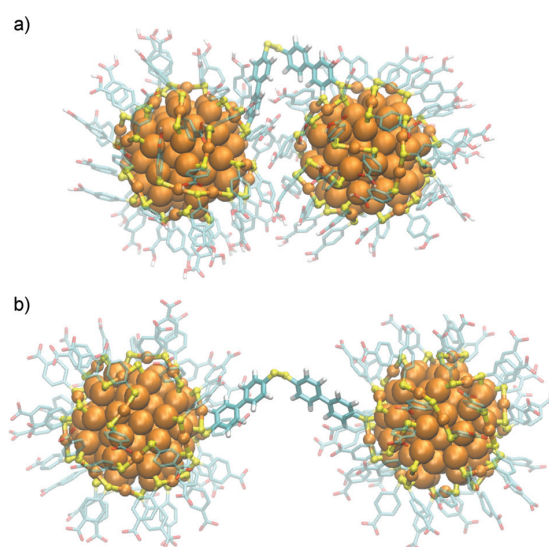Fig. 6 Snapshot from the MD simulation of (a) fully protonated and (b) fully deprotonated Au_{102}MPC–$(BPDT)_2$–Au_{102}MPC in H_2O. Orange: Au; yellow: S; cyan, C; red: O. The disulfide bridge is highlighted by a yellow bond at the center.

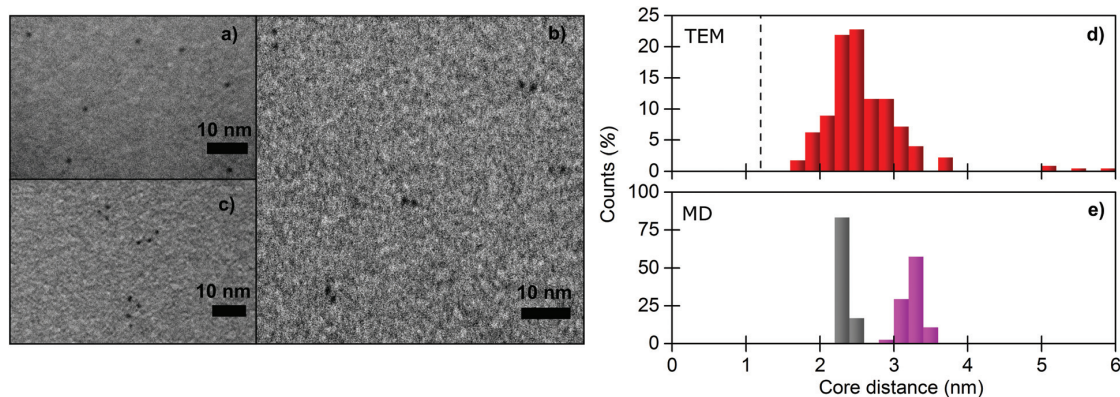
Fig. 5 TEM images of (a) monomeric, (b) dimeric, and (c) trimeric Au_{102}MPCs in M, D, and T bands, respectively. The distribution of center-to-center distances of the linked Au_{102}MPC dimers (d) from the TEM images (number of particles, n = 220), and (e) from the simulation of fully-protonated (grey) and fully-deprotonated (purple) Au_{102}MPC–$(BPDT)_2$–Au_{102}MPC in H_2O. The estimated core size of 1.2 nm is marked with a dashed vertical line.

indicated a stable and flexible system (see Fig. 6). The center-to-center distances started from 2.2 nm for the fully protonated system and extended up to 3.6 nm for the fully deprotonated systems, agreeing with the tails of the experimental distribution (see Fig. 5c). The simulated distributions of fully protonated and deprotonated clusters are relatively narrow and peak at the ends of the experimental spectrum. This suggests that Au_{102}MPCs are neither fully protonated nor fully deprotonated forming a distribution of distances based on the protonation level. Distances below 2.2 nm in the experimental distribution can be addressed to the roughness of the TEM support film leading to tilted dimers with respect to the imaging plane.

Simulations of dimers, where three BPDT molecules connect fully deprotonated MPCs yield a distribution, which spans from 3.5 nm to 4.5 nm being above experimentally observed values (see ESI Fig. S6E†). Although, this does not exclude the possibility of a triple linker, it suggests that triple linking is rare. Dimers linked with multiple BPDT bridges are very unlikely due to the low BPDT concentration used in the experiment (only two BPDT per 44 p-MBA). Therefore, the most straightforward explanation is that Au_{102}MPC dimers are linked primarily by two BPDT molecules with a single disulfide bridge between them.

Analysis of $Au_{\sim250}(p\text{-MBA})_n$ multimers

We did a similar PAGE analysis and separation for the crude product of $Au_{\sim250}(p\text{-MBA})_n$ ligand exchange reaction as for $Au_{102}(p\text{-MBA})_{44}$. PAGE showed several distinct bands, however, the bands were less mobile than linked Au_{102}MPCs by a factor comparable to the mobility difference between unlinked MPCs (see Fig. 2 and ESI Fig. S1†). TEM imaging of the three lowest bands, M, D, and T, revealed dominantly monomeric, dimeric,

and trimeric structures of $Au_{\sim250}(p\text{-MBA})_n$, respectively (see Fig. 7a–d and ESI Fig. S7–9†). The distributions of multimer core counts in M, D, and T bands in Fig. 7d were obtained from a concentrated sample prepared for UV-vis spectroscopy. The purity of the samples can be further increased by using a less concentrated material in PAGE (see ESI Fig. S10†).

Note that the D and T bands are very narrow, as in the case of $Au_{102}(p\text{-MBA})_{44}$. This provides additional evidence that $Au_{\sim250}(p\text{-MBA})_n$ is a monodisperse MPC.

TEM analysis of center-to-center distances in the D band of $Au_{\sim250}$MPCs was rather broad spanning from 2.6 nm up to 4.4 nm (see Fig. 7e). The larger diameter of $Au_{\sim250}(p\text{-MBA})_n$ adds a constant shift of 0.4 nm to the $Au_{102}(p\text{-MBA})_{44}$ distribution. The tail of the distribution extending up to 4.4 nm can be explained by the contribution from dimers bound by three (or more) BPDT molecules. The larger electrostatic repulsion between $Au_{\sim250}$MPCs compared to Au_{102}MPCs might favor longer linkers. Remarkably, the distribution of the angles in the TEM analysis of trimers showed a dominant peak at 60° indicating equilateral triangular multimers (see Fig. 7f), which is also clearly visible in the micrographs in addition to the bent or linear geometries (see Fig. 7c and ESI Fig. S9†). The preference for equilateral triangles could be explained by a covalent bridge between each pair of MPCs in a trimer (see Fig. 1 and ESI Fig. S11†).

Plasmon coupling in $Au_{\sim250}(p\text{-MBA})_n$ multimers

To study the optical properties of the plasmonic $Au_{\sim250}(p\text{-MBA})_n$, we ran PAGE multiple times to prepare concentrated samples from M, D, and T bands. The UV-vis absorption spectrum from the concentrated M band was equal to unlinked $Au_{\sim250}(p\text{-MBA})_n$ in the visible region, but it showed changes in the UV region as in the case of Au_{102}MPCs. Comparison of
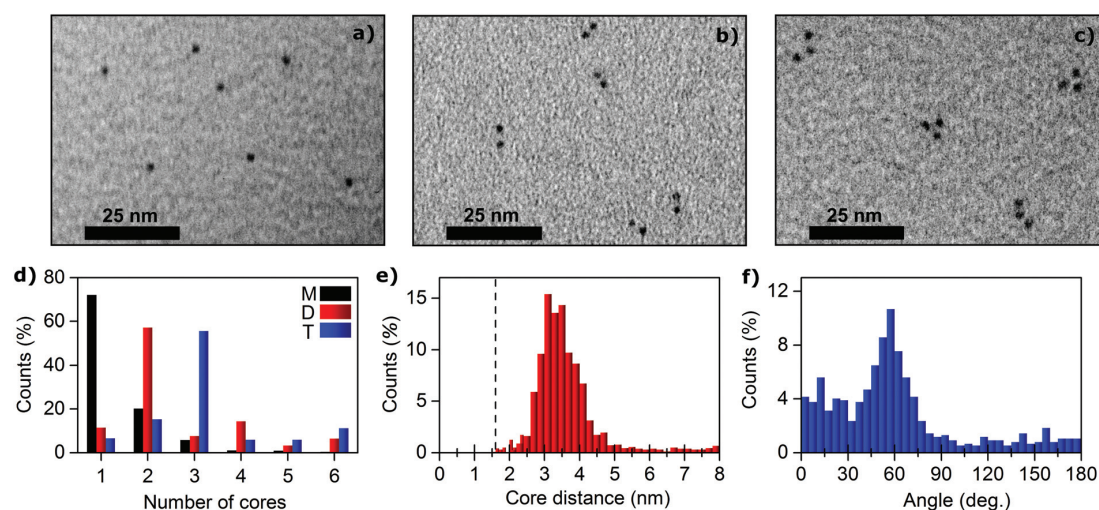

Fig. 7 TEM images of (a) monomeric, (b) dimeric, and (c) trimeric $Au_{\sim250}$MPCs. (d) Statistics of multimers from M (number of particles, $n = 1119$), D ($n = 227$), and T ($n = 624$) bands of linked $Au_{\sim250}$MPCs. The distribution of (e) center-to-center distances for dimers ($n = 1863$), and (f) angles for trimers ($n = 770$) analyzed from TEM images of linked $Au_{\sim250}$MPCs. The estimated core size of 1.6 nm is marked with a dashed vertical line.
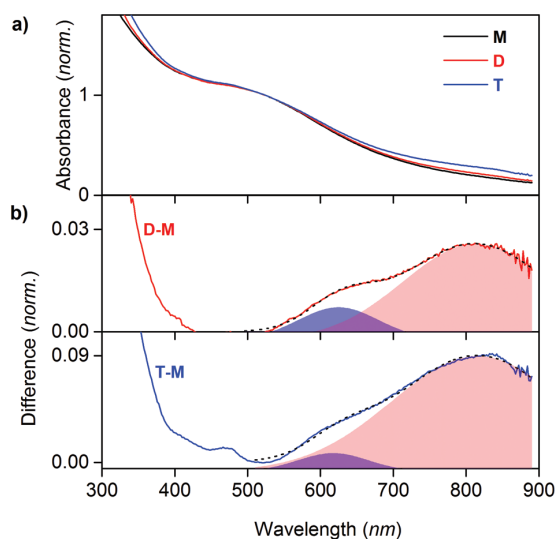
Fig. 8 (a) Normalized UV-vis spectra of purified samples from M, D, and T bands. (b) Difference spectra between samples from D and M bands (top) as well as from T and M bands (bottom). The shaded areas indicate Gaussian components found in the data and the dashed curves indicate the totals.

spectra from M, D, and T bands, normalized to the main LSPR peak at 530 nm (see Fig. 8a, and ESI Fig. S12†), shows interesting new features for the linked Au$_{\sim250}$MPCs in the visible region. The difference between normalized spectra of D and M bands (Fig. 8b) has two broad and significantly red-shifted peaks. These features become stronger in the difference spectrum between T and M bands. If we fit two Gaussian functions with an exponential background to the difference spectra, the fit reproduces these features extremely well in both cases. The obtained peak positions, 630 nm and 810 nm, are the same for the D and T bands. The features are weak compared to the main LSPR band, but they are locally significant altering absorption intensity up to ~10%. More importantly, they are reproducible (see ESI Fig. S13†).

It is difficult to ascertain the origin of these modes experimentally. We observed, however, a significant red shift of the main LSPR peak when unlinked Au$_{\sim250}$MPCs were agglomerated by reducing the pH down to 3.5 (see ESI Fig. S14†). This is a typical plasmonic nanoparticle behavior, which originates from the coupling of LSPR modes between nearby NPs.[3] The observed feature peaks at 635 nm in the difference spectrum between low and high pH (see ESI Fig. S14†). This strongly suggests that the peak at 630 nm in the spectra of Au$_{\sim250}$MPC dimers and trimers originates from a coupled plasmon mode, called the bonding dipolar plasmon (BDP) mode, where the LSPRs of two nearby particles oscillate in-phase.[3] Therefore, this feature would not be directly related to the linker molecule, but only to the fact that the two plasmonic particles are close to each other.

Using parameters relevant to our system (particle diameter 1.6 nm and edge-to-edge distance 1.4 nm), the well-known "plasmon ruler equation"[43] predicts a minor plasmon shift (<10 nm) as compared to the observed shift of 100 nm from 530 nm to 630 nm. The failure of the plasmon ruler equation here could be due to its incompatibility with sub-2 nm MPCs for which atomistic details play an important role. The thickness of the ligand layer is comparable to the diameter of the metal core, and therefore, hybridization of the metallic core with the pi-electrons of the ligand layer might have a significantly larger influence than in larger NPs.

We did not observe the peak at 810 nm in unlinked Au$_{\sim250}$MPC agglomerates, and the peak is sensitive to the number of cores in the multimer. Therefore, we assign this mode to the quantum-mechanical effects depending on the electronic structure of the molecular bridge. Previous studies of linked NPs have shown that a tunneling charge transfer plasmon (tCTP) can form between NPs when they are connected with a molecular linker or a similar structure.[44–48] This mode typically exists together with the BDP mode, it is red-shifted with respect to the BDP mode, and it depends sensitively on the tunneling properties of the NP–molecule–NP junction. Moreover, tunneling through the molecular states allows coupling over much longer distances than the normal charge transfer plasmon (CTP) that happens only over very short (<1 nm) insulating gaps and causes a blue-shift instead of a red-shift.[44,49,50]

Simulations of a simple two-level system between plasmonic NPs have showed that the tCTP mode forms when a molecular state localized on the linker is near the Fermi level of the combined system.[47] To examine whether such localized states could exist in Au$_{\sim250}$MPC multimers, we performed DFT simulations on a model system. While we do not have currently information of the atomic structure of Au$_{\sim250}$MPC, we have previously performed density functional theory (DFT) calculations on a slightly larger plasmonic Au$_{314}$(SH)$_{96}$ model MPC.[40] We now built a model system (see Fig. 9) by linking two such clusters *via* a disulfide-bridged BPDT pair and solved for its electronic structure using DFT. Several molecular states that are localized on BPDT were found starting 0.8 eV below (occupied states) and 1.7 eV above (unoccupied states) the Fermi level (see Fig. 9). These states are close enough to the Fermi level that when coupled to LSPRs of MPCs in an optical excitation they could act as tunneling channels for the tCTP mode, and therefore, account for the observed absorption in the 700–900 nm range and possibly longer wavelengths.

Another possible explanation for the observed 810 nm peak is that the incoming BPDT ligand would alter the electronic structure of Au$_{\sim250}$(*p*-MBA)$_n$ and thus introduce new transitions near 800 nm. This is highly unlikely as the 810 nm mode does not appear in the spectrum of the Au$_{\sim250}$MPC monomer or linked Au$_{102}$MPCs. Another BDP mode as the origin of 810 nm peak is also not plausible, because the larger spectral red-shift would require a shorter interparticle distance, which is not possible based on our MD simulations. All observations are in agreement with our proposed interpret-
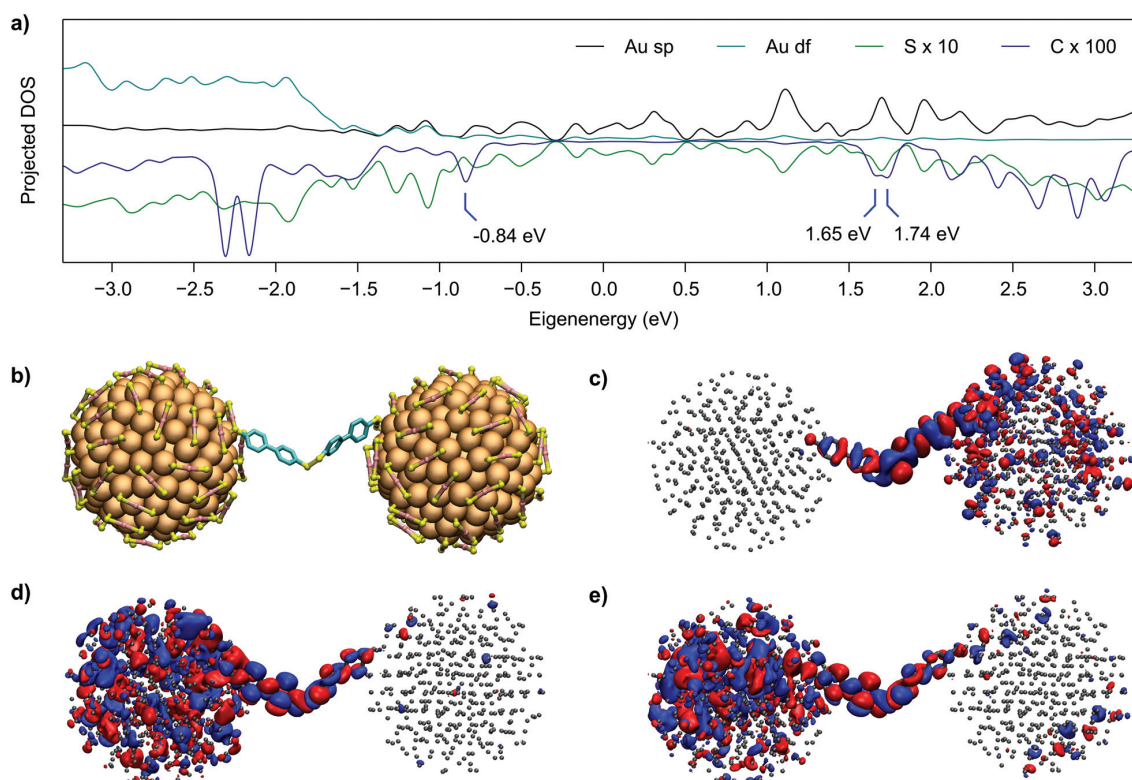
Fig. 9 (a) Projected density of states for Au$_{314}$(SH)$_{95}$−BPDT−BPDT−Au$_{314}$(SH)$_{95}$ calculated using DFT. Projection to sulfur (green) is scaled by 10 and projection to carbon (blue) is scaled by 100 with respect to projection to s/p (black) and d/f (cyan) orbitals of gold. (b) Geometry of the Au$_{314}$(SH)$_{95}$− BPDT−BPDT−Au$_{314}$(SH)$_{95}$ dimer used in the calculation. Hydrogens are omitted for clarity. Isosurfaces for orbitals corresponding eigenenergies of (c) −0.84 eV, (d) 1.65 eV, and (e) 1.74 eV with respect to the Fermi level.

ation that the 810 nm peak originates from a tCTP or similar mode, nevertheless, further theoretical and experimental studies are needed to uncover the details of the plasmonic coupling in the linked Au$_{\sim250}$MPC multimers.

Conclusions

We have achieved covalent linking between two gold nanoparticles which have a precisely known atomic structure, Au$_{102}$(*p*-MBA)$_{44}$. In our approach, a BPDT molecule replaces a *p*-MBA ligand molecule in a ligand exchange reaction and becomes a part of the protecting ligand layer. The covalent disulfide bridge between two BPDT ligands joins the ligand layers and metal cores of two clusters forming a single unit with a well-defined atomic structure comparable to a molecule. This is an important step towards the synthesis of atomically precise MPC superstructures. Our approach differs from the previous studies, where linking has been noncovalent or the atomic-level structure of the particle was unknown.

Moreover, we synthesized a larger, plasmonic monodisperse MPC, Au$_{\sim250}$(*p*-MBA)$_n$, and its multimers. Changes in the

UV-vis spectra of the Au$_{\sim250}$MPC multimer indicated two hybridized LSPR modes with much larger red-shifts than expected from the experiments of colloidal NPs. We assigned the first mode as the typical BDP mode in plasmonic NP aggregates. The second mode, however, is likely to originate from a tCTP, where tunneling happens through the molecular states of disulfide bridged BPDT molecules. Au$_{\sim250}$MPC multimers are the smallest systems reported which are essentially monodisperse, and show plasmonic coupling over a single covalently bound molecular bridge. Therefore, these systems are ideal candidates for connecting experimental observations to *ab initio* level theory in the field of nanoplasmonics.

Acknowledgements

spectrum of $Au_{102}(p\text{-MBA})_{44}$ in the University of Tokyo, during a visit (T.-R. T.) supported by the University of Jyväskylä. We acknowledge Drs A. Johansson, G. Groenhof, P. Papponen, and Ms E. Pohjolainen for technical help and Drs X. Chen, J. Koivisto, S. Malola, and K. Salorinne for fruitful discussions.

Notes and references

1 U. Kreibig and M. Vollmer, *Optical Properties of Metal Clusters*, Springer-Verlag, Berlin Heidelberg, 1995.

2 C. Bréchignac, P. Houdy and M. Lahmani, *Nanomaterials and Nanochemistry*, Springer-Verlag, Berlin, Heidelberg, 2010.

3 N. J. Halas, S. Lal, W. S. Chang, S. Link and P. Nordlander, *Chem. Rev.*, 2011, **111**, 3913–3961.

4 C. Sönnichsen, B. M. Reinhard, J. Liphardt and A. P. Alivisatos, *Nat. Biotechnol.*, 2005, **23**, 741–745.

5 B. M. Reinhard, M. Siu, H. Agarwal, A. P. Alivisatos and J. Liphardt, *Nano Lett.*, 2005, **5**, 2246–2252.

6 E. C. Le Ru and P. G. Etchegoin, *Annu. Rev. Phys. Chem.*, 2012, **63**, 65–87.

7 S. Yampolsky, D. A. Fishman, S. Dey, E. Hulkko, M. Banik, E. O. Potma and V. A. Apkarian, *Nat. Photonics*, 2014, **8**, 650–656.

8 M. Quinten, U. Kreibig, D. Schönauer and L. Genzel, *Surf. Sci.*, 1985, **156**, 741–750.

9 X. Wang, G. Li, T. Chen, M. Yang, Z. Zhang, T. Wu and H. Chen, *Nano Lett.*, 2008, **8**, 2643–2647.

10 S. L. Kleinman, B. Sharma, M. G. Blaber, A.-I. Henry, N. Valley, R. G. Freeman, M. J. Natan, G. C. Schatz and R. P. Van Duyne, *J. Am. Chem. Soc.*, 2013, **135**, 301–308.

11 A. Cunningham, S. Mühlig, C. Rockstuhl and T. Bürgi, *J. Phys. Chem. C*, 2011, **115**, 8955–8960.

12 C. L. Haynes and R. P. Van Duyne, *J. Phys. Chem. B*, 2001, **105**, 5599–5611.

13 S. J. Tan, M. J. Campolongo, D. Luo and W. Cheng, *Nat. Nanotechnol.*, 2011, **6**, 268–276.

14 G. A. DeVries, M. Brunnbauer, Y. Hu, A. M. Jackson, B. Long, B. T. Neltner, O. Uzun, B. H. Wunsch and F. Stellacci, *Science*, 2007, **315**, 358–361.

15 R. Sardar, T. Heap and J. S. Shumaker-Parry, *J. Am. Chem. Soc.*, 2007, **129**, 5356–5357.

16 H. Cha, J. H. Yoon and S. Yoon, *ACS Nano*, 2014, **8**, 8554–8563.

17 T. Peterle, P. Ringler and M. Mayor, *Adv. Funct. Mater.*, 2009, **19**, 3497–3506.

18 D.-H. Tsai, T. J. Cho, F. W. DelRio, J. M. Gorham, J. Zheng, J. Tan, M. R. Zachariah and V. A. Hackley, *Langmuir*, 2014, **30**, 3397–3405.

19 *Protected Metal Clusters: From Fundamentals to Applications*, ed. T. Tsukuda and H. Häkkinen, Elsevier, Amsterdam, 2015.

20 P. D. Jadzinsky, G. Calero, C. J. Ackerson, D. A. Bushnell and R. D. Kornberg, *Science*, 2007, **318**, 430–433.

21 M. Walter, J. Akola, O. Lopez-Acevedo, P. D. Jadzinsky, G. Calero, C. J. Ackerson, R. L. Whetten, H. Grönbeck and H. Häkkinen, *Proc. Natl. Acad. Sci. U. S. A.*, 2008, **105**, 9157–9162.

22 C. L. Heinecke, T. W. Ni, S. Malola, V. Mäkinen, O. A. Wong, H. Häkkinen and C. J. Ackerson, *J. Am. Chem. Soc.*, 2012, **134**, 13316–13322.

23 S. Knoppe, A. C. Dharmaratne, E. Schreiner, A. Dass and T. Bürgi, *J. Am. Chem. Soc.*, 2010, **132**, 16783–16789.

24 S. Mustalahti, P. Myllyperkiö, S. Malola, T. Lahtinen, K. Salorinne, J. Koivisto, H. Häkkinen and M. Pettersson, *ACS Nano*, 2015, **9**, 2328–2335.

25 E. Hulkko, O. Lopez-Acevedo, J. Koivisto, Y. Levi-Kalisman, R. D. Kornberg, M. Pettersson and H. Häkkinen, *J. Am. Chem. Soc.*, 2011, **133**, 3752–3755.

26 C. Yi, H. Zheng, L. M. Tvedte, C. J. Ackerson and K. L. J. Knappenberger Jr., *Phys. Chem. C*, 2015, **119**, 6307–6313.

27 Y. Negishi, T. Nakazaki, S. Malola, S. Takano, Y. Niihori, W. Kurashige, S. Yamazoe, T. Tsukuda and H. Häkkinen, *J. Am. Chem. Soc.*, 2015, **137**, 1206–1212.

28 V. Marjomäki, T. Lahtinen, M. Martikainen, J. Koivisto, S. Malola, K. Salorinne, M. Pettersson and H. H. Häkkinen, *Proc. Natl. Acad. Sci. U. S. A.*, 2014, **111**, 1277–1281.

29 W. S. Compel, O. A. Wong, X. Chen, C. Yi, R. Geiss, H. Häkkinen, K. L. Knappenberger Jr. and C. J. Ackerson, *ACS Nano*, 2015, **9**, 11690–11698.

30 K. Salorinne, T. Lahtinen, S. Malola, J. Koivisto and H. Häkkinen, *Nanoscale*, 2014, **6**, 7823–7826.

31 Y. Levi-Kalisman, P. D. Jadzinsky, N. Kalisman, H. Tsunoyama, T. Tsukuda, D. A. Bushnell and R. D. Kornberg, *J. Am. Chem. Soc.*, 2011, **133**, 2976–2982.

32 K. Salorinne, S. Malola, O. A. Wong, C. D. Rithner, X. Chen, C. J. Ackerson and H. Häkkinen, *Nat. Commun.*, 2016, **7**, 10401.

33 M. Azubel, J. Koivisto, S. Malola, D. Bushnell, G. L. Hura, A. H. Koh, H. Tsunoyama, T. Tsukuda, M. Pettersson, H. Häkkinen and R. D. Kornberg, *Science*, 2014, **345**, 909–912.

34 B. Hess, C. Kutzner, D. van der Spoel and E. Lindahl, *J. Chem. Theory Comput.*, 2008, **4**, 435–447.

35 E. Pohjolainen, X. Chen, S. Malola, G. Groenhof and H. Häkkinen, *J. Chem. Theory Comput.*, 2016, **12**, 1342–1350.

36 M. D. Case, T. A. Darden, T. E. Cheatham III, C. L. Simmerling, J. Wang, R. E. Duke, R. Luo, R. C. Walker, W. Zhang, K. M. Merz, B. Roberts, S. Hayik, A. Roitberg, G. Seabra, J. Swails, A. W. Götz, I. Kolossváry, K. F. Wong, F. Paesani, J. Vanicek, R. M. Wolf, J. Liu, X. Wu, S. R. Brozell, T. Steinbrecher, H. Gohlke, Q. Cai, X. Ye, J. Wang, M.-J. Hsieh, G. Cui, D. R. Roe, D. H. Mathews, M. G. Seetin, R. Salomon-Ferrer, C. Sagui, V. Babin, T. Luchko, S. Gusarov, A. Kovalenko and P. A. Kollman, *AMBER 12*, University of California, San Francisco, 2012.

37 M. Frisch, G. W. Trucks, H. B. Schlegel, G. E. Scuseria, M. A. Robb, J. R. Cheeseman, G. Scalmani, V. Barone, B. Mennucci, G. A. Petersson, H. Nakatsuji, M. Caricato,

X. Li, H. P. Hratchian, A. F. Izmaylov, J. Bloino, G. Zheng, J. L. Sonnenberg, M. Hada, M. Ehara, K. Toyota, R. Fukuda, J. Hasegawa, M. Ishida, T. Nakajima, Y. Honda, O. Kitao, H. Nakai, T. Vreven, J. A. Montgomery Jr., J. E. Peralta, F. Ogliaro, M. Bearpark, J. J. Heyd, E. Brothers, K. N. Kudin, V. N. Staroverov, R. Kobayashi, J. Normand, K. Raghavachari, A. Rendell, J. C. Burant, S. S. Iyengar, J. Tomasi, M. Cossi, N. Rega, J. M. Millam, M. Klene, J. E. Knox, J. B. Cross, V. Bakken, C. Adamo, J. Jaramillo, R. Gomperts, R. E. Stratmann, O. Yazyev, A. J. Austin, R. Cammi, C. Pomelli, J. W. Ochterski, R. L. Martin, K. Morokuma, V. G. Zakrzewski, G. A. Voth, P. Salvador, J. J. Dannenberg, S. Dapprich, A. D. Daniels, Ö. Farkas, J. B. Foresman, J. V. Ortiz, J. Cioslowski and D. J. Fox, *Gaussian 09, Revision D.01*, Gaussian Inc., Wallingford, CT, 2009.

38 C. I. Bayly, P. Cieplak, W. Cornell and P. A. Kollman, *J. Phys. Chem.*, 1993, **97**, 10269–10280.

39 J. Enkovaara, R. Rostgaard, J. J. Mortensen, J. Chen, M. Dulak, L. Ferrighi, J. Gavnholt, C. Glinsvad, V. Haikola, H. A. Hansen, H. H. Kristoffersen, M. Kuisma, A. H. Larsen, L. Lehtovaara, M. Ljungberg, O. Lopez-Acevedo, P. G. Moses, J. Ojanen, T. Olsen, V. Petzold, N. A. Romero, J. Stausholm, M. Strange, G. A. Tritsaris, M. Vanin, M. Walter, B. Hammer, H. Häkkinen, G. K. H. Madsen, R. M. Nieminen, J. K. Nørskov, M. Puska, T. T. Rantala, J. Schiøtz, K. S. Thygesen and K. W. Jacobsen, *J. Phys.: Condens. Matter*, 2010, **22**, 253202.

40 S. Malola, L. Lehtovaara, J. Enkovaara and H. Häkkinen, *ACS Nano*, 2013, **7**, 10263–10270.

41 G. Plascencia-Villa, B. Demeler, R. L. Whetten, W. P. Griffith, M. Alvarez, D. M. Black and M. Jose-Yacaman, *J. Phys. Chem. C*, 2016, **120**, 8950–8958.

42 L. M. Tvedte and C. J. Ackerson, *J. Phys. Chem. A*, 2014, **118**, 8124–8128.

43 P. K. Jain, W. Huang and M. A. El-Sayed, *Nano Lett.*, 2007, **7**, 2080–2088.

44 W. Zhu, R. Esteban, A. G. Borisov, J. J. Baumberg, P. Nordlander, H. J. Lezec, J. Aizpurua and K. B. Crozier, *Nat. Commun.*, 2016, **7**, 11495.

45 S. F. Tan, L. Wu, J. K. W. Yang, P. Bai, M. Bosman and C. A. Nijhuis, *Science*, 2014, **343**, 1496–1499.

46 N. Zabala, O. Pérez-González, P. Nordlander and J. Aizpurua, *Proc. SPIE*, 2011, **8096**, 80961L.

47 V. Kulkarni and A. Manjavacas, *ACS Photonics*, 2015, **2**, 987–992.

48 T. P. Rossi, A. Zugarramurdi, M. J. Puska and R. M. Nieminen, *Phys. Rev. Lett.*, 2015, **115**, 236804.

49 K. I. Savage, M. M. Hawkeye, R. Esteban, A. G. Borisov, J. Aizpurua and J. J. Baumberg, *Nature*, 2012, **491**, 574–577.

50 H. Jung, H. Cha, D. Lee and S. Yoon, *ACS Nano*, 2015, **9**, 12292–12300.

II

TOWARDS CONTROLLED SYNTHESIS OF WATER-SOLUBLE GOLD NANOCLUSTERS: SYNTHESIS AND ANALYSIS

by

Karolina Sokołowska, Sami Malola, Manu Lahtinen, Ville Saarnio, Perttu Permi, Katariina Koskinen, Matti Jalasvuori, Hannu Häkkinen, Lauri Lehtovaara, and Tanja Lahtinen 2019.

Towards Controlled Synthesis of Water-Soluble Gold Nanoclusters: Synthesis and Analysis

Karolina Sokołowska,[†] Sami Malola,[‡] Manu Lahtinen,[†] Ville Saarnio,[†] Perttu Permi,[†,§] Katariina Koskinen,[§] Matti Jalasvuori,[§] Hannu Häkkinen,[†,‡] Lauri Lehtovaara,[†] and Tanja Lahtinen*,[†]

[†]Department of Chemistry, Nanoscience Center, [‡]Department of Physics, Nanoscience Center, and [§]Department of Biological and Environmental Science, Nanoscience Center, University of Jyväskylä, P.O. Box 35, 40014 Jyväskylä, Finland

Ⓢ *Supporting Information*

ABSTRACT: Water-soluble gold nanoclusters with well-defined molecular structures and stability possess particular biophysical properties making them excellent candidates for biological applications as well as for fundamental spectroscopic studies. The currently existing synthetic protocols for atomically monodisperse thiolate-protected gold nanoclusters (AuMPCs) have been widely expanded with organothiolates, yet the direct synthesis reports for water-soluble AuMPCs are still deficient. Here, we demonstrate a wet-chemistry pH-controlled synthesis of two large water-soluble nanoclusters utilizing *p*-mercaptobenzoic acid (*p*MBA), affording different sizes of plasmonic AuMPCs on the preparative scale (∼7 mg). AuMPCs are essentially homogenous in size and are stable in solution and the solid state. Number of characterization methods were used to gain detailed information about the size, symmetry, molecular composition, and structure of these systems, i.e., high-resolution transmission electron microscopy, powder X-ray diffraction, NMR, UV−vis, thermogravimetry, and polyacrylamide gel electrophoresis. On the basis of the conducted experimental analyses and computationally aided predictions it can be evidenced that both clusters exhibit twinned face-centered cubic symmetry with the molecular composition of $Au_{210-230}(pMBA)_{70-80}$ and $Au_{426-442}(pMBA)_{112-115}$, referred from now on as Au250 and Au500, respectively. For future reference, toxicity of both gold clusters in various concentrations on cultures of Gram-positive and Gram-negative bacteria was investigated.
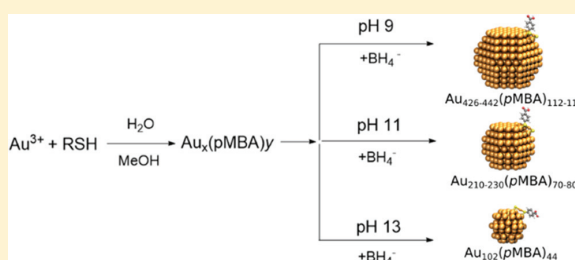
1. INTRODUCTION

The unique properties of gold nanoparticles have been studied extensively.[1−4] The size and shape of the particles define their electronic and physical properties, whereas tuning the nature of the protecting organic layer gives a control of the solubility and chemical functionality of the particles.[1] The versatile surface chemistry and size-dependent properties make them universal materials in high technology applications such as sensory probes, electronic conductors, therapeutic agents, drug delivery in biological and medical applications, and catalysis.[4−11]

Colloidal nanoparticles are not well suited for accurate studies of their chemistry. A typical nanoparticle synthesis produces a polydisperse sample of different sizes, shapes, and surface structures. Therefore, experiments that require atomic-level control are extremely difficult to carry out. In this regard, monolayer-protected gold clusters (AuMPCs) are small (usually <2 nm) nanoparticles with well-defined structures, consisting of a metallic core and a protecting ligand layer.[12−14] The structures range from small, more molecular-like species, with quantized electronic transitions, to larger, more nanoparticle-like clusters with hundreds of metal atoms, exhibiting localized surface plasmon resonance (SPR).[3,15,16] Contrary to colloidal gold nanoparticles, AuMPC synthesis produces a well-organized structure, with a specific number of atoms,

similar to a molecule that has enabled accurate studies of their chemistry, as well as the direct comparison of experimental and theoretical results.[17] Currently, many sizes of organosoluble nanoclusters are widely deployed;[18−23] however, the direct syntheses of larger (>200 gold atoms) water-soluble nanoclusters are still not yet fully understood.

Water-soluble gold nanoclusters were previously reported as universal labeling tools for bioimaging due to contrast properties, low toxicity, and high solubility. For example, $Au_{102}(pMBA)_{44}$ was described as a good tracking candidate for accurate site-specific covalent conjugation to the viral capsid surface where the covalently bound nanoclusters keep the viruses stable, allowing better visualization of their entry into complex endosomal structures.[4] The surface properties, particularly the solvent/organic interface of *p*-mercaptobenzoic acid (*p*MBA)-protected gold clusters, are altered depending on the protonation state of the cluster.[1] The clusters become water-soluble only when the carboxylic group of the *p*MBA-ligand is deprotonated, which is an important aspect for chemical modifications. Moreover, water-soluble clusters do

not require any toxic solvent treatment, which makes them a good candidate for green chemistry approaches, and widen the range of applicability to more polar solvents.

AuMPCs have a great response to light at the resonant wavelength.[23,24] The plasmonic and near-infrared (NIR) absorbance is well detectable in deep-tissue samples. We have previously studied covalently bound multimers of gold nanoclusters and discovered that the examined system displays coupled plasmonic modes in the NIR therapeutic spectral window (650−1350 nm) which could be potentially used for imaging biological samples.[25] Ability to covalently link AuMPCs through the conductive molecule opens up new prospects to study the fundamental physical properties of molecular electronic devices and internal motions of the particles and binding ligands.[26] Recently, Bürgi et al. reported the successful assembly of $Au_{25}(SBut)_{18}$ multimers via ligand exchange and studied electron transfer between clusters.[27] Developments of larger precise analogs of structures that can be modeled with the ab initio (density functional theory) level of theory could expand the knowledge of quantum plasmonics and emergence of bulk properties of metals.

Currently existing synthetic protocols for producing AuMPCs are most extensively carried out using organosoluble ligands, organothiolates, in particular phenylethane-thiol.[18−22,30] The synthesis generally produces a set of heterogeneous particles, requiring etching, size focusing, and/or other methods to narrow size distribution.[18,27−33] The key, to the characteristic stability and the atomically precise size control of those particles is the role of the protecting ligand layer. Covalently bound ligands govern the kinetic control and thermodynamic selection of the robust sizes in synthesis.[3] In contrast to the AuMPCs, the colloidal gold nanoparticles are typically protected by a weakly bound surfactant or even without any protecting ligand layer, significantly affecting their stability leading to extensive aggregation. For water-soluble gold nanoclusters, the synthetic control is obtained by the precise selection of reaction conditions, in a way that the single-sized product is favored.[34,35] To produce a large panel of uniform clusters of chosen sizes, the synthetic parameters of these direct synthesis methods need to be explored thoroughly.[36] Among several water-soluble thiols that can stabilize gold nanoclusters, mercaptobenzoic acid (MBA) has been actively used.[31−41] More specifically, syntheses have been developed for 3-MBA $(mMBA)$[37−40]- and 4-MBA $(pMBA)$[31−36,42]-protected clusters, e.g., $Au_{68}(mMBA)_{32}$, $Au_{144}(mMBA)_n$, and $Au_{144}(pMBA)_{60}$, $Au_{102}(pMBA)_{44}$ and $Au_{146}(pMBA)_{57}$. Among $pMBA$-stabilized particles, only $Au_{144}(pMBA)_{60}$ and $Au_{102}(pMBA)_{44}$ were synthesized without any size focusing methods, resulting in the direct synthesis protocol. In this work, we are focusing on $pMBA$-stabilized gold nanoclusters to study synthetic parameters of direct synthesis methods.

Precise characterization of individual gold nanoclusters with respect to their composition and structure has been made by various techniques.[38,40,41] However, despite significant development in structure determination techniques within past few years, atomic-level information of clusters bigger than 100 gold atoms is still a grand challenge to achieve, particularly for water-soluble clusters. Thereby, with the lack of information on structure−property relationship applicability of the clusters remains limited.

In this paper, through the systematic variation of reaction conditions, we synthesized stable, water-soluble $pMBA$-thiolate

gold nanoclusters. We found that controlling pH in different $MeOH/H_2O$ conditions produces different sizes of $pMBA$-clusters. To our knowledge, this is the first straightforward wet-chemistry synthesis to produce larger, water-soluble $pMBA$-protected gold nanoclusters in milligram scale. Experimental and theoretical evidence helped us to predict molecular composition of these larger $pMBA$-clusters to be $Au_{210−230}(pMBA)_{70−80}$ and $Au_{426−442}(pMBA)_{112−115}$ referred further on as Au250 (synthesis previously published by us)[25,42] and Au500, respectively. The synthesized clusters are stable in both solid and solution at room temperature for at least 6 months, as determined by polyacrylamide gel electrophoresis (PAGE) and UV−vis analysis. For future studies, the toxicity of both gold clusters was also studied. As a result, neither Au250 or Au500 caused significant decrease or elevation in the growth densities of *Bacillus thuringiensis* HER1410, *Escherichia coli* HB101, or *Klebsiella pneumoniae*.

2. MATERIALS AND EXPERIMENTAL METHODS

2.1. Materials. All reagents were commercial and used as received unless otherwise mentioned.

2.2. Synthesis and Separation. $pMBA$-thiol-protected AuMPCs were synthesized under pH-controlled conditions. Different solvent compositions were used to fine-tune the reduction kinetics of the MPC growth leading to the discrete cluster size (Figure 1). Smaller nanocluster Au250 was


Figure 1. PAGE bands of Au102, Au250, and Au500 nanoclusters.

synthesized at higher pH (around 11) with a mixed solvent of 26% MeOH (v/v) in water,[25] whereas larger nanocluster Au500 was synthesized at a slightly lower pH (around 9) with a solvent mixture of 24% MeOH in water.

In a typical synthesis, $HAuCl_4$ first reacts with excess $pMBA$-thiol in basic aqueous solution to form colorless Au(I)SR aggregated complexes. Then, $NaBH_4$ is added to reduce Au(I)SR into $Au_x(pMBA)_y$. The synthesis of smaller Au250 nanocluster produces one single size of AuMPCs. Detailed description of the syntheses and purification are given in the Supporting Information (SI).

Due to the lack of crystal structure, several characterization techniques were conducted to gain detailed information about the size, symmetry, molecular composition, and structure of these systems. The as-obtained products were analyzed using polyacrylamide gel electrophoresis (PAGE), thermogravimetric analysis (TGA), powder X-ray diffraction (PXRD), NMR

Scheme 1. Schematic Representation of Gold Nanocluster Synthesis
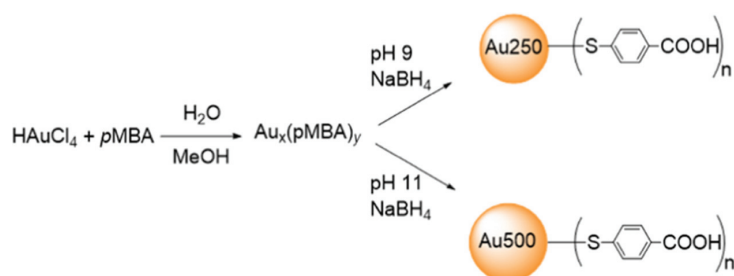
spectroscopy, high-resolution transmission electron microscopy (HR-TEM), UV−vis spectroscopy, and mass spectrometry. Unfortunately, all the attempts to measure ESI-mass spectrometry have not been successful, most likely due to large amounts of possible charge states of the protective *p*MBA-ligand layer as shown in Scheme 1.

2.3. Polyacrylamide Gel Electrophoresis (PAGE). PAGE was run on a 15% polyacrylamide gel (29:1 acrylamide/bisacrylamide) using 2× TBE run buffer in a Bio-Rad Mini-Protean Tetra System gel electrophoresis apparatus at 130 V.

2.4. Spectroscopy. *2.4.1. NMR.* ^{1}H NMR spectra were recorded on a Bruker Avance III HD 800 MHz spectrometer, equipped with a cryogenically cooled ^{1}H, ^{13}C, ^{15}N triple-resonance PFG Cryoprobe. All spectra were measured at 303 K.

2.4.2. UV−vis Spectroscopy. The spectra of AuMPCs were measured in dH$_2$O using quartz cuvettes and a PerkinElmer Lambda 850 UV/Vis-spectrometer with 2 nm resolution.

2.4.3. Thermogravimetric Analysis (TG). Thermal properties of Au nanoclusters were examined by a PerkinElmer Pyris 1 thermogravimetric analyzer. TG runs were carried out in an open platinum pan under an air atmosphere (flow rate of 60 mL/min) with a heating rate of 10 °C/min in the temperature range of 20−800 °C. Analyses were made twice for each cluster type. Temperature calibration of the analyzer was made by using Curie transition temperatures of Alumel, nickel, Perkalloy, and Fe standards. The weight balance was calibrated by measuring the standard weight of 50 mg at room temperature. The sample weights used in the measurements were about 1−3 mg.

2.4.4. Powder X-ray Diffraction (PXRD) Measurements. The powder X-ray diffraction data were measured by a PANalytical X'Pert PRO diffractometer in Bragg−Brentano geometry using Cu Ka1 radiation (Johannsson type monochromator; λ = 1.5406 Å) with 45 kV and 40 mA power settings. A sample was prepared on a reflection-free silicon-made plate with an aid of petrolatum jelly. Diffraction patterns were recorded from a spinning sample by an X'Celerator detector using a continuous scanning mode in a 2θ range of 2−140° with a step size of 0.017° and with the overall data recording time of ~45 h per pattern. Data processing was made with the PANalytical HighScore Plus version 4.7 program and phase identification data were retrieved from ICDD PD4+ database.[43] Theoretical powder diffraction curves were calculated as described in ref 44.

2.4.5. High-Resolution Transmission Electron Microscopy (HR-TEM). HR-TEM samples were prepared by drop-casting 8 μL of aqueous solution of clusters on a glow discharged 400 mesh lacey carbon copper grid. Solution was allowed to adsorb

for 15 min, after which the excess sample was removed and washed with water and MeOH. Grid was allowed to dry overnight. The samples were imaged with 0.2 nm point resolution using JEOL JEM-2200FS Cs-corrected HR-TEM operated at 200 kV.

Simulated HR-TEM images were created from a cluster model with the following algorithm. A unit vector with random orientation was sampled from uniform angular distribution. Each gold atom in the cluster model was replaced by a Gaussian density distribution with a variance of 1.4 Å and the density was projected onto the plane defined by the random unit vector. Finally, the resulting projected density was converted to a grayscale image.

2.5. Prediction of the Molecular Composition. Computationally aided predictions of the molecular composition were done in three ways. In the first approach, theoretically calculated TG percentages of the selected structurally known reference systems were correlated with the number of Au atoms and the ligands in the systems. In the second approach, the bare Au-cluster models of twinned face-centered cubic (fcc) symmetry were used to estimate the number of metal atoms in the core of the synthesized clusters. In the third approach, compositions were predicted by using linear dependence of the number of gold atoms in the cluster on the volume of the cluster and also by the linear dependence of the number of ligands on the surface area of the cluster. More detailed information is provided in the SI.

2.6. Bacteria/Toxicity Test. Bacterial biotoxicity of Au250 and Au500 was spectroscopically determined against three bacterial species, *B. thuringiensis* strain HER1410 (Gram-positive), common lab-strain *E. coli* K-12 HB101 (Gram-negative), and multidrug-resistant patient isolate *K. pneumoniae.* (Gram-negative). All strains were initially cultured in 5 mL of LB medium in +37 °C and shaken at 210 rpm overnight. Cultures for spectroscopic assay were prepared by adding aqueous solution of Au250 or Au500 in the final concentrations of 0.14, 1.4, 14, or 140 and 0.13, 1.3, 13, or 130 μg/mL, respectively, into 1:1000 diluted bacterial cultures. The absorbance of bacterial cultures was measured at +37 °C at 595 nm in 5 min intervals for 20 h to determine the bacterial growth and the maximum population densities. The absorption of Au250, Au500, and growth media was subtracted from the maximum population densities to measure the bacterial cell-induced absorption under different Au250 and Au500 exposures. Each measurement was conducted three times.

3. RESULTS AND DISCUSSION

3.1. Synthesis Products. Two parameters, pH and MeOH concentrations affected the outcome of the synthesis. Au nanoclusters were synthesized by pH control in different

Table 1. Synthesis Protocols of pMBA-Protected Gold Nanoclusters[a]

nanoclusters	polymerization				reduction		purification MeOH (%)
	pMBA	HAuCl₄	MeOH (%)	pH	MeOH (%)	NaBH₄	
Au102	3	1	47	13	47	1.1	60
Au250	6	1	28	11	26	1.8	pure product without fractional precipitation
Au500	6	1	25	9	25	1.8	25

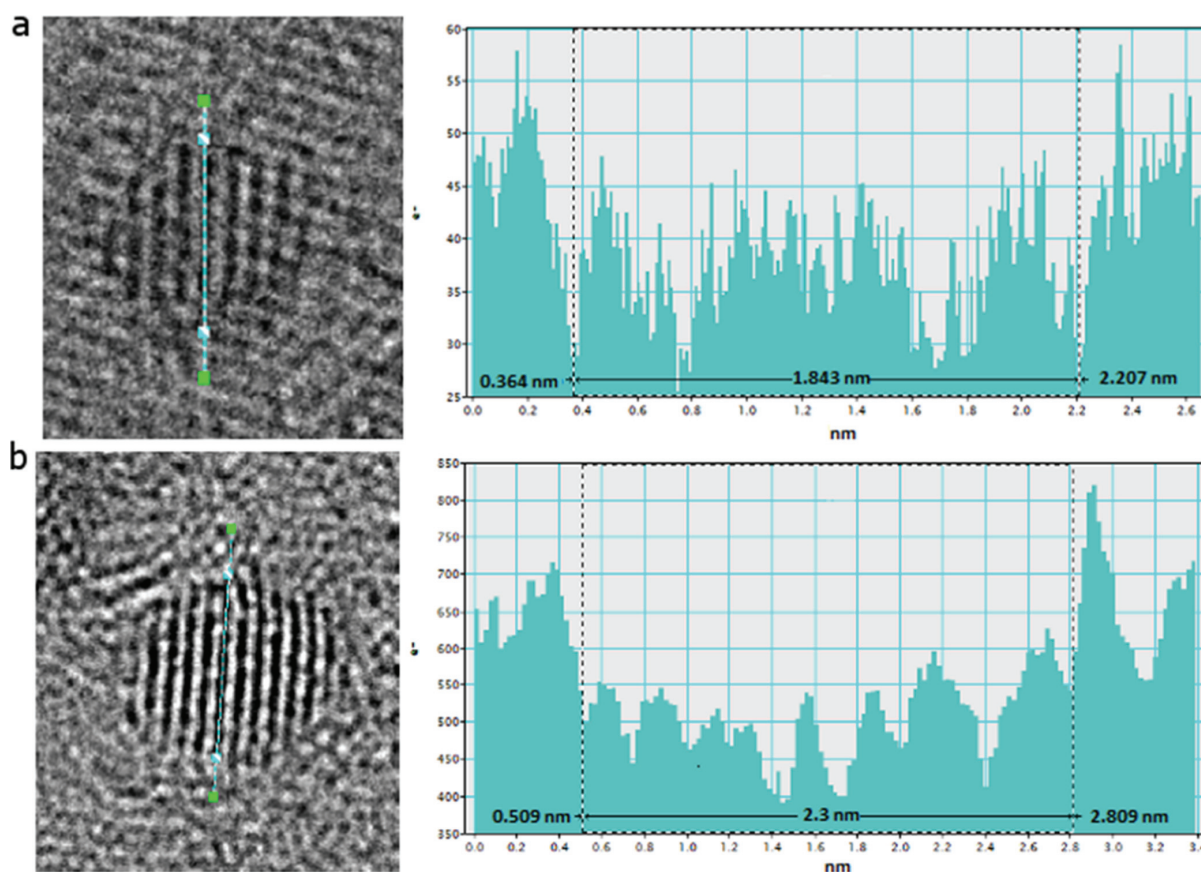[a]The values in columns 2nd, 3rd, and 7th correspond to the molar ratios

Figure 2. HR-TEM images of the assumed (a) Au250 and (b) Au500 pMBA-protected nanoclusters. Right panel corresponds to the histogram showing the upper size of the selected particle on the left panel.

MeOH compositions yielding two different discrete products of a stable water-soluble cluster protected by pMBA-thiol in milligram scale. These syntheses do not involve any additional size-focusing step and in the case of Au250, the synthesis produces only one discrete size of particle. Additionally, the $Au_{102}(pMBA)_{44}$ nanocluster was synthesized as a good reference point to compare synthetic trends, dispersity, and the size of the particles. The reference $Au_{102}(pMBA)_{44}$ nanocluster was synthesized following previously reported synthesis.[34] The polymerization step requires a relatively high pH of ~13 and conditions of 47% of MeOH. To enable facile comparison of the reaction conditions, we divided the reaction protocols into 3 stages to extract the information on direct synthesis conditions. The first stage involves the polymerization process, second stage involves reduction, and the last stage involves purification (Table 1).

To synthesize smaller Au250 nanoclusters, HAuCl₄ and pMBA-thiol were dissolved in methanol and mixed, leading to the formation of a white precipitate. The initial $Au_x(pMBA)_y$ polymerization step requires treatment at a pH of ~11 prior to reduction, nucleating the growth of the metal core. After reduction of Au(I)−pMBA precursors with NaBH₄, excess of methanol is added and the reaction is quenched producing one discrete size of particle.

Upon lowering the pH, a larger Au500 nanocluster was found. HAuCl₄ and pMBA-thiol were dissolved in 86% of methanol rapidly forming a white precipitate, which was dissolved at pH ~ 9. The final product still contains a polydisperse cluster mixture, similar to $Au_{102}(pMBA)_{44}$ synthesis, and requires fractional precipitation. The separation is done at 25% of methanol and centrifuged at 5000g for 15 min. Next, the supernatant is adjusted to 80% methanol and

centrifuged. The pellet from precipitation at 80% methanol is the final product.

The pH value of the *p*MBA-cluster effects its protonation state and surface properties. The solvent/organic interface of the protecting ligand can be easily altered becoming water-soluble when the carboxylic group of the *p*MBA-ligand is deprotonated and methanol-soluble when protonated. At the same time, by tuning the pH value during the polymerization step, the size of the cluster can be controlled. The larger Au500 cluster favors slightly lower but still alkaline pH 9 and low MeOH concentration of 25%, whereas Au250 was synthesized at pH 11 and the solvent mixture of 28% (v/v) MeOH in water.

When dissolved in water the new products display different colors (yellowish, brownish, reddish) indicating that they have different sizes. The syntheses of both sizes produced mg-quantities (~7 mg) of solid material. Each reaction product was analyzed using polyacrylamide gel electrophoresis (PAGE) and based on the initial size estimation they were assigned as Au250 and Au500, respectively.

Recently, Azubel and Kornberg reported that apart from the thiol-to-gold ratio, the size and uniformity of *m*MBA gold particles is highly dependent on the adjustment of pH.[37] In contrast to 4-MBA (*p*MBA), the *m*MBA ligand induces different properties for the Au nanocluster mainly due to the meta-position of the acidic group in the phenyl ring, thus resulting in a dissimilar ligand orientation and geometry.[39] Nevertheless, smaller *m*MBA clusters of 68 and 144 gold atoms were synthesized at pH 13.[37] In the case of 4-MBA clusters, $Au_{102}(pMBA)_{44}$ (Au102) is synthesized also at pH 13 and these larger ones Au250 and Au500 by lowering the pH from 11 to 9. The synthesis conditions for smaller water-soluble MBA-protected nanocluster seem to favor high pH conditions.

3.2. Characterization of AuMPCs. The size range information of the crude product was preliminarily acquired from their mobility in PAGE gel (Figure 2). The size information and the number of gold atoms per product were further examined with HR-TEM. The determined Au contents were further used for estimating number of ligands by thermogravimetry. With UV−vis spectroscopy, new insight into size-dependent evolution of surface plasmon resonance (Figure 3) was obtained. The powder X-ray diffraction (PXRD) technique was used to validate the structural features that were obtained by HR-TEM. Finally, based on all the gathered data about the size, symmetry, molecular composition, and structure of these clusters, computational prediction was developed for representing structural features of water-soluble *p*MBA-protected Au250 and Au500 nanoclusters.

3.2.1. PAGE. Dispersity and the size of the prepared AuMPCs were compared with the reference cluster $Au_{102}(pMBA)_{44}$ (Figures 1 and S1). The products formed by the wet-chemistry approach showed up as a single well-defined band in PAGE, indicating monodispersity of AuMPCs. The particles were initially analyzed by the determination of electrophoretic mobility. Both products had lower mobility than $Au_{102}(pMBA)_{44}$ in the same PAGE run indicating larger sized clusters. Using Au102 as a reference sample, retention factors (r_f) were determined to be 0.77 and 0.64 for Au250 and Au500, respectively. The product possesses stability in both solid and solution at room temperature for at least 6 months, as determined by PAGE and UV−vis analysis.

3.2.2. HR-TEM. Images of the AuMPCs were acquired by the Gatan software, which was also used to determine the diameter
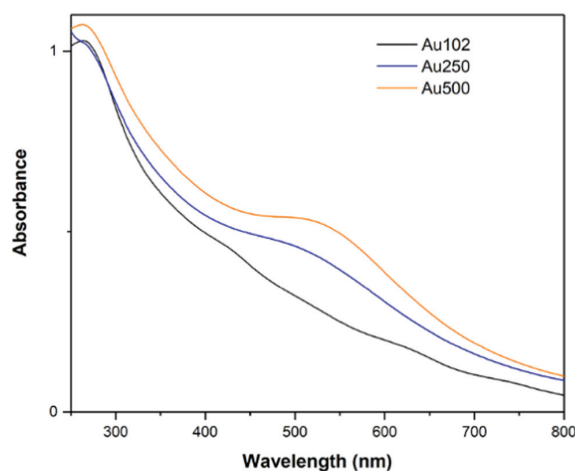
Figure 3. UV−vis spectra of Au102 (black), Au250 (blue), and Au500 (orange) clusters in dH₂O. A distinct absorption feature corresponding to a localized surface plasmon resonance is observed at 530 nm for the Au250 and Au500 nanoclusters.

of the selected particles (Figures 2 and S2−S4). The biggest challenge in HR-TEM measurements is its interpretation due to the number of interferences (and low signal-noise ratio when measuring at atomic resolution). Therefore, edge-to-edge particle size determination is often difficult. The diameters in Figure 2 correspond to the maximum limit of the size, in other words, the size with an error limit of 0.1 nm. We estimated the diameter of the smaller product to be 1.7 ± 0.1 nm, which fits to our previously reported size estimation[25] that was based on the Gaussian fit from low-resolution TEM images, yielding the diameter in the range of 1.6 ± 0.3 nm (Figure 2a). The metal core diameter of the larger product was determined to be 2.2±0.1 nm (Figures 2b and S4).

3.2.3. UV−vis. The optical spectra obtained from the two clusters were also compared to the reference spectrum of $Au_{102}(pMBA)_{44}$ (Figure 3). In contrast to $Au_{102}(pMBA)_{44}$, both clusters exhibited an absorption peak at 530 nm which is consistent with the surface plasmon resonance (SPR).[23] With an increase in the cluster size, the SPR features increases. The same properties were observed in the case of Au250 and Au500 clusters. As far as we know, the prepared particles are the biggest water-soluble nanoclusters synthesized by direct chemical approaches and demonstrating SPR. The spectrum of Au250 is compatible to the recently published spectra of 51,[33] 45,[23] and 53 kDa clusters,[23] with the estimated number of gold atoms at 250, 226, and 253, respectively. In case of Au500, the absorption spectrum is compatible with the reported spectra of 75[23] and 88 kDa clusters[33] with estimated gold atoms at 356 and 459.

3.2.4. ¹H NMR. ¹H spectra of Au250 and Au500 exhibit a typical broad signal for gold clusters between 5.2 and 9.2 ppm (Figure S5). Additionally, two sharp signals (doublets) can be seen at 7.60 and 7.79 ppm in both spectra, which fit to the free *p*MBA-ligand. However, the ¹H spectrum of Au500 shows an additional fine structure in comparison to Au250, which is relatively featureless. Without considering the free *p*MBA signals, the Au500 spectrum shows 14 doublet signals (7.92, 7.82, 7.70, 7.65, 7.34, 7.30, 7.14, 6.66, 6.62, 6.55, 6.51, 6.25, 6.19, and 5.79 ppm) and a singlet at 7.61 ppm. These peaks are characteristic for the Au500 nanocluster, but it is still not clear

whether they belong to the cluster structures. In different synthesis products, they appear at the same positions, but with varying intensities.

3.2.5. Thermogravimetric Analysis (TG). The weight loss of organic substance upon heating is commonly used to estimate the number of ligands in monolayer-protected gold clusters (the image of the Au residuals after a TG run, see Figure S6). Thermal stability and number of organosulfur ligands on the Au$_n$ nanoclusters (n = 102, 250, 500) were examined by thermogravimetric analysis (TG). In Figure 4, recorded TG
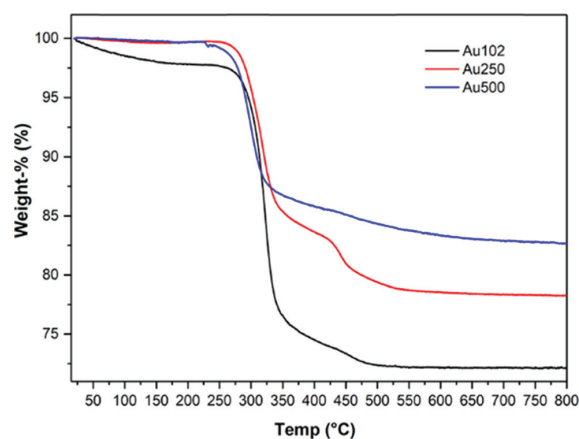

Figure 4. TG curves of Au102, Au250, and Au500 clusters measured with a heating rate of 10 °C/min under an air atmosphere.

curves show gentle descending weight loss (sample dependently 0.4−2 wt %) from 20 up to about 200 °C (Table 2) that is caused by the gradual evaporation of residual surface bound water. Thermal decomposition of all three Au-clusters initiate slowly above 220 °C followed by major weight loss from 270 to 500, 600, and 700 °C along with an increase in the size of the Au-cluster. The observed weight loss of the major steps corresponds to thermal decomposition processes and/or desorption of surface ligands (*p*MBA), and were determined to be 25.92, 21.32, and 19.60 wt % for Au102, Au250, and Au500 clusters, respectively (Table 2).

The number of surface ligands can be estimated via the observed residual weight of each TG run (74.08, 78.68, and 83.11% for Au102, Au250, and Au500, respectively) by calculating those as moles of Au. The number of gold atoms used here are based on computationally aided predictions explained in detail later in Section 3.2.6. The original molar mass of the Au$_x$(SR)$_y$ cluster can then be calculated based on the expected 1 to 1 stoichiometry between the gold containing residual and the original Au$_x$(SR)$_y$ cluster, from which the number of surface ligands (SR)$_y$ can then be evaluated by taking into account the molar mass of the (SR) ligand. Functionality of the method was confirmed by the reference

cluster Au102 for which 45 ± 1 surface ligands are determined by the analysis, agreeing well with the number of ligands (44) reported in the single crystal structure of the cluster by Jadzinsky et al.[45] Similarly, 73−80 and 111−116 surface ligands were determined for Au250 and Au500 clusters, respectively. The determined number of ligands also match remarkably well with those obtained by our computational predictions (see Section 3.2.6).

3.2.6. Toxicity on Bacteria. Neither Au250 nor Au500 caused significant decrease or elevation in the growth densities of *B. thuringiensis* HER1410, *E. coli* HB101, or *K. pneumoniae* in concentrations 0.14−14 μg/mL of Au250 or 0.13−13 μg/mL of Au500 (Figure 5). In higher concentrations (140 and 130
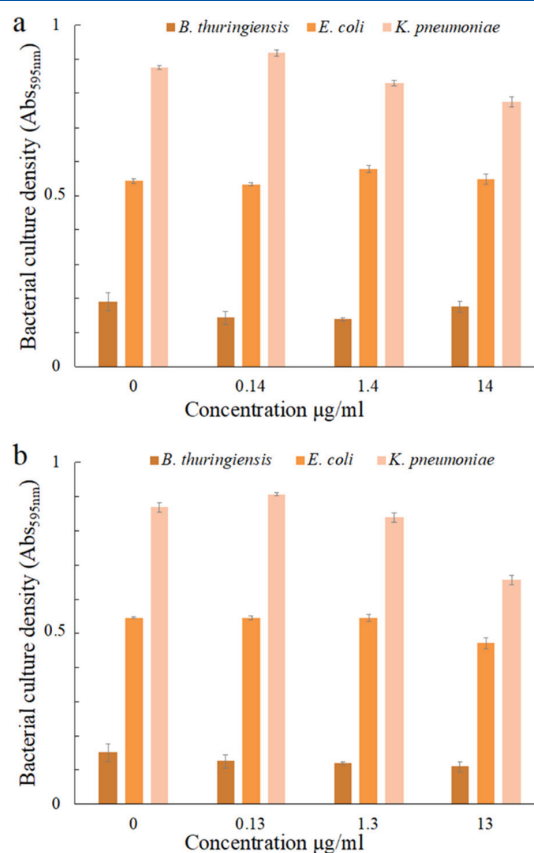

Figure 5. Spectroscopic biotoxicity assay of gold nanoclusters (a) Au250 and (b) Au500 on bacterial species *B. thuringiensis*, *E. coli*, and *K. pneumoniae*. Maximum absorption (595 nm) of bacterial cultures were measured in the presence of either Au250 or Au500 in different concentrations during 20 h of cultivation (N = 3). The slight decline of absorbance in the highest concentration was due to increasing background absorption. Error bars: standard deviation.

**Table 2. TG Results for Au102, Au250, and Au500 Nanoclusters**

sample name	1st weight loss[a] (%)	temp. (°C)	2nd weight loss[b] (%)	temp. (°C)	residual[c] (%)	no. of ligands	no. of Au atoms
Au102	2.13	24−214	25.92	214−800	74.08	45	102
Au250	0.37	24−190	21.32	190−800	78.68	73−80	210−230
Au500	0.40	24−192	16.90	192−800	83.11	111−116	426−442

[a]Residual water. [b]Ligand removal. [c]Residual weight corresponding to gold content.

μg/mL), the self-absorption of Au250 and Au500 obscured the optical density of the cultures, and thus the changes in bacterial growth could not be reliably observed. Nevertheless, based on the results, Au250 and Au500 do not seem to affect bacterial viability.

3.3. Exploring the Atomic Structure. Before predicting the molecular compositions of the clusters, we first present a short discussion on the structural patterns of water-soluble *p*MBA-protected cluster systems. We compare measured powder X-ray diffraction results of the synthesized clusters with the symmetries of selected, structurally known, thiolate-protected clusters. We also present a range for possible basis for the metal core structure of Au250 and Au500 nanoclusters based on experimental and theoretical data.

3.3.1. Powder X-ray Diffraction (PXRD) Analysis. Comparison of the experimental XRD patterns of Au250 and Au500 nanoclusters with the calculated reference systems of $Au_{146}(pMBA)_{57}$, $Au_{246}(SC_6H_4CH_3)_{80}$, and $Au_{279}(TBBT)_{84}$ is illustrated in Figure 6. The Au_{246} nanocluster displays the
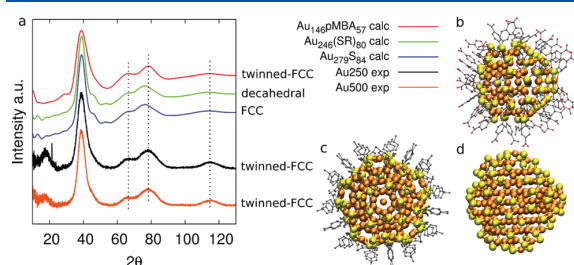

Figure 6. (a) Diffraction patterns of the nanoclusters. Comparison of the experimental patterns of Au250 (black line) and Au500 (orange line) with the calculated patterns of Au146, Au246, and Au279 clusters. The diffraction hump and very sharp peak at 20° 2θ in experimental patterns are caused by the sample holder and the adhesive used for attaching the samples to the holder. Structural models of (b) $Au_{146}(pMBA)_{57}$, (c) $Au_{246}(SR)_8$, and (d) $Au_{279}S_{84}$.

decahedral core and $Au_{146}(pMBA)_{57}$ represents the largest so far solved water-soluble cluster with the fcc-based twinned core.[41] The XRD patterns of both clusters show the strongest diffraction peak at ~40° 2θ, two relatively broad peaks at ~60−80° 2θ, and some minor peaks at ~45 and ~50° 2θ. With phase identification routine, the observed diffraction peaks are characteristic for gold phase crystallizing in the cubic face-centered crystal system and no additional unindexed peaks remain in the patterns (large hump 15−20° and very sharp

peak at 21.4° 2θ originates from a sample holder/adhesive substance).[43] The calculated XRD pattern of $Au_{146}(pMBA)_{57}$ is remarkably similar to the experimental data of Au250 and Au500 clusters. The diffraction peaks at 38.8, 66.2, and 75.7° in both experimental patterns have similar shape features and are located at the equal diffraction angles compared to that in the Au146 pattern. Instead, the simulated patterns of decahedral Au246 and fcc Au279 clusters show additional minor peaks at ~45 and ~50° 2θ that are not visible in the XRD patterns of Au500 and Au250 clusters. Moreover, the peak maximums of the main peaks in Au246 and Au279 are also somewhat shifted to lower 2θ angles and the shape properties of the peaks are subtly different. Described observations suggest that the metal core of both Au250 and Au500 nanoclusters most likely adopts the fcc symmetry, which is also twinned as indicated by the computational analyses represented in the following chapters.

3.3.2. Building Model for Twinned fcc Metal Core Structures of Au250 and Au500. On the basis of the obtained information from powder XRD analysis, we start evaluating possible basis for the metal core structure of Au250 and Au500 nanoclusters. Ranges of possible candidates with the same twinned fcc arrangement are shown in Figure 7. The size range of the clusters was estimated based on PAGE. Furthermore, the estimated diameters of the clusters from HR-TEM, 1.7 ± 0.1 nm for Au250 and 2.2 ± 0.1 nm for Au500 are in agreement with the modeled metal core of Au_{201} and Au_{405}, respectively. Therefore, we believe that they are possible candidates to start building a structural model of the synthesized clusters.

3.3.3. HR-TEM Image versus Twinned fcc Core. HR-TEM images represent further the symmetries of the AuMPCs. The simulated HR-TEM images of the Au_{201} metal core clearly support the imaging experiments of Au250 (Figure 8). The observation of the lattice fringes in Figure 8c clearly shows the effects that can be only seen in both, fcc and twinned fcc arrangements. The experimental Figure 8c shows 7−9 rows of atomic layer giving excellent estimation of structural information at atomic resolution. The uncertainty in image interpretation is often due to poor contrast and number of interferences. Therefore, we simulated images of the Au_{201} metal core and compared them with our experimental findings. In the simulated image, there are 7 rows of the atomic layer (Figure 8c). The simulated images contain only the metal core atoms and the question arises how protected is the gold core under electron beam. In other words, for analysis, it is important to know whether the Au−S layer protecting the gold
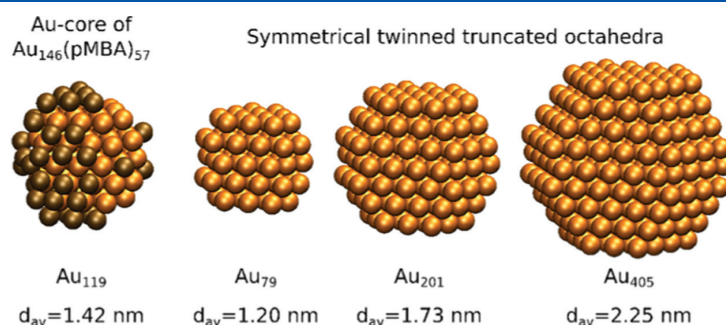
Figure 7. Range for possible basis for a metal core structure in twinned fcc octahedral arrangement. Orange color represents gold atoms and brown color represents the additional layer of atoms on top of symmetrical Au_{79} (left) representing together the Au-core of $Au_{146}(pMBA)_{57}$.
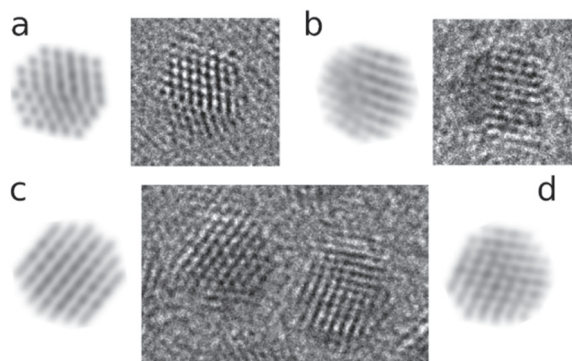
Figure 8. Comparison of HR-TEM images of Au250 and simulated images of the Au201 metal core from different directions.

core is visible in the HR-TEM images. Simulated HR-TEM images and experimental equivalents (Figure 8a,b,d) show the effects that are reproducible only with the stacking fault defect for fcc symmetry. Nevertheless, the symmetry found from powder XRD and HR-TEM are the same, which indicates that the core structure will remain the same under electron beam.

3.4. Predicting Molecular Composition. There is enough complementary experimental information for attempting the determination of the molecular composition of the investigated clusters. Herein, we provide computationally aided predictions for the molecular compositions by reflecting the measured results of the synthesized clusters to the properties of selected, structurally known, thiolate-protected clusters of a similar size. Selected known reference systems include clusters with a close to spherical shape such as $Au_{102}(pMBA)_{44}$, $Au_{146}(pMBA)_{57}$, $Au_{246}(SC_6H_4CH_3)_{80}$, and $Au_{271}(TBBT)_{84}$, matching the overall shape of the synthesized $pMBA$-protected particles. The clusters are selected from the size ranging from 100−300, including the two known $pMBA$-clusters. Due to the absence of experimentally resolved structures of larger size water-soluble clusters, we included two of the largest thiolate-protected clusters, despite them being protected with different types of aromatic ligands.

By assuming the $pMBA$-ligand for the selected known cluster compositions, trends of theoretical TG weight loss percentages can be predicted with respect to the number of Au atoms and the number of ligands as shown in Figure 9. Behavior shown in the figure is quite monotonous and by assuming that the behavior is valid also for the synthesized clusters, the composition $Au_{210}(pMBA)_{72}$ can be predicted for the smaller cluster. It is noteworthy that this composition would match perfectly with the magic electron shell closing of spherical clusters at 138 e, by assuming that gold provides 210 Au(6s)-based free electrons to the system and the Au-$pMBA$ bonding withdraws 72 electrons out from the system.[46]

The second method for size estimation is based on the diameters of the clusters determined from the HR-TEM images, the probable sizes of the metal core of the clusters can be estimated computationally. Figure 10 shows the number of metal atoms as a function of diameter as calculated for the bare metal clusters of twinned fcc symmetry. Model clusters were generated as described in the Materials and Experimental Methods Section. Using the experimentally measured diameters, the two synthesized clusters have approximately 187 ± 30 and 385 ± 50 Au atoms in their metal cores based on the correlation shown in Figure 10. The number of metal atoms in
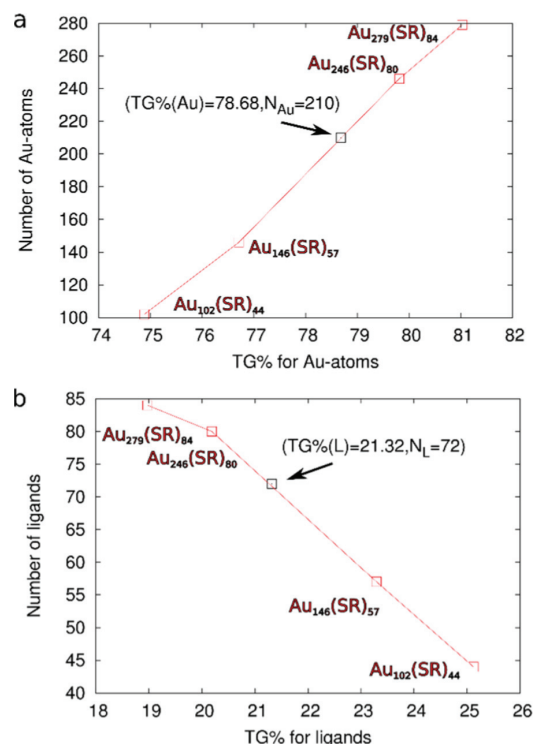

Figure 9. (a) Number of Au atoms in the thiolated clusters as a function of theoretically calculated thermogravimetric (TG) weight loss percentages of Au content. (b) Number of ligands in the thiolated clusters as a function of theoretically calculated ligand TG percentages. Both are drawn using the $pMBA$-ligand.

the Au−S interface varies from 23 to 40 in the case of the selected four known reference clusters. Assuming further that 30−40 Au atoms would participate in protecting units, the smaller synthesized particle would have approximately 220−230 Au atoms in total, depending on the actual Au−S interface conformation. Furthermore, we can estimate that at least 40 Au atoms should be contributing to the Au−S interface of the larger synthesized cluster increasing the size to >425 Au atoms in total.

Third, we did linear fitting on the properties of the selected known clusters. We correlated the diameter of the cluster including the metal core and the Au−S interface to the number of gold atoms in the cluster as shown in Figure 11a. We also correlated the number of ligands in the cluster to the spherical surface area as shown in Figure 11b. The two linear correlations can be used to predict the molecular composition by relying on experimentally measured diameters or on the estimated total number of gold atoms in the synthesized clusters.

For the smaller Au250 cluster, the size ranging from 210−230 Au atoms was already estimated to be realistic. Fixing the number of gold atoms to 210 gives a prediction of 2.1 nm diameter for the cluster (including the metal core and the Au−S interface) and further 71 ligands for the protecting layer. Both are in agreement with the experimentally measured results. For example, the 1.7 nm diameter of the metal core should be increased at maximum twice the Au−S bond (0.235 nm) when adding the metal−ligand interface. With the same
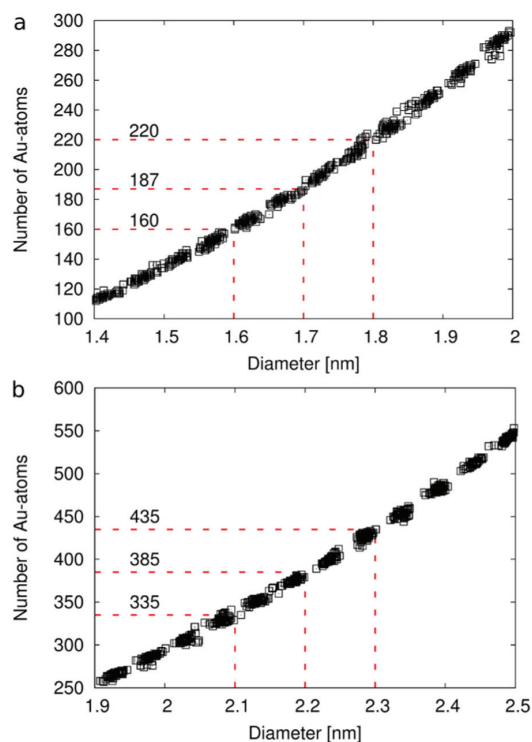
Figure 10. Number of Au atoms of the spherical bare twinned fcc Au-clusters in the size range relevant for the investigated *p*MBA-clusters in (a) and (b). The plausible sizes 187 and 385 of the metal core for the measured diameters are labeled in the figure. On the basis of the 0.1 nm error limits the minimum and maximum values are also given.

Figure 11. (a) Linear fitting done by correlating the number of Au atoms in the cluster to the diameter of the cluster taking into account the metal core and Au−S interface atoms and (b) by correlating the corresponding spherical surface area to the number of ligands. Fitted parameters: (a) $a = 0.328$ nm, $b = 0.129$ nm and (b) $a = 5.40$ nm^{-2}, $b = -2.02$. Diameters of the clusters are determined including the Au-core and the Au−S interface as described in the Materials and Experimental Methods Section.

procedure, the upper size limit for the number of gold atoms at 230 gives a prediction of 2.1 nm diameter and 75 ligands, for which the closest composition matching the measured TG percentages would be $Au_{230}(pMBA)_{80}$.

For the larger Au500 cluster, prediction of the molecular composition can be also made although the reliability is not equally good due to the lack of reference structures. For the larger cluster, we take the measured diameter 2.2 nm of the core and add to it approximately 0.4 nm from the metal−ligand interface. For the 2.6 nm spherical particle, correlations predict that the total number of Au atoms should be 429 and the number of ligands should be 113. Molecular composition would be $Au_{429}(SR)_{113}$, which has a very good match with the measured TG weight loss percentages. All the nearby compositions within 0.1 TG-percentage units from the measured results are included in compositions $Au_{426-442}(pMBA)_{112-115}$. The prediction of 426−442 gold atoms in total is reasonable compared to the estimated core size of 385 Au atoms, which would mean that 40−60 Au atoms were included in the protecting units. The number of single bridged ligands, not resembling a conformation of any protecting unit, increases in the Au−S interface as the cluster size increases. This can be realized by analyzing the structures of the known reference clusters $Au_{102}(SR)_{44}$, $Au_{146}(SR)_{57}$, $Au_{246}(SR)_{80}$, and $Au_{279}(SR)_{84}$. Their Au−S interfaces include respectively 0% (0/44), 12.3% (7/57), 12.5% (10/80), and 21.4% (18/84) of bridged ligands. At the same time the relative number of Au atoms in the Au−S interface decreases as the cluster size increases, at least within the represented size range.

As a summary, the best computationally aided predictions for the molecular compositions are $Au_{210-230}(pMBA)_{70-80}$ for the smaller cluster and $Au_{426-442}(pMBA)_{112-115}$ for the larger cluster.

4. CONCLUSIONS

In this work, we synthesized, in milligram scale, stable sizes of water-soluble *p*MBA-protected gold nanoclusters by controlling the pH in different MeOH/H$_2$O conditions. The products were carefully analyzed by various analytical techniques and characterized for approximate mass and structural composition. So far, water-soluble clusters have been observed in decahedral $(Au_{102}(pMBA)_{44})$,[45] fcc-like $(Au_{68}(mMBA)_{32}$ and $Au_{144}(mMBA)_n)$[38] and twinned fcc $(Au_{146}(pMBA)_{57})$ symmetries.[41] The results in this paper indicate that twinned fcc symmetry is favored in larger *p*MBA-protected clusters as shown in the case of Au250 and Au500. Combining all the experimental information and computational analysis, we came to the final prediction of the molecular composition of the synthesized clusters, namely $Au_{210-230}(pMBA)_{70-80}$ and $Au_{426-442}(pMBA)_{112-115}$. The structural knowledge of these clusters is crucial when applying these to biological studies. There is still a lack of well-defined, water-soluble particles, which could serve as universal labeling tools for bioimaging. Attaching gold nanoclusters to the biological systems will allow

the investigation of viruses, including their entry mechanism into cells. The development of cluster-based sensors by chemically modifying the ligand layer of the water-soluble gold nanoclusters is one of the possibilities to achieve controllable application in biosciences and to study, for example, the nature of viral genome release in cells (during infection). In addition, in the field of spectroscopy in physical chemistry, the plasmonic nanoclusters are important model systems to study the emergence of bulk properties in metal, and using them as building blocks could deepen the understanding of energy transfer processes, which are of interest in molecular electronics.

This work introduces some overall trends in synthetic methods and structural compositions for two larger water-soluble AuMPCs. These play a crucial role in understanding the relation of their diverse properties and increase the usability of gold nanoclusters.

■ ASSOCIATED CONTENT

ⓢ Supporting Information

The Supporting Information is available free of charge on the ACS Publications website at DOI: 10.1021/acs.jpcc.8b11056.

> Detailed experimental procedures and methods for the prediction of molecular composition; PAGE gel showing a fractional precipitation procedure; TEM images taken from Au250 and Au500 nanoclusters; full spectrum of ^{1}H NMR of Au250 and Au500 nanoclusters; image of the residue after TG run (PDF)

■ AUTHOR INFORMATION

Corresponding Author

*E-mail: tanja.m.lahtinen@jyu.fi. Phone: +358 40805 3697.

ORCID ◉

Manu Lahtinen: 0000-0001-5561-3259
Hannu Häkkinen: 0000-0002-8558-5436
Tanja Lahtinen: 0000-0002-1747-6959

Notes

The authors declare no competing financial interest.

■ REFERENCES

(1) Salorinne, K.; Lahtinen, T.; Malola, S.; Koivistoa, J.; Häkkinen, H. Solvation Chemistry of Water-Soluble Thiol Protected Gold Nanocluster Au102 from DOSY NMR Spectroscopy and DFT Calculations. *Nanoscale* **2014**, *6*, 7823−7826.

(2) Plascencia-Villa, G.; Demeler, B.; Whetten, R. L.; Griffith, W. P.; Alvarez, M.; Black, D. M.; José-Yacamán, M. Analytical Characterization of Size-Dependent Properties of Larger Aqueous Gold Nanoclusters. *J. Phys. Chem. C* **2016**, *120*, 8950−8958.

(3) Jin, R. Atomically precise metal nanoclusters: stable sizes and optical properties. *Nanoscale* **2015**, *7*, 1549−1565.

(4) Marjomäki, V.; Lahtinen, T.; Martikainen, M.; Koivisto, J.; Malola, S.; Salorinne, K.; Pettersson, M.; Häkkinen, H. *Proc. Natl. Acad. Sci. U.S.A.* **2014**, *111*, 1277−1281.

(5) Homberger, M.; Simon, U. On the Application Potential of Gold Nanoparticles in Nanoelectronics and Biomedicine. *Philos. Trans. R. Soc., A* **2010**, *368*, 1405−1453.

(6) Nie, S.; Emory, S. R. Probing Single Molecules and Single Nanoparticles by Surface- Enhanced Raman Scattering. *Science* **1997**, *275*, 1102−1106.

(7) Brongersma, M. L.; Halas, N. J.; Nordlander, P. Plasmon-Induced Hot Carrier Science and Technology. *Nat. Nanotechnol.* **2015**, *10*, 25−34.

(8) Tapio, K.; Leppiniemi, J.; Shen, B.; Hytönen, V. P.; Fritzsche, W.; Toppari, J. J. Toward Single Electron Nanoelectronics Using Self-Assembled DNA Structure. *Nano Lett.* **2016**, *16*, 6780−6786.

(9) Martikainen, M.; Salorinne, K.; Lahtinen, T.; Malola, S.; Permi, P.; Häkkinen, H.; Marjomäki, V. Hydrophobic pocket targeting probes for enteroviruses. *Nanoscale* **2015**, *7*, 17457−17467.

(10) Stark, M. C.; Baikoghli, M. A.; Lahtinen, T.; Malola, S.; Xing, L.; Nguyen, M.; Nguyen, M.; Sikaroudi, A.; Marjomäki, V.; Häkkinen, H.; et al. Structural Characterization of Site-Modifed Nanocapsid with Monodispersed Gold Clusters. *Sci. Rep.* **2017**, *7*, No. 17048.

(11) Calard, F.; Wani, I. H.; Hayat, A.; Jarrosson, T.; Lère-Porte, J.-P.; Jafri, S. H. M.; Serein-Spirau, F.; Leifer, K.; Orthaber, A. Designing Sterically Demanding Thiolate Coated AuNPs for Electrical Characterization of BPDT in a NP−Molecule−Nanoelectrode Platform. *Mol. Syst. Des. Eng.* **2017**, *2*, 133−139.

(12) Häkkinen, H. The Gold-Sulfur Interface at the Nanoscale. *Nat. Chem.* **2012**, *4*, 443−455.

(13) Jin, R.; Zeng, C.; Zhou, M.; Chen, Y. Atomically Precise Colloidal Metal Nanoclusters and Nanoparticles: Fundamentals and Opportunities. *Chem. Rev.* **2016**, *116*, 10346−10413.

(14) Chakraborty, I.; Pradeep, T. Atomically Precise Clusters of Noble Metals: Emerging Link between Atoms and Nanoparticles. *Chem. Rev.* **2017**, *117*, 8208−8271.

(15) Sakthivel, N. A.; Theivendran, S.; Ganeshraj, V.; Oliver, A. G.; Dass, A. Crystal Structure of Faradaurate-279: $Au_{279}(SPh-tBu)_{84}$ Plasmonic Nanocrystal Molecules. *J. Am. Chem. Soc.* **2017**, *139*, 15450−15459.

(16) Kumara, C.; Zuo, X.; Ilavsky, J.; Chapman, K.-W.; Cullen, D.-A.; Dass, A. Super-Stable Highly Monodisperse Plasmonic Faradaurate-500 Nanocrystals with 500 Gold Atoms: $Au_{\sim500}(SR)_{\sim120}$. *J. Am. Chem. Soc.* **2014**, *136*, 7410−7417.

(17) Jin, R.; Qian, H.; Wu, Z.; Zhu, Y.; Zhu, M.; Mohanty, A.; Garg, N. Size Focusing: A Methodology for Synthesizing Atomically Precise Gold Nanoclusters. *J. Phys. Chem. Lett.* **2010**, *1*, 2903−2910.

(18) Qian, H.; Zhu, Y.; Jin, R. Size-Focusing Synthesis, Optical and Electrochemical Properties of Monodisperse $Au_{38}(SC_2H_4Ph)_{24}$ Nanoclusters. *ACS Nano* **2009**, *3*, 3795−3803.

(19) Qian, H.; Zhu, Y.; Jin, R. Atomically Precise Gold Nanocrystal Molecules with Surface Plasmon Resonance. *Proc. Natl. Acad. Sci. U.S.A.* **2012**, *109*, 696−700.

(20) Qian, H.; Jin, R. Ambient Synthesis of $Au_{144}(SR)_{60}$ Nanoclusters in Methanol. *Chem. Mater.* **2011**, *23*, 2209−2217.

(21) Schaaff, T.; Whetten, R. Controlled Etching of Au:SR Cluster Compounds. *J. Phys. Chem. B* **1999**, *103*, 9394−9396.

(22) Dharmaratne, A. C.; Krick, T.; Dass, A. Nanocluster Size Evolution Studied by Mass Spectrometry in Room Temperature $Au_{25}(SR)_{18}$ Synthesis. *J. Am. Chem. Soc.* **2009**, *131*, 13604−13605.

(23) Negishi, Y.; Nakazaki, T.; Malola, S.; Takano, S.; Niihori, Y.; Kurashige, W.; Yamazoe, S.; Tsukuda, T.; Häkkinen, H. A Critical Size for Emergence of Nonbulk Electronic and Geometric Structures in Dodecanethiolate-Protected Au Clusters. *J. Am. Chem. Soc.* **2015**, *137*, 1206−1212.

(24) Yi, C.; Zheng, H.; Tvedte, L. M.; Ackerson, C. J.; Knappenberger, K. L. J. Nanometals: Identifying the Onset of Metallic Relaxation Dynamics in Monolayer-Protected Gold Clusters Using Femtosecond Spectroscopy. *J. Phys. Chem. C* **2015**, *119*, 6307−6313.

(25) Lahtinen, T.; Hulkko, E.; Sokołowska, K.; Tero, T.-R.; Saarnio, V.; Lindgren, J.; Pettersson, M.; Häkkinen, H.; Lehtovaara, L.

Covalently Linked Multimers of Gold Nanoclusters $Au_{102}(pMBA)_{44}$ and Au $\sim_{250}$ $(pMBA)_n$. *Nanoscale* **2016**, *8*, 18665−18674.

(26) Yampolsky, S.; Fishman, D. A.; Dey, S.; Hulkko, E.; Banik, M.; Potma, E. O.; Apkarian, V. A. Seeing a Single Molecule Vibrate Through Time-Resolved Coherent Anti-Stokes Raman Scattering. *Nat. Photonics* **2014**, *8*, 650−656.

(27) Sels, A.; Salassa, G.; Cousin, F.; Lee, L.-T.; Bürgi, T. Covalently Bonded Multimers of $Au_{25}(SBut)_{18}$ as a Conjugated System. *Nanoscale* **2018**, *10*, 12754−12762.

(28) Schaaff, T.; Knight, G.; Shafigullin, M.; Borkman, R.; Whetten, R. Isolation and Selected Properties of a 10.4 kDa Gold:Glutathione Cluster Compound. *J. Phys. Chem. B* **1998**, *102*, 10643−10646.

(29) Schaaff, T.; Whetten, R. Controlled Etching of Au:SR Cluster Compounds. *J. Phys. Chem. B* **1999**, *103*, 9394−9396.

(30) Dass, A. Faradaurate Nanomolecules: A Superstable Plasmonic 76.3 kDa Cluster. *J. Am. Chem. Soc.* **2011**, *133*, 19259−19261.

(31) Alvarez, M. M.; Chen, J.; Plascencia-Villa, G.; Black, D. M.; Griffith, W. P.; Garzon, I. L.; Jose-Yacaman, M.; Demeler, B.; Whetten, R. L. Hidden Components in Aqueous "Gold-144" Fractionated by PAGE: High-Resolution Orbitrap ESI-MS Identifies the Gold-102 and Higher All-Aromatic Au-pMBA Cluster Compounds. *J. Phys. Chem. B* **2016**, *120*, 6430−6438.

(32) Plascencia-Villa, G.; Demeler, B.; Whetten, R. L.; Griffith, W. P.; Alvarez, M.; Black, D. M.; Jose-Yacaman, M. Analytical Characterization of Size-Dependent Properties of Larger Aqueous Gold Nanoclusters. *J. Phys. Chem. C* **2016**, *120*, 8950−8958.

(33) Tvedte, L. M.; Ackerson, C. J. Size-Focusing Synthesis of Gold Nanoclusters with *p*-Mercaptobenzoic Acid. *J. Phys. Chem. A* **2014**, *118*, 8124−8128.

(34) Levi-Kalisman, Y.; Jadzinsky, P. D.; Kalisman, N.; Tsunoyama, H.; Tsukuda, T.; Bushnell, D. A.; Kornberg, R. D. Synthesis and Characterization of $Au_{102}(pMBA)_{44}$ Nanoparticles. *J. Am. Chem. Soc.* **2011**, *133*, 2976−2982.

(35) Ackerson, C. J.; Jadzinsky, P. D.; Sexton, J. Z.; Bushnell, D. A.; Kornberg, R. D. Synthesis and Bioconjugation of 2 and 3 nm-Diameter Gold Nanoparticles. *Bioconjugate Chem.* **2010**, *21*, 214−218.

(36) Wong, O. A.; Compel, W. S.; Ackerson, C. J. Combinatorial Discovery of Cosolvent Systems for Production of Narrow Dispersion Thiolate-Protected Gold Nanoparticles. *ACS Comb. Sci* **2015**, *17*, 11−18.

(37) Azubel, M.; Kornberg, R. D. Synthesis of Water-Soluble, Thiolate-Protected Gold Nanoparticles Uniform in Size. *Nano Lett.* **2016**, *16*, 3348−3351.

(38) Azubel, M.; Koivisto, J.; Malola, S.; Bushnell, D.; Hura, G. L.; Koh, A.-L.; Tsunoyama, H.; Tsukuda, T.; Pettersson, M.; Häkkinen, H.; et al. Electron Microscopy of Gold Nanoparticles at Atomic Resolution. *Science* **2014**, *345*, 909−912.

(39) Tero, T.-R.; Malola, S.; Koncz, B.; Pohjolainen, E.; Lautala, S.; Mustalahti, S.; Permi, P.; Groenhof, G.; Pettersson, M.; Häkkinen, H. Dynamic Stabilization of the Ligand−Metal Interface in Atomically Precise Gold Nanoclusters Au_{68} and Au_{144} Protected by *meta*-Mercaptobenzoic Acid. *ACS Nano* **2017**, *11*, 11872−11879.

(40) Azubel, M.; Koh, A.-L.; Koyasu, K.; Tsukuda, T.; Kornberg, R.-D. Structure Determination of a Water-Soluble 144-Gold Atom Particle at Atomic Resolution by Aberration-Corrected Electron Microscopy. *ACS Nano* **2017**, *11*, 11866−11871.

(41) Vergara, S.; Lukes, D. A.; Martynowycz, M. W.; Santiago, U.; Plascencia-Villa, G.; Weiss, S. C.; Cruz, M. J.; Black, D. M.; Alvarez, M. M.; López-Lozano, X.; et al. MicroED Structure of $Au_{146}(pMBA)_{57}$ at Subatomic Resolution Reveals a Twinned fcc Cluster. *J. Phys. Chem. Lett.* **2017**, *8*, 5523−5530.

(42) Sokolowska, K.; Hulkko, E.; Lehtovaara, L.; Lahtinen, T. Dithiol-Induced Oligomerization of Thiol-Protected Gold Nanoclusters. *J. Phys. Chem. C* **2018**, *122*, 12524−12533.

(43) International Centre for Diffraction Data, ICDD-PDF4+. http://www.icdd.com/ (accessed Dec 10, 2018).

(44) Lopez-Acevedo, O.; Akola, J.; Whetten, R. L.; Grönbeck, H.; Häkkinen, H. Structure and Bonding in the Ubiquitous Icosahedral Metallic Gold Cluster $Au_{144}(SR)_{60}$. *J. Phys. Chem. C* **2009**, *113*, 5035−5038.

(45) Jadzinsky, P. D.; Calero, G.; Ackerson, C. J.; Bushnell, D. A.; Kornberg, R. D. Structure of a Thiol Monolayer-Protected Gold Nanoparticle at 1.1 Å Resolution. *Science* **2007**, *318*, 430−433.

(46) Walter, M.; Akola, J.; Lopez-Acevedo, O.; Jadzinsky, P.-D.; Calero, G.; Ackerson, C.-J.; Whetten, R.-L.; Grönbeck, H.; Häkkinen, H. A Unified View of Ligand-Protected Gold Clusters as Superatom Complexes. *Proc. Natl. Acad. Sci. U.S.A.* **2008**, *105*, 9157−9162.

III

DEVELOPMENT OF FUNCTIONALIZED SYBR GREEN II RELATED CYANINE DYES FOR VIRAL RNA DETECTION

by

Ville Saarnio, Kirsi Salorinne, Visa Ruokolainen, Jesper Nilsson, Tiia-Riikka Tero, Sami Oikarinen, L. Marcus Wilhelmsson, Tanja Lahtinen, and Varpu Marjomäki 2020
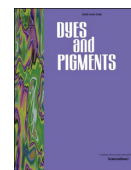
ELSEVIER

Development of functionalized SYBR green II related cyanine dyes for viral RNA detection

Ville K. Saarnio [a], Kirsi Salorinne [a], Visa P. Ruokolainen [b], Jesper R. Nilsson [c], Tiia-Riikka Tero [a], Sami Oikarinen [d], L. Marcus Wilhelmsson [c], Tanja M. Lahtinen [a,*], Varpu S. Marjomäki [b,**]

[a] Department of Chemistry, Nanoscience Center, Finland
[b] Department of Cell and Molecular Biology, Nanoscience Center, University of Jyväskylä, Jyväskylä, FI-40500, Finland
[c] Department of Chemistry and Chemical Engineering, Chemistry and Biochemistry, Chalmers University of Technology, Gothenburg, SE-41296, Sweden
[d] Faculty of Medicine and Life Sciences, University of Tampere, Tampere, FI-33014, Finland

ARTICLE INFO

ABSTRACT

Fluorescent probes for sensing nucleic acids have found widespread use in the field of cell and molecular biology. However, probes combined with potential for post-synthetic conjugation, *e.g.* for intra-endosomal measurements of RNA, are unavailable. Herein we developed cyanine dyes that can be conjugated to viral capsid or other targets. First, we solved the crystal structure of SYBR Green II. The structural elucidation of this commonly used RNA probe provided the basis for synthesizing similar molecules with much desired function for post-synthetic conjugation. To address this need, cyanine dyes were prepared using an alternative synthesis protocol. All studied compounds showed considerable brightness upon binding to nucleic acids. However, regardless of the common chromophore on the dyes, the observed fluorescence emission intensities varied significantly, where methyl-substituted dye **1** gave values higher than SYBR Green II, whereas compounds **2–5** containing undecyl spacers had lower values. Studying the structure-activity relationship revealed the longer alkyl chains to induce slight perturbation in dye intercalation, as well as demand larger binding area on the nucleic acid lattice, explaining these differences. To study the potential biological use of the dyes, the RNA genome of enterovirus echovirus 1 was studied *in vitro* with the probes. A novel method employing the low binding space requirement of **1** was developed to determine the single-to-double-stranded RNA ratio of a sample, whereas compound **4** was covalently bound to the viral capsid and used successfully to monitor the viral RNA release from within the capsid. The presented results open new possibilities for preparation and use of SYBR Green-based nucleic acid probes to further apply these compounds for increasingly demanding targeting in biological contexts.

1. Introduction

Many fluorescent probes for sensing nucleic acids are available nowadays. However, targeting possibilities for excluding interfering background signal from the molecules of interest remain suboptimal. For example, tools for sensing viral RNA from the background DNA/RNA present in a cellular environment are lacking. For such detection, a combination of light-up upon target binding and control over localization is desired. Cyanine dyes are defined as an organic molecule containing two nitrogen substituted heterocycles sharing a cationic charge through a polymethine bridge [1]. They are usually prepared with classical cyanine condensation reactions between two quaternary amine

salts [2]. Among their widespread applications, one of particular interest is their use as fluorescent probes [3]. For example, the Cy-family of symmetrical cyanine dyes is widely employed in different biological applications [4]. Most of these compounds have molar absorptivities in the magnitude of 10^4–10^5 cm^{-1}M^{-1}, with different compounds covering the whole visible light spectrum [2]. However, arguably the most important application of these compounds as fluorophores has been the use of unsymmetrical dyes for detection of nucleic acids through non-covalent binding, exhibiting an up to 1000-fold increase in fluorescence intensity upon binding [1]. A well-studied example from such dyes exhibiting this behavior is the thiazole orange (TO), consisting of monomethine bridged benzothiazolium and quinolinium units [5]. TO

---

* Corresponding author.
** Corresponding author.
E-mail addresses: tanja.m.lahtinen@jyu.fi (T.M. Lahtinen), varpu.s.marjomaki@jyu.fi (V.S. Marjomäki).

together with oxazole yellow (YO) and their homodimers (TOTO and YOYO) have served as a foundation for continuous development of these dyes [6–10]. The research on these dyes has also led to a wide range of commercially available nucleic acid stains [11]. Important and widely used commercial fluorophores include SYBR Green I, SYBR Green II, SYBR Safe, SYBR Gold and PicoGreen. While the chemical structures of PicoGreen [12], SYBR Safe [13] and SYBR Green I [12] have been reported, many routinely used compounds are still unknown [11]. A common descriptor for these dyes is their ability to interact with DNA and RNA, by intercalation [14].

Intercalators bind to double-stranded nucleic acids by assuming a planar conformation and inserting between stacked basepairs, forming π-π interactions with the target [14]. The reason for the great fluorescence enhancement is thought to be the result of restriction of the torsional motion of the molecule [15]. The group of Geddes [16,17] has shown that both PicoGreen and SYBR Green I form a similar complex with dsDNA, in which the aromatic quinolinium core unit intercalates into the dsDNA, while the benzothiazolium unit, carrying a localized positive charge enhances the binding affinity by providing additional electrostatic interactions with the DNA backbone. In addition, the dimethylaminopropyl side chains are positioned in the minor groove of the DNA for added stability of the complex [16,17]. However, knowledge on this family of dyes is mostly based on very few examples. Thus, understanding the structural and binding properties of the dye molecules is highly important when studying their binding and interaction with RNA or DNA. It is also crucial for future development of more selective, efficient and versatile dyes that enable the study of more complex biological systems, such as viruses and their mode of action in living cells.

The development of cyanine dyes for selective binding to nucleic acids has enabled the quantification of RNA or DNA content in various biological samples, and inspired their use as fluorescent probes in cell and molecular biology [18]. Nowadays, visualization of nucleic acids in electrophoresis gels using such dyes is performed routinely in cell and molecular biology laboratories [19]. Additionally, recent developments have enabled increasingly selective detection of different base content or secondary structure of nucleic acids [20,21]. However, imaging of larger macromolecular assemblies containing nucleic acids, such as RNA-containing viruses upon internalization into cells, is more challenging due to lower number of viruses in endosomes against a high background of messenger and transfer RNA in the cytoplasm. In addition, dynamic imaging of virus opening in cellular vesicles, a key step during infection, is problematic due to difficulties in targeting the dye to the same structures exclusively. The presently available dyes such as SYBR Green II are hydrophobic and easily cross all cellular membranes thus labeling all RNA in the cell. For successful imaging of *e.g.* virus particles in endosomes, one needs to have a nucleic acid detecting dye which can be conjugated to the virus or a suitable solid support to be endocytosed to the same structures, and not leaking to the cytoplasm. In addition, an optimal dye should also be highly specific for nucleic acids over other contaminating background material, sufficiently high in brightness for imaging by microscopy techniques, and low in cytotoxicity when working with living cells.

The aim of this work was to create cyanine dyes that can be covalently bound to the target material, such as virus capsids or nanoparticles for targeted RNA detection in microscopy imaging. As a basis for this, we used the widely employed RNA probe SYBR Green II after resolving its previously unknown chemical structure. Hence, the dyes synthesized in this work are all 2-thiol substituted and carry an oxazole moiety. A new synthetic pathway to produce similar such dyes was developed and five new compounds (**1–5**) were made. The rationale behind the use of a longer 11 carbon chain was to minimalize steric hindrance after conjugation. Spectroscopic evaluation of these dyes gave plausible explanations to the differences in brightness and revealed new information on the structure-activity relationships of these types of compounds. As a proof of principal, two of the most promising

compounds **1** and **4** were applied in our case study, to probe the RNA genome of echovirus 1 (EV1), in novel ways impossible to implement with SYBR Green II.

2. Results and discussion

2.1. Synthesis and structural properties

The synthetic pathway designed and used to produce molecules is presented in Scheme 1. First the 2-quinolone **6** was chlorinated using phosphorus oxychloride [22] in order to produce chloroiminium ion **7**. To avoid any undesired side reactions with the thiols, the solvents were evaporated before the next step. For the nucleophilic substitution of the chlorine, the thiol was added together with triethylamine and mixed for 4–6 days at room temperature in dry dichloromethane. After this, the cyanine condensation was carried out as described by Karlsson *et al.* in order to obtain the desired products [8]. Despite the efforts made to avoid reactions with the methyl thiolate, compound **1** was obtained as a side product from each synthesis due to the active thiolate from benzoxazole **9**. The intermediates and products were separated with flash column chromatography and gave MeS **1** with 10%–15% and the other dyes with 10%–37% yields. Individual yields and synthetic details are presented in the SI. From compound **3** the NHS-ester **4** was synthesized with N-hydroxysuccinimide (NHS) using Steglich esterification [23]. As the carboxylic acid moiety **3** proved very difficult to work with due to apparent impurities in the product, the methyl ester **5** was produced in an identical manner using methanol instead of NHS.

The presented synthesis procedure is straightforward, giving 2-thiol substituted cyanine dyes in three steps. Although a limited number of derivatives were made, the synthesis should be applicable with any other thiol, provided the compound is not sensitive to the basic conditions of the cyanine condensation. The yields of desired products could be improved by for example employing a stronger base in the nucleophilic substitution step to further promote thiolate formation. The substitution of the leaving group could be used as an advantage by manipulating the benzoxazole **9** to already contain the desired arm moiety. The structures of the synthesized dyes and the commercial ones used as comparison are presented in Fig. 1.
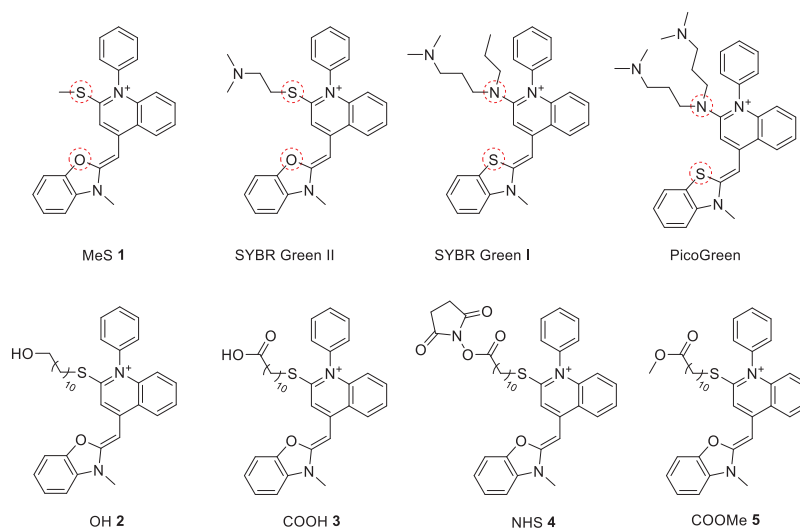
While the structures of SYBR Green I and PicoGreen are known from literature, the structure of SYBR Green II was here elucidated through X-ray crystallography, together with MeS **1** (Fig. 2a and b). The only difference in structure between the MeS dye **1** and SYBR Green II is the different pendant arm on the molecule. Comparing the crystal structure of SYBR Green II (Fig. 2c and d) to SYBR Green I and PicoGreen, the thiazole moiety is replaced with an oxazole and the 2-substituent is a thiol instead of a tertiary amine. As a result, SYBR Green I and PicoGreen have two propyl chains attached to the chromophore whereas SYBR Green II only has a 2-(dimethylamino)-ethyl group as the single "arm" on the molecule. The crystallographic details of the two compounds are summarized in Tables S1–S3. Dyes **2–5** did not crystallize in similar conditions, presumably due to the long alkyl chains hindering the crystal lattice formation. The functional group of the pendant arm affects the charge of the molecule. At slightly acidic pH, the *N*-2-(dimethylamino)-ethylthiolate arm of SYBR Green II can take on an additional positive charge by protonation of the amino group. This significantly improves the water solubility of the dye in comparison to the MeS dye **1**, as observed in the UV–vis measurements presented below.

2.2. Chromophore and binding properties

The structure of the chromophore unit of SYBR Green I related compounds is known from literature, and we discovered the structure of SYBR Green II to differ only by two hetero atoms (Fig. 1). These minor structural differences lead to a hypsochromic shift in the absorption of SYBR Green II compared to SYBR Green I, as shown in Fig. 3. The novel dyes presented in this work display absorption spectra that are similar to
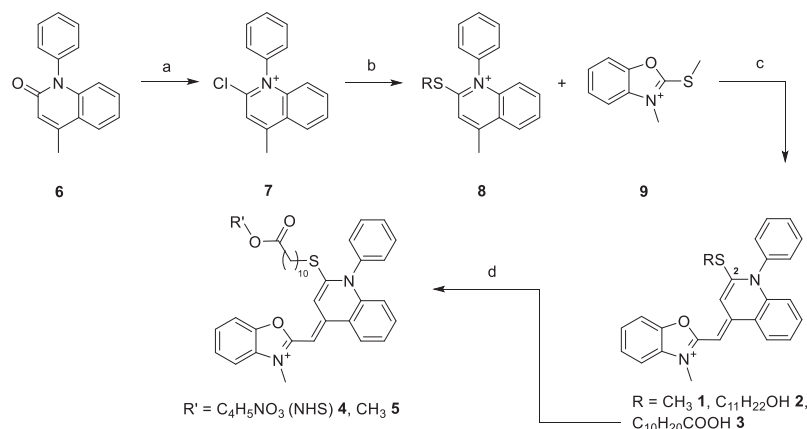
Scheme 1. Synthesis scheme for SYBR Green II related compounds. Reagents: a) POCl₃, 1,2-DCE, Δ; b) HSR (R = C₁₁H₂₂OH, C₁₀H₂₀COOH), Et₃N, DCM c) Et₃N, DCM d) DCC, DMAP and methanol or N-hydroxysuccinimide.


Fig. 1. Structures of the synthesized dyes (**1–5**). The structures of SYBR Green I, SYBR Green II and PicoGreen are shown for reference. The structural differences on the chromophores of the commercial dyes and MeS **1** are highlighted. (For interpretation of the references to color in this figure legend, the reader is referred to the Web version of this article.)

each other and to that of SYBR Green II. The differences in spectral characteristics can thus be attributed to the differences in the indoline (S *vs.* O) and the arm-binding hetero atom (N *vs.* S) shown with red circles in Fig. 1. Given the structural similarity, it would be expected that these molecules have molar absorptivities similar to that of SYBR Green II. Initial attempts to determine the molar absorptivity for the synthesized molecules (**1–5**) in TE buffer did, however, result in significantly different values for each dye. This is explained by the formation of aggregates (most likely H-type) and was particularly notable for the dyes aimed for biofunctionalization (**2–5**), as evidenced by scattering and hypsochromically shifted shoulders in the absorption spectra caused by H-aggregates (see Figs. S8–S12). The problem of aggregation was circumvented by changing the solvent to DCM (Table 1).

While the absorption characteristics of different dyes greatly impact their brightness, it is equally important to evaluate the binding properties of said dyes. One way to gain insight on the orientation of

molecules in a ligand-substrate interaction is to employ flow-oriented linear dichroism (LD). A short introduction to the method is presented in the SI page 7. To determine the binding mode to double-stranded DNA and investigate if the attachment of an alkyl-linker to the ligands affects the binding characteristics, LD was measured on the synthesized dyes. The alkyl-containing compounds, MeS **1**, OH **2**, NHS **4**, and COOMe **5** (see Fig. 1 for structures) were included in the LD-analysis. LD^r at 260 nm for a sample containing only DNA ($\theta = 90°$ for DNA bases in B-form duplex) was used to determine the orientation factor (found to be $S = 0.017$, Fig. 4). When studying the samples containing both DNA and ligand, using identical shear flow orientation conditions as for only DNA, a distinct negative LD band corresponding to the lowest energy electronic transition (centered at 484 nm, Fig. 4, middle panel) was observed for MeS **1**, OH **2**, and NHS **4**. For COOMe **5**, only a very weak overall LD signal was observed, also appearing as a negative band in the 480 nm region (data not shown). The weak LD signal for **5** is likely
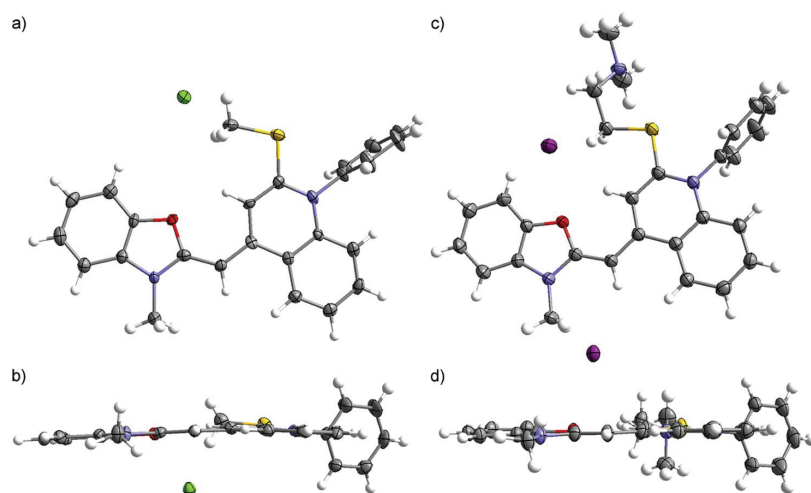
Fig. 2. Ortep drawing at 50% probability level of the crystal structure of MeS dye **1** shown from a) top and b) side views, and of SYBR Green II shown from c) top and d) side views. Element colors: carbon = grey, hydrogen = white, oxygen = red, nitrogen = blue, sulfur = yellow, chlorine = green and iodine = purple. (For interpretation of the references to color in this figure legend, the reader is referred to the Web version of this article.)
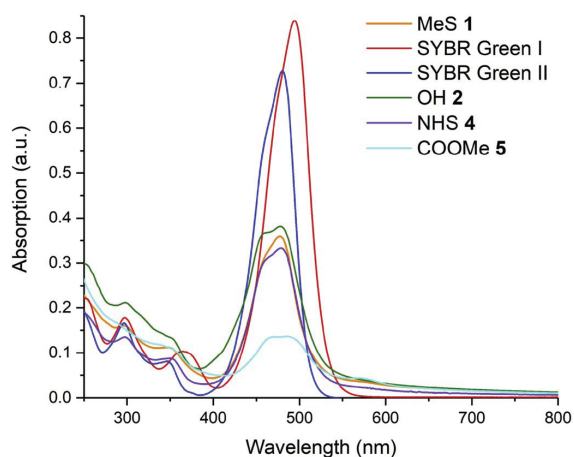
Fig. 3. UV–vis spectrum of MeS **1**, OH **2**, NHS **4** and COOMe **5** measured in TE Buffer at 19.6 µM concentration together with SYBR Green I and SYBR Green II at 1:1000 dilution from their respective stock solutions. (For interpretation of the references to color in this figure legend, the reader is referred to the Web version of this article.)

Table 1
Molar absorptivity measured in TE buffer and DCM at their lowest energy absorption maxima (*ca.* 478 nm) derived from Figs. S26 and S27.

Solvent	MeS **1**	OH **2**	NHS **4**	COOMe **5**	
TE buffer	19.2 ± 0.6	22.0 ± 0.5	18.5±0.2	7.9 ± 0.5	$\times 10^3$ $cm^{-1}mol^{-1}$
Dichloromethane	31.1 ± 0.3	38.8 ± 0.5	30.3 ± 0.9	11.6 ± 0.4	

the sole chromophore (with a transition dipole moment assumed to be in the plane of the essentially coplanar benzoxazolium and quinolinium heterocycles), was used to evaluate the binding angles relative to the DNA long axis. These were determined to be 86°, 70°, and 69° for MeS **1**, OH **2**, and NHS **4**, respectively. The calculated binding angles, in combination with the exclusively negative LD spectra, suggest DNA-binding by intercalation for the three analyzed compounds. It is noteworthy that OH **2** and NHS **4** (both having the alkyl linker) exhibit similar binding angles, yet lower than that of MeS **1**. This suggests that the binding mode of OH **2** and NHS **4** to DNA, although of evident intercalation character, is slightly affected by the presence of the attached linkers. From the
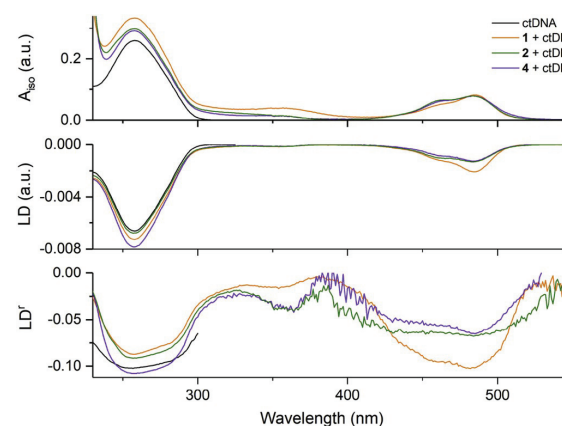
Fig. 4. Absorption and LD spectra of DNA in TE buffer with and without ligand. Concentration of DNA and ligand (where present) were 100 µM and 0.5 µM, respectively. DNA only (black line), DNA + MeS **1** (orange line), DNA + NHS **4** (violet line) and DNA + OH **2** (olive line). Top panel: Isotropic absorption. Middle panel: Linear dichroism. Bottom panel: Reduced linear dichroism (LD^r). Note that the difference in optical path length of the LD Couette cell (1 mm) and the cuvette used to determine A_{iso} (4 mm) was considered when calculating LD^r, *i.e.* $LD^r = 4 \times LD/A_{iso}$. (For interpretation of the references to color in this figure legend, the reader is referred to the Web version of this article.)

caused by poor compound solubility and aggregation in the aqueous solution, as evidenced by significant scattering in the isotropic absorption, hampering the evaluation of COOMe **5** under these experimental conditions. For MeS **1**, OH **2**, and NHS **4** LD^r at 484 nm, where the dye is

differences in binding angles it is conceivable that the linker participates in the binding by associating to one of the grooves of the DNA duplex, causing a slight displacement (tilt) of the ligand between the stacked bases and possibly also a slight distortion from exact coplanarity of the benzoxazolium and quinolinium moieties. This notion of a slight change in binding mode is further supported by the observed differences in binding constants and binding site size as described below. Understanding the impact the linking arms have on the nucleic acid binding modes of these dyes, before putting them into use in biological applications, is imperative.

For all synthesized compounds and SYBR Green II, the emission maximum wavelength was very close to 505 nm (Fig. 5), leading to compounds containing similar Stokes shifts in comparison to SYBR Green I. The emission maxima, when bound to fully double-stranded DNA remain the same, but as the portion of single-stranded nucleic acid is enhanced, increasing bathochromic shifts are also observed. This was observed as a small bathochromic shift to 515 nm when binding to cellular RNA (rRNA), while the fully linear 50 base ssDNA (liDNA) exhibits a significant shift to *ca.* 560 nm, as shown in Figs. S13–S18. Similar to the commercial dyes, the fluorescence of the synthesized dyes in solution without DNA was negligible, presumably due to non-radiative relaxation pathways (such as the rotation of the N-phenyl ring). Upon intercalation the fluorescence increases over a thousand-fold with SYBR Green I and similar enhancements are observed with the dyes prepared here (**1–5**). It is evident that higher intensity of emission was obtained for MeS **1** compared to SYBR Green II for all four types of nucleic acids used (see Fig. 6, Figs. S19, S20, and S22). These nucleic acids included rRNA, calf thymus DNA (ctDNA), bacterial double-stranded plasmid DNA (λDNA), liDNA and self-pairing hairpin forming 50 base ssDNA (hpDNA). SYBR Green I emits most strongly, but noticeably as the binding DNA gets more sterically demanding, the intensity difference compared to MeS dye **1** starts to diminish. This is clearly observed when moving from fully double-stranded DNA to rRNA, but the difference between SYBR Green I and MeS **1** gets significantly lower, when moving from ctDNA to hpDNA. The emission spectra of the dyes upon binding to liDNA (Fig. S13-S18, and S21) shows a large bathochromic shift compared to binding to the other nucleic acids but the intensity of this fluorescence remains small. The dyes containing longer 2-substituents seem to exhibit this characteristic more strongly, possibly indicating a different type of binding mode than intercalation that contributes to the lower energy emission. This suggestion is further supported by the divergence in intercalation angle observed for dyes **2**
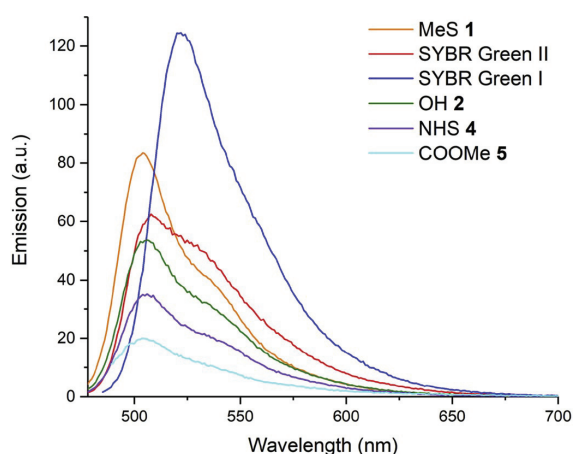
and **4** in the LD experiments. The emission intensities of thiol-substituted dyes stay proportional between each other with the different nucleic acids, whereas SYBR Green I experiences dramatic loss in emission when it is measured with nucleic acids that are not fully double-stranded. The fluorescence intensities of the long alkyl chain-containing dyes **2**, **4**, and **5** are significantly lower compared to the MeS dye **1**, yet still sufficiently bright to be applicable for the biological systems of interest here. In order to better understand the dye-nucleic acid interactions that lead to these differences in emission intensities with probes containing the same aromatic unit, a detailed analysis of fluorescence titration data was conducted, presented below.

Titration experiments conducted at pH 7.6 with each of the nucleic acids and plotting the highest values of emission intensity as the concentration increases gave binding isotherms for the interaction with dsDNA, displayed in Fig. 6 for ctDNA and Figs. S19–S22 for the other nucleic acids studied here. From this data it is possible to determine the binding constant to double-stranded DNA according to the methods employed by Dragan *et al.* for SYBR Green I [17] and PicoGreen [16]. In short, the theoretical expression for DNA-ligand interactions, McGhee von Hippel equation [24] for non-cooperative binding of ligands can be used to gain deeper insight into interactions between dyes and double-stranded nucleic acids:

$$v/L = K_a(1-nv)^n / (1-nv + v)^{n-1} \qquad (1)$$

where *v* is binding density of ligands in DNA, *L* is unbound ligands, K_a is the binding constant for complex formation and *n* is the size of the binding site of ligand in base pairs. The formation of supramolecular complex between the dye and dsDNA is an equilibrium reaction as shown in equation (2):

$$\text{Dye} + \text{dsDNA} \rightleftarrows [\text{Dye:dsDNA}] \qquad (2)$$

that can be described with the McGhee and Von Hippel equation [24]. From the binding isotherms, it is possible to express the fraction of dye molecules bound to DNA (θ) with the fraction of fluorescence observed (*F*) compared to fluorescence from 100% binding (F_b) as shown in equation (3):

$$\theta \approx F/F_b. \qquad (3)$$

The F_b was obtained from titration of dyes to high excess of DNA and the resulting linear behavior (Fig. S23). Equation (3) ignores the effect of non-bound dye to the fluorescence, which is reasonable as its contribution is negligible in all cases presented here.

Fig. 5. Fluorescence spectra of the tested cyanine dyes measured in TE buffer with 0.52 μM ctDNA at 21 °C. A 1:200 000 dilution from each stock was made corresponding 0.1 μM concentration except for COOMe **5** 1.0 μM was used.

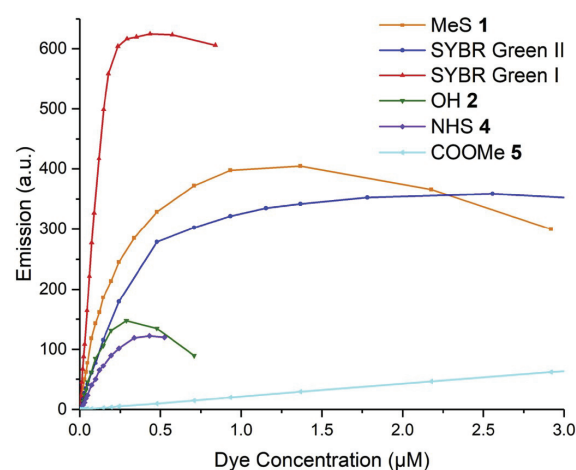**Fig. 6.** Binding isotherms from titrations of different dyes in 0.52 μM ctDNA in TE buffer at 21 °C.

Table 2
Summarized ctDNA binding parameters attained from fluorescence spectroscopy titrations. Fluorescence quantum yields were derived from Fig. S28.

Dye	Binding constant K_a (10^6 M^{-1})	Binding site size n (bp)	Gibbs free energy ΔG (kJ/mol)	Fluorescence quantum yield Φ
MeS **1**	3.9 ± 0.1	2.2 ± 0.03	-37	0.60
SYBR Green II	15 ± 2	2.8 ± 0.5	-40	0.36 [25]
SYBR Green I	5.9 ± 0.05	3.2 ± 0.11	-38	0.80 [26]
OH **2**	2.8 ± 0.4	3.4 ± 0.3	-36	0.47
NHS **4**	1.3 ± 0.06	3.2 ± 0.15	-34	0.63

Using θ it is possible to determine the concentration of free molecules in solution (L) according to equation (4)

$$L = (1 - \theta)c \qquad (4)$$

and binding density (v) of bound dye molecules

$$v = \theta c/c_{DNA}, \qquad (5)$$

where c is the concentration of the dye and c_{DNA} is the concentration of the nucleic acid in solution. Processing the generated data according to equations (3)–(5) gives the Scatchard plots shown in Fig. 7, Fig. S24 and S25, where a fit to equation (1) was done in order to get the binding constant and the binding site size for individual dye molecules expressed in base pairs. The data for ctDNA from this procedure is summarized in Table 2.

The binding affinity seems to increase as the arm moiety on the molecules gets longer, suggesting a positive effect of hydrophobic interactions between the nucleic acid groove and the dye arm in binding with λDNA (Table S4). However, as can be seen in Fig. 8, this also causes an increase in the size demanded by an individual molecule. The fit done on known values for different dyes indicates a linear dependence between binding site size and the arm length. The outlier in the series, OH **2** is the only molecule with an extended, completely linear 2-substituent and because of this, might be able to insert more completely to the dsDNA lattice. The results of binding site size acquired from ctDNA and λDNA are highly similar for the dyes with shorter "arm" lengths, but discrepancies appear for OH **2** and NHS **4**. Reasons for the better accommodation of long-armed dyes with λDNA could be better uniformity and more continuous dsDNA lattice, whereas ctDNA constitutes of a size distribution of dsDNA oligomers (and ssDNA as a side product). The effect is even more pronounced with hpDNA (Table S4), where unrealistic results are acquired because the theory does not account for the finite length of the dsDNA.

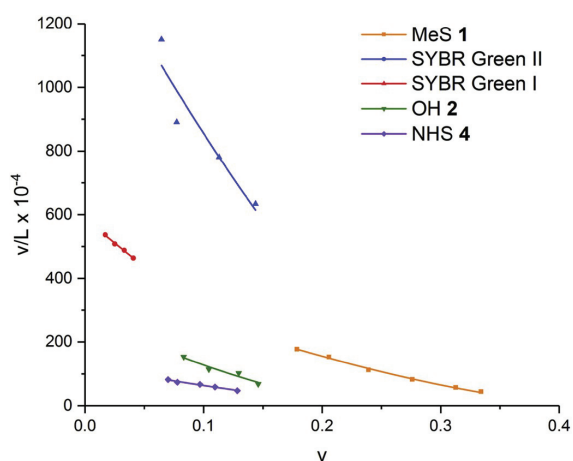The positively charged dimethyl amine groups seem to contribute

positively to the binding affinity, as evidenced by significantly higher association constants for SYBR Green I and SYBR Green II. The hydroxyl (OH **2**) and carboxylic acid (COOH **3** and COOMe **5**) groups on the other hand carry a negative partial charge, which could affect the groove binding negatively. An indication of this was given by the lower binding affinity of OH **2** compared to SYBR Green I despite its longer arm moiety, but a clear relationship cannot be established. The carboxylic acid functionalized dye **3** posed significant problems considering the sample purity and heavy aggregation in solution and hence the titration experiments were not successful. The fluorescence of the COOMe-functionalized compound **5** varied linearly with concentration throughout the titration, making determination of the binding constants impossible in the attempted concentration regime. The highest obtained fluorescence intensities for each dye with each nucleic acid are presented in Fig. 9.

The fluorescence quantum yield for MeS dye **1** when bound to ctDNA is 60%, which is comparable to the value of 54% given for SYBR Green II with RNA [25]. The corresponding value for SYBR Green II when bound to ctDNA is 36%. SYBR Green I, on the other hand, shows a higher quantum yield of 80% when bound to ctDNA and combined with its higher molar absorptivity, meaning that the thiazole chromophore with a N-linked arm moiety is brighter of the two [26]. The reason for the lower fluorescence saturation of SYBR Green I with rRNA compared to MeS **1** is most likely due to limitations in the number of binding sites available, as each molecule requires a longer stretch of double-stranded nucleic acid for binding. For SYBR Green II, the difference in fluorescence saturation intensity with rRNA should be a result of different binding site size, as the chromophores are the same in both molecules. Thus, the quality of a nucleic acid binding fluorophore is determined by two factors. First, the brightness of the bound chromophore plays a crucial role but, equally important are the parameters affiliated with the binding. With a longer arm on the molecule, the strength of binding

Fig. 7. Scatchard plot for cyanine dyes binding to ctDNA based on the data from Fig. 6 and Fig. S23 and fitting based on McGhee von Hippel equation (1).
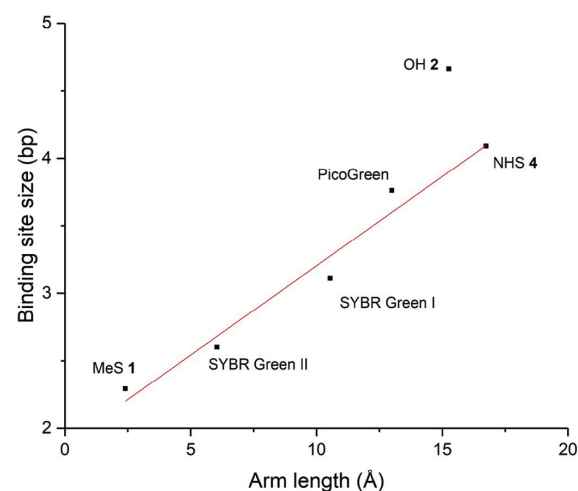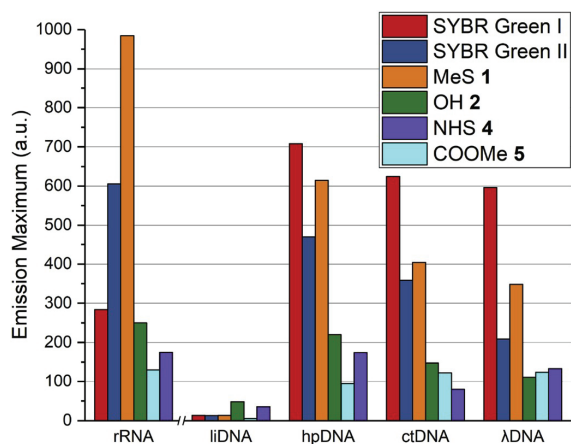

Fig. 8. Relationship between the length of the arm moiety on a molecule and corresponding binding site size in binding to λDNA (Table S4).

Fig. 9. Highest fluorescence values achieved from titrations with different nucleic acids. All the DNA samples were measured using the same settings on the spectrophotometer. All samples were measured in constant nucleic acid concentration in TE buffer at 21 °C and aliquots of respective dye were added until highest value of emission was reached. rRNA = cellular RNA, liDNA = 50 base linear ssDNA, hpDNA = 50 base self-pairing DNA, ctDNA = calf thymus DNA and λDNA = bacterial GLP-GPI plasmid DNA.

increases but in turn so does the size of the binding site. However, packing the probes too tightly on the double-stranded nucleic acids leads to homo-quenching between dye molecules. This means a careful balance exists between maximizing the number of probes bound to a nucleic acid without inducing such proximity between individual probes that leads to quenching. With this information, rational design can be used to synthesize probes that bind to nucleic acids with high affinity, such as SYBR Green I, or probes with slightly lower affinity but higher brightness as an effect of increased number of molecules bound to the target at maximum load, such as MeS **1**.

As the structures show, the differences between SYBR Green I and SYBR Green II are found in the different hetero atom on the 2-quinoline and 3-indole positions together with the linking arm of the molecules. Surprisingly, for our synthesized dyes, this leads to a significant decrease in the brightness of the chromophore, with the molar absorptivity decreasing by almost a half and the fluorescence quantum yield by 10%–20% compared to SYBR Green I. For the molecules synthesized in this work, this leads to a brightness that is ~40% of that of SYBR Green I. Although the chromophore of SYBR Green I has a higher brightness in nucleic acid contexts, the emission intensity of SYBR Green II is higher, when binding to rRNA. Importantly, compound **1** reaches even higher intensity when associating to rRNA. This can be explained by the characteristics of the complex formation across different dyes and especially the sizes of the binding site, (n) as shown in Table 2. While a single molecule of SYBR Green I occupies (in average) 3.1 base pairs on the dsDNA lattice, the length of lattice required by SYBR Green II and MeS dye **1** is only 2.8 and 2.2 base pairs, respectively. With lower available binding sites for the dyes, MeS **1** is the better nucleic acid probe as it makes better use of the limited binding sites. As proposed by the group of Geddes [16,17] the higher binding affinity comes as an effect of the arm moiety as the alkyl chains settle along the groove. This is something that we also observed here from the high binding constant value of compounds **2** and **4** with λDNA. Additionally, the cationic charge of the dimethylamine group in the arm of SYBR Green I and SYBR Green II adds an electrostatic component to the interaction and also increases the water solubility of the dyes. The synthesized products carry only one positive charge, which is insufficient for solubilizing the compounds and thus results in aggregation in aqueous solutions, as observed by scattering and aggregation in UV–vis absorption. This

should be taken into account in future work by either replacing the arm with a more hydrophilic molecule, such as ethyl glycol, or increasing the charge of the chromophore. Despite the drawbacks in solubility and increased binding site size, the biofunctionalized dyes **2** and **4** are still potent fluorophores. To show this, we evaluated the use of MeS **1** and NHS **4** in *in vitro* experiments on a viral genomic sample, Echovirus 1 RNA, as shown in the following section.

2.3. Case study: echovirus 1 genomic RNA

Viral RNA, as well as cellular RNA, typically forms secondary structures, which is the basis of fluorescence emission upon binding of the dyes synthesized in this work. Presently, there are very few RNA/DNA detecting molecules that could be used to detect viral genome release in cellular vesicles. Therefore, in this study, we aimed at developing RNA binding dyes that can be targeted to cellular vesicles by conjugating to carrier materials that are internalized to vesicles.

In order to prove that MeS **1** is able to detect viral RNA, we first tested the compound with a conventional method to detect RNA released from enterovirus echovirus 1 particles, namely a PaSTRy assay [27]. In this method, the viral genome is released from its capsid by gradually increasing the temperature to 90 °C. Melting temperature is measured to describe the stability of the virus and, for example, to test if drugs stabilize or destabilize the viruses. In the melting curve of virus particles, upon opening of the virus the emission values rapidly rose until about 60 °C, due to the release of viral RNA followed from capsid opening, after which the emission values then started to decrease again, as the rising temperature dissociates the dye-nucleic acid complex (Fig. 10). In the measurement, the emission of MeS **1** was significantly higher compared to that of SYBR Green II. This result further supports the observation that MeS **1** provides higher emission intensities compared to SYBR Green II (with sufficiently adjusted concentration). While the improvement in fluorescence intensity with MeS **1** in comparison to SYBR Green II was highly desirable, our initial objective was to develop a similar dye with potential for covalent attachment. To examine the potential of using NHS **4** as such a probe to sense RNA release from the virus capsid, the dye was conjugated to the free lysine residues found on EV1 capsid (see SI for details). NHS **4** conjugated on the echovirus 1 capsid surface gave an observable fluorescence peak (Fig. 10), despite being only a fraction in intensity compared to MeS **1**. Such a result was expected because less molecules are present on the
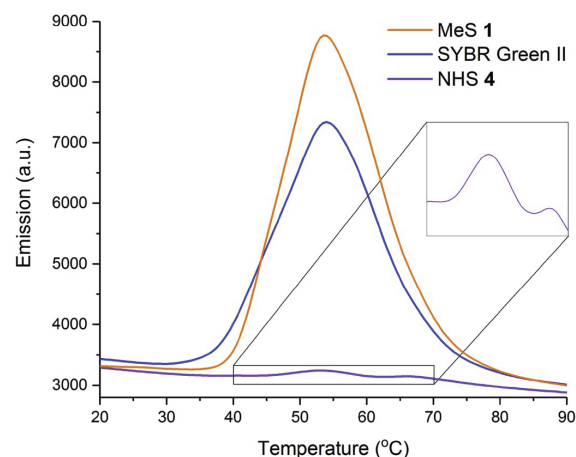
Fig. 10. Thermal assay melting curve of EV1 monitored with SYBR Green II, MeS **1**, as well as NHS **4**-conjugated virus particles. Inset: Magnification of the emission trace of **4**. (For interpretation of the references to color in this figure legend, the reader is referred to the Web version of this article.)

capsid surface compared to dye **1** that is free in solution. However, the long alkyl chain on **4** might contribute to weaker binding in higher temperature as well.

Next, we tested how our compounds detect viral RNA at physiological temperature in a real-time assay that was previously established in our laboratory [28]. Virus, nucleic acid probes and salt solution, that forces opening of the virus particles, were mixed together at 37 °C and fluorescence emission was followed for 3 h in a 96-well plate setup in a spectrofluorometer (Fig. 11). The results showed that the MeS **1** emission increased within 30 min to high values, due to addition of the opening buffer. Similarly, we tested NHS **4** which was directly conjugated to the virus capsid, thus being very close to the RNA in the event of RNA release. NHS **4** conjugated to the virus understandably showed much lower intensities but still detected virus opening at 37 °C. Thus, the two newly synthesized dyes MeS **1** and NHS **4** demonstrated their usability in nucleic acid sensing. While MeS **1** gave a good signal in the experiment, the values of NHS **4** conjugated on the viral particle surface were only 20% that of the former (Fig. 11). This was an expected result, as the amount of dye **4** molecules bound on the viral capsid surface is significantly lower compared to concentration of MeS **1** in solution. Interestingly, at around 20 min the emission of NHS **4** peaked in fluorescence before plateauing to 80% of the peak emission intensity, possibly indicating the moment where majority of the viral RNA is released from the viral particles before diffusing to the total sample volume. While the emission intensity of NHS **4** is lower *in vitro* compared to MeS **1**, it should be noted that the conjugation to the viral capsid means the emission is better localized.

As MeS **1** binding was based on binding to double stranded nucleic acid, we next tested whether we could quantify the portion of RNA that is in double-based conformation. Previously, many calculation-based estimations about secondary structures in viral RNA genomes have been made [29,30], but to our best knowledge no empirical studies on the degree of RNA duplex in the viral context have been made before. A method monitor the single-to-double-stranded RNA ratio in solution using PicoGreen has been previously reported [31,32]. However, our method aimed to utilize total fluorescence intensity instead of specific wavelengths or fluorescence lifetimes as the variable.

To evaluate this approach, a 50 base ssRNA template was mixed with excess amount of complementary ssRNA of varying length (15, 30 and 45 bases) and annealing was carried out to achieve base-pairing. Measuring the fluorescence from these samples with SYBR Green I, SYBR Green II, and MeS **1** present, gave four measurement points for each dye-RNA combination, as shown in Fig. 12. While neither of the
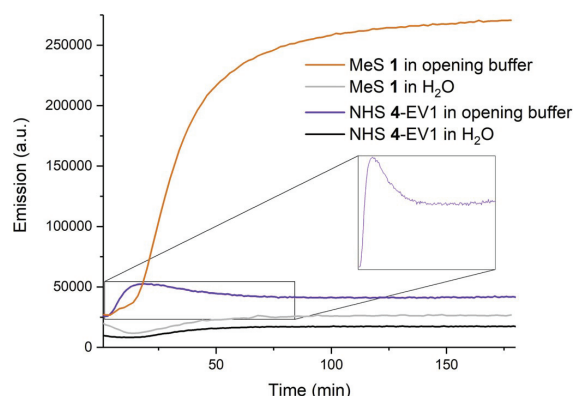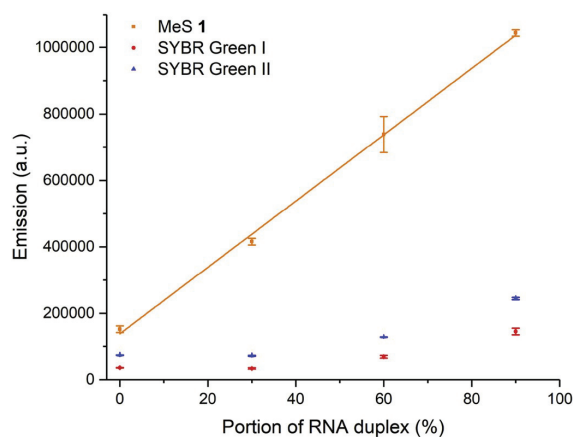

Fig. 12. MeS **1**, SYBR Green I, and SYBR Green II mixed with RNA constructs having varying amounts of double-strand. A 50-mer ssRNA was mixed with equimolar amounts of complementary ssRNA with lengths 15, 30, and 45 bases, respectively. Also shown is a linear fit for compound **1**. Measurements were performed in triplicates at room temperature (21 °C) in water. (For interpretation of the references to color in this figure legend, the reader is referred to the Web version of this article.)

SYBR Green dyes exhibited a linear dependence on RNA duplex, it was possible to construct a linear calibration curve for the MeS **1**. To further test this in practice, we attempted to determine the fraction of double-stranded RNA in released enterovirus EV1 RNA genome. As before, the virus opening was induced by adjusting the salt concentrations and increasing the temperature to 37 °C [28] allowing dyes to intercalate into the viral RNA. After preparing a calibration curve for MeS **1** in the capsid opening conditions, an EV1 sample containing equal amounts of RNA and dye (as applied to construct the calibration curve) was measured over the course of 180 min (Fig. S29). From this, the highest attained emission value was compared to the calibration curve (Fig. 13). This result corresponds to 51% of the viral RNA is in duplex form, which supports previous estimations stating that the viral RNA is expected to have large secondary structures [29,30].

Fig. 11. Emission of MeS **1** and NHS **4**-conjugated EV1 capsid in water and buffer solution (20 mM NaCl, 6 mM KH_2PO_4, 12 mM K_2HPO_4, pH ~7.2) promoting capsid opening for the EV1 at 37 °C. Inset: Magnification of the Y-axis to display NHS **4** curve better.
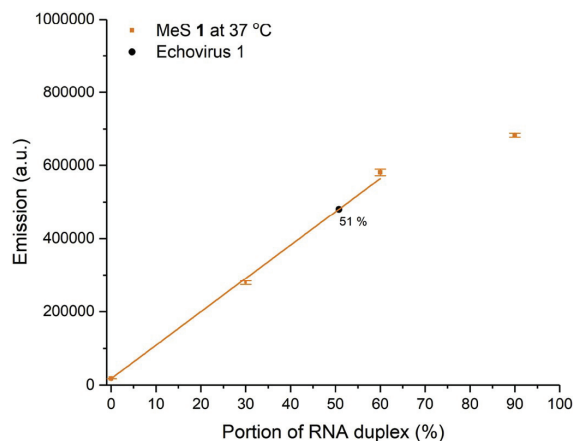

Fig. 13. MeS **1** measured with partially double-stranded RNA oligomers. The emission value from a sample of EV1 containing equal concentration of RNA and MeS **1** (Fig. S29) was inserted to the linear fit to yield the fraction of duplex RNA found in the sample. Measurements were performed in triplicates at 37 °C in 20 mM NaCl, 6 mM KH_2PO_4, 12 mM K_2HPO_4.

As an effect of the increased temperature and/or salt concentrations, the linearity of the calibration curve does not hold with the 45-mer sample, which underlines the importance of careful parametrization of the experiment for achieving reliable results throughout the full range of duplex formation. By increasing the amount of MeS **1** in experiments, the overall emission intensity can be increased to higher values compared to those attainable with SYBR Green II. Additionally, MeS **1** dye is more accommodating in this regard, because of its combined binding site size requirement and affinity for nucleic acid binding, as described in the previous section. Admittedly, similar results could be achieved with SYBR Green I and SYBR Green II, but the lower binding affinity and binding site size make MeS **1** a more universal choice, due to increased ease in adjusting concentrations in the experiments to achieve linearity. With such a calibration curve, the single-to-double-stranded RNA ratio of an unknown sample of equal mass of RNA can be determined. In this work, viral RNA of EV1 was used as an example. Information regarding the state of secondary structure of ssRNA should provide useful insight for the continuously increasing number of studies on RNA.

In conclusion, the two newly synthesized dyes MeS **1** and NHS **4** expand the potential of nucleic acid sensing with SYBR Green related cyanine dyes in two very different ways. While MeS **1** can be used to increase fluorescence emission intensity with RNA samples, its linear response to changes in portion of double-stranded RNA offers an enhanced application as shown above. NHS **4** on the other hand offers new possibilities for better targeting, as shown above by covalently linking the dye on a viral capsid surface. Similar click chemistry can be applied to any primary amine group from antibodies to nanoparticles, opening countless possibilities for refined nucleic acid sensing.

3. Conclusion

The successful crystallization of SYBR Green II led to elucidation of the previously unknown structural characteristics of this well-established RNA marker. Knowledge of the structure of the indolequinolinium-based cyanine dye enabled us to design a synthesis protocol to easily produce other 2-thiol substituted cyanine dyes at an analytical scale. This procedure was then employed to synthesize dyes **1**–**5** with varying 2-substituents, with the aim to add the potential of post-synthetic conjugation to *e.g.* antibodies or solid support.

The synthesized MeS **1** provides the highest fluorescence intensity when bound to nucleic acids and, importantly, higher in comparison to SYBR Green II, whereas compounds **2**–**5** gave lower values. Detailed studies between the synthesized and commercial dyes suggest that all the compounds are sensitive for nucleic acid sensing but MeS **1** as the smallest molecule takes less space in binding leading to higher overall emission compared to SYBR Green II. This is because the increasing size of the 2-substituent makes single molecules occupy more space on the nucleic acid strand and hence fewer molecules saturate the binding area available, leading to decreased fluorescence. These results offer fundamental understanding on the effects that different substituents might have on such intercalators. Regardless, all the synthesized dyes **1**–**5** exhibited considerable brightness.

Importantly, we could show with viral RNA samples that the produced dyes can sensitively detect RNA in biologically relevant assays. The dyes detected virus opening and RNA release *in vitro*: both unconjugated and a functionalized dye conjugated directly to viral particles detected virus opening in our developed real-time assay. This promises that in the future the conjugated dyes can be used to detect uncoating in cellular vesicles *in situ*. Similarly, the NHS-functionalized compound **4** can readily be employed for conjugation to any primary amine, providing added function for detection of nucleic acids with this class of fluorophores. Furthermore, the hydroxyl- and carboxylic acid functionalized dyes **2** and **3** can readily be employed to conjugate these dyes to a solid support or a biomolecule using carbodiimide crosslinking chemistry and thereby preventing dilution effects such as diffusion

through cell membranes. Although the brightness of these dyes (**2**–**5**) is lower due to their longer 2-substituents, these functional groups offer the possibility of a localized, non-diffusing source of fluorescence, which can be an attractive option for various microscopy imaging applications.

4. Experimental section

All reagents are commercially available and used as received unless otherwise mentioned. 1,2-dichloroethane (DCE) was distilled over $CaCl_2$ and stored under nitrogen over 3 Å molecular sieves. K_2CO_3 was dried in an oven at 120 °C and stored in a desiccator. SYBR Green I and II were purchased from Invitrogen as a solution in DMSO. Double-stranded bacterial plasmid λDNA (GLP-GPI 0.52 µg/µl) was received from ETH Zurich. Calf thymus (ct) DNA was purchased from Sigma-Aldrich. The 50 base long, single stranded DNAs were purchased from TAG Copenhagen A/S (Fredriksberg, Denmark) with sequences 5′-ACC AAA CTC AAC ACA CGA ACC CAA CGT TGG GTT CGT GTG TTG AGT TTG GT-3′ (hairpin DNA, hpDNA) and 5′-ACC CAC ACA ACC ACA AAC CAC ACC CAA CCC AAA CCC ACA CAC CCA ACA AC-3′ (linear DNA, liDNA) designed to promote hairpin and linear conformation of the oligomers, respectively. Both oligomers were dissolved in ddH$_2$O and the hpDNA was heated in boiling water bath for 3 min and allowed to cool down prior to use. Single stranded RNA oligomers were purchased from Eurofins Genomics (Ebersberg, Germany) as a 50 base template with sequence 5′-CCC AAC ACA ACC ACC AAC CAC AAA CAA CCC AAA CCC ACA CCA ACA ACA AAC-3′ and three complementary U/G strands of 15, 30 and 45 bases in length from the 3′ end (5′-UGU UGG UGU GGG UUU GGG UUG UUU GUG GUU GGU GGU UGU GUU GGG-3′). Cellular RNA (rRNA) was harvested from adenocarcinomic human alveolar basal epithelial cells (A549). The extraction was conducted using High Pure Viral RNA kit from Roche (Indianapolis, USA) following the instructions provided by the manufacturer. The concentration and purity of the extracted RNA was measured using Thermo Scientific NanoDrop One UV–vis spectrophotometer.

^{1}H, ^{13}C and 2D NMR (HSQC and HMBC) spectra were recorded with Bruker Avance 500 MHz and Bruker Avance 300 MHz spectrometers and chemical shifts were calibrated to the residual proton or carbon resonance of the solvent. Accurate HRMS spectra were measured with Micromass LCT ESI-TOF mass spectrometer using Leucine Enkephalin as the internal calibration. Atomic coordinates and structure factors for the reported crystal structures have been deposited with the Cambridge Crystallographic Data Centre (CCDC) under accession numbers 1482404 (SYBR Green II) and 1482405 (MeS **1**).

For comprehensive synthetic and experimental details please see the Supporting Information.

Pelkmans from ETH Zurich.

Appendix A. Supplementary data

Supplementary data to this article can be found online at https://doi.org/10.1016/j.dyepig.2020.108282.

References

[1] Bruce A. Armitage. Cyanine dye–nucleic acid interactions. In: Strekowski L, editor. Top. Heterocycl. Chem.. fourteenth ed. Pittsburgh: Springer; 2008. p. 11–29. https://doi.org/10.1007/7081_2007_109.

[2] Mojzych M, Maged H. Synthesis of cyanine dyes. Top. Heterocycl. Chem.. Springer; 2008. p. 1–9.

[3] Shindy HA. Fundamentals in the chemistry of cyanine dyes: a review. Dyes Pigments 2017;145:505–13. https://doi.org/10.1016/j.dyepig.2017.06.029.

[4] Choyke PL, Alford R, Simpson HM, Duberman J, Craig Hill G, Ogawa M, et al. Toxicity of organic fluorophores used in molecular imaging: literature review. Mol Imag 2009;8:341–54. https://doi.org/10.2310/7290.2009.00031.

[5] Lee LG, Chen C, Chiu LA. Thiazole orange: a new dye for reticulocyte analysis. Cytometry 1986;7:508–17. https://doi.org/10.1002/cyto.990070603.

[6] Vasilev AA, Kandinska MI, Stoyanov SS, Yordanova SB, Sucunza D, Vaquero JJ, et al. Halogen-containing thiazole orange analogues - new fluorogenic DNA stains. Beilstein J Org Chem 2017;13:2902–14. https://doi.org/10.3762/bjoc.13.283.

[7] Guo RJ, Yan JW, Chen S Bin, Gu LQ, Huang ZS, Tan JH. A simple structural modification to thiazole orange to improve the selective detection of G-quadruplexes. Dyes Pigments 2016;126:76–85. https://doi.org/10.1016/j.dyepig.2015.11.010.

[8] Karlsson HJ, Bergqvist MH, Lincoln P, Westman G. Syntheses and DNA-binding studies of a series of unsymmetrical cyanine dyes: structural influence on the degree of minor groove binding to natural DNA. Bioorg Med Chem 2004;12:2369–84. https://doi.org/10.1016/j.bmc.2004.02.006.

[9] Deligeorgiev TG, Gadjev NI, Vasilev AA, Maximova VA, Timcheva II, Katerinopoulos HE, et al. Synthesis and properties of novel asymmetric monomethine cyanine dyes as non-covalent labels for nucleic acids. Dyes Pigments 2007;75:466–73. https://doi.org/10.1016/j.dyepig.2006.06.023.

[10] Shank NI, Pham HH, Waggoner AS, Armitage BA. Twisted cyanines: a non-planar fluorogenic dye with superior photostability and its use in a protein-based fluoromodule. J Am Chem Soc 2013;135:242–51. https://doi.org/10.1021/ja308629w.

[11] Invitrogen. The molecular probes handbook: a guide to fluorescent probes and labeling technologies. Life Technologies Corporation; 2010.

[12] Zipper H, Brunner H, Bernhagen J, Vitzthum F. Investigations on DNA intercalation and surface binding by SYBR Green I, its structure determination and methodological implications. Nucleic Acids Res 2004;32:e103. https://doi.org/10.1093/nar/gnh101.

[13] Evenson WE, Boden LM, Muzikar KA, Oleary DJ. 1H and 13C NMR assignments for the cyanine dyes SYBR safe and thiazole orange. J Org Chem 2012;77:10967–71. https://doi.org/10.1021/jo3021659.

[14] Ihmels H, Otto D. Intercalation of Organic dye molecules into double-stranded DNA - general principles and recent developments. Top Curr Chem 2005;258:161–204. https://doi.org/10.1007/b135804.

[15] Karunakaran V, Pérez Lustres JL, Zhao L, Ernsting NP, Seitz O. Large dynamic Stokes shift of DNA intercalation dye Thiazole Orange has contribution from a high-frequency mode. J Am Chem Soc 2006;128:2954–62. https://doi.org/10.1021/ja056862n.

[16] Dragan AI, Casas-Finet JR, Bishop ES, Strouse RJ, Schenerman MA, Geddes CD. Characterization of PicoGreen interaction with dsDNA and the origin of its fluorescence enhancement upon binding. Biophys J 2010;99:3010–9. https://doi.org/10.1016/j.bpj.2010.09.012.

[17] Geddes CD, Dragan AI, Casas-Finet JR, Schenerman MA, McGivney JB, Strouse RJ, et al. SYBR green I: fluorescence properties and interaction with DNA. J Fluoresc 2012;22:1189–99. https://doi.org/10.1007/s10895-012-1059-8.

[18] Fei X, Gu Y. Progress in modifications and applications of fluorescent dye probe. Prog Nat Sci 2009;19:1–7. https://doi.org/10.1016/j.pnsc.2008.06.004.

[19] Jin X, Yue S, Singer VL, Jones LJ, Beaudet MP, Cheung C-Y, et al. Characterization of SYBR Gold nucleic acid gel stain: a dye optimized for use with 300-nm ultraviolet transilluminators. Anal Biochem 2003;288:278–88. https://doi.org/10.1006/abio.1998.3067.

[20] Crnolatac I, Rogan I, Majić B, Tomić S, Deligeorgiev T, Horvat G, et al. Small molecule probes finely differentiate between various ds- and ss-DNA and RNA by fluorescence, CD and NMR response. Anal Chim Acta 2016;940:128–35. https://doi.org/10.1016/j.aca.2016.08.021.

[21] Das AK, Ihmels H, Kölsch S. Diphenylaminostyryl-substituted quinolizinium derivatives as fluorescent light-up probes for duplex and quadruplex DNA. Photochem Photobiol Sci 2019;18:1373–81. https://doi.org/10.1039/c9pp00096h.

[22] Ying L. Nucleic acid detections and methods of their use. 2013. 2013/0137875.

[23] Neises B, Steglich W. Simple method for the esterification of carboxylic acids. Angew Chem Int Ed 1978;17:522–4.

[24] McGhee JD, von Hippel PH. Theoretical aspects of DNA-protein interactions: Cooperative and non-co-operative binding of large ligands to a one-dimensional homogeneous lattice. J Mol Biol 1974;86:469–89. https://doi.org/10.1016/0022-2836(74)90031-X.

[25] Molecular probes. SYBR ® green II RNA gel stain product information sheet, vols. 1–3; 2001.

[26] Invitrogen. SYBR ® green I nucleic acid gel stain product information sheet, vols. 1–5; 2006.

[27] Martikainen M, Salorinne K, Lahtinen T, Malola S, Permi P, Häkkinen H, et al. Hydrophobic pocket targeting probes for enteroviruses. Nanoscale 2015:17457–67. https://doi.org/10.1039/c5nr04139b.

[28] Ruokolainen V, Domanska A, Laajala M, Pelliccia M, Butcher SJ, Marjomäki V. Extracellular albumin and endosomal ions prime enterovirus particles for uncoating that can be prevented by fatty acid saturation. J Virol 2019. https://doi.org/10.1128/jvi.00599-19.

[29] Simmonds P, Tuplin A, Evans DJ. Detection of genome-scale ordered RNA structure (GORS) in genomes of positive-stranded RNA viruses: implications for virus-evolution and host persistence. Bioinformatics 2004;10:1337–51. https://doi.org/10.1261/rna.7640104.

[30] Davis M, Sagan SM, Pezacki JP, Evans DJ, Simmonds P. Bioinformatic and physical characterizations of genome-scale ordered RNA structure in Mammalian RNA viruses. J Virol 2008;82:11824–36. https://doi.org/10.1128/jvi.01078-08.

[31] Cosa G, Focsaneanu KS, McLean JRN, Scaiano JC. Direct determination of single-to-double stranded DNA ratio in solution applying time-resolved fluorescence measurements of dye-DNA complexes. Chem Commun 2000;8:689–90. https://doi.org/10.1039/b000473l.

[32] Beach L, Schweitzer C, Scaiano JC. Direct determination of single-to-double stranded DNA ratio in solution using steady-state fluorescence measurements. Org Biomol Chem 2003;1:450–1. https://doi.org/10.1039/b209284k.

IV

SYSTEMATIC STUDY OF SYBR GREEN CHROMOPHORE REVEALS MAJOR IMPROVEMENT WITH ONE HETEROATOM DIFFERENCE

by

Ville Saarnio, Johanna Alaranta, and Tanja Lahtinen

Submitted manuscript.

Request a copy from the author.

V

LINK AND RELEASE – COUPLING OF A GOLD NANOCLUSTER WITH A FLUOROPHORE FOR INTRACELLULAR PH IMAGING

by

Eero Hulkko, Tanja Lahtinen, Varpu Marjomäki, Emmi Pohjolainen, Ville Saarnio, Karolina Sokołowska, Ardra Ajitha, Mikael Kuisma, Lauri Lehtovaara, Gerrit Groenhof, Hannu Häkkinen, and Mika Pettersson

Submitted manuscript.

Request a copy from the author.

DEPARTMENT OF CHEMISTRY, UNIVERSITY OF JYVÄSKYLÄ
RESEARCH REPORT SERIES

1. Vuolle, Mikko: Electron paramagnetic resonance and molecular orbital study of radical ions generated from (2.2)metacyclophane, pyrene and its hydrogenated compounds by alkali metal reduction and by thallium(III)trifluoroacetate oxidation. (99 pp.) 1976

2. Pasanen, Kaija: Electron paramagnetic resonance study of cation radical generated from various chlorinated biphenyls. (66 pp.) 1977

3. Carbon-13 Workshop, September 6-8, 1977. (91 pp.) 1977

4. Laihia, Katri: On the structure determination of norbornane polyols by NMR spectroscopy. (111 pp.) 1979

5. Nyrönen, Timo: On the EPR, ENDOR and visible absorption spectra of some nitrogen containing heterocyclic compounds in liquid ammonia. (76 pp.) 1978

6. Talvitie, Antti: Structure determination of some sesquiterpenoids by shift reagent NMR. (54 pp.) 1979

7. Häkli, Harri: Structure analysis and molecular dynamics of cyclic compounds by shift reagent NMR. (48 pp.) 1979

8. Pitkänen, Ilkka: Thermodynamics of complexation of 1,2,4-triazole with divalent manganese, cobalt, nickel, copper, zinc, cadmium and lead ions in aqueous sodium perchlorate solutions. (89 pp.) 1980

9. Asunta, Tuula: Preparation and characterization of new organometallic compounds synthesized by using metal vapours. (91 pp.) 1980

10. Sattar, Mohammad Abdus: Analyses of MCPA and its metabolites in soil. (57 pp.) 1980

11. Bibliography 1980. (31 pp.) 1981

12. Knuuttila, Pekka: X-Ray structural studies on some divalent 3d metal compounds of picolinic and isonicotinic acid N-oxides. (77 pp.) 1981

13. Bibliography 1981. (33 pp.) 1982

14. 6th National NMR Symposium, September 9-10, 1982, Abstracts. (49 pp.) 1982

15. Bibliography 1982. (38 pp.) 1983

16. Knuuttila, Hilkka: X-Ray structural studies on some Cu(II), Co(II) and Ni(II) complexes with nicotinic and isonicotinic acid N-oxides. (54 pp.) 1983

17. Symposium on inorganic and analytical chemistry May 18, 1984, Program and Abstracts. (100 pp.) 1984

18. Knuutinen, Juha: On the synthesis, structure verification and gas chromatographic determination of chlorinated catechols and guaiacols occuring in spent bleach liquors of kraft pulp mill. (30 pp.) 1984

19. Bibliography 1983. (47 pp.) 1984

20. Pitkänen, Maija: Addition of BrCl, B_2 and Cl_2 to methyl esters of propenoic and 2-butenoic acid derivatives and ^{13}C NMR studies on methyl esters of saturated aliphatic mono- and dichlorocarboxylic acids. (56 pp.) 1985

21. Bibliography 1984. (39 pp.) 1985

22. Salo, Esa: EPR, ENDOR and TRIPLE spectroscopy of some nitrogen heteroaromatics in liquid ammonia. (111 pp.) 1985

23. Humppi, Tarmo: Synthesis, identification and analysis of dimeric impurities of chlorophenols. (39 pp.) 1985

24. Aho, Martti: The ion exchange and adsorption properties of sphagnum peat under acid conditions. (90 pp.) 1985

25. Bibliography 1985 (61 pp.) 1986

26. Bibliography 1986. (23 pp.) 1987

27. Bibliography 1987. (26 pp.) 1988

28. Paasivirta, Jaakko (Ed.): Structures of organic environmental chemicals. (67 pp.) 1988

29. Paasivirta, Jaakko (Ed.): Chemistry and ecology of organo-element compounds. (93 pp.) 1989

30. Sinkkonen, Seija: Determination of crude oil alkylated dibenzothiophenes in environment. (35 pp.) 1989

31. Kolehmainen, Erkki (Ed.): XII National NMR Symposium Program and Abstracts. (75 pp.) 1989

32. Kuokkanen, Tauno: Chlorocymenes and Chlorocymenenes: Persistent chlorocompounds in spent bleach liquors of kraft pulp mills. (40 pp.) 1989

33. Mäkelä, Reijo: ESR, ENDOR and TRIPLE resonance study on substituted 9,10-anthraquinone radicals in solution. (35 pp.) 1990

34. Veijanen, Anja: An integrated sensory and analytical method for identification of off-flavour compounds. (70 pp.) 1990

35. Kasa, Seppo: EPR, ENDOR and TRIPLE resonance and molecular orbital studies on a substitution reaction of anthracene induced by thallium(III) in two fluorinated carboxylic acids. (114 pp.) 1990

36. Herve, Sirpa: Mussel incubation method for monitoring organochlorine compounds in freshwater recipients of pulp and paper industry. (145 pp.) 1991

37. Pohjola, Pekka: The electron paramagnetic resonance method for characterization of Finnish peat types and iron (III) complexes in the process of peat decomposition. (77 pp.) 1991

38. Paasivirta, Jaakko (Ed.): Organochlorines from pulp mills and other sources. Research methodology studies 1988-91. (120 pp.) 1992

39. Veijanen, Anja (Ed.): VI National Symposium on Mass Spectrometry, May 13-15, 1992, Abstracts. (55 pp.) 1992

40. Rissanen, Kari (Ed.): The 7. National Symposium on Inorganic and Analytical Chemistry, May 22, 1992, Abstracts and Program. (153 pp.) 1992

41. Paasivirta, Jaakko (Ed.): CEOEC'92, Second Finnish-Russian Seminar: Chemistry and Ecology of Organo-Element Compounds. (93 pp.) 1992

42. Koistinen, Jaana: Persistent polychloroaromatic compounds in the environment: structure-specific analyses. (50 pp.) 1993

43. Virkki, Liisa: Structural characterization of chlorolignins by spectroscopic and liquid chromatographic methods and a comparison with humic substances. (62 pp.) 1993

44. Helenius, Vesa: Electronic and vibrational excitations in some

biologically relevant molecules. (30 pp.) 1993

45. Leppä-aho, Jaakko: Thermal behaviour, infrared spectra and x-ray structures of some new rare earth chromates(VI). (64 pp.) 1994

46. Kotila, Sirpa: Synthesis, structure and thermal behavior of solid copper(II) complexes of 2-amino-2- hydroxymethyl-1,3-pr opanediol. (111 pp.) 1994

47. Mikkonen, Anneli: Retention of molybdenum(VI), vanadium(V) and tungsten(VI) by kaolin and three Finnish mineral soils. (90 pp.) 1995

48. Suontamo, Reijo: Molecular orbital studies of small molecules containing sulfur and selenium. (42 pp.) 1995

49. Hämäläinen, Jouni: Effect of fuel composition on the conversion of fuel-N to nitrogen oxides in the combustion of small single particles. (50 pp.) 1995

50. Nevalainen, Tapio: Polychlorinated diphenyl ethers: synthesis, NMR spectroscopy, structural properties, and estimated toxicity. (76 pp.) 1995

51. Aittola, Jussi-Pekka: Organochloro compounds in the stack emission. (35 pp.) 1995

52. Harju, Timo: Ultrafast polar molecular photophysics of (dibenzylmethine)borondifluoride and 4-aminophthalimide in solution. (61 pp.) 1995

53. Maatela, Paula: Determination of organically bound chlorine in industrial and environmental samples. (83 pp.) 1995

54. Paasivirta, Jaakko (Ed.): CEOEC'95, Third Finnish-Russian Seminar: Chemistry and Ecology of Organo-Element Compounds. (109 pp.) 1995

55. Huuskonen, Juhani: Synthesis and structural studies of some supramolecular compounds. (54 pp.) 1995

56. Palm, Helena: Fate of chlorophenols and their derivatives in sawmill soil and pulp mill recipient environments. (52 pp.) 1995

57. Rantio, Tiina: Chlorohydrocarbons in pulp mill effluents and their fate in the environment. (89 pp.) 1997

58. Ratilainen, Jari: Covalent and non-covalent interactions in molecular recognition. (37 pp.) 1997

59. Kolehmainen, Erkki (Ed.): XIX National NMR Symposium, June 4-6, 1997, Abstracts. (89 pp.) 1997

60. Matilainen, Rose: Development of methods for fertilizer analysis by inductively coupled plasma atomic emission spectrometry. (41 pp.) 1997

61. Koistinen, Jari (Ed.): Spring Meeting on the Division of Synthetic Chemistry, May 15-16, 1997, Program and Abstracts. (36 pp.) 1997

62. Lappalainen, Kari: Monomeric and cyclic bile acid derivatives: syntheses, NMR spectroscopy and molecular recognition properties. (50 pp.) 1997

63. Laitinen, Eira: Molecular dynamics of cyanine dyes and phthalimides in solution: picosecond laser studies. (62 pp.) 1997

64. Eloranta, Jussi: Experimental and theoretical studies on some

quinone and quinol radicals. (40 pp.) 1997

65. Oksanen, Jari: Spectroscopic characterization of some monomeric and aggregated chlorophylls. (43 pp.) 1998

66. Häkkänen, Heikki: Development of a method based on laser-induced plasma spectrometry for rapid spatial analysis of material distributions in paper coatings. (60 pp.) 1998

67. Virtapohja, Janne: Fate of chelating agents used in the pulp and paper industries. (58 pp.) 1998

68. Airola, Karri: X-ray structural studies of supramolecular and organic compounds. (39 pp.) 1998

69. Hyötyläinen, Juha: Transport of lignin–type compounds in the receiving waters of pulp mills. (40 pp.) 1999

70. Ristolainen, Matti: Analysis of the organic material dissolved during totally chlorine-free bleaching. (40 pp.) 1999

71. Eklin, Tero: Development of analytical procedures with industrial samples for atomic emission and atomic absorption spectrometry. (43 pp.) 1999

72. Välisaari, Jouni: Hygiene properties of resol-type phenolic resin laminates. (129 pp.) 1999

73. Hu, Jiwei: Persistent polyhalogenated diphenyl ethers: model compounds syntheses, characterization and molecular orbital studies. (59 pp.) 1999

74. Malkavaara, Petteri: Chemometric adaptations in wood processing chemistry. (56 pp.) 2000

75. Kujala Elena, Laihia Katri, Nieminen Kari (Eds.): NBC 2000, Symposium on Nuclear, Biological and Chemical Threats in the 21st Century. (299 pp.) 2000

76. Rantalainen, Anna-Lea: Semipermeable membrane devices in monitoring persistent organic pollutants in the environment. (58 pp.) 2000

77. Lahtinen, Manu: *In situ* X-ray powder diffraction studies of Pt/C, CuCl/C and Cu_2O/C catalysts at elevated temperatures in various reaction conditions. (92 pp.) 2000

78. Tamminen, Jari: Syntheses, empirical and theoretical characterization, and metal cation complexation of bile acid-based monomers and open/closed dimers. (54 pp.) 2000

79. Vatanen, Virpi: Experimental studies by EPR and theoretical studies by DFT calculations of α-amino-9,10-anthraquinone radical anions and cations in solution. (37 pp.) 2000

80. Kotilainen, Risto: Chemical changes in wood during heating at 150-260 °C. (57 pp.) 2000

81. Nissinen, Maija: X-ray structural studies on weak, non-covalent interactions in supramolecular compounds. (69 pp.) 2001

82. Wegelius, Elina: X-ray structural studies on self-assembled hydrogen-bonded networks and metallosupramolecular complexes. (84 pp.) 2001

83. Paasivirta, Jaakko (Ed.): CEOEC'2001, Fifth Finnish-Russian Seminar: Chemistry and Ecology of Organo-Element Compounds. (163 pp.) 2001

84. Kiljunen, Toni: Theoretical studies on spectroscopy and

atomic dynamics in rare gas solids. (56 pp.) 2001

85. Du, Jin: Derivatives of dextran: synthesis and applications in oncology. (48 pp.) 2001

86. Koivisto, Jari: Structural analysis of selected polychlorinated persistent organic pollutants (POPs) and related compounds. (88 pp.) 2001

87. Feng, Zhinan: Alkaline pulping of non-wood feedstocks and characterization of black liquors. (54 pp.) 2001

88. Halonen, Markku: Lahon havupuun käyttö sulfaattiprosessin raaka-aineena sekä havupuun lahontorjunta. (90 pp.) 2002

89. Falábu, Dezsö: Synthesis, conformational analysis and complexation studies of resorcarene derivatives. (212 pp.) 2001

90. Lehtovuori, Pekka: EMR spectroscopic studies on radicals of ubiquinones Q-n, vitamin K$_3$ and vitamine E in liquid solution. (40 pp.) 2002

91. Perkkalainen, Paula: Polymorphism of sugar alcohols and effect of grinding on thermal behavior on binary sugar alcohol mixtures. (53 pp.) 2002

92. Ihalainen, Janne: Spectroscopic studies on light-harvesting complexes of green plants and purple bacteria. (42 pp.) 2002

93. Kunttu, Henrik, Kiljunen, Toni (Eds.): 4th International Conference on Low Temperature Chemistry. (159 pp.) 2002

94. Väisänen, Ari: Development of methods for toxic element analysis in samples with environmental concern by ICP-AES and ETAAS. (54 pp.) 2002

95. Luostarinen, Minna: Synthesis and characterisation of novel resorcarene derivatives. (200 pp.) 2002

96. Louhelainen, Jarmo: Changes in the chemical composition and physical properties of wood and nonwood black liquors during heating. (68 pp.) 2003

97. Lahtinen, Tanja: Concave hydrocarbon cyclophane π-prismands. (65 pp.) 2003

98. Laihia, Katri (Ed.): NBC 2003, Symposium on Nuclear, Biological and Chemical Threats – A Crisis Management Challenge. (245 pp.) 2003

99. Oasmaa, Anja: Fuel oil quality properties of wood-based pyrolysis liquids. (32 pp.) 2003

100. Virtanen, Elina: Syntheses, structural characterisation, and cation/anion recognition properties of nano-sized bile acid-based host molecules and their precursors. (123 pp.) 2003

101. Nättinen, Kalle: Synthesis and X-ray structural studies of organic and metallo-organic supramolecular systems. (79 pp.) 2003

102. Lampiselkä, Jarkko: Demonstraatio lukion kemian opetuksessa. (285 pp.) 2003

103. Kallioinen, Jani: Photoinduced dynamics of Ru(dcbpy)$_2$(NCS)$_2$ – in solution and on nanocrystalline titanium dioxide thin films. (47 pp.) 2004

104. Valkonen, Arto (Ed.): VII Synthetic Chemistry Meeting and XXVI Finnish NMR Symposium. (103 pp.) 2004

105. Vaskonen, Kari: Spectroscopic studies on atoms and small molecules isolated in low temperature rare gas matrices. (65 pp.) 2004

106. Lehtovuori, Viivi: Ultrafast light induced dissociation of Ru(dcbpy)(CO)$_2$I$_2$ in solution. (49 pp.) 2004

107. Saarenketo, Pauli: Structural studies of metal complexing Schiff bases, Schiff base derived *N*-glycosides and cyclophane π-prismands. (95 pp.) 2004

108. Paasivirta, Jaakko (Ed.): CEOEC'2004, Sixth Finnish-Russian Seminar: Chemistry and Ecology of Organo-Element Compounds. (147 pp.) 2004

109. Suontamo, Tuula: Development of a test method for evaluating the cleaning efficiency of hard-surface cleaning agents. (96 pp.) 2004

110. Güneş, Minna: Studies of thiocyanates of silver for nonlinear optics. (48 pp.) 2004

111. Ropponen, Jarmo: Aliphatic polyester dendrimers and dendrons. (81 pp.) 2004

112. Vu, Mân Thi Hong: Alkaline pulping and the subsequent elemental chlorine-free bleaching of bamboo (*Bambusa procera*). (69 pp.) 2004

113. Mansikkamäki, Heidi: Self-assembly of resorcinarenes. (77 pp.) 2006

114. Tuononen, Heikki M.: EPR spectroscopic and quantum chemical studies of some inorganic main group radicals. (79 pp.) 2005

115. Kaski, Saara: Development of methods and applications of laser-induced plasma spectroscopy in vacuum ultraviolet. (44 pp.) 2005

116. Mäkinen, Riika-Mari: Synthesis, crystal structure and thermal decomposition of certain metal thiocyanates and organic thiocyanates. (119 pp.) 2006

117. Ahokas, Jussi: Spectroscopic studies of atoms and small molecules isolated in rare gas solids: photodissociation and thermal reactions. (53 pp.) 2006

118. Busi, Sara: Synthesis, characterization and thermal properties of new quaternary ammonium compounds: new materials for electrolytes, ionic liquids and complexation studies. (102 pp.) 2006

119. Mäntykoski, Keijo: PCBs in processes, products and environment of paper mills using wastepaper as their raw material. (73 pp.) 2006

120. Laamanen, Pirkko-Leena: Simultaneous determination of industrially and environmentally relevant aminopolycarboxylic and hydroxycarboxylic acids by capillary zone electrophoresis. (54 pp.) 2007

121. Salmela, Maria: Description of oxygen-alkali delignification of kraft pulp using analysis of dissolved material. (71 pp.) 2007

122. Lehtovaara, Lauri: Theoretical studies of atomic scale impurities in superfluid ^{4}He. (87 pp.) 2007

123. Rautiainen, J. Mikko: Quantum chemical calculations of structures, bonding, and spectroscopic properties of some sulphur and selenium iodine cations. (71 pp.) 2007

124. Nummelin, Sami: Synthesis, characterization, structural and

retrostructural analysis of self-assembling pore forming dendrimers. (286 pp.) 2008

125. Sopo, Harri: Uranyl(VI) ion complexes of some organic aminobisphenolate ligands: syntheses, structures and extraction studies. (57 pp.) 2008

126. Valkonen, Arto: Structural characteristics and properties of substituted cholanoates and *N*-substituted cholanamides. (80 pp.) 2008

127. Lähde, Anna: Production and surface modification of pharmaceutical nano- and microparticles with the aerosol flow reactor. (43 pp.) 2008

128. Beyeh, Ngong Kodiah: Resorcinarenes and their derivatives: synthesis, characterization and complexation in gas phase and in solution. (75 pp.) 2008

129. Välisaari, Jouni, Lundell, Jan (Eds.): Kemian opetuksen päivät 2008: uusia oppimisympäristöjä ja ongelmalähtöistä opetusta. (118 pp.) 2008

130. Myllyperkiö, Pasi: Ultrafast electron transfer from potential organic and metal containing solar cell sensitizers. (69 pp.) 2009

131. Käkölä, Jaana: Fast chromatographic methods for determining aliphatic carboxylic acids in black liquors. (82 pp.) 2009

132. Koivukorpi, Juha: Bile acid-arene conjugates: from photoswitchability to cancer cell detection. (67 pp.) 2009

133. Tuuttila, Tero: Functional dendritic polyester compounds: synthesis and characterization of small bifunctional dendrimers and dyes. (74 pp.) 2009

134. Salorinne, Kirsi: Tetramethoxy resorcinarene based cation and anion receptors: synthesis, characterization and binding properties. (79 pp.) 2009

135. Rautiainen, Riikka: The use of first-thinning Scots pine (*Pinus sylvestris*) as fiber raw material for the kraft pulp and paper industry. (73 pp.) 2010

136. Ilander, Laura: Uranyl salophens: synthesis and use as ditopic receptors. (199 pp.) 2010

137. Kiviniemi, Tiina: Vibrational dynamics of iodine molecule and its complexes in solid krypton - Towards coherent control of bimolecular reactions? (73 pp.) 2010

138. Ikonen, Satu: Synthesis, characterization and structural properties of various covalent and non-covalent bile acid derivatives of N/O-heterocycles and their precursors. (105 pp.) 2010

139. Siitonen, Anni: Spectroscopic studies of semiconducting single-walled carbon nanotubes. (56 pp.) 2010

140. Raatikainen, Kari: Synthesis and structural studies of piperazine cyclophanes – Supramolecular systems through Halogen and Hydrogen bonding and metal ion coordination. (69 pp.) 2010

141. Leivo, Kimmo: Gelation and gel properties of two- and three-component Pyrene based low molecular weight organogelators. (116 pp.) 2011

142. Martiskainen, Jari: Electronic energy transfer in light-harvesting complexes isolated from *Spinacia oleracea* and from three

photosynthetic green bacteria *Chloroflexus aurantiacus*, *Chlorobium tepidum*, and *Prosthecochloris aestuarii*. (55 pp.) 2011

143. Wichmann, Oula: Syntheses, characterization and structural properties of [O,N,O,X´] aminobisphenolate metal complexes. (101 pp.) 2011

144. Ilander, Aki: Development of ultrasound-assisted digestion methods for the determination of toxic element concentrations in ash samples by ICP-OES. (58 pp.) 2011

145. The Combined XII Spring Meeting of the Division of Synthetic Chemistry and XXXIII Finnish NMR Symposium. Book of Abstracts. (90 pp.) 2011

146. Valto, Piia: Development of fast analysis methods for extractives in papermaking process waters. (73 pp.) 2011

147. Andersin, Jenni: Catalytic activity of palladium-based nanostructures in the conversion of simple olefinic hydro- and chlorohydrocarbons from first principles. (78 pp.) 2011

148. Aumanen, Jukka: Photophysical properties of dansylated poly(propylene amine) dendrimers. (55 pp.) 2011

149. Kärnä, Minna: Ether-functionalized quaternary ammonium ionic liquids – synthesis, characterization and physicochemical properties. (76 pp.) 2011

150. Jurček, Ondřej: Steroid conjugates for applications in pharmacology and biology. (57 pp.) 2011

151. Nauha, Elisa: Crystalline forms of selected Agrochemical actives: design and synthesis of cocrystals. (77 pp.) 2012

152. Ahkola, Heidi: Passive sampling in monitoring of nonylphenol ethoxylates and nonylphenol in aquatic environments. (92 pp.) 2012

153. Helttunen, Kaisa: Exploring the self-assembly of resorcinarenes: from molecular level interactions to mesoscopic structures. (78 pp.) 2012

154. Linnanto, Juha: Light excitation transfer in photosynthesis revealed by quantum chemical calculations and exiton theory. (179 pp.) 2012

155. Roiko-Jokela, Veikko: Digital imaging and infrared measurements of soil adhesion and cleanability of semihard and hard surfaces. (122 pp.) 2012

156. Noponen, Virpi: Amides of bile acids and biologically important small molecules: properties and applications. (85 pp.) 2012

157. Hulkko, Eero: Spectroscopic signatures as a probe of structure and dynamics in condensed-phase systems – studies of iodine and gold ranging from isolated molecules to nanoclusters. (69 pp.) 2012

158. Lappi, Hanna: Production of Hydrocarbon-rich biofuels from extractives-derived materials. (95 pp.) 2012

159. Nykänen, Lauri: Computational studies of Carbon chemistry on transition metal surfaces. (76 pp.) 2012

160. Ahonen, Kari: Solid state studies of pharmaceutically important molecules and their derivatives. (65 pp.) 2012

161. Pakkanen, Hannu: Characterization of organic material dissolved during alkaline pulping of wood and non-wood feedstocks. (76 pp.) 2012

162. Moilanen, Jani: Theoretical and experimental studies of some main group compounds: from closed shell interactions to singlet diradicals and stable radicals. (80 pp.) 2012

163. Himanen, Jatta: Stereoselective synthesis of Oligosaccharides by *De Novo* Saccharide welding. (133 pp.) 2012

164. Bunzen, Hana: Steroidal derivatives of nitrogen containing compounds as potential gelators. (76 pp.) 2013

165. Seppälä, Petri: Structural diversity of copper(II) amino alcohol complexes. Syntheses, structural and magnetic properties of bidentate amino alcohol copper(II) complexes. (67 pp.) 2013

166. Lindgren, Johan: Computational investigations on rotational and vibrational spectroscopies of some diatomics in solid environment. (77 pp.) 2013

167. Giri, Chandan: Sub-component self-assembly of linear and non-linear diamines and diacylhydrazines, formulpyridine and transition metal cations. (145 pp.) 2013

168. Riisiö, Antti: Synthesis, Characterization and Properties of Cu(II)-, Mo(VI)- and U(VI) Complexes With Diaminotetraphenolate Ligands. (51 pp.) 2013

169. Kiljunen, Toni (Ed.): Chemistry and Physics at Low Temperatures. Book of Abstracts. (103 pp.) 2013

170. Hänninen, Mikko: Experimental and Computational Studies of Transition Metal Complexes with Polydentate Amino- and Aminophenolate Ligands: Synthesis, Structure, Reactivity and Magnetic Properties. (66 pp.) 2013

171. Antila, Liisa: Spectroscopic studies of electron transfer reactions at the photoactive electrode of dye-sensitized solar cells. (53 pp.) 2013

172. Kemppainen, Eeva: Mukaiyama-Michael reactions with α-substituted acroleins – a useful tool for the synthesis of the pectenotoxins and other natural product targets. (190 pp.) 2013

173. Virtanen, Suvi: Structural Studies of Dielectric Polymer Nanocomposites. (49 pp.) 2013

174. Yliniemelä-Sipari, Sanna: Understanding The Structural Requirements for Optimal Hydrogen Bond Catalyzed Enolization – A Biomimetic Approach.(160 pp.) 2013

175. Leskinen, Mikko V: Remote β-functionalization of β'-keto esters. (105 pp.) 2014

176. 12th European Conference on Research in Chemistry Education (ECRICE2014). Book of Abstracts. (166 pp.) 2014

177. Peuronen, Anssi: N-Monoalkylated DABCO-Based N-Donors as Versatile Building Blocks in Crystal Engineering and Supramolecular Chemistry. (54 pp.) 2014

178. Perämäki, Siiri: Method development for determination and recovery of rare earth elements from industrial fly ash. (88 pp.) 2014

179. Chernyshev, Alexander, N.: Nitrogen-containing ligands and their platinum(IV) and gold(III) complexes: investigation and basicity and nucleophilicity, luminescence, and aurophilic interactions. (64 pp.) 2014

180. Lehto, Joni: Advanced Biorefinery Concepts Integrated to Chemical Pulping. (142 pp.) 2015

181. Tero, Tiia-Riikka: Tetramethoxy resorcinarenes as platforms for fluorescent and halogen bonding systems. (61 pp.) 2015

182. Löfman, Miika: Bile acid amides as components of microcrystalline organogels. (62 pp.) 2015

183. Selin, Jukka: Adsorption of softwood-derived organic material onto various fillers during papermaking. (169 pp.) 2015

184. Piisola, Antti: Challenges in the stereoselective synthesis of allylic alcohols. (210 pp.) 2015

185. Bonakdarzadeh, Pia: Supramolecular coordination polyhedra based on achiral and chiral pyridyl ligands: design, preparation, and characterization. (65 pp.) 2015

186. Vasko, Petra: Synthesis, characterization, and reactivity of heavier group 13 and 14 metallylenes and metalloid clusters: small molecule activation and more. (66 pp.) 2015

187. Topić, Filip: Structural Studies of Nano-sized Supramolecular Assemblies. (79 pp.) 2015

188. Mustalahti, Satu: Photodynamics Studies of Ligand-Protected Gold Nanoclusters by using Ultrafast Transient Infrared Spectroscopy. (58 pp.) 2015

189. Koivisto, Jaakko: Electronic and vibrational spectroscopic studies of gold-nanoclusters. (63 pp.) 2015

190. Suhonen, Aku: Solid state conformational behavior and interactions of series of aromatis oligoamide foldamers. (68 pp.) 2016

191. Soikkeli, Ville: Hydrometallurgical recovery and leaching studies for selected valuable metals from fly ash samples by ultrasound-assisted extraction followed by ICP-OES determination. (107 pp.) 2016

192. XXXVIII Finnish NMR Symposium. Book of Abstracts. (51 pp.) 2016

193. Mäkelä, Toni: Ion Pair Recognition by Ditopic Crown Ether Based bis-Urea and Uranyl Salophen Receptors. (75 pp.) 2016

194. Lindholm-Lehto, Petra: Occurrence of pharmaceuticals in municipal wastewater treatment plants and receiving surface waters in Central and Southern Finland. (98 pp.) 2016

195. Härkönen, Ville: Computational and Theoretical studies on Lattice Thermal conductivity and Thermal properties of Silicon Clathrates. (89 pp.) 2016

196. Tuokko, Sakari: Understanding selective reduction reactions with heterogeneous Pd and Pt: climbing out of the black box. (85 pp.) 2016

197. Nuora, Piia: Monitapaustutkimus LUMA-Toimintaan liittyvissä oppimisympäristöissä tapahtuvista kemian oppimiskokemuksista. (171 pp.) 2016

198. Kumar, Hemanathan: Novel Concepts on The Recovery of By-Products from Alkaline Pulping. (61 pp.) 2016

199. Arnedo-Sánchez, Leticia: Lanthanide and Transition Metal Complexes as Building Blocks for Supramolecular Functional Materials. (227 pp.) 2016

200. Gell, Lars: Theoretical Investigations of Ligand Protected Silver Nanoclusters. (134 pp.) 2016

201. Vaskuri, Juhani: Oppiennätyksistä opetussuunnitelman perusteisiin - lukion kemian kansallisen opetussuunnitelman kehittyminen Suomessa vuosina 1918-2016. (314 pp.) 2017

202. Lundell Jan, Kiljunen Toni (Eds.): 22nd Horizons in Hydrogen Bond Research. Book of Abstracts. 2017

203. Turunen, Lotta: Design and construction of halogen-bonded capsules and cages. (61 pp.) 2017

204. Hurmalainen, Juha: Experimental and computational studies of unconventional main group compounds: stable radicals and reactive intermediates. (88 pp.) 2017

205. Koivistoinen Juha: Non-linear interactions of femtosecond laser pulses with graphene: photo-oxidation, imaging and photodynamics. (68 pp.) 2017

206. Chen, Chengcong: Combustion behavior of black liquors: droplet swelling and influence of liquor composition. (39 pp.) 2017

207. Mansikkamäki, Akseli: Theoretical and Computational Studies of Magnetic Anisotropy and Exchange Coupling in Molecular Systems. (190 p. + included articles) 2018.

208. Tatikonda, Rajendhraprasad: Multivalent N-donor ligands for the construction of coordination polymers and coordination polymer gels. (62 pp.) 2018

209. Budhathoki, Roshan: Beneficiation, desilication and selective precipitation techniques for phosphorus refining from biomass derived fly ash. (64 pp.) 2018

210. Siitonen, Juha: Synthetic Studies on 1-azabicyclo[5.3.0]decane Alkaloids. (140 pp.) 2018

211. Ullah, Saleem: Advanced Biorefinery Concepts Related to Non-wood Feedstocks. (57 pp.) 2018

212. Ghalibaf, Maryam: Analytical Pyrolysis of Wood and Non-Wood Materials from Integrated Biorefinery Concepts. (106 pp.) 2018

DEPARTMENT OF CHEMISTRY, UNIVERSITY OF JYVÄSKYLÄ
DISSERTATIONS PUBLISHED IN THE JYU DISSERTATIONS RESEARCH SERIES

1. Bulatov, Evgeny: Synthetic and structural studies of covalent and non-covalent interactions of ligands and metal center in platinum(II) complexes containing 2,2′-dipyridylamine or oxime ligands. (58 pp.) 2019. JYU Dissertations 70.

2. Annala, Riia: Conformational Properties and Anion Complexes of Aromatic Oligoamide Foldamers. (80 pp.) 2019. JYU Dissertations 84.

3. Isoaho, Jukka Pekka: Dithionite Bleaching of Thermomechanical Pulp - Chemistry and Optimal Conditions. (73 pp.) 2019. JYU Dissertations 85.

4. Nygrén, Enni: Recovery of rubidium from power plant fly ash. (98 pp.) 2019. JYU Dissertations 136.

5. Kiesilä, Anniina: Supramolecular chemistry of anion-binding receptors based on concave macromolecules. (68 pp.) 2019. JYU Dissertations 137.

6. Sokolowska, Karolina: Study of water-soluble p-MBA-protected gold nanoclusters and their superstructures. (60 pp.) 2019. JYU Dissertations 167.

7. Lahtinen, Elmeri: Chemically Functional 3D Printing: Selective Laser Sintering of Customizable Metal Scavengers. (71 pp.) 2019. JYU Dissertations 175.

8. Larijani, Amir: Oxidative reactions of cellulose under alkaline conditions. (102 pp.) 2020. JYU Dissertations 217.

9. Kolari, Kalle: Metal-metal contacts in late transition metal polymers. (60 pp.) 2020. JYU Dissertations 220.

10. Kauppinen, Minttu: Multiscale computational investigation of catalytic properties of zirconia supported noble metals. (87 pp.) 2020. JYU Dissertations 231.

11. Ding, Xin: Halogen Bond in Crystal Engineering: Structural Studies on Crystals with Ruthenium Centered Complexes and 1-(4-Pyridyl)-4-thiopyridine Zwitterion as Halogen Bond Acceptors. (59 pp.) 2020. JYU Dissertations 323.

12. Neuvonen, Antti: Toward an Understanding of Hydrogen-Bonding Bifunctional Organocatalyst Conformations and Their Activity in Asymmetric Mannich Reactions. (77 pp.) 2020. JYU Dissertations 336.

13. Kortet, Sami: 2,5-Diarylpyrrolidines and Pyroglutamic-Acid-Derived 2-Diarylmethyl-5-Aryl-Pyrrolidines: Their Synthesis and Use in Asymmetric Synthesis. (221 pp.) 2020. JYU Dissertations 337.